Numerical Study of Fluid Flows in a Cavity

By:

Muhammad Arshad Siddiqui
Reg. No. 20-FBAS/PHDMA/F12

Department of Mathematics and Statistics
Faculty of Basic and Applied Sciences
International Islamic University, Islamabad
Pakistan
2019

Numerical Study of Fluid Flows in a Cavity

By:

Muhammad Arshad Siddiqui
Reg. No. 20-FBAS/PHDMA/F12

Supervised By:

Dr. Tariq Javed

Department of Mathematics and Statistics
Faculty of Basic and Applied Sciences
International Islamic University, Islamabad
Pakistan
2019

Numerical Study of Fluid Flows in a Cavity

By:

Muhammad Arshad Siddiqui
Reg. No. 20-FBAS/PHDMA/F12

A Dissertation

Submitted in the Partial Fulfillment of the

Requirements for the Degree of

DOCTOR OF PHILOSOPHY

In

MATHEMATICS

Supervised By:

Dr. Tariq Javed

Department of Mathematics and Statistics
Faculty of Basic and Applied Sciences
International Islamic University, Islamabad
Pakistan
2019

Author's Declaration

I, **Muhammad Arshad Siddiqui** Reg. No. **20-FBAS/PHDMA/F12** hereby state that my Ph.D. thesis titled: **Numerical Study of Fluid Flows in a Cavity** is my own work and has not been submitted previously by me for taking any degree from this university, **International Islamic University, Sector H-10, Islamabad, Pakistan** or anywhere else in the country/world.

At any time if my statement is found to be incorrect even after my Graduation the university has the right to withdraw my Ph.D. degree.

Name of Student: ***(Muhammad Arshad Siddiqui)***
Reg. No. **20-FBAS/PHDMA/F12**
Dated: **23/01/2019**

Plagiarism Undertaking

I solemnly declare that research work presented in the thesis titled: **Numerical Study of Fluid Flows in a Cavity** is solely my research work with no significant contribution from any other person. Small contribution/help wherever taken has been duly acknowledged and that complete thesis has been written by me.

I understand the zero tolerance policy of the HEC and University, **International Islamic University, Sector H-10, Islamabad, Pakistan** towards plagiarism. Therefore, I as an Author of the above titled thesis declare that no portion of my thesis has been plagiarized and any material used as reference is properly referred/cited.

I undertake that if I am found guilty of any formal plagiarism in the above titled thesis even after award of Ph.D. degree, the university reserves the rights to withdraw/revoke my Ph.D. degree and that HEC and the University has the right to publish my name on the HEC/University Website on which names of students are placed who submitted plagiarized thesis.

Student/Author Signature: _____

Name: **(Muhammad Arshad Siddiqui)**

Certificate of Approval

This is to certify that the research work presented in this thesis, entitled: **Numerical Study of Fluid Flows in a Cavity** was conducted by **Mr. Muhammad Arshad Siddiqui,** Reg. No. **20-FBAS/PHDMA/F12** under the supervision of **Dr. Tariq Javed** no part of this thesis has been submitted anywhere else for any other degree. This thesis is submitted to the **Department of Mathematics & Statistics, FBAS, IIU, Islamabad** in partial fulfillment of the requirements for the degree of **Doctor of Philosophy in Mathematics, Department of Mathematics & Statistics, Faculty of Basic & Applied Science, International Islamic University, Sector H-10, Islamabad, Pakistan.**

Student Name: Muhammad Arshad Siddiqui Signature: _____

Examination Committee:

a) External Examiner 1:
Name/Designation/Office Address **Signature: _____**

Prof. Dr. Tasawar Hayat
Professor of Mathematics,
Department of Mathematics,
QAU, Islamabad.

b) External Examiner 2:
Name/Designation/Office Address) **Signature: _____**

Prof. Dr. Saleem Asghar
Professor of Mathematics,
Department of Mathematics,
COMSATS, IIT, Park Road, Chak Shahzad,
Islamabad.

c) Internal Examiner:
Name/Designation/Office Address) **Signature: _____**

Prof. Dr. Muhammad Sajid T.I
Professor

Supervisor Name:
Dr. Tariq Javed **Signature: _____**

Name of Dean/HOD:
Prof. Dr. Muhammad Sajid, T.I **Signature: _____**

Acknowledgements

In the name of **Allah** (سبحانہ وتعالیٰ) who is the creator of the universe. The only one to whom all the praise belongs. Millions of Daroods upon **Prophet Muhammad (PBUH)** who is the role model for every believer. Although only my name appears on the title of the dissertation however there is generous contribution and support of many people who have encouraged and helped me throughout the process of innovative task.

First of all I would like to extend my gratitude to my supervisor **Dr. Tariq Javed** for his tremendous academic and moral support. I thank him for encouraging my research. Similar profound gratitude goes to **Prof. Dr. Muhammad Sajid**, Chairman Department of Mathematics and Statistics, International Islamic University, Islamabad, for providing research platform to the department. All the faculty members of department have been so kind to extend their help whenever I approached them, I acknowledge all of them.

This research work would not have come to successful completion without the support and help given by my seniors, colleagues and fellows at research lab. A special mention goes to **Dr. Ziafat Mehmood** who was available for discussions and help throughout the tenure of my research. I consider myself privileged to have **Dr. Bilal Ahmed** and **Mr. Abdul Haleem Hamid** as my colleagues and friends at the lab and for their availability to share my feelings and ideas un-hesitantly. I appreciate the enormous help and support through fruitful discussions with my respected seniors **Dr. Ahmed Zeeshan, Dr. Hussain Ahmad (late)**, **Dr. Abuzar Ghaffari**, **Dr. Irfan Mustafa** and **Dr. Abid Majeed,** I learnt a lot from them. I would like to extend my thanks to my junior colleagues and MS scholars **Mr. Sohail Ahmed Channar**, **Mr. Wassi-ur-Rehman**, **Mr. Taimor bin Zain**, **Mr. Muhammad Aiyaz**, **Mr. Ahmed Ali** and **Mr. Waqas Nazeer** for helping me in a special way. The role my friends, **Mr. Shoukat Ali Khan**, **Mr. Ramzan Mani**, **Mr. Malik Farooq**, **Mr. Mazhar Iqbal**, **Mr. Raja Ghufran Kiani**, **Mr. Waqas Ahmed** and **Mr. Touseef Tufail** is also worthy to be mentioned over here whose moral support and encouragement helped me a lot to fulfill my research work.

Words cannot express my gratitude towards my family for supporting and helping me in every possible way to see the completion of my dissertation. I am very much indebted to my father **Ghulam Muhammad Siddiqui** for their priceless prayers, help and encouragement at every stage of my academic and personal life. My brothers **Abdul Razzaq, Fazal Razzaq, Muhammad Akhtar and Muhammad Asif**, sisters **Aisha Bibi**, **Sughra Zulfiqar**, **Asifa Qasim**, **Qurrat ul Ain**, **Rashida** my wife **Maryam** her father **Dr. Abdul Rauf** along with his family, my daughter **Aimen** and son **Abdul Rehman** waited long to see this achievement come true. I am truly thankful to all my family members as your prayers sustained me thus far. I deeply miss my mother **Jannat un Nissa (late)** as she is not with me to share this joy. May her soul be granted high ranks in Jannah-tul-firdos (Ameen).

I also want to acknowledge the support provided by "**Higher Education Commission (HEC)**" of Pakistan through project number 3713 under the scheme "National Research Program for Universities"

At the end, I am highly grateful to all those whom I couldn't mention namely but they played their supportive role towards the completion of my doctoral thesis.

Muhammad Arshad Siddiqui

Dedicated

To

My Honorable Father

Ghulam Muhammad Siddiqui

Who has always been a source of inspiration,

motivation and role model

throughout my life.

Preface

Convective heat transfer through cavities of various geometrical shapes is an important research area because of its significant practical and engineering applications. Most of time, energy flow with respect to natural or mixed convection is considered in engineering system for example, solar ponds, dynamics of lakes, cooling of electronic devices, heating and cooling buildings, thermal hydraulics of nuclear reactors, growth of crystals, chemical reactors, production of float glass, heat exchangers and food processing etc. In most of cases, several of such practical flow conditions of energy transport and fluid flow take place in an enclosure in which flow is produced by buoyant force, shear force or both together. Shape of the cavities plays a dynamic role in transfer of heat in order to obtain higher energy transport rates. This dissertation comprises of the investigations regarding natural and mixed convective energy transport in triangular, rectangular, square and entrapped triangular enclosures containing different type of fluids in vacuum or flows through saturated porous medium. Furthermore, present study also contains the studies on heat transfer through pure fluid, micropolar fluid, nanofluid and ferrofluid enclosed in the cavities. Investigations are performed against different shapes of cavities subjected to the various thermal boundary conditions. In this dissertation, Galerkin weighted residual technique of finite element analysis is applied to solve governing nonlinear coupled partial differential equations (e.g. conservation of mass, linear momentum, angular momentum and conservation of energy) for the pure fluid or fluids saturated in porous media against different velocities and thermal boundary conditions.

The first chapter mainly includes basic definitions related to heat transfer phenomena, non-dimensional quantities and some basic laws considered in this study. This chapter

also includes a brief literature review on cavity flows. The detail of numerical scheme used in this dissertation is also provided in this chapter.

Chapter two contains numerical simulations of free convection heat transfer through fluid saturated in the isosceles triangular porous medium influenced by magnetic force. The inclined walls of an isosceles triangular cavity are supposed to be heated uniformly/non-uniformly. Effects of involved flow parameters are shown through graphs of streamline contours, isotherm contours, heat transfer rate and average heat transfer rate. The investigation presented in this chapter is **published** in **Zeitschrift für naturforschung A (ZNA) 70 (11) (2015) 919 - 928.**

Computational study of natural convection energy transport through liquid gallium saturated in porous medium enclosed in square cavity influenced by inclined magnetic force has been performed in chapter three. Bottom wall of the cavity is considered to be heated uniformly, top wall is taken insulated, left side of enclosure is heated linearly and right side is subject to linear heating or taken cold. Governing nonlinear coupled partial differential equations are solved by using Galerkin weighted residual method and obtained results are presented through graphs. The study presented in this chapter has been **published** in **Thermophysics and Aeromechanics 25 (3) (2018).**

Chapter four comprises numerical simulations of mixed convection through micropolar fluid contained in square cavity influenced by constant magnetic field. Bottom wall of the cavity is subject to non-uniform heating profile while remaining walls are maintained at low temperature. Numerical results are computed incorporating Galerkin method of finite element technique against different values of involved parameters in terms of micropolar parameter, Grashof, Reynolds and Hartmann numbers. The investigation considered in this chapter is **published** in **Journal of Molecular Liquids 249 (2018) 831 - 842.**

Numerical simulations of free convective heat transfer affected by external magnetic field through ferrofluid contained in a square cavity when a heated square blockage with different aspect ratios is placed at the centre of enclosure have been discussed in chapter five. Results are shown against various ranges of physical flow parameters such as Hartmann, Prandtl and Rayleigh numbers. This chapter is **published** in **International Journal of Thermal Sciences 125 (2018) 419–427.**

Chapter six includes computational results for mixed convective energy flow in cobalt-based ferrofluid enclosed in a two-sided lid-driven square container provided heat from left vertical moving boundary under MHD effects influenced by a source of heat generation/absorption when a square adiabatic block of different aspect ratios located in a center of a square container. The obtained numerical results against flow parameters such as nano-scale ferromagnetic particles, heat generation/absorption coefficient, Hartmann, Reynolds and Richardson numbers are shown through graphs of streamlines, isotherms, local and average heat transfer rates. The findings of this chapter are **accepted** for publication in **The European Physical Journal Plus (2018).**

Numerical computations for free convective heat transfer through nanofluid saturated porous medium in entrapped triangular cavities have been discussed in chapter seven. Inclined walls of cavities are taken cold while horizontal walls are assumed heated uniformly. Obtained numerical results are shown in the form of flow patterns, isotherms, temperature gradient and average temperature gradient for wide range of physical parameters including solid volume fraction, porosity parameter, Darcy, Prandtl and Rayleigh numbers. The outcomes of this chapter are **submitted** in **Advances in Mechanical Engineering** for possible publication.

Chapter eight conveys the mixed convection heat transfer within entrapped triangular enclosures saturated with a micropolar. The horizontal upper and lower walls of the

enclosures are moving with uniform velocity and these are subjected to uniform heat however inclined walls are kept as cold. The pertinent flow parameters under discussion are solid volume fraction, Hartmann number, Richardson number, Reynolds number, microrotation coefficient and heat source/sink coefficient. Obtained solutions are illustrated through graphs of isotherms, local and average heat transfer rates. The contents of this chapter have been **accepted** for publication in **Canadian Journal of Physics (2018).**

Contents

Nomenclature

A	Height of the heated/adiabatic block, m
Ar	Aspect ratio ($Ar = \frac{A}{H}$), m
B	Micropolar parameter
B_0	Magnetic induction, Tesla
c_p	Specific heat, $\frac{J}{kg\ K}$
Da	Darcy number
g	Gravitational acceleration, m/s^2
Gr	Grashof Number
H	Cavity height, m
Ha	Hartmann number
j	Micro-inertia density
k	Thermal conductivity
K	Permeability of porous medium
K_1	Microrotation coefficient
L	Cavity length
N	Microrotation, m
Nu	Nusselt number
p	Modified pressure
P	Non-dimensional pressure
Pr	Prandtl Number
Q_0	Heat generation/absorption
Q	Non-dimensional heat generation/absorption
Ra	Rayleigh number
Re	Reynolds Number
T	Temperature
T_c	Temperature at cold wall
T_h	Temperature at cold wall
(u, v)	Dimensional velocity components
(U, V)	Non-dmensional velocity components
(U_0, V_0)	Velocities of moving walls

V	Velocity field
(x, y)	Dimensional Cartesian coordinates
(X, Y)	Non-dimensional Cartesian coordinates

Greek Symbols

α	Thermal diffusivity
β	Coefficient of thermal expansion
γ	Penalty parameter
γ_1	Spin-gradient viscosity
ΔT	Temperature difference
ε	Porosity parameter
θ	Non-dimensional temperature
κ	Vortex viscosity
μ	Dynamic viscosity
ν	Kinematic viscosity
ρ	Local density
ρ_0	Characteristic density
σ	Electrical conductivity
ϕ	Solid volume fraction
φ_i	Base functions
ψ	Non-dimensional stream function
Ω	Internal Domain

Subscripts

f	Base fluid
ff	Ferrofluid
nf	Nanofluid
s	Solid particles

Chapter 1

Preliminaries

This chapter contains some qualitative concepts of convective heat transfer, Non-dimensional numbers, fundamental laws, mathematical models and numerical study related to the research presented in this dissertation. The comprehensive literature survey from the very beginning of the heat transfer in enclosures/cavities has also been included for better understanding of the readers.

1.1 Convective Heat Transfer

Generally convective heat transfer, indicated as simply convection in which energy is transmitted from one place to another because of the movement of fluid particles. During the process of heat transfer in liquid and gases, convection is found dominant. In most cases it is referred as a distinct mode of heat transfer. Instead of this combination of convection and conduction is known as convective transfer of heat.

The heat transfer rate (q) can be measure with the help of given formula:

$$q = -hA\left(T_{surface} - T_{\infty}\right), \tag{1.1}$$

here $T_{surface}$ represents the surface temperature, T_{∞} be the ambient temperature, A be the surface area and h is convection coefficient. The convection coefficient is a measure of how effectively a fluid transport energy away and towards the surface. It depends on the factors such as velocity, viscosity and density of a flowing fluid. Heat transfer coefficient usually has greater values for the fluids having higher velocity and/or higher density.

Here, we can distinguish between three types of convection

(i) Natural convection

(ii) Forced convection

(iii) Mixed convection

1.1.1 Natural Convection

Transfer of heat through natural convection is a heat transfer among the surface and fluid flowing over it and fluid movement is caused by the buoyance force that arises because of changes in density due to temperature variations. In natural convection, fluid expands when temperature increases and density decreases. Since hot fluids are less dense or more buoyant than cold fluid, therefore when a hot surface is in contact

with surrounding fluid, its molecules disperse and distributes within the domain, which then arises because of buoyancy force. Then hot fluid molecules are exchanged by cold fluid molecules. Similarly, cold substances will draw energy away from the flowing fluid over the surface, which then collapse because of augmentation in fluid density. The molecules of cold fluid are then exchanged by the molecules of the hot fluid, originating convective flows. Familiar examples related to natural convection are hot body and circulations of fluid in a pot subject to the heated from below and flow of air because of fire.

1.1.2 Forced Convection

In forced convection flows, motion of fluid is caused by other than buoyant forces or by means of some external forces such that fan or pump. Thermal expansion of fluid may also be an example of forced convection. The term forced convective heat transfer is only applicable to flows in which the influence of buoyant forces is unimportant. Generally forced convective heat transfer is more effective as compared to natural convective heat transfer because of the faster velocity of a flowing fluid. Most common example related to forced convection is water pump placed in an automobile engine.

1.1.3 Mixed Convection

The buoyance force arises due to change in temperature which originates the flow in natural convective heat transfer, it also exist when there is a forced convective heat transfer. During forced flows, the effects of buoyancy forces are usually negligible. In many cases, buoyancy forces have a significant influence on heat transfer and flow rates. In such cases, transfer of heat around the body is a mixture of natural and forced convective heat transfer flows and this phenomenon is called combined or mixed convective heat transfer flow.

Convective heat transfer is involved in many engineering applications e.g. cooling and heating of buildings, cooling and heating of electronic components in computer, cooking, thermal control of reentering spacecraft, generation and condensation in a thermal power plant and cooling and heating of the cutting tool during a matching operation.

1.2 Basic Equations

1.2.1 Law of Conservation of Mass

The mass conservation law yields the so-called continuity equation. The continuity equation states that mass cannot be created or destroyed. Continuity equation may be obtained by using the law of conservation of mass and expressed mathematically as:

$$\frac{\partial \rho}{\partial t} + \boldsymbol{\nabla}.(\rho \boldsymbol{V}) = 0. \tag{1.2}$$

For steady and incompressible flows equation (1.2) becomes

$$\boldsymbol{\nabla}.(\boldsymbol{V}) = 0. \tag{1.3}$$

1.2.2 Law of Conservation of Momentum

Each particle of fluid obeys Newton's second law which is at rest or in steady state or accelerated motion. This law states that the quantity of net external forces applied on a set of particles must be equal to the time rate of change of the momentum of a set of particles. Newton's second law of motion acting on fluid particles may be defined mathematically as:

$$\rho \frac{D\boldsymbol{V}}{Dt} = \boldsymbol{\nabla}.\boldsymbol{\tau} + \boldsymbol{f}, \tag{1.4}$$

where $\boldsymbol{\tau}$ represents the Cauchy stress tensor which may be written as:

$$\begin{pmatrix} \sigma_{xx} & \tau_{yx} & \tau_{zx} \\ \tau_{xy} & \sigma_{yy} & \tau_{zy} \\ \tau_{xz} & \tau_{yz} & \sigma_{zz} \end{pmatrix}, \tag{1.5}$$

here σ_{xx}, σ_{yy} and σ_{zz} denotes normal stresses along x, y and $z-$axis directions respectively, while all remaining elements in symbol $\boldsymbol{\tau}$ with different subscripts given in Eq. (1.13) represents shear stresses.

For micropolar fluid in the absence of the body forces, momentum equation along with law of angular momentum becomes

$$\rho j \frac{d\boldsymbol{N}}{dt} = \gamma_1 \boldsymbol{\nabla}(\boldsymbol{\nabla}.\boldsymbol{N}) - \gamma_1 \boldsymbol{\nabla} \times (\boldsymbol{\nabla} \times \boldsymbol{N}) + \kappa \boldsymbol{\nabla} \times \boldsymbol{V} - 2\kappa \boldsymbol{N}, \tag{1.6}$$

where $\boldsymbol{N}$ and $\boldsymbol{V}$ are micro-rotation and velocity vectors, j is gyration parameter of the fluid, κ and γ_1 are vortex viscosity and spin gradient viscosity respectively.

1.2.3 Law of Conservation of Energy

The energy conservation law, which is also known as energy equation may be described mathematically as:

$$\rho c_p \frac{DT}{Dt} = \nabla.(k\nabla T) + Q_o \Delta T, \tag{1.7}$$

where ρ represents density of fluid, c_p be the specific heat, T be the temperature of fluid and Q_o be the heat generation/absorption coefficient.

1.2.4 Maxwell's Equations

Expression of Maxwell's equations represents law like other well-known laws for example gravitational law. A magnetic field is generated due to the production of electric current and if this current changes with respect to time it will cause the generation of electric field. Mathematically we may express Maxwell's equations as:

$$\nabla.\mathbf{E} = 0, \nabla.\mathbf{B} = 0,$$
$$\nabla \times \mathbf{E} = -\frac{\partial \mathbf{B}}{\partial \mathbf{t}}, \nabla \times \mathbf{B} = \mu_m \mathbf{J}. \tag{1.8}$$

These Maxwell's equations are valid only in the case of displacement current is ignored.

1.2.5 Ohm's Law

$$\mathbf{J} = \sigma(\mathbf{E} + \mathbf{V} \times \mathbf{B}). \tag{1.9}$$

In above Equation $\boldsymbol{J}$ represents the electric current density, σ be the electric conductivity, $\boldsymbol{E}$ be the electric field in vector form, $\mathbf{V}$ be the velocity vector of the moving charges and $\boldsymbol{B}$ be the magnetic field vector.

1.3 Non-Dimensional Quantities

The following numbers are the common non-dimensional numbers which are used in fluid mechanics as well as in this dissertation.

1.3.1 Reynolds Number (Re)

Reynolds number may be expressed as a relationship between inertial and viscous forces thus making Reynolds number useful for predicting the nature of the flow (Laminar, Turbulent or transition) thus making some approximations valid by knowing nature of the flow. Mathematically, it can be expressed as:

$$\mathrm{Re} = \frac{\text{inertial force}}{\text{viscous force}} = \frac{UL}{\nu}, \tag{1.10}$$

where U represents the speed of moving surface, L be its length and ν is kinematics viscosity of the fluid.

1.3.2 Prandtl Number (Pr)

Ludwig Prandtl a German physicist, introduced Prandtl number as a dimensionless parameter which also represents the ratio of viscous diffusivity to thermal diffusivity. In mathematics, it may be defined as:

$$\mathrm{Pr} = \frac{\text{viscous diffusivity}}{\text{thermal diffusivity}} = \frac{\nu}{\alpha} = \frac{c_p \mu}{k}, \tag{1.11}$$

where c_p denotes the specific heat, α be the thermal diffusivity, k be the thermal conductivity and μ be the dynamic viscosity.

1.3.3 Grashof number (Gr)

The ratio of buoyant forces to the viscous forces acting on fluid particles is known as Grashof number, named by the German engineer Franz Grashof. Mostly it occurs during the study which involves natural or free convection and is similar to the Reynolds number (Re). Mathematically, Grashof number denoted by

$$\mathrm{Gr} = \frac{\text{buoyancy forces}}{\text{viscous forces}} = \frac{g\beta\Delta T L^3}{\nu^2}, \tag{1.12}$$

where g represents the gravitational acceleration, L be a length of the cavity, β be coefficient of thermal expansion, ΔT be temperature difference and ν be the kinematic viscosity

1.3.4 Rayleigh Number (Ra)

In fluid dynamics Rayleigh number is represented as non-dimensional parameter and it is also associated with buoyancy driven flow. The magnitude of the Rayleigh number is a good indicator of either natural or free convective boundary layer is turbulent or laminar. Mathematically, it represents the product of Prandtl number (Pr*)* and Grashof number (Gr*)* may be expressed as:

$$\mathrm{Ra} = \mathrm{GrPr} = \frac{\text{buoyancy}}{\text{viscous} \times \text{rate of heat diffusion}} = \frac{g\beta\Delta T L^3}{\nu^2}\frac{\nu}{\alpha}. \tag{1.13}$$

1.3.5 Richardson Number

Lewis Fry Richardson first introduced Richardson number as a non-dimensional parameter and it also associated with buoyance forces and inertial forces. It represents the ratio between the buoyant forces to the inertial forces. If the Richardson number is very small nearly equal to zero then buoyancy force becomes unimportant in the flow. On the other hand dominance of buoyance force occurs if it is much greater than unity. If it is equal to one then the flow is expected to be buoyance driven flow. Mathematically it can be written in the form:

$$\mathrm{Ri} = \frac{\mathrm{Gr}}{\mathrm{Re}^2} = \frac{\text{buoyance force}}{\text{inertial force}} = \frac{g\beta\Delta TL}{U^2}. \tag{1.14}$$

1.3.6 Nusselt Number (Nu)

German mathematician Nusselt, introduced Nusselt number as a non-dimensional parameter which is also expressed as a ratio of convection mode to conduction mode under same conditions. Furthermore, it is used to investigate heat transfer rate numerically at boundaries between the surface and flowing fluid. Nusselt number is close to conduction and convection of same magnitude and it also described as laminar flow. Mathematically, it is defined as follows:

$$\mathrm{Nu} = \frac{\text{Convective heat transfer}}{\text{Conductive heat transfer}} = \frac{hL}{k}, \tag{1.15}$$

here h represents heat transfer coefficient, L be cavity length and k be thermal conductivity of the flowing fluid.

In differential form it can be expressed as:

$$\mathrm{Nu} = \frac{\partial\theta}{\partial X}, \tag{1.16}$$

where θ represents the non-dimensional temperature.

The average Nusselt number may be measured by performing integration on equation (1.8) over the range of interest, which can be expressed mathematically as:

$$\overline{\mathrm{Nu}} = \frac{1}{H}\int_0^H Nu(y)dy. \tag{1.17}$$

1.4 Methodology

The fluid flows proposed in this study will be considered via two dimensional Navier-Stokes equations which are represented by the set of nonlinear partial differential equations. The nonlinearity occurs due to convective part in Navier-Stokes equations. This is due to the reason why Navier-Stokes equations are difficult and are even impossible to solve analytically. There are several circumstances in which fluid flows may be associated with Navier-Stokes equations such as the fluid flowing inside or around a pipe, flow in a channel, blood flow, flow inside a cavity, airflow around a wing and many more. Recently, there are several numerical schemes which are in use by various investigators to simplify these equations numerically e.g. finite difference scheme, Keller box method, spectral method, finite volume technique, Lattice Boltzmann simulation and finite element method. All these approaches are in wide use to obtain numerical results of linear or nonlinear flow problems. It has been noticed that the finite element technique is established as a precious tool for solving

Navier-Stokes flow problems particularly where complex geometrical domains or thermal conditions on boundaries are involved in comparison with other numerical and analytical methods through which computing accurate solution is difficult or impossible. To show this numerical methodology is more consistent, we can summarize the advantages and disadvantages of these methods in few words as follows:

Finite difference technique is very easy to implement and in programming for the domain which may be divided in rectangles of equal dimensions. However, it has major drawbacks because it is difficult for the curved domain, secondly it has difficult convergence analysis and stability and finally, it is very difficult in mesh adaptation, which is essential in future, investigation. The finite volume scheme depends on the physical conservation laws of the system to be studied. It is problematic on the unstructured meshed and its convergence analysis and stability are difficult as for finite difference method. Opposite to this, finite element method is high in accuracy and provides easy treatment for the complex boundary conditions with complex geometries.

1.5 Finite Element Method (FEM)

FEM is a powerful numerical tool to analyze the nonlinear or linear differential equations. It mainly assists the finding of the numerical results of the boundary value problems for nonlinear or linear differential equations. In this method, a large domain is subdivided into collection of smaller, simpler domain using mesh levels called finite elements. Basically this method is an easy presentation of whole domain (Reddy (1993)).

1.5.1 Galerkin Weighted Residual Method

Explaining the observation numerically, the Galerkin weighted residual method is used in finite element scheme. Final calculations are easily originated by combining the local system into global system with set of elements. Moreover, Galerkin method is also compatible for linear and non-linear coupled partial differential equations. For convergence, both Newton Iteration method and Jacobi method are applicable through finite element coding (Atalla and Sgard (2015)).

- Define the strong formulation of governing equations.
- Multiply both sides of the governing equations by weighted function also called test function w with given test space W where $w \epsilon W$.

- Use integration by parts method to distribute the higher order of differentiation among the test function w and unknown function U.
- Evaluate the boundary integral values via induction of weighted function to fulfill the essential boundary conditions and also unknown functions are used to fulfill natural boundary conditions called as variational formulation.
- Generate mesh which divides the entire domain into non-overlapping elements depending upon the dimensions used for present problem.
- Approximate the infinite dimensional trial space U, V and test space W by finite dimensional spaces U_h, V_h and W_h, respectively where U_h (finite dimensional space) U (solution space).
- Choose basis functions $\phi_1, \phi_2, \dots, \phi_N$ of w_h, so that every weighted function $w_h \epsilon W_h$ can be written as $w_h = \sum_{i=1}^{N} w_i \varphi_i \epsilon W_h$
- Find $u_h \epsilon U_h$ such that

$$a(u_h, w_h) = b(w_h) \quad \forall\, w_h = \sum_{i=1}^{N} w_i \varphi_i \,\epsilon\, W_h$$

$$\Longrightarrow a(u_h, \varphi_i) = b(\varphi_i), \text{ where } (i = 1, 2, 3, \dots, N).$$

Substituting $u_h = \sum_{j=1}^{N} u_j \varphi_j$, in above equation gives a linear system, that is

$$a\left(\sum_{j=1}^{N} u_j \varphi_j \,, \varphi_i\right) = b(\varphi_i), \qquad \text{for } i = 1, 2, 3, \dots, N.$$

$$\Longrightarrow \sum_{j=1}^{N} a(\varphi_j \,, \varphi_i) u_j = b(\varphi_i), \text{ for } i = 1, 2, 3, \dots, N.$$

where u_j are the solution values at the points. Separate into linear $b(w)$ and bilinear forms $a(u, w)$.

- $(AU = B)$ is transformed which assembles the algebraic equations by varying *i* and *j* in row and column wise.

1.5.2 Penalty Method

The penalty model is very similar to Lagrange multiplier method that allows us to reformulate the constrained problem into unconstrained problem. In this method, we use continuity equation to obtain pressure distribution (Reddy and Gartling (2010)) by introducing penalty parameter γ as follows:

$$\gamma\left(\frac{\partial u}{\partial x} + \frac{\partial v}{\partial y}\right) = -p. \tag{1.18}$$

For large value of γ i.e. $\gamma \gg 0$, the continuity equation is satisfied automatically. Penalty function allows us to eliminate pressure terms from momentum equations by incorporating this function into the momentum equations.

1.6 Literature Survey

Natural convection is an important heat transfer phenomena. Based on geometry and flow structure, natural convection may be categorized as internal or external. While in an internal flows, moving fluid is covered by the solid boundaries. The flowing fluid inside the duct or a pipe is a common example of internal flow systems. Opposite to this in the case of external flows solid objects are surrounded by the flowing fluid. Flows over the sphere, cylinder and flat plate are example of external flow systems. However, thermal flow fields and essential hydrodynamic coupling complicates natural convective flows. Mostly internal flow arrangements are complex as compare to external flow arrangements. The arrangements of external flow may be modeled with the help of classical boundary layer concept by using the assumption that solid boundaries do not affect the region outside of boundary layer (Bejan (2013)). On the other hand in case of internal convective flows, the collaborations between core and boundary layer create a considerable complication in the problem.

The internal convective flow arrangements depending upon the thermal boundary conditions can be categorized into two classes (a) enclosures heating through bottom wall in which gradient of temperature is in the same direction of gravitational force (b) enclosures heating through side walls which means that gradient of temperature is perpendicular to the direction of gravitational force (Bejan (2013)). Rayleigh-Benard convective flow within the two infinite parallel horizontal plates is related to class (a) and natural convective flow within the differentially heated enclosures is related to class (b). Furthermore, various thermal conditions may be incorporated with the permutation of differential and Rayleigh-Benard heated from different parts of walls and many more. Different sorts of heating configurations within the internal convective flow involved in many engineering applications e.g. heat exchanger (Haese (2002)), solar purification systems (Dayem (2006)), lubrication systems (Payvar (1991)), electronic equipment of cooling (Chiang (1991)), solar energy collectors (Joudi (2004)), melting and solid fraction process (Kalaiselvam (2008) and Wang (2010)), electric ovens (Mistry (2006)) and many others.

A natural convective flow in a square, rectangular, triangular or any regular or irregular shapes of enclosure has been investigated experimentally, analytically and numerically in the literature. These investigations are mostly based upon the influence of thermal boundary conditions, medium in which energy is transferred and aspect ratios of heated medium on natural convective flow. These type of investigations are studied by (Hoogendoorm (1986)), (Ostrach (1972) and (1988)) and (Fusegi and Hyun (1994)). (Ayden et al. (1999)) has been reported the influence of aspect ratios on heat and fluid flows insides a rectangular shape of an enclosure subject to the heated side walls and cooled ceiling with the help of stream function vorticity formulation. Later, free convective flow inside a rectangular enclosure subject to the non-uniform temperature profile on ceiling top wall and an insulated condition applied on side and bottom walls has been inspected by (Sarris et al. (2002)). They observed that the augmentation in thermal penetration depth and fluid circulation intensity with increase in aspect ratios. (Basak et al. (2006)) reported the natural convective heat transfer flow affected by thermal boundary conditions inside a square enclosure with the help of penalty finite element analysis. They investigated augmentation in average Nusselt number against uniform heating case as compared to non-uniform heating. Natural convective flow affected by the distributed within the square cavity via heatline approach has been studied by (Kaluri and Basak (2010)). Their analysis revealed that the thermal mixing and heat distribution in an enclosure is highly augmented in the case of disseminated heating as compared to isothermally heated from lower side.

A lot of research works on free convective transfer of heat in cavities through complex geometries besides regular shapes such as rectangular/square had been stated within literature because of their uses in several engineering problems (Philip (1982), Lee (1984) and Hyun and Choi (1990)). Mathematical modeling of the combination of thermal fields and hydrodynamic of buoyancy in complicated geometries are quit challenging. As a result, researchers conducted significant studies on natural convective heat transfer inside the non-rectangular cavities through wavy side walls, inclined, curved and triangular for last two decades. Some of previous research on free convective heat transfer within different non-rectangular cavities is noted below. First, (Philip (1982)) obtained exact solutions against low Rayleigh number within the natural convective heat transfer with different geometries of different shapes e.g. triangular, elliptic and rectangular cavities. He studied, flow field affected by the

orientation and aspect ratios of a cavity and was reported that the convective flows are not depending upon the orientation of a cavity at small Rayleigh number. (Lee (1984)) analyzed numerical and experimental studies related to convection energy transfer and fluid motion inside a differentially heated non-rectangular cavity. He presented in his analysis that flow and thermal characteristic are affected by the inclination, aspect ratios of a cavity and Rayleigh number. One of the interesting results in his investigation was that overall heat transfer rate manages maximum and minimum values at the inclination angles of 180^{o} and 270^{o} respectively. Transient free convection heat transfer inside a parallelogram shape of cavity for large Rayleigh number with the help of finite difference scheme has been studied by (Hyun and Choi (1990)). Their study revealed that the probability of employing the parallelogram shape of cavity as a thermal diode for controlling the angle of inclination of an enclosure. (Iyian et al. (1980)) presented natural convection transfer of heat inside a trapezoidal cavity having similar cylindrical upper and lower boundaries maintained at different temperature profiles and plane side walls considered as adiabatic. Natural convective flow contained in isosceles trapezoidal enclosures has been studied by (Karyakin (1989)). (Verol et al. (2009)) explored free convective flow contained in trapezoidal cavities in which inclined walls kept as cold temperature. A detail review related to natural convective flow inside triangular cavities is studied by (Kamiyo et al. (2010)). The main purpose of their study based on complete variety of buoyancy flow regimes within triangular shaped cavities. Furthermore, the influences of different thermal boundary conditions, Rayleigh number and pitch inclination on a heat and fluid flows were also reported comprehensively.

Moreover, laminar free convective heat transfer within right angled triangular enclosure full with air subject to the heated vertical side, inclined side as cold and insulated horizontal side has been carried out by the (Ridouane et al. (2005)). They employed finite volume technique and investigated that the heat and fluid flow affected by apex angle 5^{o}-63^{o} for different Rayleigh number 10^{3}-10^{6}. Laminar free convective transfer of heat in an isosceles triangular enclosure subject to the cold horizontal side with heated inclined sides has been investigated by (Kent (2009)). Later, (Kent et al. (2007)) executed numerical analysis to investigate phenomena of free convective transfer of heat in air contained in right triangular cavity. Furthermore, (Sahar et al. (2007)) presented tilted triangular cavity filled with air subject to the discrete bottom heating. (Basak et al. (2007)) reported natural

convective flow inside the right triangular cavity subject to thermal boundary conditions (a) linear or uniform heating vertical and cold inclined walls (b) linear or uniform heating inclined and isothermally cold vertical walls with the help of penalty finite element scheme. Later, (Basak et al. (2007)) extended their work to investigate the free convective flow within isosceles triangular enclosure affected by the two dissimilar circumstances of thermal boundary conditions (i) isothermally cold bottom wall with inclined walls are heated uniformly and (ii) isothermally cold bottom wall with inclined walls are heated non-uniformly. (Koca et al. (2007)) investigated free convective flow in air filled triangular enclosure affected by the Prandtl number by emplying finite difference scheme. Further, (Verol et al. (2006)) numerically explored free convective flow within a triangular cavity with the presence of heater on vertical wall where remaining segment of this wall is supposed to be insulated. (Basak and co-workers (2009), (2010), (2010) and (2017)) also studied free convective flow phenomenon with the visualization of heat flow within triangular cavity via heatline method.

A number of research works studied the large collection of applications related to convective flows inside the porous cavities, which include grain storage and dying (Togrul (2003)), thermal insulation (Kodah (1999)), thermal energy storage systems (Dhifaoui (2007)) and many more. Such studies on natural convective flows inside rectangular or square cavities full of porous media may be observed in the recent work (Trevisan (1986), Lage (1993), Song (1994), Bin Kim (2001) and Hossain (2002)). Natural convection through vertical slot packed with the porous media has been reported numerically and analytically by (Trevisan and Bejan (1986). They analyzed the correlation of average heat and mass transfer for buoyancy effects governed by both concentration and temperature variation within porous media at Le =1. Afterwards, (Lage and Bejan (1993)) has been investigated that natural convective flow inside a porous enclosure affected by pulsating heat input. They reported numerical experiment for Rayleigh number varying within 10^3-10^9, Prandtl number 0.01-7 and dimensionless frequency range 0-0.3. Natural convective flow inside a rectangular cavity partially saturated with anisotropic porous media is investigated experimentally and theoretically by (Song and Viskanta (1994)). They noticed that energy and fluid flow affected by anisotropic flow characteristics of a porous media. (Kim et al. (2001)) analyzed free convective flow inside a porous square cavity by considering Brinkman-extended Darcy simulation. They investigated that in

conductive dominant system, the porous section acts as a solid block of energy generation. The result shows that there exists a convection regime of asymptotic nature in which the flow is approximately free from the conductivity and permeability of porous media. Unsteady laminar free convective transfer heat in a flowing fluid soaked in a porous rectangular cavity subject to the heated lower side, non-isothermally left side and right and ceiling sides kept as cold temperature has been studied by (Hossain and Wilson (2002)). The results obtained during their study represent the Nusselt number at the walls and volumetric flow rate are decreases with augmentation in porosity. Two dimensional free convective flows inside porous right angled triangular enclosure subject to fluctuating left wall are carried out by the (Bharadwaj et al. (2013), (2015) and (2015)) . Convective heat transfer of flow within two entrapped cavities is also visualized by (Basak et al. (2010)). A number of qualitative research investigations contained free convective transfer of heat in porous triangular enclosures ((Varol et al. (2007), (2008), (2009) and (2011)), (Basak et al. (2008), (2010), (2011) and (2013)), (Baytas (1999)) and (Moukalled et al. (2010))).

The buoyance forces that rises due to the temperature differences and which cause the fluid flow in natural convective flows. In forced convective flows effects of these buoyancy forces usually supposed to be negligible. Mixed or combined convection takes place when buoyancy forces do have some significance on heat transfer and consequently on the flow fields. Most of the time flow and transfer of heat with respect to combined convective are considered in engineering system e.g., solar ponds, dynamics of lakes, cooling of electronic devices, heating and cooling buildings, thermal hydraulics of nuclear reactors, growth of crystals, chemical reactors, production of float glass, heat exchangers and food processing etc. The simplest structure, several of such practical flow conditions is energy transport and fluid flow in an enclosure in which flow is produced with the help of a combination of buoyant force and shear force.

These problems are studied earlier by several researchers for various flow problems with subject to the thermal boundary conditions e.g. one sided, double sided lid-driven enclosures from bottom, upper, lower or side walls, oscillation of walls, non-isothermally, partially or fully heated walls. (Ghia et al. (1982)) studied the problem related to lid driven cavity in the absence of thermal effects for sake of validation of CFD's code with benchmark computations. Natural convection for small Prandtl number fluids with specific essential frequency of 16.1 contains in square enclosure

has been investigated numerically by (Mohammad and Viskanta (1991)). They showed numerical simulations for Grashof ($Gr = 10^7$) and low Prandtl ($Pr = 0.005$) numbers and also Hopf bifurcation is predicted in their work. In their another numerical study (1995), they investigated 3-D simulation of heat and fluid flow in a stably stratified fluid contains in a shallow lid driven enclosure and obtained results related to moving lid on the flow configuration against the different important parameters of the governing flow. Flow visualization and measurements of heat flux conducted inside an adiabatic lid driven enclosure of fixed rectangular cross sectional area with the variation of cavity depth subject to the heated bottom wall is carried out by (Prasad and Koeseff (1996)). (Hsu et al. (1997)) studied the numerical simulations of mixed convective heat transfer in a partially divided enclosure under the influence of finite size heat source in it. They found numerical results against typical parameter values and alternative structures resulting by placement of heating device in different positions, opening of the outflows and baffle. In another study (Hsu (2000)), they analyzed the effects of combined convective heat transfer on the thermal phenomena within a rectangular lid driven cavity. (Aydm (1999)) examined the effects generated by lid driven wall on the aiding and opposing flows and (Oztop and Dagtekin (2004)) extended his work to double lid driven enclosure. A numerical simulation of unsteady, laminar and combined convective heat and fluid flow inside a square enclosure under the influence of energy generation or absorption with MHD impact is investigated by (Chamkha (2002)) by using finite volume method. A numerical simulations of combined convection heat and fluid flow inside a U-shaped cavity with the help of finite element technique has been studied by (Manca et al. (2003)), in their investigation they considered three basic modes of heating. Different kinds of energy related applications (Dalal (2003), and Sigey (2004)) have consumed the flow driven by buoyancy force contained in an enclosed cavity. Several investigators have examined the dynamics of heat and fluid flow inside rectangular or square enclosures, which are stated widely in literature. Various investigations are found regarding irregular shape of the sides of a cavity (Yapici (2015)), cavity structures (Gau et al (2004), Cheng et al. (2014) and Waheed (2009)), transport media (Tiwari et al. (2007) and Ramakrishna et al. (2012)) and imposed boundary condition of various combinations (Ismael et al. (2014, Sivakumar et al. (2010), Barletta et al. (2009), Wahba et al. (2009), Mahapatra et al. (2006) and Ji et al. (2007)). A complete literature review on the lid-driven cavity has been studied by (Shankar and Deshpande

(2000)). Furthermore, it has been observed that intricacy in fluid and heat flow characteristics rises once the enclosure is driven by from one side (Ramakrishna et al. (2012) and Barletta et al. (2009)) to double (Oztop et al. (2004), Guo et al. (2004), Tiwari et al. (2007) and Ismael et al. (2014)) and to more sides (Wahba et al. (2009)).

The uniform magnetic force applied externally is broadly used, for instance to control molten flow in crystal growth of semiconductors and in many other scientific applications like water treatment device, corrosion inhibition treatment, manufacturing processes of materials, magnetic cooling, magnetic refrigerator and microelectronic heat transfer devices. The heat flow through conducting liquid metals under the influence of a magnetohydrodynamics (MHD) has grabbed the attention of many researchers because of its various applications to different scientific phenomena including crystal growth processes. In particular gallium is considered to be a good choice for magnetohydrodynamic (MHD) studies due to the suitable physical properties of gallium including low melting point (gallium is a metal that appears in liquid state at room temperature 29.8^{o} C) close to ambient temperature, low viscosity, high surface tension depending upon temperature and high thermal conductivity. In general, the analysis of free convection through metals is of practical interest for the crystal growing community as instabilities in molten state may be frozen in solid product. Only a few simple problems could be solved analytically while most of the problems of practical interest require numerical solutions when additional difficulty is introduced under dealing with opaque material like liquid gallium.

(Braunsfurth et al. (1997)) has discussed heat transfer through natural convection in liquid gallium with one end hot and another cold and gave comparison of numerical with experimental results. They observed a great agreement in results for low Grashof number while results diverge systematically for large Grashof number. (Ben-David et al. (2014)) analyzed melting of gallium inside a closed enclosure, when heat is provided one wall. They used COMSOL multi physics software to carryout numerical simulations and validated his results against experimental results. They found that 3D computational and experimental results are quite similar indicating profound effects of boundaries. (Yamanaka et al. (1998)) examined free convective heat transfer in the layer of liquid gallium placed between horizontal flat copper plates heated from lower plate and above plate is taken cold with water flowing between plates. (Sathiyamoorthy and Chamkha (2010)) investigated electrically conducting free convection in liquid metal filled linearly heated cavity of square shape. They

considered uniform heating along bottom and top walls of enclosure is considered adiabatic where side walls were heated linearly while, inclined magnetic field is applied with angles $\phi = 0$ and $\phi = \frac{\pi}{2}$. (Mohammad and Viskanta (1994)) worked on experimental and numerical investigation of lid driven mixed convective heat flow inside a rectangular enclosure full of liquid gallium. In their investigation, they considered hot lower wall and hot upper wall while upper boundary is considered in motion with constant velocity. They observed significant effects of moving lid on flow and thermal structure.

In addition to its other uses, gallium is used in semiconductor industry also, this metal is of interest for possessing many properties which make it different from other metals, for instance, it is found in liquid form at room temperature (melting point of gallium is 29.78 ^{0}C) and retains its liquid form for the large temperature range (boiling point of gallium is 2403 ^{0}C). Therefore it may be used for high temperature thermometers, high temperature lubricants and pressure gauges. Furthermore contrary to most of other metals, gallium expands upon freezing and hence can't be stored in rigid container, gallium is known to be paramagnetic and it is good conductor of heat and electricity.

Micropolar fluids are fluids having microstructure characteristic in it. Physically micropolar fluids are combination of unsystematically oriented rigid particles suspended in some viscous medium in which deformation of fluid particle is generally not considered. The micropolar fluid simulation proposed by (Eringen (1966)), which contracts with a type of fluid and shows specific microscopic results from the local structure and microscopic movement of the fluid elements. Such fluids strengthen stress moments as well as body moments and are affected by the spin inertia. The applications of micropolar fluids include lubrication theory, blood flow, modelling of pharmaceutical drug carrier, haematological devices, float glass production, heat exchanger plants, automotive cooling and many more applications of engineering and industrial processes.

Heat transfer through natural and forced convection within micropolar fluids contained in containers of different geometries have been subject to extensive investigation for past few decades because of its several applications in industry and engineering, e.g. reactor designs, room ventilation, crystal growth, heat exchange devices and various other systems of fluid transportation. Microstructure effects are

generally not taken into account in classical Navier Stokes model. Applying shear stress on particles, they may contract, expand, change their shapes or may rotate about their own axis. These fluids have application in animal blood, liquid colloidal solutions, crystals, suspensions and polymer fluids.

Using boundary element method (Zadravec et al. (2009)) conveyed numerical simulations against natural convective flow within a square container carrying micropolar fluid and shown results against various values of Rayleigh number and microrotation. (Wang and Hsu (1993)) studied natural convection in buoyancy driven flow of micropolar fluid inside a tilted enclosure of rectangular shape when heated and cooled from side walls considering insulated top and bottom wall. They presented numerical results for various Rayleigh number and aspect ratios of enclosure. (Hsu et al. (1997)) numerically studied energy transmission in micropolar fluid in a container of rectangular shape inclined at some angle when source of heat is present. Numerical solutions for convection energy flow within micropolar fluid in rectangular container when lower boundary is heated and vertical walls are taken cold are presented by (Saleem et al. (2011)). (Gibanov et al. (2016)) chose wavy enclosure with heated bottom wall to analysed heat flow through natural convection in micropolar fluid. They found that microrotations increases and velocity attenuates with augmentation of vortex viscosity parameter. (Hsu and Hong (2006)) numerically studied the heat and fluid flow patterns through micropolar fluid filled in open cavity using cubic spline collocation method and obtained results for different characteristic parameters of microfluid and other flow parameters. (Hsu et al. (1995)) has been reported numerical simulations for thermal convective flow within a lid-driven container containing micropolar fluid. They obtained results against different values of involved parameters like Reynolds number, Grashof number, spin gradient viscosity, vortex viscosity etc. and gave a comparison with the results of Newtonian fluid. Computational results of free convection through micropolar fluid in a rectangular enclosure are also presented by (Hsu (1996)). (Aydin and Pop (2007)) conveyed numerical results for convective energy flow in micropolar fluid flowing through a square enclosure by providing heat to vertical walls where horizontal walls are insulated. They computed results using finite difference scheme against different Prandtl and Rayleigh numbers and shown that energy flow is low in micropolar fluids comparing to Newtonian fluids. (Bourantas and Loukopoulos (2014)) extended the idea of (Wang and Hsu (1993)) by considering micropolar nanofluid in an inclined

rectangular cavity and analysed heat transfer under magnetic effects. (Aydin and Pop (2005)) presented natural convection in a cavity affected by discrete heater when heater is centrally placed of its walls. They computed results for various physical parameters including heater length, material parameter of micropolar fluid, Prandtl and Rayleigh number. (Alloui and Vesseur (2010)) reported on analytic and numerical results for natural convective energy flow in micropolar fluid contained within shallow enclosure for numerous values of pertinent flow parameters. (Hsu and Wang (2000)) presented numerical results for laminar combined convective flow contained in a square enclosure carrying micropolar fluid influenced by localised heat source. (Ahmed et al. (2016)) numerically analysed the physical properties of mixed convective heat transfer from discrete heat source inside an enclosure with oscillating wall containing water based micropolar nanofluid. They considered couple of adjacent walls of cavity moving with the same speed while source of heat is present at centre of static lower boundary and different types of nanoparticles are used to evaluate results for four different moving lid orientation cases using finite volume method. (Periyadurani et al. (2016)) examined the influence of inclined Lorentz force on free convective energy flow through micropolar fluid in square container influenced by a thin plate provided with uniform and non-uniform heat. (Gibanov et al. (2016)) took into account the trapezoidal cavity to examine free convective heat transfer in micropolar fluid and computed numerical results using finite difference method for variety of physical flow parameters. Recently, (Miroshnichenko et al. (2017)) investigated the effects of local energy source on free convective flows through various positions of trapezoidal enclosure filled with micropolar fluid. (Sheremet et al. (2017)) analysed natural convective heat transfer in micropolar fluid contained in an isosceles triangular cavity by using finite difference method. In other study (2017), they carried out numerically, effects of Prandtl number, undulation number and vortex viscosity parameter at $Ra = 10^5$ on unsteady free convective flow inside a wavy triangular cavity subject to hot wavy wall containing micropolar fluid.

Ferrofluid is a combination of nanoscale ferromagnetic particles with some base fluid in which these particles are mixed like water as in our case. Ferrofluids are known to become heavily magnetized when strong magnetic field is applied upon it and this property make the ferrofluids suitable for many scientific and engineering applications like rocket fuel in space, high speed computer disk drives, audio speakers and to form liquid seals around spinning drive shafts etc. Ferrofluids are also used in

material sciences, medical applications, analytical instrumentations, optics, domain detection, switches, solenoids and heat transfer etc. (Scherer (2005)). Some interesting research work has been done on ferrofluids in recent years. Free convection in ferrofluid flow contained in an inclined square container under the influence of uniform magnetic field has been investigated numerically by (Kefayati (2014)). In his work he has analysed the effects of the external magnetic device and pertinent flow parameters on nano-scale ferromagnetic particles in an enclosure by using lattice Boltzman method. Later on, he has extended his idea (Kefayati (2014)) to analyse the effects of imposed magnetic field on nano-scale ferromagnetic particles of cobalt along kerosene as a carrier fluid present in a square enclosure with linear temperature distribution. (Sheikholeslami and Gorji-Bandpy (2014)) has numerically investigated natural convection in ferrofluid flow contained inside a container under the influence of imposed magnetic field when heat is provided from bottom side of the enclosure with the help of lattice Boltzman technique. Free convective heat transfer flow in ferrofluid contained inside C-shaped cavity in the presence of uniform magnetic field has been investigated by (Satyajit et al. (2015)). They employed Galerkin weighted residual technique to analyse the effects of MHD and Rayleigh number for two types of fluid. (Rahman (2016)) used two-component nonhomogeneous thermal equilibrium simulation to investigte the hydromagnetic free convection in water and kerosene based ferrofluid contained inside of an equilateral triangular cavity by using weighted residual technique. Other studies related with ferrofluid contains in an enclosures can be found in (Rabbi et al. (2016)), (Gibanov et al. (2017)), (Jhumur and Bhattacharjee (2017)), (Javed et al. ((2017)) and many more.

Chapter 2

Heat Transfer of Hydromagnetic Flow in a Porous Triangular Cavity

In this chapter, numerical simulations of free convective heat transfer inside isosceles triangular enclosure saturated with an isotropic porous medium influenced by magnetic force is investigated. The inclined walls of the cavity are supposed to be heated uniformly/non-uniformly. Initially, pressure terms are eliminated from the momentum equations with the help of penalty function. Afterwards, Galerkin weighted residual method is evoked to obtain the results for various ranged of involved parameters in terms of Hartmann, Rayleigh and Darcy numbers. The obtained solution is first verified to achieve grid independence and then compared with the results available in a literature against limiting case. Computed findings are represented graphically by using streamlines, isotherms, temperature gradient and average temperature gradient. It is noticed that the increase in the value of Rayleigh number causes augmentation in the strength of streamline circulations and reduction in strength of streamline circulation has been investigated due to increase in Hartmann number against the case of uniformly heated inclined walls. For non-uniform heating case, temperature gradient is seen to be maximum at the edges of bottom wall.

2.1 Problem Formulation

The configuration considered in the current investigation consists of isosceles triangular enclosure enclosing porous media of an isotropic nature as shown in **Figure 2.1**. The electrically conducting viscous incompressible fluid is flowing through the porous medium inside the enclosure. The fluid density has been considered to be function of temperature and its variations causes buoyancy forces term in the momentum equations after applying Boussinesq approximation (Gray (1976)). In porous region, temperatures of fluid phase and solid phase are supposed to be equal and local thermal equilibrium is applicable for present investigation (Nield and Bejan (2006)).

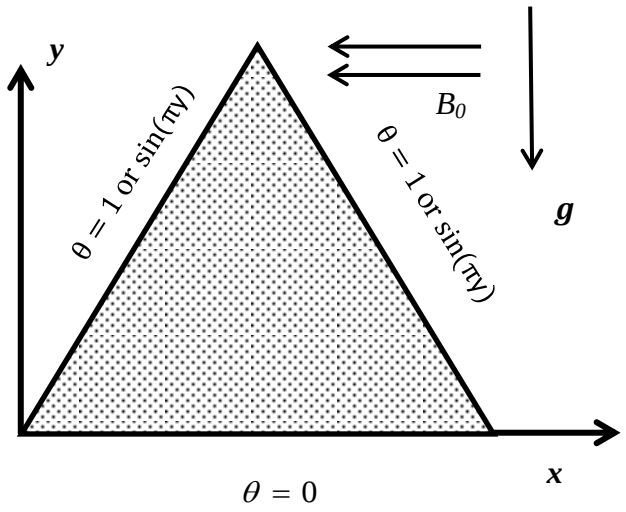

Figure 2.1: Geometrical description of the flow problem.

Moreover a uniform magnetic field is applied parallel to horizontal wall of a cavity. Here induced magnetic field has been ignored being sufficiently small in comparison to applied magnetic field B_0 under low-R_m approximation (Davidson (2001)). Considering all boundaries of the container to be electrically insulated without Hall effects, magnetic term can be simplified to a restraining factor $-B_0^2 v$ (Garandet (1992)). Therefore, electromagnetic force becomes a function of velocity component v acting normal to magnetic field. Under the above assumptions in the absence of Forchheimer's inertia term, and following the earlier work (Du and Bilgen (1992) and Ganzarolli and Milanez (1995)), the governing equations for conservation of mass, momentum and energy in the absence of viscous dissipation may be expressed as:

$$\frac{\partial u}{\partial x} + \frac{\partial v}{\partial y} = 0, \tag{2.1}$$

$$u\frac{\partial u}{\partial x} + v\frac{\partial u}{\partial y} = -\frac{1}{\rho}\frac{\partial p}{\partial x} + \upsilon\left(\frac{\partial^2 u}{\partial x^2} + \frac{\partial^2 u}{\partial y^2}\right) - \frac{\upsilon}{K}u, \tag{2.2}$$

$$u\frac{\partial v}{\partial x} + v\frac{\partial v}{\partial y} = -\frac{1}{\rho}\frac{\partial p}{\partial y} + \upsilon\left(\frac{\partial^2 v}{\partial x^2} + \frac{\partial^2 v}{\partial y^2}\right) - \frac{\upsilon}{K}v + \frac{g\beta(T-T_c)}{\rho} - \frac{\sigma B_O^2}{\rho}v, \tag{2.3}$$

$$u\frac{\partial T}{\partial x} + v\frac{\partial T}{\partial y} = \alpha\left(\frac{\partial^2 T}{\partial x^2} + \frac{\partial^2 T}{\partial y^2}\right). \tag{2.4}$$

where x, y are the components in Cartesian coordinate system, u, v represents components of velocity along horizontal and vertical directions respectively, p be the pressure, ρ is density, K is specific permeability of the medium, α is thermal diffusivity, L denotes the length of inclined wall of isosceles triangular enclosure and υ is kinematic viscosity.

The boundary conditions can be defined as:

$u(x,0) = v(x,0) = 0, T(x,0) = T_c$ and $0 \le x \le 2L$,

$u(x,y) = 0 = v(x,y), T = (T_h - T_c)sin\left(\pi\frac{y}{L}\right) + T_c$ at $x = y$

& $0 \le x, y \le L$

$u(x,y) = 0 = v(x,y), T = (T_h - T_c)sin\left(\pi\frac{y}{L}\right) + T_c$ at y$= 2 - x$

& $0 \le y \le L, L \le x \le 2L,$ (2.5)

The non-dimensional variables are introduced as follows:

$X = \frac{x}{L}, Y = \frac{y}{L}, U = \frac{uL}{\alpha}, V = \frac{vL}{\alpha}, P = \frac{pL^2}{\rho\alpha^2}, \theta = \frac{T-T_c}{T_h-T_c}, \mathrm{Pr} = \frac{\nu}{\alpha}, \mathrm{Da} = \frac{K}{L^2},$ Ra $=$

$\frac{g\beta L^3(T_h-T_c)Pr}{\nu^2}, \mathrm{Ha}^2 = \frac{\sigma {B_O}^2 L^2}{\mu}, \alpha = \frac{k}{\rho C_p}.$ (2.6)

By using Eq. (2.6) in Eqs. (2.1) - (2.4), we get

$$\frac{\partial U}{\partial X} + \frac{\partial V}{\partial Y} = 0, \tag{2.7}$$

$$U\frac{\partial U}{\partial X} + V\frac{\partial U}{\partial Y} = -\frac{\partial P}{\partial X} + \mathrm{Pr}\left(\frac{\partial^2 U}{\partial X^2} + \frac{\partial^2 U}{\partial Y^2}\right) - \frac{\mathrm{Pr}}{\mathrm{Da}}U, \tag{2.8}$$

$$U\frac{\partial V}{\partial X} + V\frac{\partial V}{\partial Y} = -\frac{\partial P}{\partial Y} + \mathrm{Pr}\left(\frac{\partial^2 V}{\partial X^2} + \frac{\partial^2 V}{\partial Y^2}\right) - \frac{\mathrm{Pr}}{\mathrm{Da}}V + \mathrm{RaPr}\theta - \mathrm{Ha}^2\mathrm{Pr}V, \tag{2.9}$$

$$U\frac{\partial \theta}{\partial X} + V\frac{\partial \theta}{\partial Y} = \frac{\partial^2 \theta}{\partial X^2} + \frac{\partial^2 \theta}{\partial Y^2} \tag{2.10}$$

and the boundary conditions (2.5) are reduced to

$U(X,0) = V(X,0) = 0, \theta(X,0) = 0$ and $0 \le X \le 2$,

$U = 0 = V, \theta = 1$ or $sin(\pi Y)$ at $X = Y$ and $0 \le X, Y \le 1$,

$U = V = 0, \theta = 1$ or $sin(\pi Y)$ at $Y = 2 - X$ and $0 \le Y \le 1, 1 \le X \le 2.$ (2.11)

Here U and V be the dimensionless components of velocity, θ be non-dimensional temperature, Pr, Ra, Da and Ha represents the Prandtl, Rayleigh, Darcy and Hartmann numbers respectively. The h represents the coefficient of heat transfer appearing in Newton's law of cooling which can be obtained in the dimensionless form from the temperature gradient Nu. The temperature gradient for bottom wall, left and right inclined sides are expressed mathematically as:

$$\mathrm{Nu_b} = -\sum_{i=1}^{6}\theta_i\frac{\partial \phi_i}{\partial Y},$$
$$\mathrm{Nu_l} = \sum_{i=1}^{6}\theta_i\left(\frac{-1}{\sqrt{2}}\frac{\partial \phi_i}{\partial X} + \frac{1}{\sqrt{2}}\frac{\partial \phi_i}{\partial Y}\right),$$
$$\mathrm{Nu_r} = \sum_{i=1}^{6}\theta_i\left(\frac{1}{\sqrt{2}}\frac{\partial \phi_i}{\partial X} + \frac{1}{\sqrt{2}}\frac{\partial \phi_i}{\partial Y}\right). \tag{2.12}$$

The average temperature gradient $\overline{\mathrm{Nu}}$ for the bottom, left and right walls are defined as follows:

$$\overline{\mathrm{Nu_b}} = \frac{\int_0^2 \mathrm{Nu_b} dX}{X|_0^2} = \frac{1}{2}\int_0^2 \mathrm{Nu_b} dX,$$
$$\overline{\mathrm{Nu_l}} = \overline{\mathrm{Nu_r}} = \frac{1}{\sqrt{2}}\int_0^{\sqrt{2}} \mathrm{Nu_l} dS\,. \tag{2.13}$$

2.2 Methodology

The continuity Eq. (2.7) is used as a constraint because of mass conservation and it can be used to determine pressure distribution (Reddy (1993)). In order to simplify the Eqs. (2.8) and (2.9), we have to consider penalty function where the pressure terms are eliminated with the help of penalty parameter γ and the criteria of incompressibility given in Eq. (2.7) which takes the form

$$P = -\gamma\left(\frac{\partial U}{\partial X} + \frac{\partial V}{\partial Y}\right). \tag{2.14}$$

The continuity equation (Eq. (2.7)) is automatically satisfied for large value of penalty parameter γ. Generally $\gamma = 10^7$ results into a consistent solutions. By substituting Eq. (2.14) into Eqs. (2.8) and (2.9), which takes the following form

$$U\frac{\partial U}{\partial x} + V\frac{\partial U}{\partial y} = \gamma\frac{\partial}{\partial X}\left(\frac{\partial U}{\partial X} + \frac{\partial V}{\partial Y}\right) + \mathrm{Pr}\left(\frac{\partial^2 U}{\partial X^2} + \frac{\partial^2 U}{\partial Y^2}\right) - \frac{\mathrm{Pr}}{Da}U, \tag{2.15}$$

$$U\frac{\partial V}{\partial x} + V\frac{\partial V}{\partial y} = \gamma\frac{\partial}{\partial Y}\left(\frac{\partial U}{\partial X} + \frac{\partial V}{\partial Y}\right) + \mathrm{Pr}\left(\frac{\partial^2 V}{\partial X^2} + \frac{\partial^2 V}{\partial Y^2}\right) - \frac{\mathrm{Pr}}{Da}V + \mathrm{RaPr}\theta - \mathrm{Ha}^2\mathrm{Pr}V. \tag{2.16}$$

Expanding the velocity and temperature profiles with the help of bi-quadratic basis functions $\{\phi_k\}_{k=1}^{N}$ with 6-nodal triangular elements as follows

$$U \approx \sum_{k=1}^{N} U_k\phi_k(X,Y)\,, V \approx \sum_{k=1}^{N} V_k\phi_k(X,Y)\,, \theta \approx \sum_{k=1}^{N} \theta_k\phi_k(X,Y). \tag{2.17}$$

Galerkin weighted residual method of finite element analysis has been evoked to solve the Eqs. (2.15), (2.16) and (2.10), which results into non-linear residual equations for internal domain Ω and takes the following form

$$\begin{aligned} R_i^1 = {} & \sum_{k=1}^{N} U_k \int_\Omega \left[\left(\sum_{k=1}^{N} U_k\phi_k\right)\frac{\partial\phi_k}{\partial X} + \left(\sum_{k=1}^{N} V_k\phi_k\right)\frac{\partial\phi_k}{\partial Y}\right]\phi_i dXdY + \\ & \gamma\left[\sum_{k=1}^{N} U_k \int_\Omega \frac{\partial\phi_i}{\partial X}\frac{\partial\phi_k}{\partial X}dXdY + \sum_{k=1}^{N} V_k \int_\Omega \frac{\partial\phi_i}{\partial X}\frac{\partial\phi_k}{\partial Y}dXdY\right] + \\ & \mathrm{Pr}\sum_{k=1}^{N} U_k \int_\Omega \left[\frac{\partial\phi_i}{\partial X}\frac{\partial\phi_k}{\partial X} + \frac{\partial\phi_i}{\partial Y}\frac{\partial\phi_k}{\partial Y}\right]dXdY + \frac{\mathrm{Pr}}{Da}\int_\Omega\left[\sum_{k=1}^{N} U_k\phi_k\right]\phi_i dXdY, \end{aligned} \tag{2.18}$$

$$\begin{aligned} R_i^2 = {} & \sum_{k=1}^{N} V_k \int_\Omega \left[\left(\sum_{k=1}^{N} U_k\phi_k\right)\frac{\partial\phi_k}{\partial X} + \left(\sum_{k=1}^{N} V_k\phi_k\right)\frac{\partial\phi_k}{\partial Y}\right]\phi_i dXdY + \\ & \gamma\left[\sum_{k=1}^{N} U_k \int_\Omega \frac{\partial\phi_i}{\partial Y}\frac{\partial\phi_k}{\partial X}dXdY + \sum_{k=1}^{N} V_k \int_\Omega \frac{\partial\phi_i}{\partial Y}\frac{\partial\phi_k}{\partial Y}dXdY\right] + \\ & \mathrm{Pr}\sum_{k=1}^{N} V_k \int_\Omega \left[\frac{\partial\phi_i}{\partial X}\frac{\partial\phi_k}{\partial X} + \frac{\partial\phi_i}{\partial Y}\frac{\partial\phi_k}{\partial Y}\right]dXdY + \frac{\mathrm{Pr}}{\mathrm{Da}}\int_\Omega\left[\sum_{k=1}^{N} V_k\phi_k\right]\phi_i dXdY - \\ & \mathrm{RaPr}\int_\Omega\left[\sum_{k=1}^{N} \theta_k\phi_k\right]\phi_i dXdY - \mathrm{Ha}^2\mathrm{Pr}\int_\Omega\left[\sum_{k=1}^{N} V_k\phi_k\right]\phi_i dXdY, \end{aligned} \tag{2.19}$$

$$R_i^3 = \sum_{k=1}^{N} \theta_k \int_\Omega \left[\left(\sum_{k=1}^{N} U_k \phi_k \right) \frac{\partial \phi_k}{\partial X} + \left(\sum_{k=1}^{N} V_k \phi_k \right) \frac{\partial \phi_k}{\partial Y} \right] \phi_i dX dY + \sum_{k=1}^{N} \theta_k \int_\Omega \left[\frac{\partial \phi_i}{\partial X} \frac{\partial \phi_k}{\partial X} + \frac{\partial \phi_i}{\partial Y} \frac{\partial \phi_k}{\partial Y} \right] dX dY. \quad (2.20)$$

Obtained nonlinear residual Eqs. (2.18) – (2.20) are solved by using Newton iterative method. The gesture of fluid particles in the form of stream functions may be obtained through components of velocity by defining the following relation

$$U = \frac{\partial \psi}{\partial Y} \text{ and } V = -\frac{\partial \psi}{\partial X}. \quad (2.21)$$

Which results into a single equation and takes the following form

$$\frac{\partial^2 \psi}{\partial X^2} + \frac{\partial^2 \psi}{\partial Y^2} = \frac{\partial U}{\partial Y} - \frac{\partial V}{\partial X}. \quad (2.22)$$

Expanding stream function with the help of bi-quadratic basis functions $\{\phi\}_{k=1}^{N}$ as

$$\psi \approx \sum_{k=1}^{N} \psi_k \phi_k(X, Y) \quad (2.23)$$

and again by evoking the Galerkin finite element method, the following residual equation is obtained

$$R_i^s = \sum_{k=1}^{N} \psi_k \int_\Omega \left[\frac{\partial \phi_i}{\partial X} \frac{\partial \phi_k}{\partial X} + \frac{\partial \phi_i}{\partial Y} \frac{\partial \phi_k}{\partial Y} \right] dX dY + \sum_{k=1}^{N} U_k \int_\Omega \phi_i \frac{\partial \phi_k}{\partial Y} dX dY - \sum_{k=1}^{N} V_k \int_\Omega \phi_i \frac{\partial \phi_k}{\partial X} dX dY. \quad (2.24)$$

Solution of Eq. (2.24) is obtained by considering no slip conditions along all sides.

2.3 Validation

In order to develop the mesh free solution of the discussed problem, the numerical values of the computed overall heat transfer rate at the bottom wall is demonstrated in **Table 2.1** against different refinement levels of non-uniform initial mesh. It is noted that with the increase in the number of elements or by increasing the refinement level, the percentage error of the solution with the solution at previous refinement level is decreased. It is as minimum as 0.1% at the fourth refinement level, therefore throughout the study; third refinement level is used for solution with 1776 number of 6-nodal triangular elements. Once the mesh free solution is achieved, the code is further validated against the results of (Basak et al. (2008)) as a limiting case as presented in **Figure 2.2**. The right column of the **Figure 2.2** contains results found by present investigation and left column contains the results of (Basak et al. (2008)) in case of uniformly heated side wall with $\Pr = 0.7, Ra = 10^6$ and $Da = 10^{-5}$. The results are evident to be accurate and in good agreement with the results of (Basak et al. (2008)).

2.4 Results and Discussions

This section contains the results obtained by numerical simulations for two dimensional laminar convective flows through a porous medium saturated inside the triangular cavity in the presence of MHD. Discussion is divided into two cases isothermally cold bottom wall with (i) inclined walls are heated uniformly and (ii) inclined walls are heated non-uniformly. Heat transfer rates have been computed and presented through figures. The graphs are plotted against wide ranges of parameters, which are Ra ($10^3 \leq \text{Ra} \leq 10^6$), Pr ($0.026 \leq \text{Pr} \leq 10$), Da ($10^{-5} \leq \text{Da} \leq 10^{-3}$) and Ha ($50 \leq \text{Ha} \leq 10^3$).

Uniformly Heated Inclined Walls

In this case of study, inclined sides of an isosceles triangle are maintained at uniform temperature profile ($\theta = 1$) and lower wall is maintained at low temperature. It is therefore, jump type finite discontinuity has been observed at the lower corners of the cavity, as these corners are the joining of walls with dissimilar temperature profiles. This discontinuity needs to be focused and it is discussed with respect to the criteria described by the (Ganzarolli and Milanez (1995)). Temperature at these corner nodes has been investigated by taking the average temperature of bottom and corresponding side walls. However, the adjacent nodes have been taken at corresponding wall temperature to avoid singularity. As bottom wall is kept on cold temperature and inclined side walls are heated uniformly, therefore fluid present adjacent to the side walls is at higher temperature than that of lower wall. Hence, the fluid present adjacent to inclined walls is lesser dense in comparison to fluid present adjacent to bottom cold wall due to the fact that the hot fluid is less dense than that of cold fluid. In consequence, the variation of density of fluid near the walls produces circulation of fluid in the enclosure in clockwise and anticlockwise directions. The hot fluid expands, becomes more buoyant, and transfers the energy, again descends down to the cold wall via central vertical line of a cavity, resulting two rolls of symmetric circulations as shown in figures. Streamlines with positives values are shown as anti-clockwise circulation and streamline with negative values are shown as clockwise circulations according to definition of stream function.

Figures 2.3 and **2.4** illustrate contour plots for streamlines and isotherms at $Da = 10^{-3}, Pr = 0.7, Ha = 50$ for $Ra = 4 \times 10^5$ and 10^6 respectively. It has been investigated that, heat flow in the cavity is purely due to conduction and isotherms

appear to be smooth and monotonic in this case. Also two symmetric rolls of clockwise and anti-clockwise circulation cells of streamlines are seen. The maximum value of stream function ($|\psi|_{max}$) is noted to be 1.5 as presented in **Figure 2.4**. It has been examined through this figure that with the increase in Rayleigh number, the strength of the circulations is also increased. The upper corner of a cavity is observed to be empty due to weak effects of circulation and isotherms. It may be seen from the figure that isotherms are pushed towards bottom wall and contour lines are concentrated in lower half of the cavity, where magnitude of stream function is increased to$|\psi|_{max} = 2.5$. It is due to the reason that the left and right corners are the places where the difference in the temperature is maximum.

Figures 2.5 and **2.6** contain plots for fluids for which thermal diffusivity dominates i.e. $Pr = 0.026$ and momentum diffusivity dominates i.e. $Pr = 10$ respectively when other parameters are fixed at $Ra = 10^6, Da = 10^{-3}$and $Ha = 50$. It is observed that low Prandtl number corresponds to weaker clockwise and anti-clockwise circulation of streamlines which is clearly due to conduction dominant effects. When Prandtl number is 0.026, magnitude of circulation in noted to be 2 and when Prandtl number is increased to 10, magnitude of circulation is also increased to 2.5. The isotherms for smaller Prandtl number are more pressed toward bottom wall as shown in **Figure 2.6**.

Figures 2.7 and **2.8** show numerical outputs for $Pr = 0.026$ and $Pr = 10$ respectively with large Hartmann number $Ha = 10^3$ and $Da = 10^{-3}, Ra = 10^6$. It is seen that higher values of Hartmann number results into very weak circulation of streamlines, but the isotherms which were clustered in lower portion of the cavity at $Ha = 50$ started expanding up in the cavity. Again isotherms are noted to be smooth, monotonic symmetric with respect to the perpendicular line passing through centre of horizontal side. Magnitudes of stream function are observed to be$|\psi|_{max} = 0.06$ at $Pr = 0.026$ and $|\psi|_{max} = 0.07$ at $Pr = 10$ in **Figure 2.7** and **Figure 2.8** respectively.

Non-Uniformly Heated Inclined Walls

In this case, both left and right inclined walls are subject to sinusoidal heat wave $\theta = \sin(\pi y)$. This type of heating is taken due to reason that it removes singularity from the bottom left and right corners.

Figures 2.9 - 2.11 show contour plots for stream function and isotherms for $Ra = 10^6, Pr = 0.026, 0.7, Da = 10^{-3}$and $Ha = 50, 10^3$ with non-uniformly heated inclined sides of an isosceles triangular cavity. Strong circulation is observed in the case of non-uniformly heated inclined sides and it is shifted to the centre of the enclosure from bottom corners (as observed in previous case). It is further noted that, by increasing the value of Prandtl and Hartmann numbers, streamlines and isotherms become smoother. It is pointed out that, two rolls of symmetric circulations are observed in each case and streamlines are seen to be pushed towards the inclined sides. It has been observed through **Figure 2.9** that, when sinusoidal heat wave is applied to side walls of cavity, isotherms are observed to be compressed towards inclined walls and distributed throughout the triangular enclosure. It is important to note that the high temperature gradient is seen near upper vertex of the enclosure in this figure. However, for uniform heating case, it was examined that the isotherm lines are compressed towards bottom side of a cavity and temperature gradient is observed to be concentrated in lower half of a cavity and especially near the lower two corners of a cavity due to maximum temperature difference there. It is observed that isotherms for $\theta \leq 0.6$ are pushed towards bottom sidewall and for $\theta \geq 0.7$, isotherm lines are pressed towards inclined walls. As we increase Prandtl number from 0.026 to 0.7, isotherms near bottom wall get concaved up about the centre of bottom wall from concaved down in a small interval as shown in **Figure 2.10**.

When Prandtl number is augmented from 0.026 to 0.7, magnitude of stream function is noted to increase from $|\psi|_{max} = 3$ (see **Figure 2.10**) to $|\psi|_{max} = 3.6$ (see **Figure 2.11**) it is due to the phenomenon that the convection helps the fluid flow through buoyancy. Opposite to this, when Hartmann number is increased from 50 to 10^3, magnitude of stream function is reduced from $|\psi|_{max} = 3$ (see **Figure 2.8**) to $|\psi|_{max} = 0.04$ (see **Figure 2.11**) due to the fact that Hartmann number is ratio of electromagnetic forces to the viscous forces and increase in Hartmann number is due to the dominance of electromagnetic force, which in consequence produces resistance to the flow, due to which $|\psi|_{max}$ is reduced to 0.04.

Figure 2.12 (a, b) is drawn to show the transfer of heat in the form of local Nusselt number along the bottom side (a) and along the inclined walls (b). Since the cavity under consideration is symmetric with respect to the perpendicular line passing through the centre of the bottom side and both of the side walls are subjected to the

same temperature, consequently temperature gradient at both inclined walls is observed same therefore we have shown graph of Nusselt number for left side wall only. In this figure, the solid lines represent the case of uniformly heated inclined walls and dashed lines represent the case of non-uniformly heated inclined walls. Curves have been plotted against dissimilar values of Prandtl (Pr) and Darcy (Da) numbers, where Rayleigh (Ra) and Hartmann (Ha) numbers are fixed at 10^6 and 50 respectively. It is observed that, when side walls are heated uniformly (solid curves), temperature gradient is noted very large at left and right edges of bottom wall as shown in **Figure 2.12 (a)**. This is due to the fact that both boundaries meeting at these edges are at different temperatures and causes maximum temperature difference to occur. It is further invetigated that the heat transfer rate is minimum at the centre of the bottom wall for all values of Da and Pr. Similarly, heat transfer rate along the side walls is maximum at the bottom edge where distance is taken to be zero as shown in **Figure 2.12 (b)** which is also due to having maximum temperature difference at this point. Furthermore, temperature gradient is almost zero at the upper vertex due to the fact that no temperature difference occurs at this vertex causes no transfer of energy shown in right hand side of **Figure 2.12 (b)**, the increase in Nusselt number due to Pr and Da is also observed through the **Figure 2.12**.

For the case of non-uniformly heated inclined walls (dashed curves), temperature gradient Nu along bottom wall is also maximum at vertices and minimum at the centre. The temperature gradient for this case is considerably minimum as compare to the uniformly heated inclined walls. Whereas, along the side walls (**Figure 2.12 (b)**) temperature gradient shows sinusoidal nature due to non-uniformly heated side walls. The temperature gradient at the upper vertex of the cavity for the case of non-uniformly heated inclined walls is also minimum due to minimum temperature difference at this point. The variation in heat transfer rate Nu for various values of Darcy (Da) and Prandtl (Pr) numbers is also noted from the figure as a sinusoidal wave.

Average temperature gradient at the bottom and inclined sides against Hartmann number for various values of Darcy number is drawn in **Figure 2.13**. It has been observed that average temperature gradient decreases with the increase in Hartmann number and attain a constant values against $\mathrm{Ha} > 500$. Similarly, by reducing the values of Darcy number, the average temperature gradient decreases up to fixed

values. The same observation is noted at the bottom and inclined walls and can be further proved from **Table 2.2**.

Table 2.1: Overall heat transfer rates along bottom wall against different mesh sizes

Refinements	Number of Elements	$\overline{\mathrm{Nu}_b}$	% Error
1st	111	10.4548	-
2nd	444	10.3528	0.98
3rd	1776	10.2710	0.79
4th	7104	10.2600	0.1

Table 2.2: Average Nusselt numbers along different walls of cavity against various values of flow parameters, Ha, Pr, for fixed Da

			Uniform Heating Case		Non-Uniform Heating Case	
Ha	Da	Pr	$\overline{\mathrm{Nu}_b}$	$\overline{\mathrm{Nu}_s}$	$\overline{\mathrm{Nu}_b}$	$\overline{\mathrm{Nu}_s}$
0	10^{-3}	0.026	7.4549	4.9936	5.1623	2.4169
50	-	-	7.4093	4.9625	4.9550	2.3206
100	-	-	7.3113	4.8950	4.8646	2.2807
200	-	-	7.1637	4.7919	4.7495	2.2285
500	-	-	7.0962	4.7382	4.6656	2.1876
1000	-	-	7.0922	4.7323	4.6541	2.1816
0	-	0.7	7.6294	5.1212	5.0725	2.3580
50	-	-	7.5108	5.0397	4.9990	2.3437
100	-	-	7.3350	4.9175	4.8995	2.3065
200	-	-	7.1070	4.7730	4.7418	2.2340
500	-	-	7.0822	4.6817	4.6552	2.1911
1000	-	-	7.0456	4.3435	4.6443	2.1850

(Basak et al. (2008)) Present Study

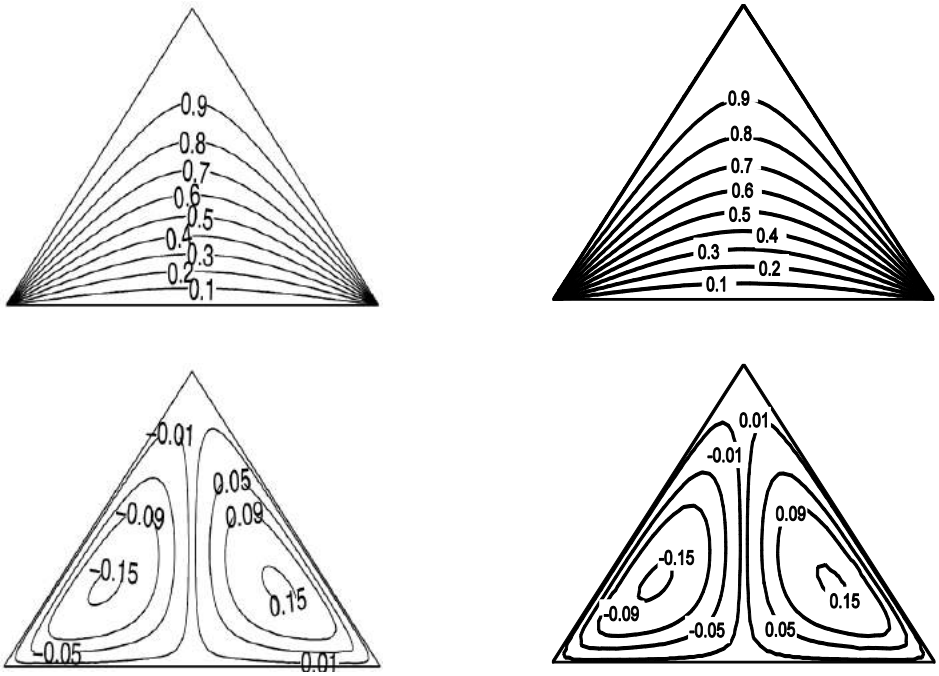

Figure 2.2: Contours for isotherms and stream function against $\mathrm{Pr} = 0.7, \mathrm{Ra} = 10^6$ and $\mathrm{Da} = 10^{-5}$

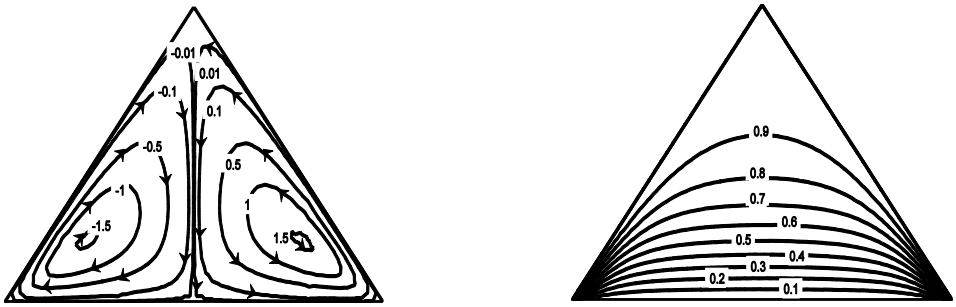

Figure 2.3: Contours for stream function and isotherms for uniformly heated inclined walls with $\mathrm{Ra} = 4 \times 10^5, \mathrm{Pr} = 0.7, \mathrm{Da} = 10^{-3}$ and $\mathrm{Ha} = 50$

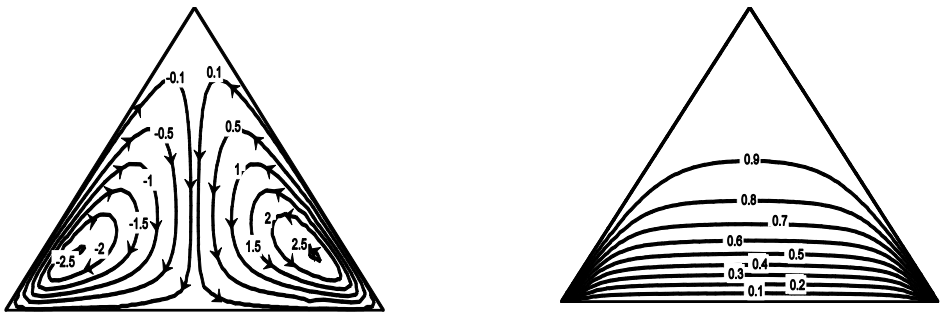

Figure 2.4: Contours for stream function and isotherms for uniformly heated inclined walls with $\mathrm{Ra} = 10^6, \mathrm{Pr} = 0.7, \mathrm{Da} = 10^{-3}$ and $\mathrm{Ha} = 50$

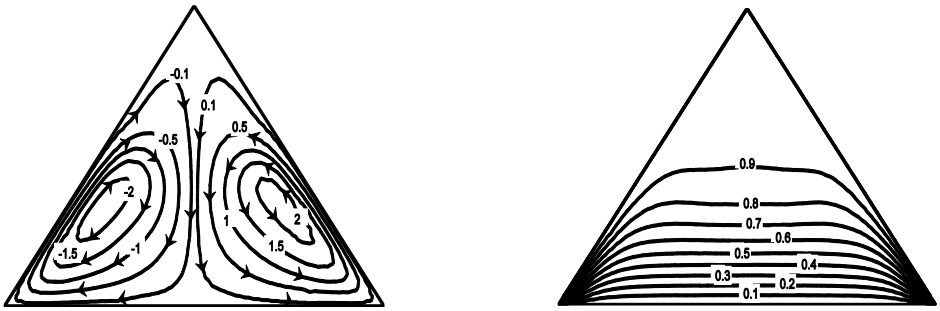

Figure 2.5: Contours for stream function and isotherms for uniformly heated inclined walls with $\mathrm{Ra} = 10^6, \mathrm{Pr} = 0.026, \mathrm{Da} = 10^{-3}$ and$\mathrm{Ha} = 50$.

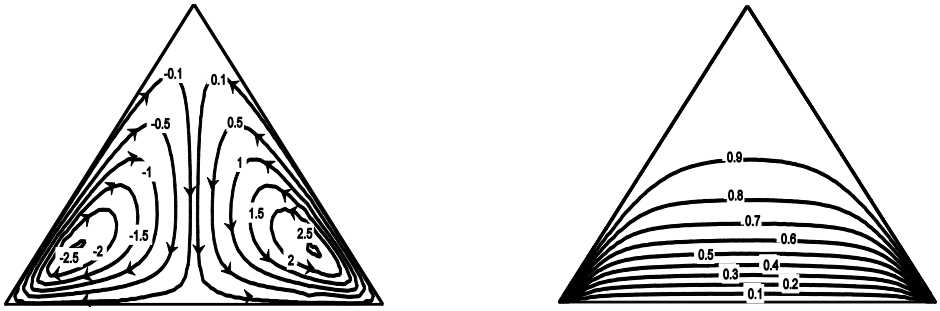

Figure 2.6: Contours for stream function and isotherms for uniformly heated inclined walls with $\mathrm{Ra} = 10^6, \mathrm{Pr} = 10, \mathrm{Da} = 10^{-3}$ and $\mathrm{Ha} = 50$

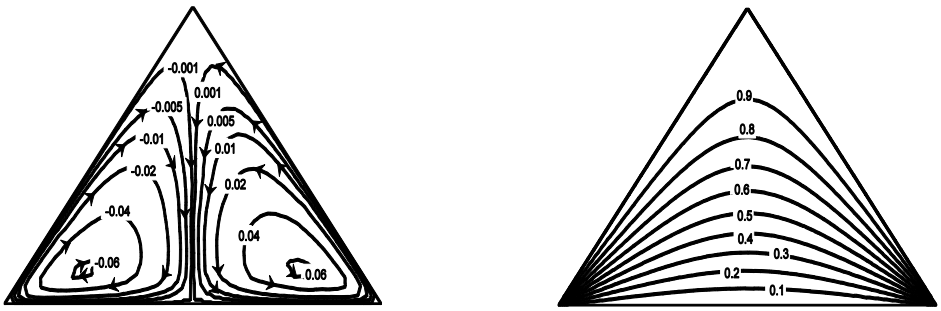

Figure 2.7: Contours for stream function and isotherms for uniformly heated inclined walls with $\mathrm{Ra} = 10^6, \mathrm{Pr} = 0.026, \mathrm{Da} = 10^{-3}$and $\mathrm{Ha} = 10^3$

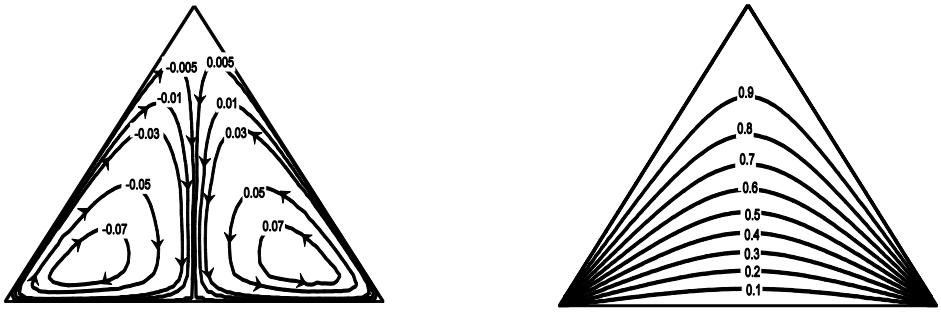

Figure 2.8: Contours for stream function and isotherms for uniformly heated inclined walls with $\mathrm{Ra} = 10^6, \mathrm{Pr} = 10, \mathrm{Da} = 10^{-3}$ and $\mathrm{Ha} = 10^3$

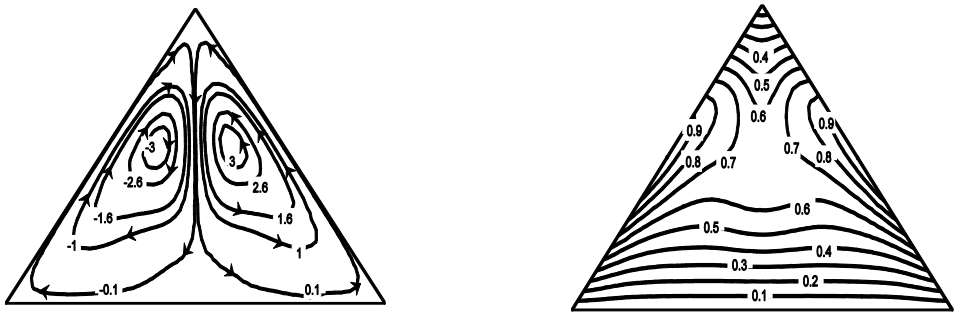

Figure 2.9: Contours for stream function and isotherms for non-uniformly heated inclined walls with $\mathrm{Ra} = 10^6, \mathrm{Pr} = 0.026, \mathrm{Da} = 10^{-3}$ and $\mathrm{Ha} = 50$

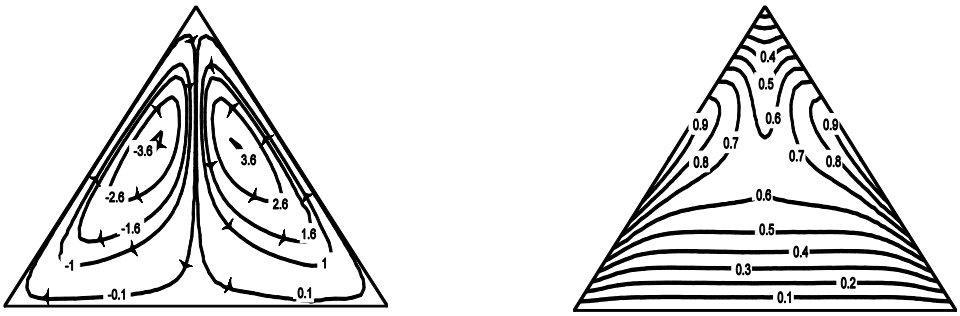

Figure 2.10: Contours for stream function and isotherms for non-uniformly heated inclined walls with $\mathrm{Ra} = 10^6, \mathrm{Pr} = 0.7, \mathrm{Da} = 10^{-3}$and $\mathrm{Ha} = 50$

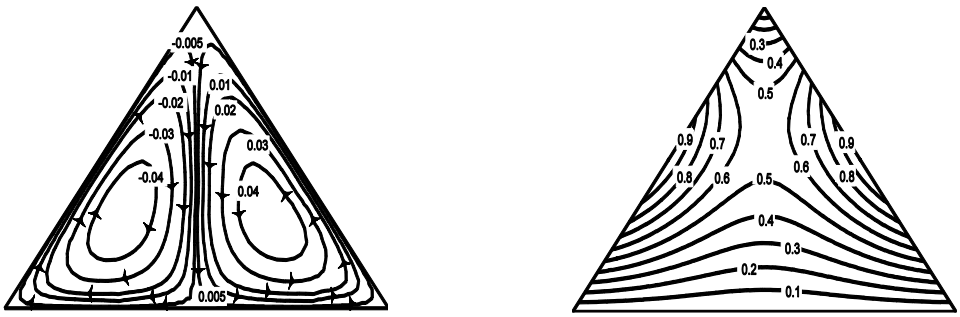

Figure 2.11: Contours for stream function and isotherms for non-uniformly heated inclined walls $\mathrm{Ra} = 10^6, \mathrm{Pr} = 0.026, \mathrm{Da} = 10^{-3}$ and $\mathrm{Ha} = 10^3$

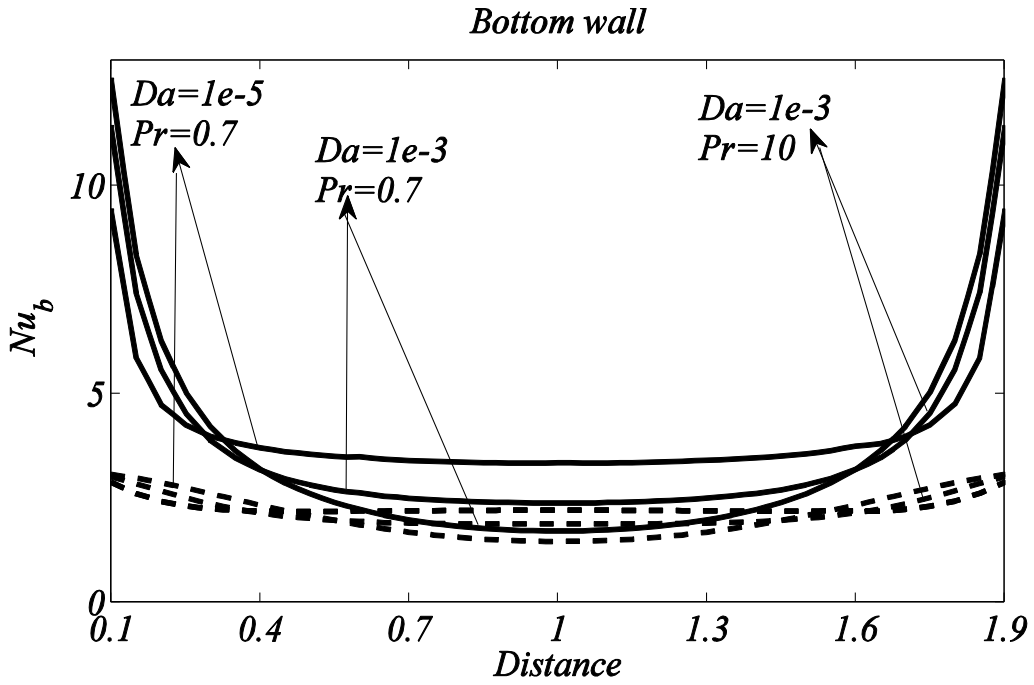

(a)

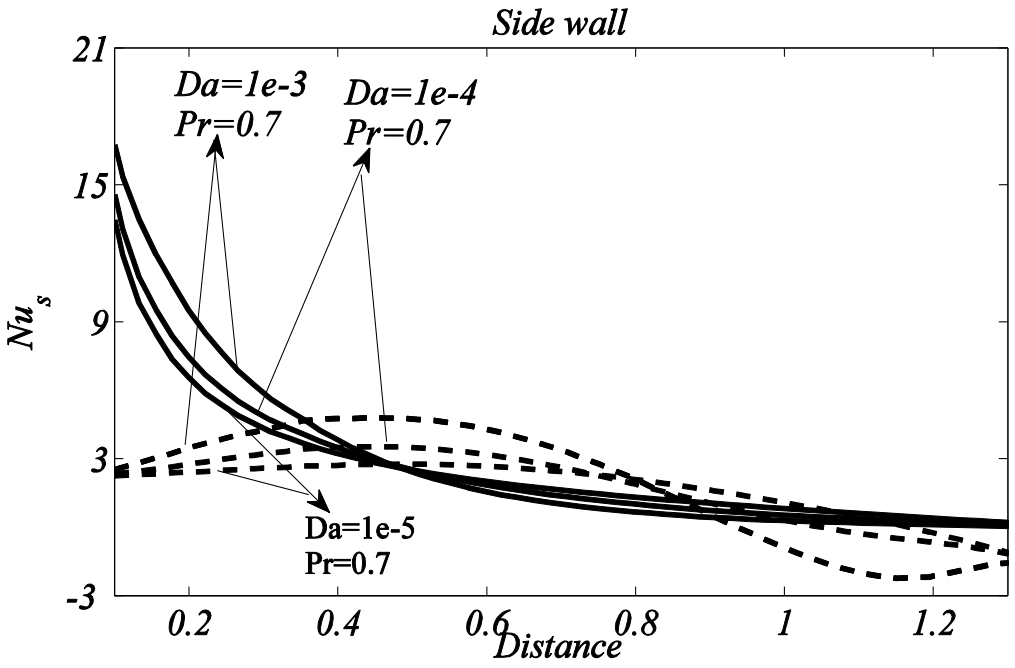

(b)

Figure 2.12(a, b): Local Nusselt numbers for cold bottom wall & inclined side walls heated uniformly (solid lines) and non-uniformly (dashed lines) with different values of Pr, and Da where Ra $= 10^6$and Ha $= 50$ are fixed

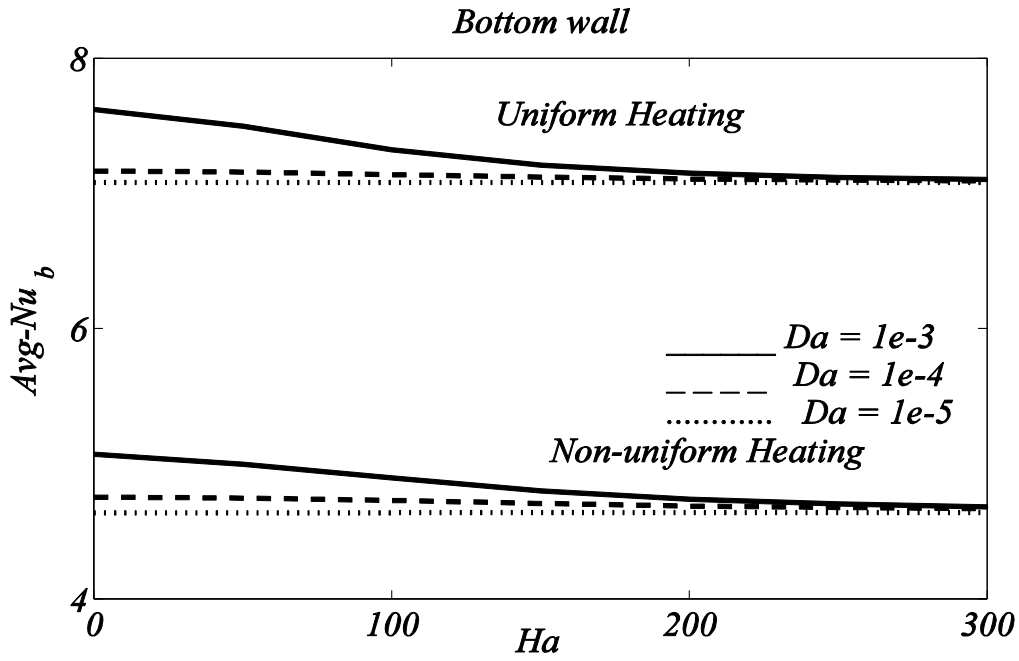

(a)

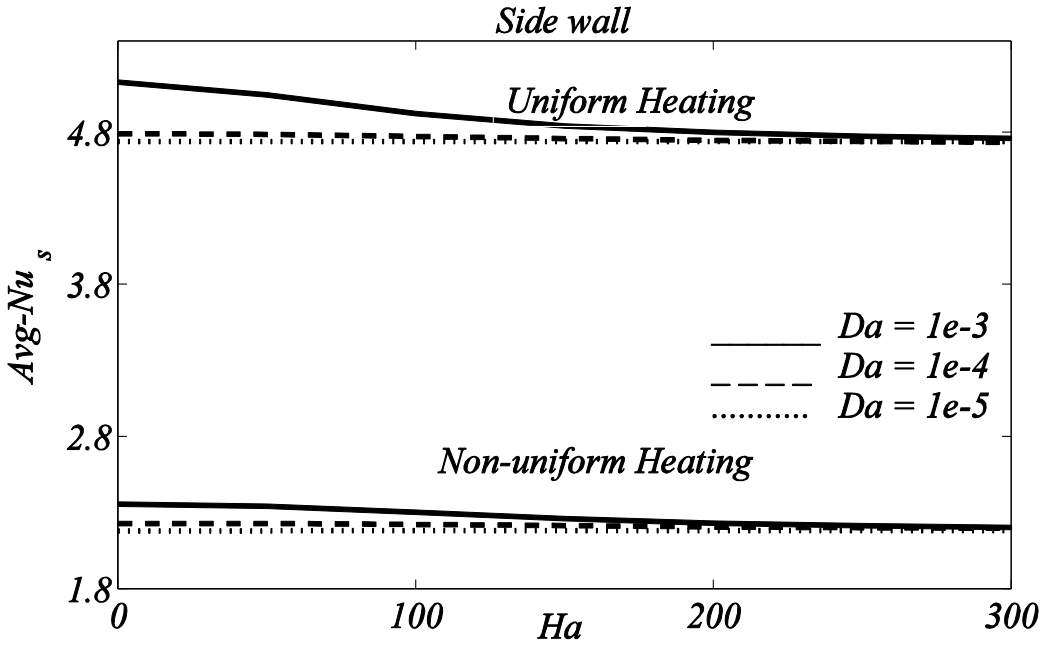

(b)

Figure 2.13(a, b): Average Nusselt number for uniform and non-uniform heating case against different values of Da, and Ha where $\mathrm{Ra} = 10^6$and $\mathrm{Pr} = 10$ are fixed

2.5 Conclusions

A computational investigation is executed to examine the two-dimensional laminar steady state MHD natural convection flow within the isosceles triangular cavity saturated with isotropic porous medium. The inclined walls of the triangular enclosure are subjected to heated uniformly or non-uniformly. Finite element technique has been employed to obtain the solution, governing conservation of mass, momentum and energy equations are nonlinear requiring an iterative technique solver to solve these equations by considering Hartmann number Ha = 50 - 10^3, Prandtl number Pr = *0.026 – 10* and Rayleigh number Ra = 10^3 - 10^7. For this purpose, we applied Galerkin weighted residual method with penalty parameter.

For the case of uniform heated side walls, it has been noticed that the increase in Rayleigh number above critical value i.e. (Ra = $4*10^5$) causes augmentation in strength of circulations of streamlines, but increase in Hartmann number results in decrease in the strength of streamline circulation. The effects on circulations of streamlines due to Prandtl number are similar to that of Rayleigh number. Isotherm contours gets closer towards the bottom of cavity due to increase in Rayleigh number or Prandtl number. Whereas, with increase in Hartmann number isotherms moves towards upper portion of the cavity. On the other hand, it is found that temperature gradient is maximum at the edges of bottom wall due to maximum temperature difference at the corner nodes and it is appeared to be constant near centre of bottom wall. Heat transfer is higher near lower end of side walls due to the same reasons and it is almost zero near upper corner, as two side walls are at same temperature. When side wall is subjected to sinusoidal heat wave, streamlines are pushed towards side walls of cavity and strength of circulation of streamline is increased with increase in Prandtl number. Whereas, isotherms greater than 0.7 are pushed towards side walls while other isotherms are pushed towards bottom wall when Hartmann and Prandtl number is increased. It has been further noticed that the circulation strength of streamlines is decreased due to escalation in Hartmann number in non-uniform heating case as well. Furthermore, temperature gradient at the bottom wall for non-uniformly heating case is considerably small as compared to that of uniform heating case and it is further minimum at a centre of the bottom wall.

Chapter 3

Heat Transfer through Hydromagnetic Flow of Liquid Gallium contained in a Porous Square Cavity

This chapter comprises a numerical investigation of natural convection in a porous square cavity saturated with liquid gallium influenced by magnetic force applied either in horizontal or in vertical direction. Bottom wall of the cavity is maintained at uniform temperature where top wall is considered to be adiabatic, left wall is supposed to be heated linearly and right side is subject to linear heating or taken cold. Computed effects are represented graphically by using streamlines, isotherms, heat transfer and overall heat transfer rates Augmentation in streamline circulations is observed due to increase in Darcy number while imposition of vertical magnetic field instead of horizontal magnetic field causes slow rate of increase in strength of streamlines circulation. Whereas, in case of linearly heated right wall, overall heat transfer rate has been observed to be increasing function of Darcy numer, and vertical magnetic field causes higher values for average Nusselt number as compare to horizontal magnetic field along bottom and side boundaries of an enclosure. Contrarily, in the case of cold right wall, horizontal magnetic field results into higher values of average Nusselt number as compare to vertical magnetic field case and average Nusselt number reduces as we move along lower and right boundary while increases along left wall with increase in distance.

3.1 Problem Formulation

Consider laminar, hydro-magnetic, natural convective heat transfer in a chemically inert porous media saturated with liquid gallium inside the square cavity in the presence of uniform magnetic field as presented in **Figure 3.1** and parameters of flow are given in **Table 3.1**. The width and height of the square enclosure are represented by L and length of the enclosure is supposed to be long enough so that the investigation can be considered as two dimensional in Cartesian co-ordinate system. It is assumed that fluid is viscous, incompressible and electrically conducting. The fluid density has been considered to be function of temperature and the density variation causes buoyancy forces terms in governing momentum equations after applying Boussinesq approximation (Gray (1976)). In porous region, temperatures of fluid and

solid phases are supposed to be equal and Local Thermal Equilibrium (LTE) is considered valid for this study (Nield and Bejan (2006)).

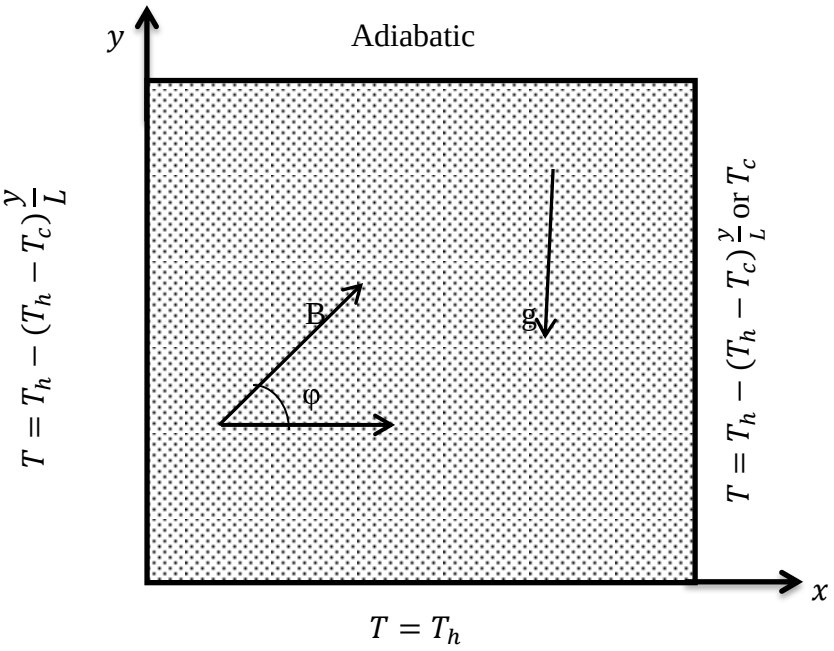

Figure 3.1: Graphical representation of the physical system

It has been further supposed that the magnetic force $\boldsymbol{B}$ having magnitude B_0 is employed in horizontal ($\phi = 0$) or vertical ($\phi = \frac{\pi}{2}$) direction inside the cavity. Here induced magnetic force has been neglected being very insignificant in comparison with applied magnetic field under low-R_m approximation (Davidson (2006)). During present study joule heating effects, Hall effects and viscous radiation are ignored. In the light of supposed assumptions, laws of mass, momentum and energy can take the form such as:

$$\frac{\partial u}{\partial x} + \frac{\partial v}{\partial y} = 0, \tag{3.1}$$

$$u\frac{\partial u}{\partial x} + v\frac{\partial u}{\partial y} = -\frac{1}{\rho}\frac{\partial p}{\partial x} + \upsilon\left(\frac{\partial^2 u}{\partial x^2} + \frac{\partial^2 u}{\partial y^2}\right) - \frac{\upsilon}{K}u + \frac{\sigma {B_0}^2}{\rho}(v\sin\phi\cos\phi - u\sin^2\phi), \tag{3.2}$$

$$u\frac{\partial v}{\partial x} + v\frac{\partial v}{\partial y} = -\frac{1}{\rho}\frac{\partial p}{\partial y} + \upsilon\left(\frac{\partial^2 v}{\partial x^2} + \frac{\partial^2 v}{\partial y^2}\right) - \frac{\upsilon}{K}v + g\beta(T - T_c) + \frac{\sigma {B_0}^2}{\rho}(u\sin\phi\cos\phi - v\cos^2\phi), \tag{3.3}$$

$$u\frac{\partial T}{\partial x} + v\frac{\partial T}{\partial y} = \alpha\left(\frac{\partial^2 T}{\partial x^2} + \frac{\partial^2 T}{\partial y^2}\right). \tag{3.4}$$

Boundary conditions for the governing problem may be expressed as:

$u(x,0) = v(x,0) = u(x,L) = v(x,L) = 0, \frac{\partial T}{\partial y}(x,L) = 0, T(x,0) =$

T_h where $0 \leq x \leq L$,

$u(0,y) = v(0,y) = u(L,y) = v(L,y) = 0, T(0,y) = T_h - (T_h - T_c)\frac{y}{L}$,

$T(L,y) = T_h - (T_h - T_c)\frac{y}{L} or\ T_c$ where $0 \leq y \leq L$, (3.5)

where x and y are defined as $x-$axis and $y-$axis respectively, u and$v$ represents velocity components along horizontal and vertical directions, ϕ is inclination angle of magnetic field with the positive $x-$axis, which is either 0 or $\frac{\pi}{2}$, T_h represents temperature at hot boundary, T_c be temperature at cold boundary.

The following non-dimensionless variables are introduced such as:

$$X = \frac{x}{L}, Y = \frac{y}{L}, U = \frac{uL}{\alpha}, V = \frac{vL}{\alpha}, P = \frac{pL^2}{\rho\alpha^2}, \theta = \frac{T-T_c}{T_h-T_c}, \mathrm{Pr} = \frac{\nu}{\alpha},$$
$$\mathrm{Da} = \frac{K}{L^2}, \mathrm{Ra} = \frac{g\beta L^3(T_h-T_c)Pr}{\nu^2}, \mathrm{Ha}^2 = \frac{\sigma {B_O}^2 L^2}{\mu}, \alpha = \frac{k}{\rho C_p}. \quad (3.6)$$

Upon substituting Eq. (3.6) into Eqs. (3.1) – (3.4), we get

$$\frac{\partial U}{\partial X} + \frac{\partial V}{\partial Y} = 0, \quad (3.7)$$

$$U\frac{\partial U}{\partial X} + V\frac{\partial U}{\partial Y} = -\frac{\partial P}{\partial X} + \mathrm{Pr}\left(\frac{\partial^2 U}{\partial X^2} + \frac{\partial^2 U}{\partial Y^2}\right) - \frac{\mathrm{Pr}}{\mathrm{Da}}U + \mathrm{Pr}Ha^2(Vsin\phi cos\phi - Usin^2\phi), \quad (3.8)$$

$$U\frac{\partial V}{\partial X} + V\frac{\partial V}{\partial Y} = -\frac{\partial P}{\partial Y} + \mathrm{Pr}\left(\frac{\partial^2 V}{\partial X^2} + \frac{\partial^2 V}{\partial Y^2}\right) - \frac{\mathrm{Pr}}{\mathrm{Da}}V + \mathrm{RaPr}\theta + \mathrm{PrHa}^2(Usin\phi cos\phi - Vcos^2\phi), \quad (3.9)$$

$$U\frac{\partial \theta}{\partial X} + V\frac{\partial \theta}{\partial Y} = \frac{\partial^2 \theta}{\partial X^2} + \frac{\partial^2 \theta}{\partial Y^2}. \quad (3.10)$$

Boundary conditions in dimensionless form may be defined in the following way

$U(X,0) = V(X,0) = U(X,1) = V(X,1) = \frac{\partial \theta}{\partial Y}(X,1) = 0, \theta(X,0) =$

1, where $0 \leq X \leq 1$,

$U(0,Y) = V(0,Y) = U(1,Y) = V(1,Y) = 0, \theta(0,Y) = 1 - Y$,

$\theta(1,Y) = 1 - Y\ or\ 0$ where $0 \leq Y \leq 1$. (3.11)

Here $\mathrm{Pr}, \mathrm{Ra}, \mathrm{Ha}$ and Da represents Prandtl, Rayleigh, Hartmann and Darcy numbers respectively, U, V represents non-dimensional components of velocity and θ be non-dimensional temperature.

3.2 Methodology

The momentum Eqs. (3.8) – (3.9) are subject to the penalty function to remove pressure term. In penalty function, we consider continuity Eq. (3.7) to obtain pressure profile by defining the penalty parameter γ as follows:

$$P = -\gamma\left(\frac{\partial U}{\partial X} + \frac{\partial V}{\partial Y}\right). \tag{3.12}$$

Generally, law of conservation of mass given in Eq. (3.7) is satisfied against large values of γ, i.e. $\gamma = 10^7$ which results into consistent solutions as shown in **Table 3.2**. Incorporating Eq. (3.12) in Eqs. (3.8) and (3.9) yields:

$$U\frac{\partial U}{\partial X} + V\frac{\partial U}{\partial Y} = \gamma\frac{\partial}{\partial X}\left(\frac{\partial U}{\partial X} + \frac{\partial V}{\partial Y}\right) + \mathrm{Pr}\left(\frac{\partial^2 U}{\partial X^2} + \frac{\partial^2 U}{\partial Y^2}\right) - \frac{\mathrm{Pr}}{\mathrm{Da}}U + \mathrm{PrHa}^2(Vsin\phi cos\phi - Usin^2\phi), \tag{3.13}$$

$$U\frac{\partial V}{\partial X} + V\frac{\partial V}{\partial Y} = \gamma\frac{\partial}{\partial Y}\left(\frac{\partial U}{\partial X} + \frac{\partial V}{\partial Y}\right) + \mathrm{Pr}\left(\frac{\partial^2 V}{\partial X^2} + \frac{\partial^2 V}{\partial Y^2}\right) - \frac{\mathrm{Pr}}{\mathrm{Da}}V + \mathrm{RaPr}\theta + \mathrm{PrHa}^2(Usin\phi cos\phi - Vcos^2\phi). \tag{3.14}$$

By considering 6 nodal triangular elements and bi-quadratic shape functions $\{\phi_k\}_{k=1}^N$,we approximate components of velocity u, v and temperature θ as follows

$$U \approx \sum_{k=1}^N U_k\phi_k(X,Y)\,, V \approx \sum_{k=1}^N V_k\phi_k(X,Y)\,, \theta \approx \sum_{k=1}^N \theta_k\phi_k(X,Y). \tag{3.15}$$

Galerkin weighted residual method of finite element analysis has been evoked to solve the Eqs. (3.13), (3.14) and (3.10), which results into non-linear residual equations for internal domain Ω and takes the following form

$$\begin{aligned} R_i^1 = {} & \sum_{k=1}^N U_k \int_\Omega \left[\left(\sum_{k=1}^N U_k\phi_k\right)\frac{\partial\phi_k}{\partial X} + \left(\sum_{k=1}^N V_k\phi_k\right)\frac{\partial\phi_k}{\partial Y}\right]\phi_i dXdY + \\ & \gamma\left[\sum_{k=1}^N U_k \int_\Omega \frac{\partial\phi_i}{\partial X}\frac{\partial\phi_k}{\partial X}dXdY + \sum_{k=1}^N V_k \int_\Omega \frac{\partial\phi_i}{\partial X}\frac{\partial\phi_k}{\partial Y}dXdY\right] + \\ & \mathrm{Pr}\sum_{k=1}^N U_k \int_\Omega \left[\frac{\partial\phi_i}{\partial X}\frac{\partial\phi_k}{\partial X} + \frac{\partial\phi_i}{\partial Y}\frac{\partial\phi_k}{\partial Y}\right]dXdY + \frac{\mathrm{Pr}}{\mathrm{Da}}\int_\Omega\left[\sum_{k=1}^N U_k\phi_k\right]\phi_i dXdY - \\ & \mathrm{PrHa}^2\int_\Omega\left(\left(\sum_{k=1}^N V_k\phi_k\right)sin\phi cos\phi - \left(\sum_{k=1}^N U_k\phi_k\right)sin^2\phi\right)\phi_i dXdY, \end{aligned} \tag{3.16}$$

$$\begin{aligned} R_i^2 = {} & \sum_{k=1}^N V_k \int_\Omega \left[\left(\sum_{k=1}^N U_k\phi_k\right)\frac{\partial\phi_k}{\partial X} + \left(\sum_{k=1}^N V_k\phi_k\right)\frac{\partial\phi_k}{\partial Y}\right]\phi_i dXdY + \\ & \gamma\left[\sum_{k=1}^N U_k \int_\Omega \frac{\partial\phi_i}{\partial Y}\frac{\partial\phi_k}{\partial X}dXdY + \sum_{k=1}^N V_k \int_\Omega \frac{\partial\phi_i}{\partial Y}\frac{\partial\phi_k}{\partial Y}dXdY\right] - \\ & \mathrm{RaPr}\int_\Omega\left[\sum_{k=1}^N \theta_k\phi_k\right]\phi_i dXdY + \mathrm{Pr}\sum_{k=1}^N V_k \int_\Omega \left[\frac{\partial\phi_i}{\partial X}\frac{\partial\phi_k}{\partial X} + \right. \\ & \left.\frac{\partial\phi_i}{\partial Y}\frac{\partial\phi_k}{\partial Y}\right]dXdY + \frac{\mathrm{Pr}}{\mathrm{Da}}\int_\Omega\left[\sum_{k=1}^N V_k\phi_k\right]\phi_i dXdY - \\ & \mathrm{PrHa}^2\int_\Omega\begin{pmatrix}\left(\sum_{k=1}^N U_k\phi_k\right)sin\phi cos\phi - \\ \left(\sum_{k=1}^N V_k\phi_k\right)cos^2\phi\end{pmatrix}\phi_i dXdY, \end{aligned} \tag{3.17}$$

$$R_i^3 = \sum_{k=1}^{N} \theta_k \int_\Omega \left[\left(\sum_{k=1}^{N} U_k \phi_k \right) \frac{\partial \phi_k}{\partial X} + \left(\sum_{k=1}^{N} V_k \phi_k \right) \frac{\partial \phi_k}{\partial Y} \right] \phi_i dX dY + \sum_{k=1}^{N} \theta_k \int_\Omega \left[\frac{\partial \phi_i}{\partial X} \frac{\partial \phi_k}{\partial X} + \frac{\partial \phi_i}{\partial Y} \frac{\partial \phi_k}{\partial Y} \right] dX dY. \quad (3.18)$$

Reduced system of nonlinear algebraic Eqs. (3.16) to (3.18) is further solved by using Newton Raphson method. After evaluating components of velocity U and V, stream function is determined by using the following relation

$$U = \frac{\partial \psi}{\partial Y} \text{ and } V = -\frac{\partial \psi}{\partial X}. \quad (3.19)$$

Which can be further reduced into a single second order equation given as:

$$\frac{\partial^2 \psi}{\partial X^2} + \frac{\partial^2 \psi}{\partial Y^2} = \frac{\partial U}{\partial Y} - \frac{\partial V}{\partial X}. \quad (3.20)$$

Expending stream function with the help of bi-quadratic basis functions $\{\phi\}_{k=1}^{N}$ as

$$\psi \approx \sum_{k=1}^{N} \psi_k \phi_k(X, Y) \quad (3.21)$$

and again by evoking the Galerkin finite element method, the following residual equation is obtained

$$R_i^s = \sum_{k=1}^{N} \psi_k \int_\Omega \left[\frac{\partial \phi_i}{\partial X} \frac{\partial \phi_k}{\partial X} + \frac{\partial \phi_i}{\partial Y} \frac{\partial \phi_k}{\partial Y} \right] dX dY + \sum_{k=1}^{N} U_k \int_\Omega \phi_i \frac{\partial \phi_k}{\partial Y} dX dY - \sum_{k=1}^{N} V_k \int_\Omega \phi_i \frac{\partial \phi_k}{\partial X} dX dY. \quad (3.22)$$

Solution of Eq. (2.24) is obtained by considering no slip conditions along all sides.

The coefficient of heat transfer h appearing in Newton's law of cooling can be obtained by using dimensionless form from energy transfer rate. The temperature gradient (Nu) and average temperature gradient ($\overline{\text{Nu}}$) for lower and side walls may take the form:

$$\text{Nu}_\text{b} = -\sum_{i=1}^{6} \theta_i \frac{\partial \phi_i}{\partial Y}, \text{Nu}_\text{l} = -\sum_{i=1}^{6} \theta_i \frac{\partial \phi_i}{\partial X}, \text{Nu}_\text{r} = \sum_{i=1}^{6} \theta_i \frac{\partial \phi_i}{\partial X} \text{ and}$$

$$\overline{\text{Nu}_\text{b}} = \int_0^1 \text{Nu}_\text{b} dX, \overline{\text{Nu}_\text{s}} = \int_0^1 \text{Nu}_\text{s} dY. \quad (3.23)$$

3.3 Validation

In order to develop the grid independent solution of discussed problem, the numerical values of average temperature gradient along bottom wall are demonstrated in **Table 3.3** against different refinement levels of non-uniform initial mesh. It has been observed that with increase in the number of elements or by increasing the refinement level, the percentage error of the solution with the solution at previous refinement level is decreased. It is as minimum as 1% at the fourth refinement level, therefore

throughout the study; third refinement level is used for solution with 2048 number of 6-nodal triangular elements.

Once the grid independence is achieved, again code is tested against the findings of (Sathiyamoorthy et al. (2010)) as a special case. **Figure 3.2** represents the comparison between results obtained by our developed code and the findings of (Sathiyamoorthy et al. (2010)) and it shows that our findings are consistent with their results. In **Figure 3.2**, left column represents graphical results obtained by our code right column shows the graphical results presented by (Sathiyamoorthy et al. (2010)).

3.4 Results and Discussions

This section contains results determined by numerical simulation of incompressible viscous flow of liquid gallium contained in a square cavity packed with chemically inert isotropic porous media (e.g. sand stone, pumice and SnO_2 based anode). We have considered the suitable range of Darcy number for sandstone as its physical parameters are more compatible with parameters considered in our problem.

Case I: Cold Right Wall

Figure 3.3 shows streamline and isotherms contours for uniform heating from the bottom side, linearly heating from left side and right side is kept cold, under the influence of horizontal $\phi = 0$ magnetic field when Darcy number varies from 10^{-5} to 10^{-3} (suitable values for sandstone porous medium (Loret and Huyghe (2004)) where other flow parameters are supposed to be fixed at $\mathrm{Pr} = 0.025$ (gallium), $\mathrm{Ra} = 10^5$ and $\mathrm{Ha} = 30$ respectively. It has been observed that there appear two circulation cells for streamline contours with one large primary clockwise circulation cell that covers most part of enclosure and the other small anticlockwise secondary circulation cell appearing near top left corner of the square cavity. It has been investigated that the fluid flow rises along the heated side and falls along cold side forming primary circulation cells and due to thermal buoyancy effects secondary circulation cells are formed near the upper left corner. Opposite to this, isotherms contours change their behavior smoothly from linearly heated wall towards cold wall as presented in **Figure 3.3 (a).**

When Darcy number is augmented to 10^{-4}, strength of secondary circulation cells are increased and it is stretched by pushing the primary circulation cell and moved the centre of primary circulation cell slightly up along the diagonal of cavity. Isotherms are increased in height and also bended towards cold right wall. Similar trend is seen

for isotherms and streamlines when Darcy number is further increased to 10^{-3} i.e. size and strength of secondary cell is further increased and centre of primary circulation cell is almost shifted to the centre of cavity by further moving along its diagonal while isotherms are also increased further in height and bended towards right cold wall owing the fact of energy transfer is maximum close to the centre of the cavity.

Figure 3.4 displays isotherm and streamline contours for same values of flow parameters as that in **Figure 3.3** but direction of magnetic field is considered to be vertical in this case. It is noticed that this direction of magnetic field causes reduction in temperature gradient inside the cavity where contours for isotherms appears to be broken towards side walls of cavity for $\theta < 0.3$. Similarly strength of streamline circulation contours has also been reduced due to appearance of vertical magnetic field. Like in the previous case, here also appear a large primary and a small secondary roll of circulation cell in upper left corner. Increasing Darcy number to 10^{-4} increases strength of circulations and height of isotherms but the rate of this increase is considerably slow as compare to that of the case of horizontal magnetic field $\phi = 0$ (**Figure 3.3 (b)**). Whereas unlike the previous case, for the case of vertical magnetic field $\phi = \frac{\pi}{2}$, increase in Darcy number beyond 10^{-4} results in sharp increase in strength circulation of primary and secondary cells and secondary circulation cell is stretched towards uniformly heated bottom wall. Similarly non-uniformity of isotherms has also been sharp in this case as shown in **Figure 3.4 (c)**.

Case II: Linearly Heated Right Wall

Figures 3.5 & **3.6** contain results for numerical simulations in the case when uniformly heated bottom wall with both sidewalls are supposed to be linearly heated while top wall is considered adiabatic. The values of parameters are considered as $\mathrm{Ra} = 10^5, \mathrm{Pr} = 0.025$ (gallium), $\mathrm{Ha} = 30, \mathrm{Da} = 10^{-5}, 10^{-4}, 10^{-3}$ and magnetic field directions are $\phi = 0, \frac{\pi}{2}$. **Figure 3.5** consist of isotherms and streamline contours for the case of horizontal magnetic field i.e. ($\phi = 0$). Since two walls of the square enclosure are subject to linear heating therefore two concentric rolls of clockwise left and anticlockwise right circulations are formed. The fluid moves up along two vertical sides and then comes down towards centre of the enclosure forming two rolls of circulation cells (**Figure 3.5 (a)**). As compared to the case of right cold wall with the case of linearly heated right wall temperature is comparatively high in the cavity

and due to similar temperature profile along two boundaries; isotherms are observed symmetric with respect to the perpendicular line passing through the centre of the enclosure. Isotherms for $\theta < 0.4$ are broken towards the side walls where isotherms for $\theta > 0.7$ are almost straight horizontal lines. Increase in the value of Darcy upto 10^{-4} increases the strength of both clockwise and anticlockwise circulations in streamlines while isotherms gain more heights near centre of horizontal walls of cavity giving them a shape of wave for $\theta > 0.4$. Further increase in Darcy number increases the strength of circulations of streamlines, height of isotherms and number of broken isotherm contours.

Figure 3.6 depicts the effects for same values of flow parameters but in the presence of vertical magnetic field. Effects of change in the direction of magnetic field are very similar as that of cold right wall i.e. strength of circulation and temperature gradient are noticed to be high for vertical magnetic field. The fluid moves up along two vertical sides and then comes down towards the middle of the enclosure creating two rolls of circulation cells.

Figure 3.7 contains the curves of temperature gradient for the case of cold right wall where upper wall is considered adiabatic, uniform energy is provided from bottom wall of a cavity and left wall is heated linearly. Curves for Nusselt numbers are plotted against distance in the presence of horizontal (solid line) and vertical (dashed line) magnetic fields with $\mathrm{Pr} = 0.025, \mathrm{Ha} = 30, \mathrm{Ra} = 10^5$ and $\mathrm{Da} = 10^{-5}, 10^{-3}$. It has been observed that along bottom wall as shown in **Figure 3.7 (a)**, there are no significant effects of Darcy number for distance $X < 0.4$ and $X > 0.9$ as curves are almost coinciding for these values of distance while between 0.4 and 0.9 higher Nusselt number is noticed for small value of Darcy number. Furthermore, the curves for horizontal and vertical magnetic field are also almost overlapping showing negligible effects of inclination of magnetic field on Nusselt number. Whereas along cold right wall (**Figure 3.7 (c)**), local Nusselt number first increases very sharply with distance up to $Y = 0.15$ then rate of increase becomes a little slower up to $Y = 0.25$ and afterwards curves are almost horizontal showing constant heat transfer rate while higher Darcy number results in higher Nusselt number for $0.15 < Y < 0.4$ and contrarily smaller heat transfer rate has been observed for larger values of Darcy number $Y > 0.4$. No significant influences of inclination angle of magnetic field are observed along right cold wall. On the other hand, along linearly heated left side as

presented in **Figure 3.7 (b)**, vertical magnetic field ($\phi = \frac{\pi}{2}$) returns higher heat transfer rate as compared to horizontal magnetic field ($\phi = 0$) for $\mathrm{Da} = 10^{-5}$ while for $\mathrm{Da} = 10^{-3}$ horizontal magnetic field returns higher heat transfer rate up to $Y = 0.8$ and reverse behavior has been noticed afterwards. Local Nusselt number increases with enhancement in vertical distance Y but at a slower rate up to $Y = 0.8$ and afterwards rate of increase becomes sharp comparatively. Furthermore enhancement in Darcy number results augmentation in heat transfer rate along left side of the cavity as presented in **Figure 3.7 (b)**.

In **Figure 3.8**, Nusselt number along bottom and side walls are shown against the case of heated right wall and values of other flow parameters are same as these were assumed in **Figure 3.7**. It is seen that along bottom wall, curve of local Nusselt number looks like sinusoidal wave when $\mathrm{Da} = 10^{-3}$, temperature gradient first reduced up to $X = 0.05$ and then increases up to $X = 0.5$ then it decreases again up to 0.95 and then increases afterwards. However, for $\mathrm{Da} = 10^{-5}$, Nu increases with increase in distance X up to 0.5 and afterwards it reduces with escalation in distance, the vertical magnetic field returns higher heat transfer rate as compare to horizontal magnetic field when $\mathrm{Da} = 10^{-5}$where for $\mathrm{Da} = 10^{-3}, \phi = 0$ returns higher Nusselt number up to $X = 0.37$ and for $0.37 < X < 0.63$ vertical magnetic field returns higher heat transfer rate as compare to horizontal one, while after $X = 0.63$ again horizontal magnetic field gives higher Nusselt number as compare to that of vertical magnetic field. Since both side walls are subject to similar temperature profile of linear heating, therefore the graph of heat transfer rate is identical for both side walls.

Table 3.1: Gallium parameters for melting problem (Hannoun (2003))

Parameters	Symbols	Gallium	Units
Density	ρ	6.093×10^3	$\mathrm{Kg/m^3}$
Dynamic viscosity	μ	1.81×10^{-3}	$\mathrm{N\ s/m^2}$
Coeff. of vol. expansion	β	1.20×10^{-4}	$\mathrm{K^{-1}}$
Kinematic Viscosity	υ	3.126×10^{-7}	$\mathrm{m^2/s}$
Electrical Conductivity	σ	3.87×10^6	$\Omega^{-1}\mathrm{m}^{-1}$
Rayleigh number	Ra	10^5	
Prandtl number	Pr	0.025	

Table 3.2: Average Nusselt numbers along bottom side against various values of γ

γ	$\overline{Nu_b}$
10^4	-0.8963
10^5	-0.9189
10^6	-0.9212
10^7	-0.9215
10^8	-0.9215
10^9	-0.9215

Table 3.3: Overall heat transfer rates along bottom wall against different mesh sizes

Refinements	Number of Elements	$\overline{Nu_b}$
1^{st}	128	-2.7126
2^{nd}	512	-3.1566
3^{rd}	2048	-3.1590
4^{th}	8192	-3.1920

Present Work (Sathiyamoorthy et al. (2010))

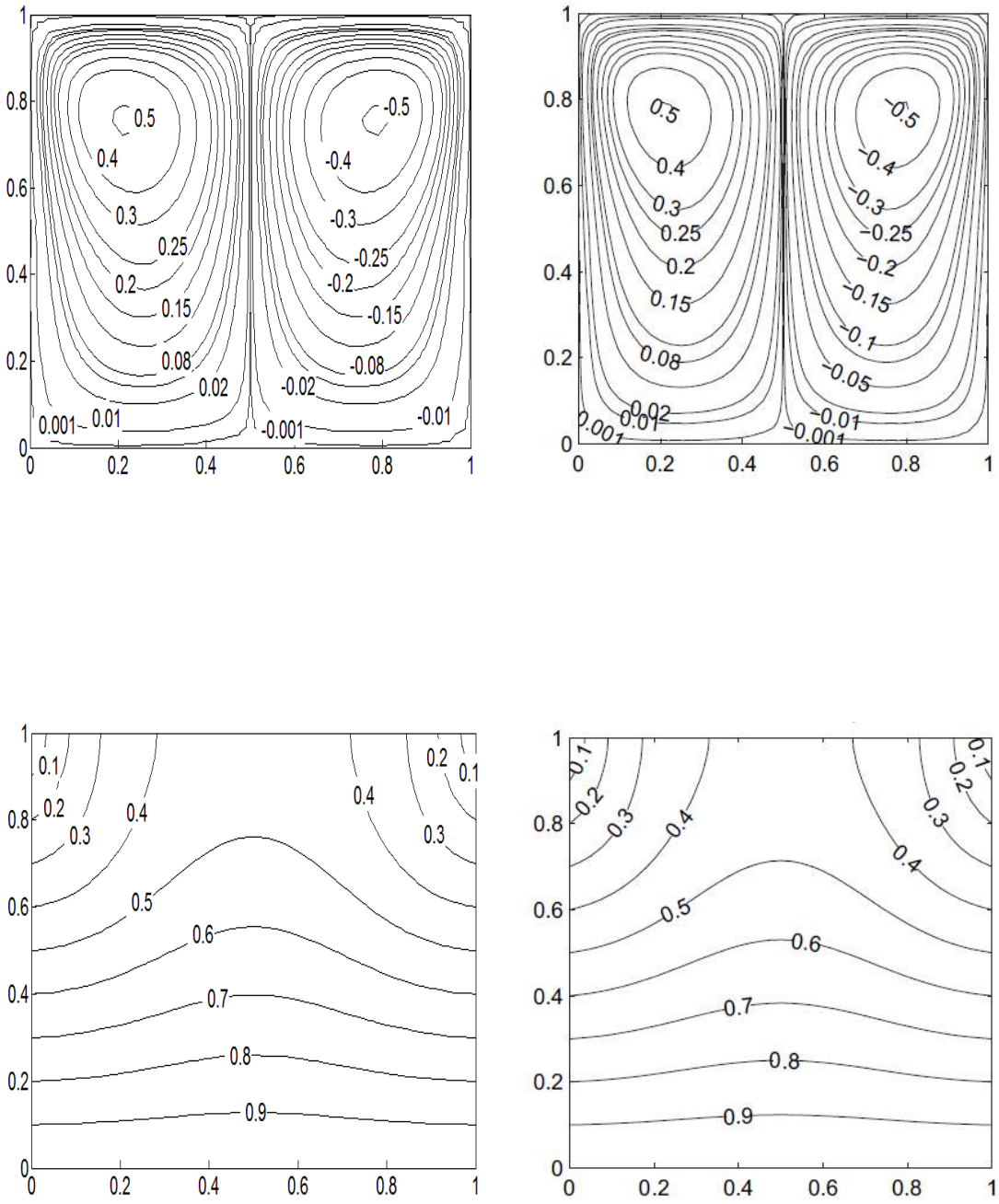

Figure. 3.2: Code validation for $Ha = 50, Ra = 10^5, Pr = 0.025, \phi = 0$ and $\theta = 1 - Y$

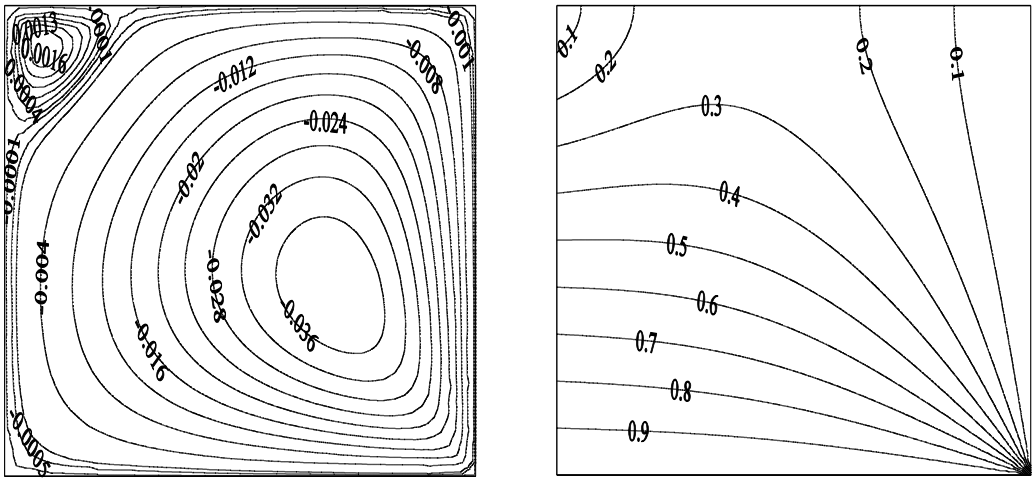

(a)

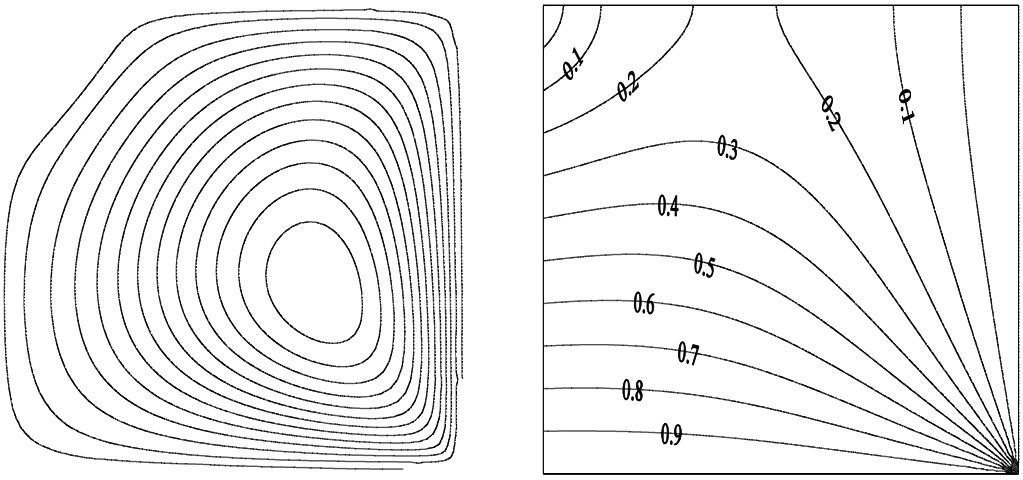

(b)

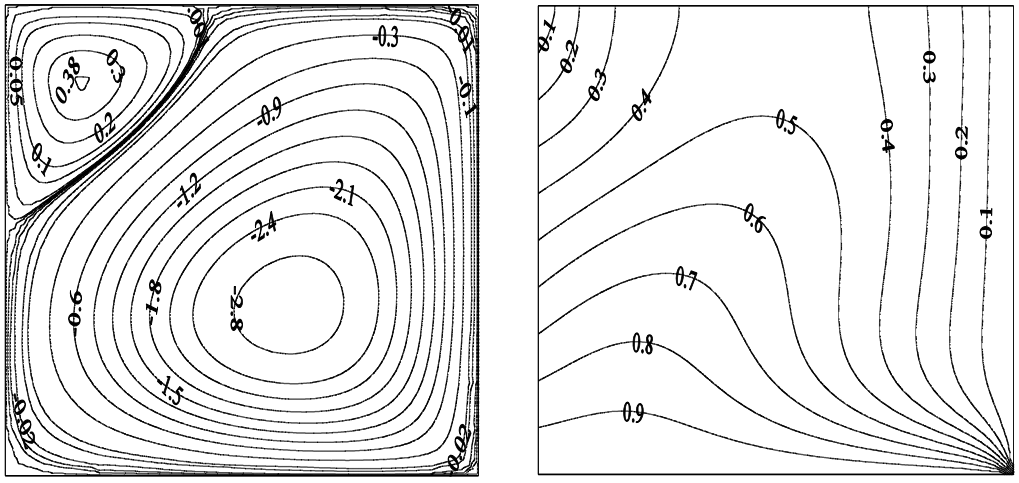

(c)

Figure 3.3: Isotherms and stream functions contours for cold right wall where $\mathrm{Ha} = 30, \mathrm{Ra} = 10^5, \mathrm{Pr} = 0.025$ (gallium), $\phi = 0$ **(a)** $\mathrm{Da} = 10^{-5}$ **(b)** $\mathrm{Da} = 10^{-4}$ **(c)** $\mathrm{Da} = 10^{-3}$

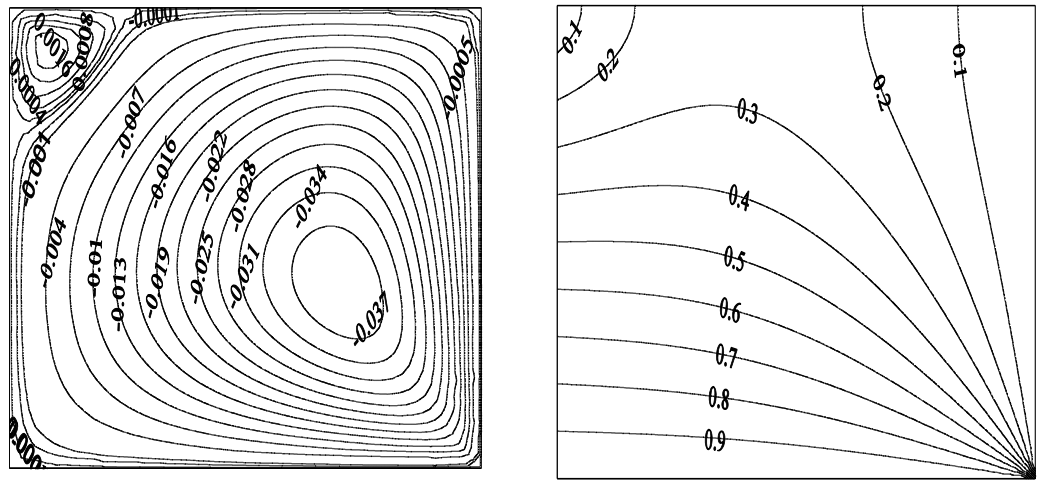

(a)

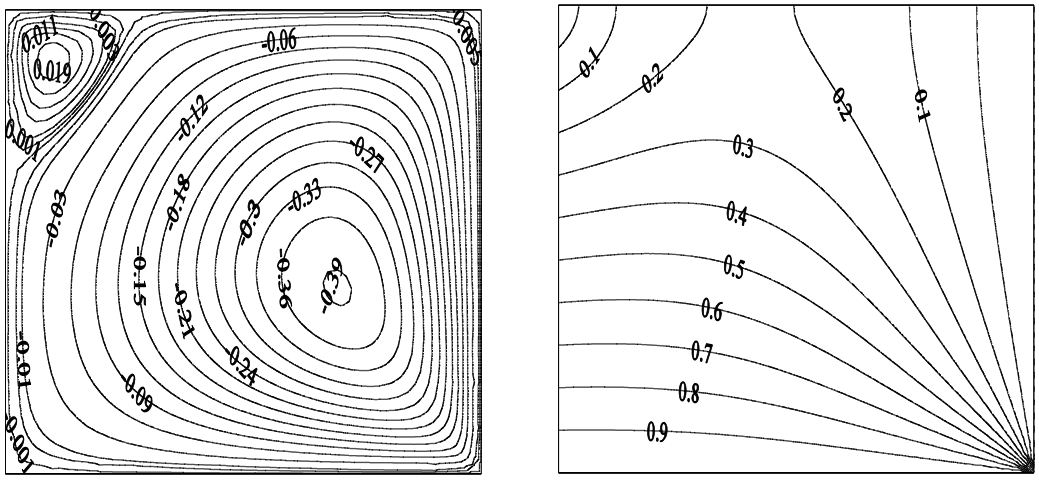

(b)

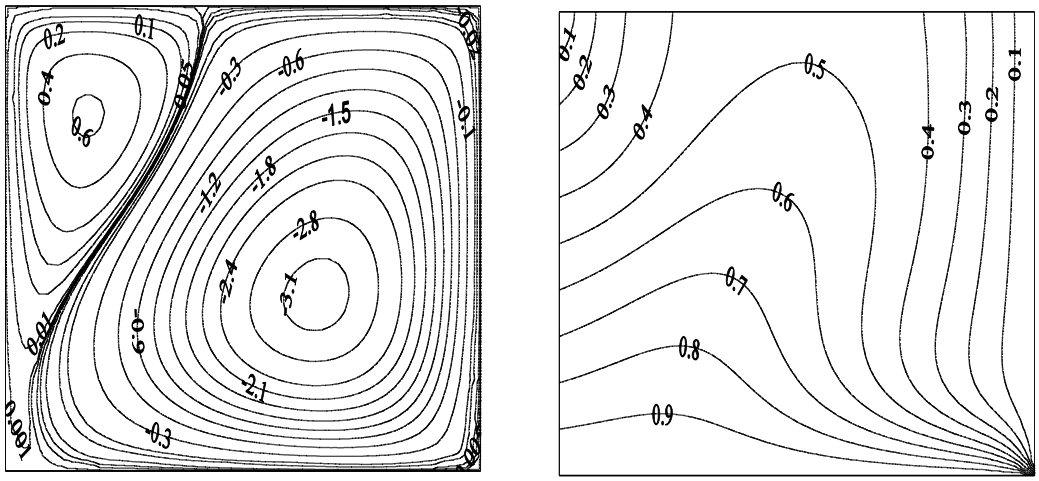

(c)

Figure 3.4: Isotherms and stream functions contours for cold right wall where, $\mathrm{Ha} = 30, \mathrm{Ra} = 10^5, \mathrm{Pr} = 0.025$ (gallium), $\phi = \frac{\pi}{2}$ **(a)** $\mathrm{Da} = 10^{-5}$ **(b)** $\mathrm{Da} = 10^{-4}$ **(c)** $\mathrm{Da} = 10^{-3}$

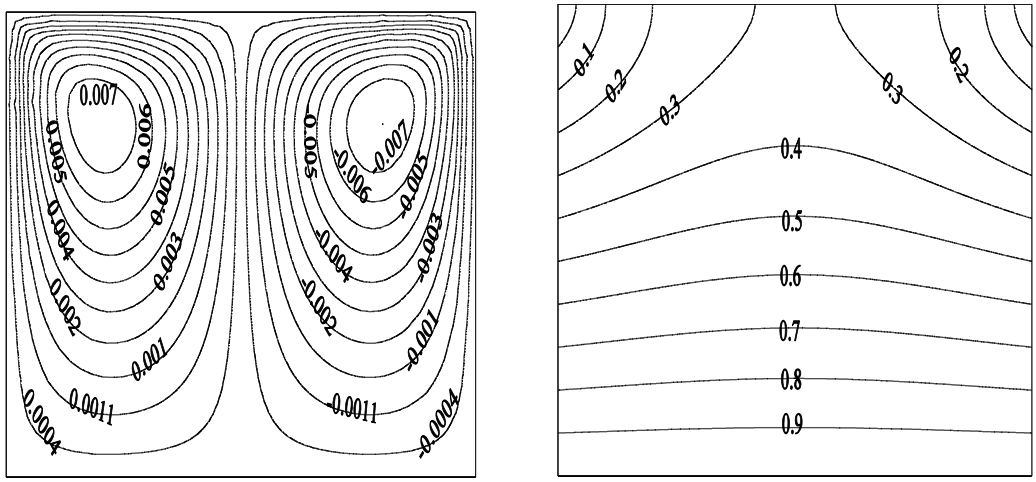

(a)

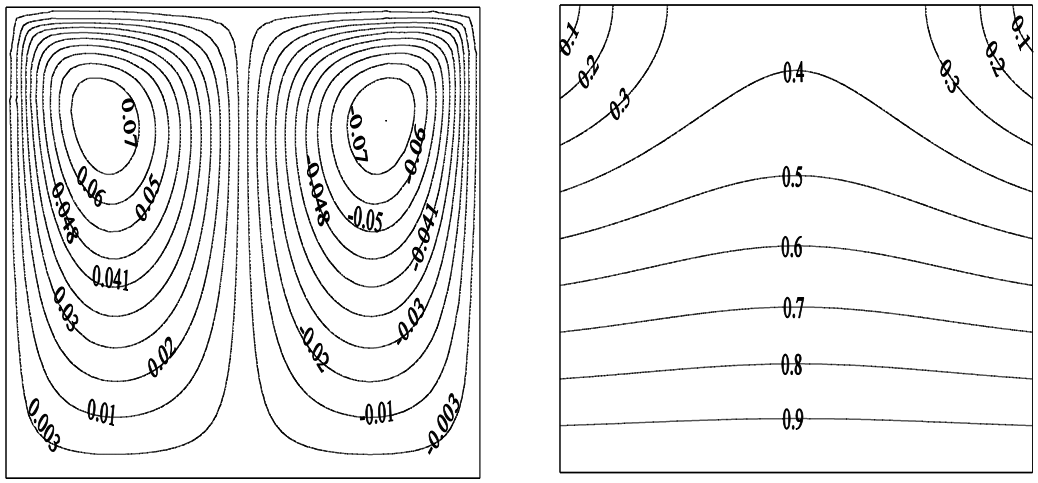

(b)

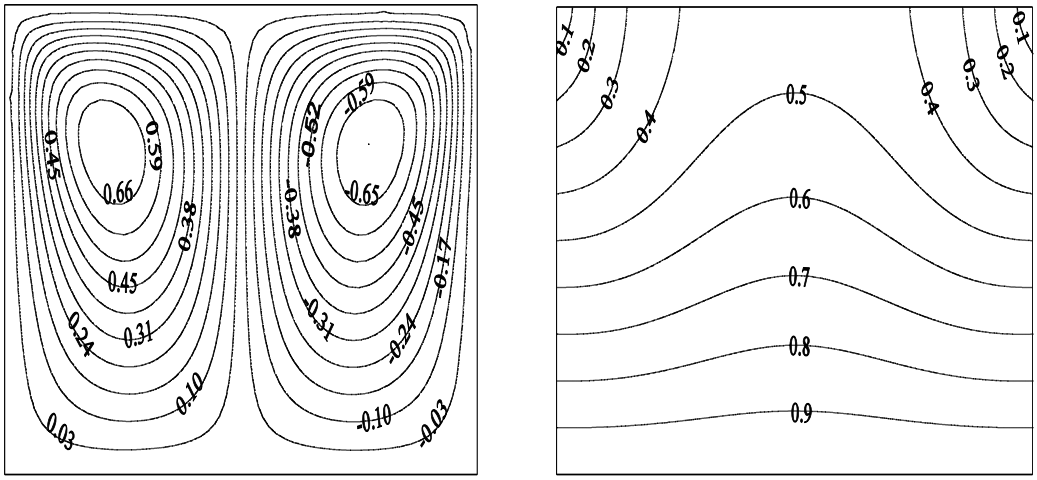

(c)

Figure 3.5: Isotherms and stream functions contours for linearly heated right wall & $\mathrm{Ha} = 30, \mathrm{Ra} = 10^5, \mathrm{Pr} = 0.025$ (gallium), $\phi = 0$ **(a)** $\mathrm{Da} = 10^{-5}$ **(b)** $\mathrm{Da} = 10^{-4}$ **(c)** $\mathrm{Da} = 10^{-3}$

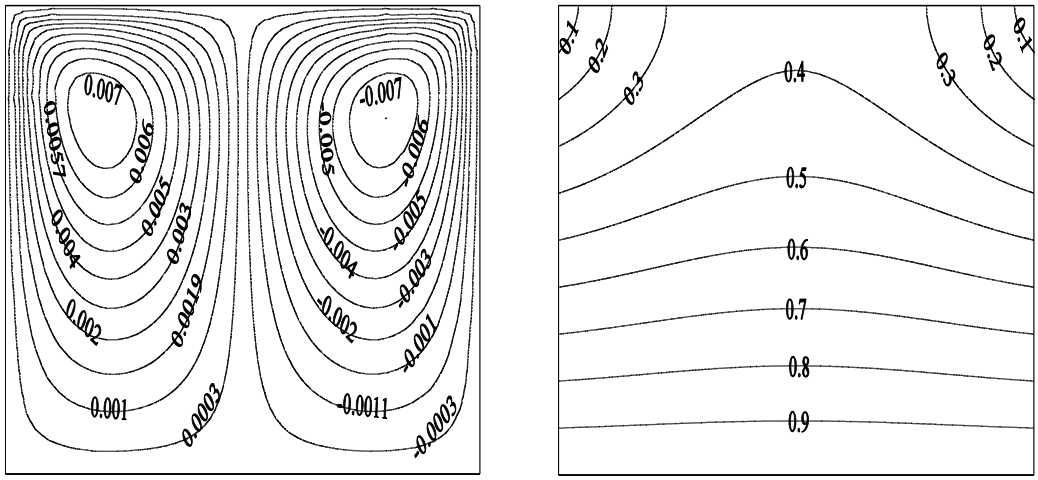

(a)

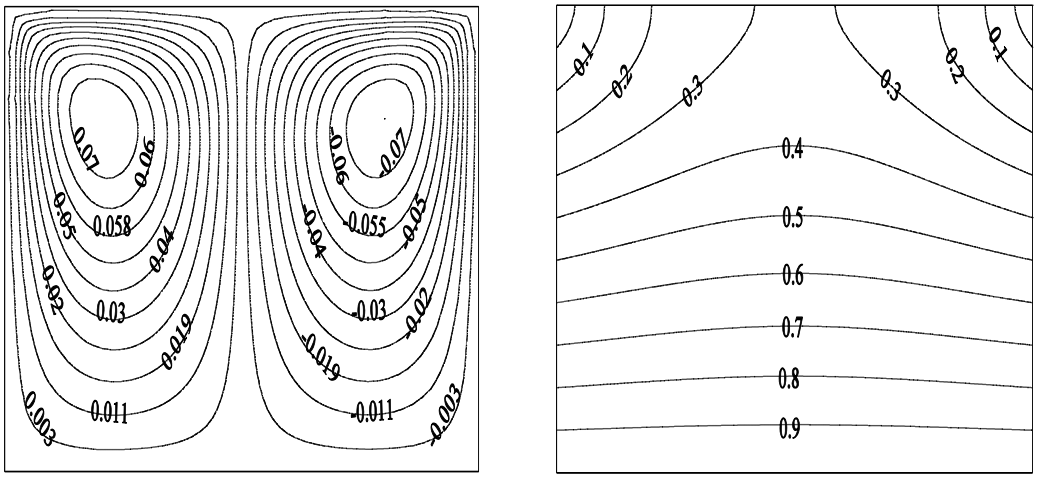

(b)

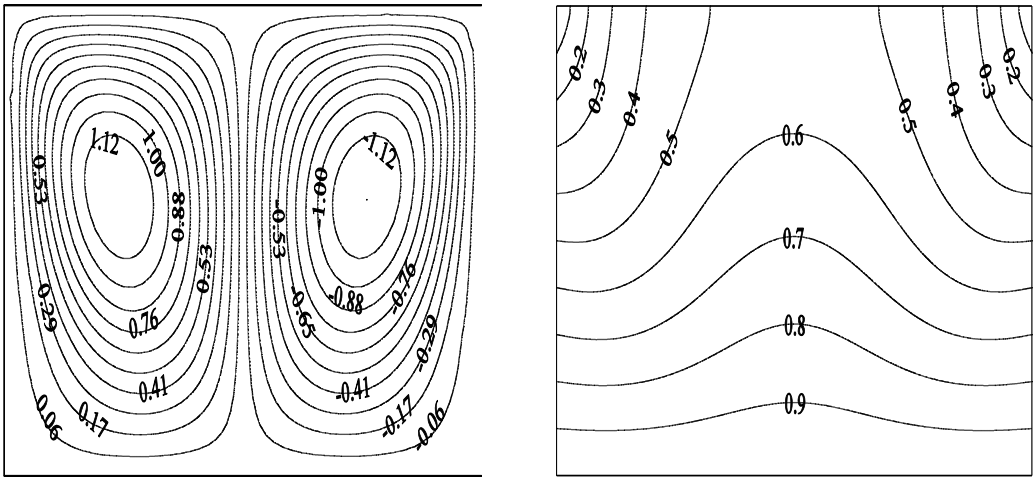

(c)

Figure 3.6: Isotherms and stream functions contours for linearly heated right wall & $\mathrm{Ha} = 30, \mathrm{Ra} = 10^5, \mathrm{Pr} = 0.025$ (gallium), $\phi = \frac{\pi}{2}$ **(a)** $\mathrm{Da} = 10^{-5}$ **(b)** $\mathrm{Da} = 10^{-4}$ **(c)** $\mathrm{Da} = 10^{-3}$

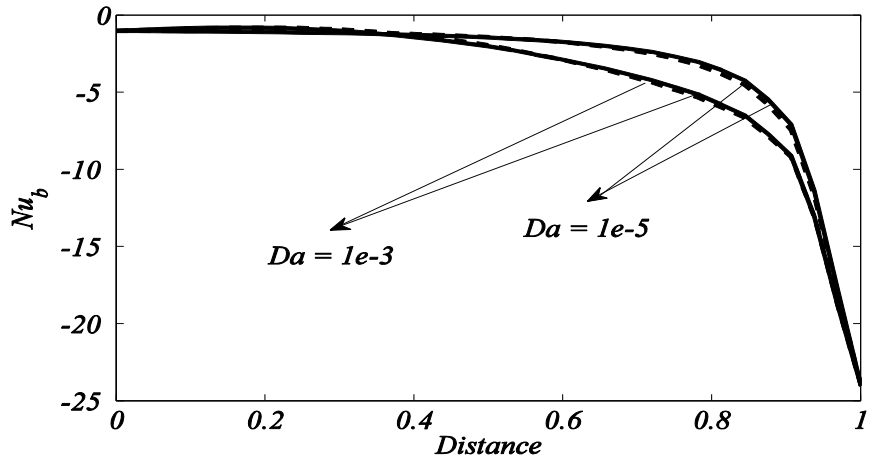

(a)

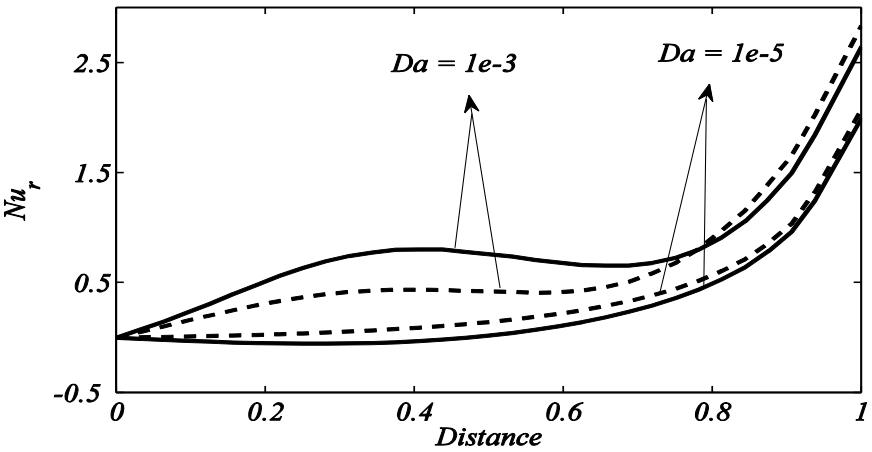

(b)

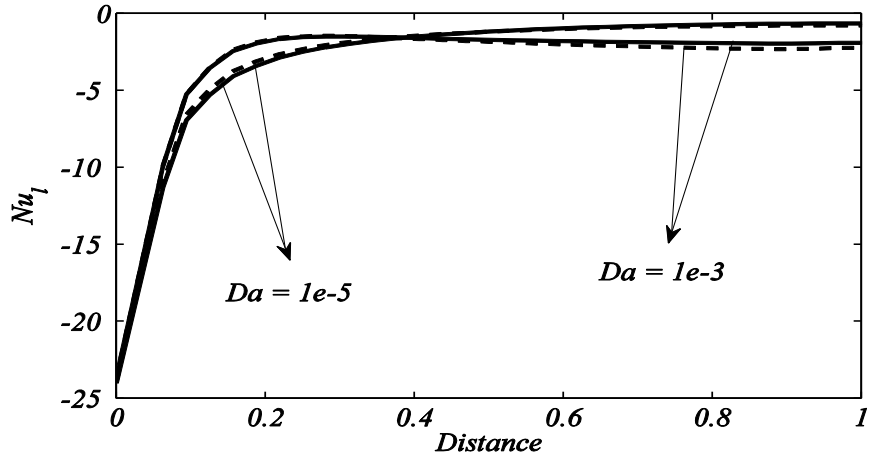

(c)

Figure 3.7: Nusselt number for cold right wall **(a)** bottom wall **(b)** left wall and **(c)** right wall

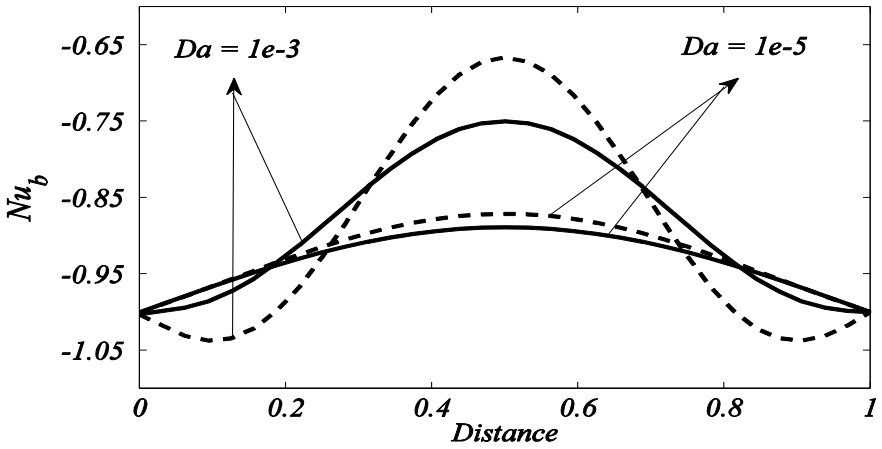

(a)

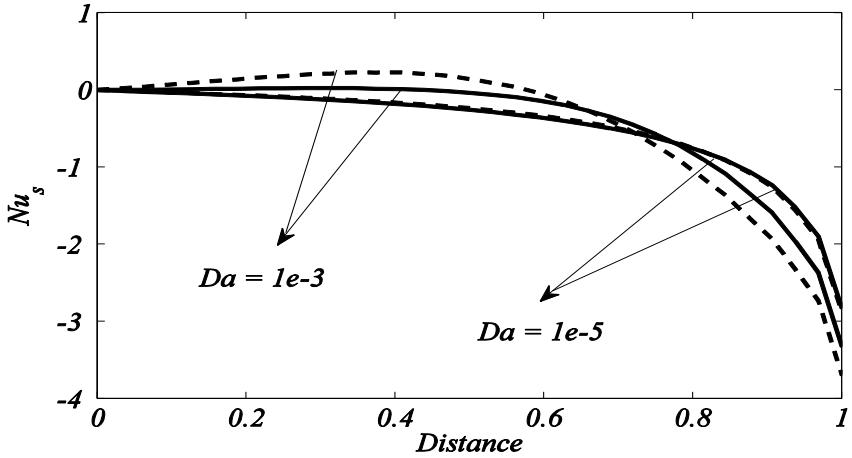

(b)

Figure 3.8: Nusselt number against linearly heated right wall **(a)** bottom wall and **(b)** Side walls

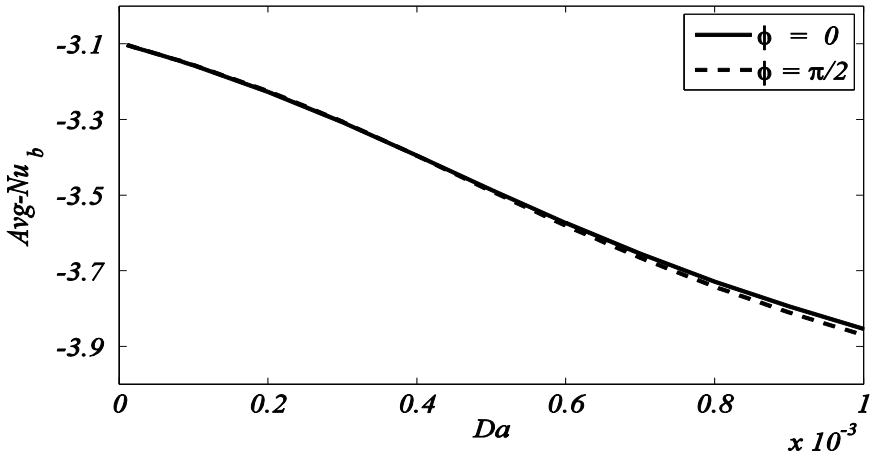

(a)

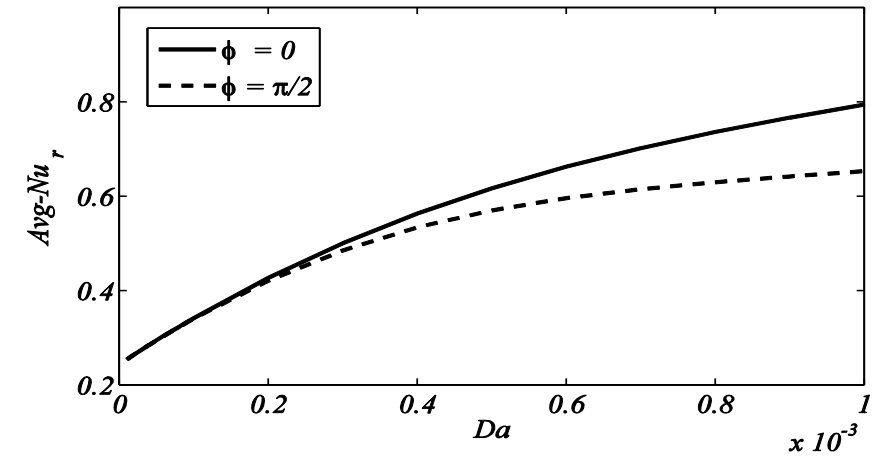

(b)

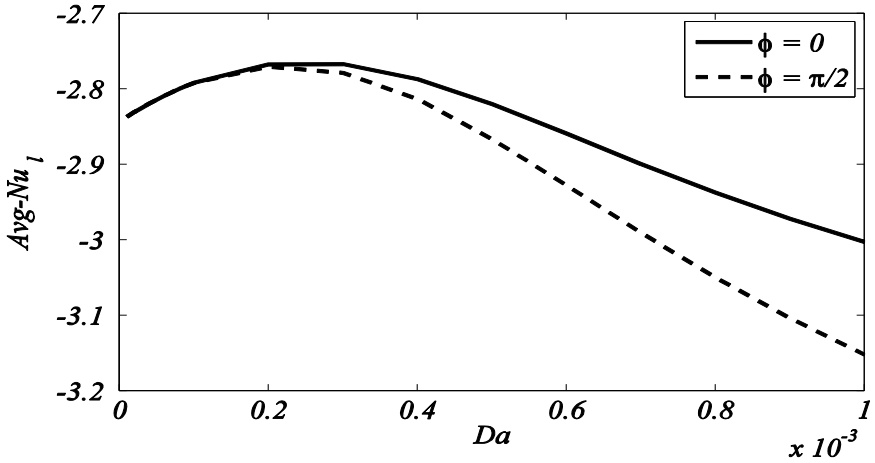

(c)

Figure 3.9: Average Nusselt number for cold right wall **(a)** bottom wall **(b)** left wall and **(c)** right wall

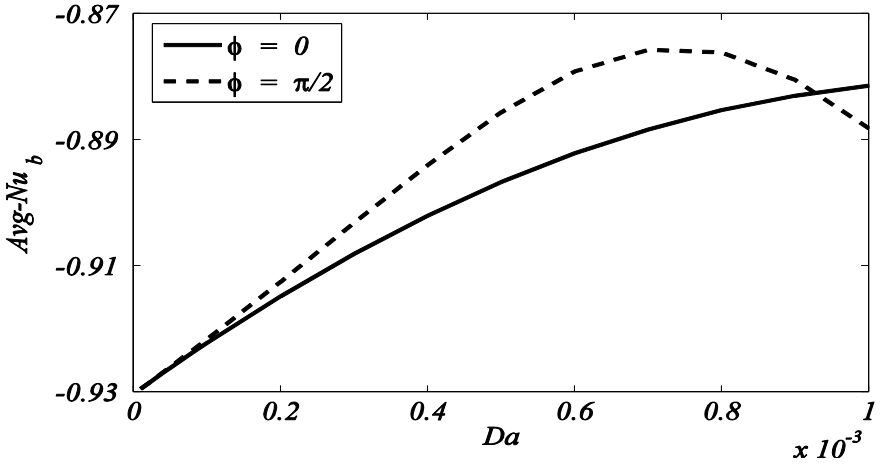

(a)

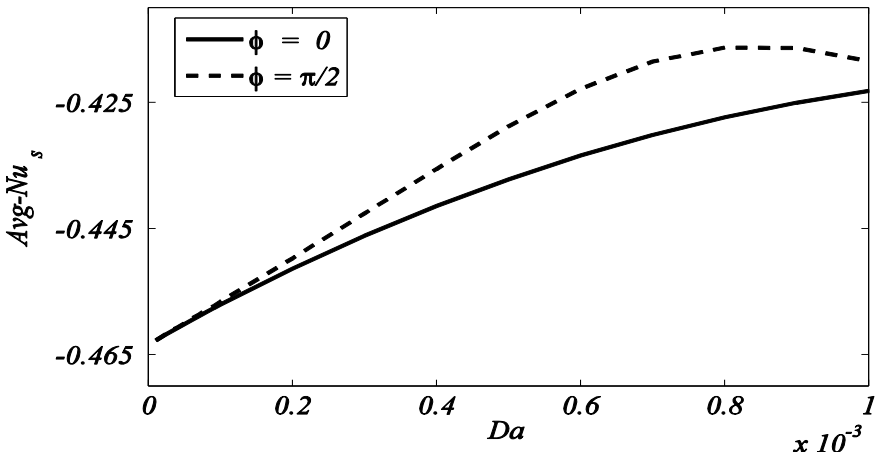

(b)

Figure 3.10: Average Nusselt Number for linearly heated right wall along **(a)** bottom wall **(b)** side walls

It is observed that for $\mathrm{Da} = 10^{-5}$, curves of Nusselt number for vertical and horizontal magnetic field are overlapping but when $\mathrm{Da} = 10^{-3}$, vertical magnetic field gives higher heat transfer rate than that of horizontal magnetic field if $Y < 0.7$ and reverse behavior is seen afterwards. It is further seen that along vertical sides of cavity Nusselt number reduces with increase in vertical distance Y and higher values of Darcy number returns higher heat transfer rate up to $Y = 0.75$ while reverse behavior is observed afterwards.

Figure 3.9 contains plots of average Nusselt numbers $\overline{\mathrm{Nu}}$ against porosity parameter and Darcy number for the case of cold right wall. It has been seen through the graphs that average temperature gradient along bottom wall decreases with increase in Darcy number while overall heat transfer rate along left wall rises with augmentation in Da and average temperature gradient along right wall first increases up to $\mathrm{Da} = 3 \times 10^{-4}$ and then decreases afterwards for growing values of Darcy number. Whereas against a particular value of Da average temperature gradient along bottom, left and right walls of cavity is higher for horizontal magnetic field $\phi = 0$ comparing to vertical magnetic field $\phi = \frac{\pi}{2}$.

Figure 3.10 consists of average temperature gradient along bottom and side walls against the case of linearly heated right side. Contrary to case of cold right wall, due to linearly heated right wall average temperature gradient along the side walls for vertical magnetic field is higher than that of horizontal magnetic field for a fixed value of Darcy number while, along bottom wall similar behavior is observed up to $\mathrm{Da} = 9 \times 10^{-4}$ and afterwards reverse behavior of average temperature gradient is seen. It is further noticed that for $\mathrm{Da} \leq 10^{-4}$, values of average temperature gradient for both horizontal and vertical magnetic fields overlaps along bottom and side walls of a cavity whereas, for $\mathrm{Da} > 10^{-4}$ average temperature gradient increases with augmentation in Darcy number along bottom and side walls.

3.5 Conclusions

In present chapter, numerical simulation has been made to investigate two dimensional laminar flow of viscous liquid gallium though a square enclosure full with porous media in the presence of horizontal/vertical magnetic field where bottom wall is heated uniformly, top wall is perfectly insulated, left wall of cavity is heated linearly and right wall is assumed either linearly heated or kept as cold. The governing equations of the flow problem are solved by applying Galerkin finite

element technique and resulting equations are subjected to Newton's method. Results are obtained for Hartmann number $\mathrm{Ha} = 30$, Rayleigh number $\mathrm{Ra} = 10^5$, Prandtl number $\mathrm{Pr} = 0.025$ (gallium) and Darcy number $10^{-5} < \mathrm{Da} < 10^{-3}$ while two inclination angles for magnetic field $\phi = 0$ or $\frac{\pi}{2}$ are considered.

After briefly examining the flow behavior, we have concluded that augmentation in Darcy number results in both, enhancement of strength of streamline circulations and growth in the height of isotherms in a cavity. Magnetic field applied in vertical direction reduces the rate of increase up to $\mathrm{Da} = 10^{-4}$ and increasing Darcy number beyond this value sharpens the rate of increase in strength of streamline circulation and height of isotherms. With increase in horizontal distance X, heat transfer rate Nu decrease along bottom wall when right side is maintained at low temperature. When the right side is subject to linear heating, Nusselt number shows sinusoidal type behavior along bottom wall and it decreases with increase in vertical distance Y along the side walls when right wall is considered to be heated linearly, while for cold right wall Nu increases along left wall of the cavity and along right side Nu first increases sharply and then becomes almost constant. Opposite to this, higher average Nusselt numbers are observed under influence of magnetic field in vertical direction as compare to applied magnetic field in horizontal direction where average Nusselt number is observed to increase along bottom and side walls with augmentation in Darcy number for the case in which right wall is supposed to be heated linearly. Whereas for cold right wall, average heat transfer rate decreases with increase in Darcy number along bottom and right wall while it increases along left wall of the cavity and horizontal magnetic field results in higher average temperature gradient as compare to that of vertical magnetic field.

Chapter 4

Energy Transfer through Micropolar Fluid saturated in a Lid-Driven Square Cavity influenced by Magnetic Force

This chapter contains computations for mixed convective energy flow through a square container carrying micropolar fluid in the presence of constant horizontal magnetic field. Bottom wall of the cavity is subject to non-uniform heat while remaining walls of the cavity are maintained at low temperature. Numerical simulations are computed incorporating Galerkin method of finite element technique against different values of involved parameters like Grashof, Reynolds, Hartmann numbers and micropolar parameter. It has been observed that the strength of streamline circulations escalates due to augmentation in Grashof number where it attenuates with augmentation in Hartmann and Reynolds numbers. Convection regime dominates in the cavity for large Grashof number and small Hartmann number. Heat transfer coefficient Nu rises with surge in Reynolds number, Hartmann number and micropolar parameter and it reduces with rise in Grashof number along top wall where overall heat flow rate is observed an increasing function of Grashof and decreasing function of both Reynolds and Hartmann numbers along bottom wall.

4.1 Problem Formulation

A geometrical representation of the square cavity which is considered in this investigation is presented in **Figure 4.1**. The width and height of the square enclosure is represented by L and length of an enclosure is supposed to be long enough so the investigation can be considered as 2D in cartesian co-ordinate system. It is supposed that the ceiling or top wall is moving with constant velocity U_0 while rest of the walls is in static position. The left and right vertical walls with top lid are maintained at a low temperature T_c, lower bottom horizontal wall is considered to be heated non-uniformly. The gravitational force considered, acts in negative y-direction. Since density variation of micropolar fluid is a function of temperature therefore, Boussinesq's approximation is valid and all remaining physical properties are supposed to be constant.

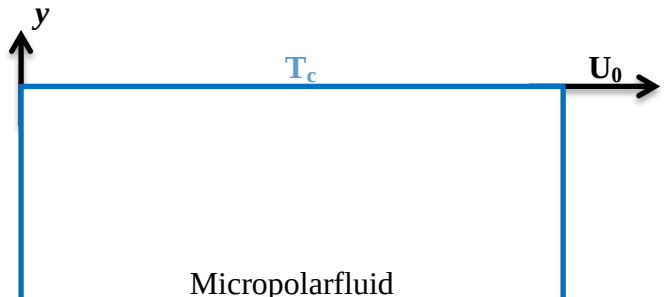

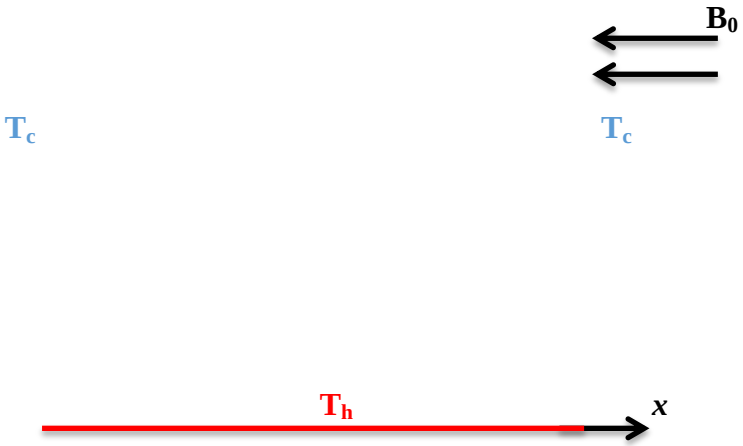

Figure 4.1: Geometrical representation of the present problem.

In present study, micropolar fluid is considered as steady, Newtonian, incompressible and laminar. Furthermore, magnetic force with magnitude of strength B_0 is assumed parallel to horizontal axis. Here induced magnetic field has been ignored being sufficiently small in comparison to applied magnetic field B_0 under low-R_m approximation (Davidson (2001)) Assuming the boundaries of container be insulated electrically with no Hall effects, the damping factor ${B_0}^2 v$ represents the total electromagnetic force; here v is vertical velocity component. Therefore, Lorentz force is a function of velocity component v. For electrically conductive micropolar fluid flow considering peripheral magnetic field, the energy, mass, linear and angular momentum conservation laws may be expressed in the form given below

$$\nabla . V = 0, \tag{4.1}$$

$$\rho(V.\nabla)V = -\nabla p + (\mu + \kappa)\nabla^2 V + \kappa \nabla \times N - g\rho\beta(T - T_c) + J \times B, \tag{4.2}$$

$$(V.\nabla)N = \gamma_1 \nabla^2 N + \kappa \nabla \times V - 2\kappa N, \tag{4.3}$$

$$(V.\nabla)T = \alpha \nabla^2 T. \tag{4.4}$$

Here **V** = *(u(x, y),v(x, y),0)* represents two dimensional velocity vector and its rectangular components are u and v, where T represents temperature of fluid everywhere in the cavity, **N** = $(0,0,N^*(x, y))$ is two dimensional micro-rotation vector, p represents the modified pressure, **g** is an acceleration vector due to gravity which is acting perpendicular to $x-$axis, ρ is density of micropolar fluid, κ is the vortex viscosity, **B** is magnetic field, j is the micro-inertia density, μ is dynamic viscosity, γ_1 is the spin-gradient viscosity, α is the thermal diffusivity of the micropolar fluid and **J** is the current density defined in the absence of an electric field as follows:

$$J = \sigma(V \times B). \tag{4.5}$$

Under the above suppositions, the governing model for two dimensional micropolar fluid flow with the help of Eqs. (4.1) – (4.4) may be reduced in the form given below

$$\frac{\partial u}{\partial x} + \frac{\partial v}{\partial y} = 0, \tag{4.6}$$

$$u\frac{\partial u}{\partial x} + v\frac{\partial u}{\partial y} = -\frac{1}{\rho}\frac{\partial p}{\partial x} + \frac{(\mu+\kappa)}{\rho}\left(\frac{\partial^2 u}{\partial x^2} + \frac{\partial^2 u}{\partial y^2}\right) + \kappa\frac{\partial N^*}{\partial y}, \tag{4.7}$$

$$u\frac{\partial v}{\partial x} + v\frac{\partial v}{\partial y} = -\frac{1}{\rho}\frac{\partial p}{\partial y} + \frac{(\mu+\kappa)}{\rho}\left(\frac{\partial^2 v}{\partial x^2} + \frac{\partial^2 v}{\partial y^2}\right) + g\beta(T - T_c) - \frac{\sigma B_0^2}{\rho}v - \kappa\frac{\partial N^*}{\partial x}, \tag{4.8}$$

$$u\frac{\partial N^*}{\partial x} + v\frac{\partial N^*}{\partial y} = \frac{\gamma_1}{\rho j}\left(\frac{\partial^2 N^*}{\partial x^2} + \frac{\partial^2 N^*}{\partial y^2}\right) - \frac{\kappa}{\rho j}\left(2N^* + \frac{\partial u}{\partial y} - \frac{\partial v}{\partial x}\right), \tag{4.9}$$

$$u\frac{\partial T}{\partial x} + v\frac{\partial T}{\partial y} = \alpha\left(\frac{\partial^2 T}{\partial x^2} + \frac{\partial^2 T}{\partial y^2}\right) \tag{4.10}$$

under the following boundary conditions

$$v = 0, u = 0, T = (T_h - T_c)sin\left(\frac{\pi x}{L}\right) + T_c \text{ and } N^* = \frac{-1}{2}\frac{\partial u}{\partial y} \text{ for } 0 \le x \le L, y = 0,$$

$$v = 0, u = U_0, T = T_c \text{ and } N^* = \frac{-1}{2}\frac{\partial u}{\partial y} \text{ for } 0 \le x \le L, y = L,$$

$$v = 0, u = 0, T = T_c \text{ and } N^* = \frac{1}{2}\frac{\partial v}{\partial x} \text{ for } 0 \le y \le L, x = 0,$$

$$v = 0, u = 0, T = T_c \text{ and } N^* = \frac{1}{2}\frac{\partial v}{\partial x} \text{ for } 0 \le y \le L, x = L. \tag{4.11}$$

The non-dimensional variables are introduced as follows:

$$X = \frac{x}{L}, Y = \frac{y}{L}, U = \frac{u}{U_0}, V = \frac{v}{U_0}, P = \frac{p}{\rho {U_0}^2}, \theta = \frac{T - T_c}{T_h - T_c}, R = \frac{\kappa}{\mu}, \gamma_1 = \left(\mu + \frac{\kappa}{2}\right)j, \Pr = \frac{\nu}{\alpha}, \mathrm{Gr} = \frac{g\beta L^3(T_h - T_c)}{\nu^2}, \mathrm{Ha}^2 = \frac{\sigma {B_o}^2 L^2}{\mu}, B = \frac{L^2}{j}, \mathrm{Re} = \frac{U_0 L}{\nu}, N = \frac{N^*\alpha}{{U_0}^2}. \tag{4.12}$$

After substitution of the above mentioned variables in Eqs. (4.6 - 4.11), we get:

$$\frac{\partial U}{\partial X} + \frac{\partial V}{\partial Y} = 0, \tag{4.13}$$

$$U\frac{\partial U}{\partial X} + V\frac{\partial U}{\partial Y} = -\frac{\partial P}{\partial X} + \frac{(1+R)}{\mathrm{Re}}\left(\frac{\partial^2 U}{\partial X^2} + \frac{\partial^2 U}{\partial Y^2}\right) + \Pr R\frac{\partial N}{\partial Y}, \tag{4.14}$$

$$U\frac{\partial V}{\partial X} + V\frac{\partial V}{\partial Y} = -\frac{\partial P}{\partial Y} + \frac{(1+R)}{\mathrm{Re}}\left(\frac{\partial^2 V}{\partial X^2} + \frac{\partial^2 V}{\partial Y^2}\right) + \frac{\mathrm{Gr}}{\mathrm{Re}^2}\theta - \mathrm{Ha}^2\Pr V - \Pr R\frac{\partial N}{\partial X}, \tag{4.15}$$

$$U\frac{\partial N}{\partial X} + V\frac{\partial N}{\partial Y} = \frac{\left(1+\frac{R}{2}\right)}{\mathrm{Re}}\left(\frac{\partial^2 N}{\partial X^2} + \frac{\partial^2 N}{\partial Y^2}\right) - \frac{RB}{\mathrm{Re}}\left(2N + \frac{\partial U}{\partial Y} - \frac{\partial V}{\partial X}\right), \tag{4.16}$$

$$U\frac{\partial \theta}{\partial X} + V\frac{\partial \theta}{\partial Y} = \frac{1}{\mathrm{RePr}}\left(\frac{\partial^2 \theta}{\partial X^2} + \frac{\partial^2 \theta}{\partial Y^2}\right). \tag{4.17}$$

Here U, V and θ be dimensionless form of velocity components and temperature respectively and R are the micropolar parameters.

The reduced boundary conditions for velocities U, V and temperature θ in dimensionless form are given below

$$V = U = 0, \theta = sin(\pi X) \text{ and } N = \frac{-1}{2}\frac{\partial U}{\partial Y} \text{ for } 0 \leq X \leq 1, Y = 0,$$

$$V = 0, U = 1, \theta = 0 \text{ and } N = \frac{-1}{2}\frac{\partial U}{\partial Y} \text{ for } 0 \leq X \leq 1, Y = 1,$$

$$V = 0, U = 0, \theta = 0 \text{ and } N = \frac{1}{2}\frac{\partial V}{\partial X} \text{ for } 0 \leq Y \leq 1, X = 0,$$

$$V = 0, U = 0, \theta = 0 \text{ and } N = \frac{1}{2}\frac{\partial V}{\partial X} \text{ for } 0 \leq Y \leq 1, X = 1. \quad (4.18)$$

The heat flow rate Nu and average heat flow rate $\overline{\text{Nu}}$ for horizontal walls are defined as follows

$$\text{Nu} = -\frac{\partial \theta}{\partial \eta} \quad (4.19)$$

$$\overline{\text{Nu}} = \frac{\int_0^1 \text{Nu} dx}{X|_0^1} = \int_0^1 \text{Nu} dx, \quad (4.20)$$

where η represents the normal direction on the surface.

4.2 Methodology

Governing non-dimensional Eqs. (4.13) – (4.17) subject to the transformed boundary conditions defined in Eq. (4.18) are solved with the help of Galerkin weighted residual method. Pressure terms are eliminated from Eqs. (4.14) – (4.15) by using penalty method. The penalty parameter γ is defined as

$$P = -\gamma\left(\frac{\partial U}{\partial X} + \frac{\partial V}{\partial Y}\right). \quad (4.21)$$

For large values of γ, ensure that continuity equation stated in Eq. (4.13) is satisfied. Generally $\gamma = 10^7$ returns consistent solutions. After substituting Eq. (4.21) in Eqs. (4.14 - 4.15), we get the following form:

$$U\frac{\partial U}{\partial X} + V\frac{\partial U}{\partial Y} = -\gamma\frac{\partial}{\partial X}\left(\frac{\partial U}{\partial X} + \frac{\partial V}{\partial Y}\right) + \frac{(1+R)}{\text{Re}}\left(\frac{\partial^2 U}{\partial X^2} + \frac{\partial^2 U}{\partial Y^2}\right) + \text{Pr}R\frac{\partial N}{\partial Y}, \quad (4.22)$$

$$U\frac{\partial V}{\partial X} + V\frac{\partial V}{\partial Y} = -\gamma\frac{\partial}{\partial X}\left(\frac{\partial U}{\partial X} + \frac{\partial V}{\partial Y}\right) + \frac{(1+R)}{\text{Re}}\left(\frac{\partial^2 V}{\partial X^2} + \frac{\partial^2 V}{\partial Y^2}\right) + \frac{\text{Gr}}{\text{Re}^2}\theta - \text{Ha}^2\text{Pr}V - \text{Pr}R\frac{\partial N}{\partial X}. \quad (4.23)$$

Galerkin weighted residual method is employed to simplify the system of Eqs. (4.16), (4.17), (4.22) and (4.23). As the solution methodology in details is described in chapter 2 (Method of Solution). Therefore the detailed explanation of solution procedure in not included in the present section.

4.3 Results and Discussions

In this section we have presented and explained the obtained numerical results in the form of plots against isotherms, streamlines, microrotations, heat transfer and overall heat transfer rates against different values of governing parameters i.e. Grashof, Rayleigh, Prandtl and Hartmann numbers and their explanation is made.

Since lower boundary is subject to heating therefore after absorbing heat from hot bottom wall, fluid near bottom wall starts moving upward along vertical boundaries and come down along the vertical line passing through centre of lower boundary causing a pair of circulation cells with clockwise and counter clockwise rotations.

Figure 4.2 displays the influence of Grashof number on streamlines, isotherms and microrotation of the flow. It has been noticed that effects of moving lid reduces with augmentation in Grashof number and thus for $\mathrm{Gr} = 10^6$, no effect of moving lid is observed on streamline contours. The augmentation in magnitude of stream function is noted due to enhancement in Grashof number where $0.25, 1.5$ and 4.5 are the maximum values of stream function against $\mathrm{Gr} = 10^4$, 10^5 and 10^6 respectively. Isotherm contours are seen to cover most part of the cavity for $\mathrm{Gr} = 10^4$ and when Gr is increased to 10^5 isotherm contour are compressed down towards bottom wall while due to further increase in Grashof number ($\mathrm{Gr} = 10^6$), isotherms are clustered near bottom wall becoming almost parallel to $x-$axis in central region near bottom wall where most of cavity appears to be empty. The significant temperature gradient near the bottom side results into appearance of thermal boundary layer alongwith lower boundary of the enclosure. Two panels of microrotation are observed in the cavity because of two circulations cells for streamlines and larger values of Grashof number return stronger isotherms for microrotations.

Figure 4.3 presents the influence of magnetic field on streamlines, isotherms and microrotation of the flow pattern. It is observed that escalation in magnitude of Lorentz force weakens strength of streamline circulations and effects of moving lid becomes prominent when Hartmann number is augmented and centre of circulation cells gets pushed towards lower horizontal wall when Ha is raised. Magnitude of stream function against $\mathrm{Ha} = 0, 30, 60$ and 100 are noted to be $2.25, 1.5, 0.86$ and 0.43 respectively. Conduction dominant regime is observed in the cavity for large values of Ha while convection effect becomes dominant when Hartmann number gets decreased. Furthermore contours for isotherms appear to be parallel to bottom wall in

central region of the cavity and are clustered near bottom wall when magnetic field is absent ($\mathrm{Ha} = 0$). Introducing magnetic field causes smooth and monotonic isotherm contours and when strength of magnetic field is increased the isotherms cover most of the region in cavity. Surge in value of Ha causes a sheer stress due to which isothermlines for microrotations are noticed to be clustered near the side walls of the enclosure and near the boundaries of circulations cells.

Figure 4.4 presents impact of Reynolds number upon streamlines, isotherms and microrotation of the flow. Just like Hartmann number Reynolds number also had opposing influence upon strength of flow rotation. For $\mathrm{Re} = 1$ there appear two symmetric circulation cells out of which one is clockwise and other is anticlockwise but when Re is increased to 10 there appears a secondary anticlockwise circulation cell near top wall because of the moving lid.

The strength of secondary circulation cells is lesser than that of primary cells while symmetry of circulation cells is lost. Magnitudes of stream function are observed to be 1.5 and 0.04 for $\mathrm{Re} = 1$ and 10 respectively while strength of secondary circulation cell against $\mathrm{Re} = 10$ is 0.03. When value of Reynolds number is further increased to 100, symmetric primary circulation cells vanish and there appears only one very weak anticlockwise circulation cell close to moving top wall because of the significant effects of sliding wall and gradual reduction in the buoyancy whereas all streamline contours in this case are clustered near top wall leaving rest of the cavity empty where magnitude of stream function for this case is 0.002. Increase in Reynolds number augments the influence of forced convection and free convection is curbed in the enclosure. For small value of Re, a small amount of energy is seen to be taken away from the moving top wall; afterwards, energy is mainly transported by conduction regime inside the enclosure. Whereas due to escalation in value of Reynolds number the isotherms get stretched towards upper wall of the cavity. Smooth, monotonic and symmetric isotherm contour are seen in the enclosure against all values of Reynolds number. The magnitude of microrotation contours has been investigated to decrease by increasing the Reynolds number.

Figure 4.5 expresses the influences of micropolar parameter R on streamlines, isotherms and micro-rotation of the flow. It is noticed that streamline rotation strength is a decreasing function of micropolar parameter R. When value of micropolar parameter is taken zero i.e. for the case of plain fluid, the effects of moving lid are

negligible and there appear two symmetric circulation cells in the cavity. However, when fluid becomes micropolar i.e. value of R is increased to 1 influence of moving lid becomes visible and cores of circulation cells are stretched a little upward while clockwise circulation cell is pushed down in upper portion of enclosure. When micropolar parameter R is further increased to 100, effects of moving lid becomes dominant and as a result a very weak counter clockwise secondary circulation cell appears near moving top wall in addition to two primary circulation cells. Magnitudes of stream function are observed to be $1.8, 0.75$ and 0.06 for $R = 0, 1$ and 10 respectively. Whereas isotherm contours are observed to stretched upward when value of R is increased. Isotherm lines get weaken with increase in R.

Figure 4.6 contains the graphs for heat flow rate Nu against varying Hartmann number along horizontal walls of enclosure. It is noticed that heat transfer rate i.e. Nu is minimum at edges along top horizontal wall and it increases while moving inward from edges achieving maximum value at the center of top boundary. Moreover, rising Ha augments the energy flow rate about top horizontal walls as represented in **Figure 4.6 (b)**, whereas along bottom wall value of Nu first decreases slightly and then increases by moving inward from corners of boundary and achieves its maximum at middle of wall making a wave like pattern. Contrary to the top wall energy flow rate decreases with augmentation in Hartmann number near central region of wall while near the edges of this boundary Nu increases with surge in Ha.

Figure 4.7 shows results for local Nusselt number along top and bottom boundaries of the cavity against various values of Grashof number. It has been noticed that the escalation in Gr increases Nusselt number close to central portion of bottom horizontal wall while Nu decreases with increase in Gr near the edges of lower boundary where heat transfer rate follows a wave pattern along bottom wall. On contrary, energy flow rate Nu attenuates due to augmentation in Grashof number along top wall of the enclosure as shown in **Figure 4.7 (b)**.

Figure 4.8 describes the behaviour of heat transfer rate along top and lower horizontal boundaries of square enclosure for various values of micropolar parameter R. It is seen in figure that following the case of effects of Grashof and Hartmann numbers on heat transfer rate, curves are of wave shape along bottom wall in this case also. Increase in the value of R results into decrease of Nusselt number in the central portion of bottom wall while near corners of the wall an opposite effect of increase in

R is observed. Whereas throughout along top wall, augmentation in Nu is found with increase in values of R where curves follow bell shaped behaviour having minimum value at the edges and maximum at middle of the top wall.

Figure 4.9 describes the behavior of overall heat transfer rate along top and lower horizontal boundaries of square enclosure against Grashof number for varying micropolar parameter R. Average Nusselt number is seen increasing with rise in micropolar parameter R along top wall. However, along bottom wall it increases with R up to $\mathrm{Gr} = 10^5$ and for $\mathrm{Gr} > 10^5$ overall heat transfer rate reduces due to augmentation in R. Whereas, average Nusselt number first decreases slightly and then escalates along bottom wall with augmentation in Grashof number against fixed value of R while along top wall, augmentation in Gr results into attenuation in average energy flow rate.

Figure 4.10 shows the graphs for overall energy flow rate along upper and lower boundaries against Hartmann number for varying Reynolds number. It has been observed that with increasing the Hartmann number, overall energy flow rate first decreases and then increases for a fixed Reynolds number along with bottom and top walls. Whereas increase in Reynolds number is observed to augment overall energy flow rate along top boundary but the overall heat transfer rate reduces due to augmentation in Re if $\mathrm{Ha} < 30$ along the bottom wall.

Figure 4.11 contains the graphs for average energy flow rate along top and lower boundaries of enclosure against Hartmann number for different micropolar parameter R. Figure shows that increase in the value of micropolar parameter R augments the mean heat flow rate along top boundary against all Ha and also along bottom wall when $\mathrm{Ha} > 23$ while for $\mathrm{Ha} < 23$ average energy flow rate attenuates with augmentation in R. Whereas for large values of micropolar parameter e.g. ($R = 5,10$) magnetic field have insignificant effects on average heat transfer rate and curves appears to be straight line along bottom wall but for small R mean heat flow rate decreases with rise in Ha. Furthermore, increasing Hartmann number escalate average Nusselt number along top wall of enclosure for any fixed R.

Streamlines Isotherms Microrotations

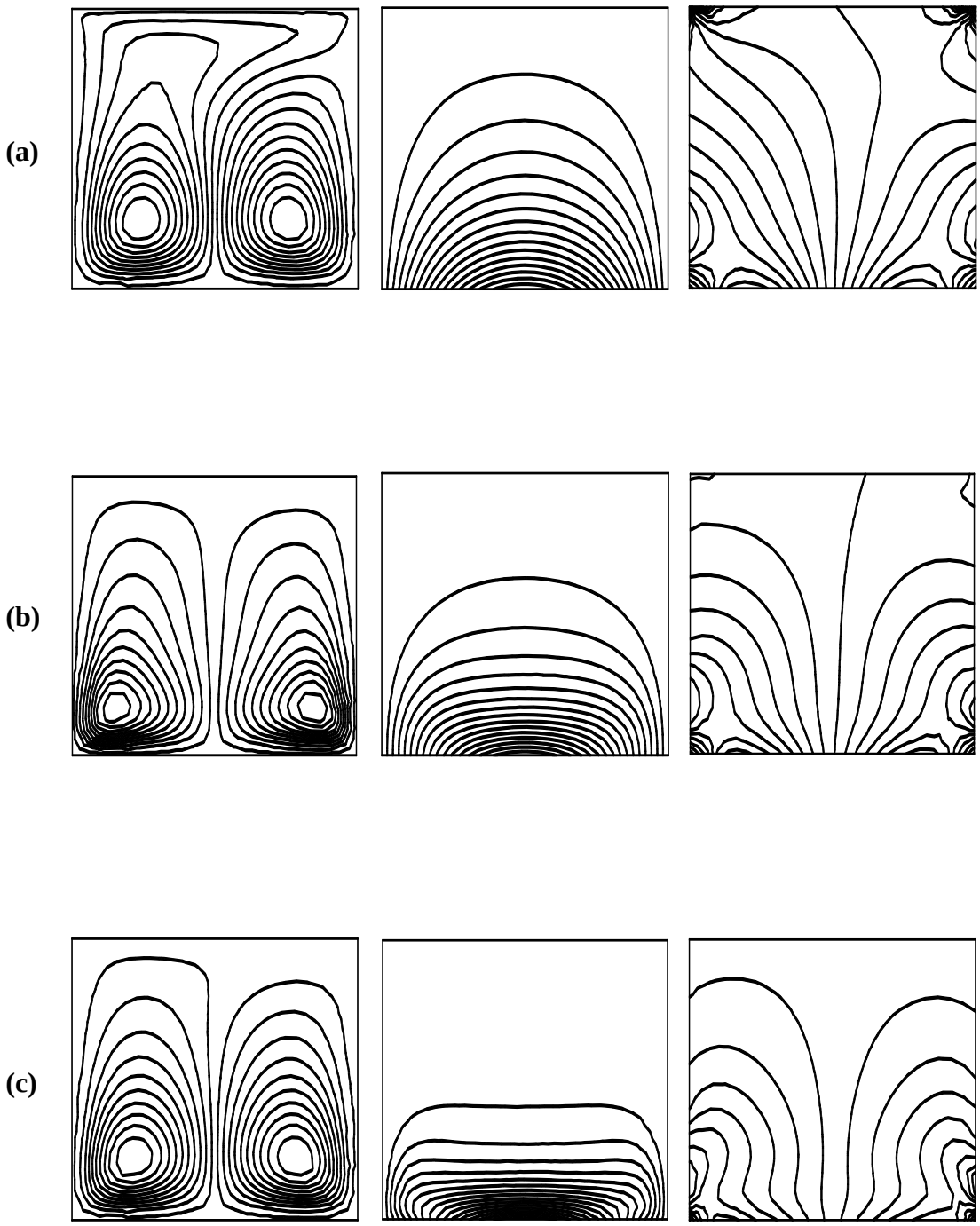

Figure 4.2: Streamlines, isotherms and microrotations for Re=1, Pr=7.2, Ha=30 and **(a)** $Gr=10^4$ **(b)** $Gr=10^5$ **(c)** $Gr=10^6$

Streamlines Isotherms Microrotations

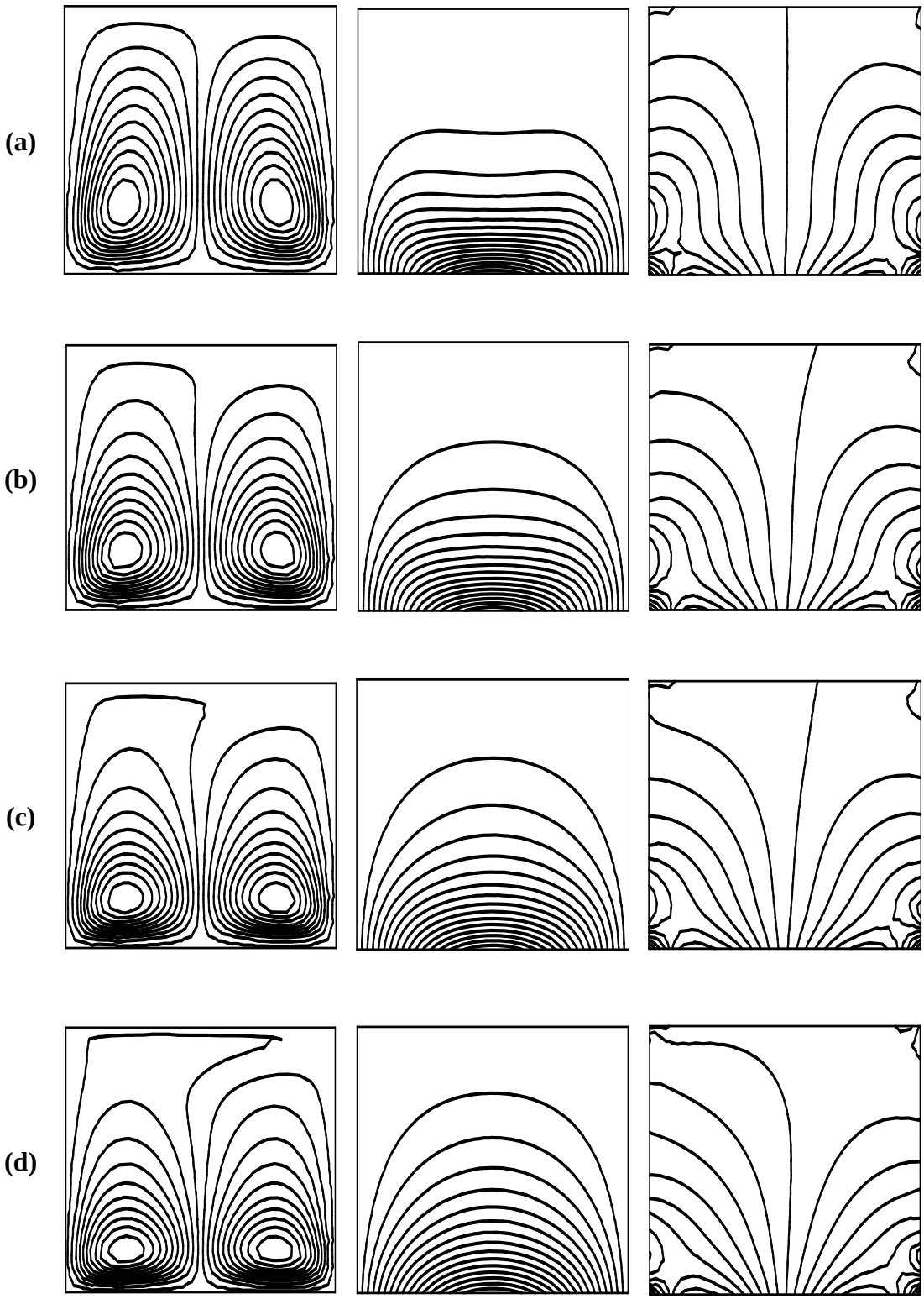

Figure 4.3: Streamlines, isotherms and microrotations for Re=1, Pr=7.2, Gr=10^5 and **(a)** Ha=0 **(b)** Ha=30 **(c)** Ha=60 **(d)** Ha=100

Streamlines Isotherms Microrotations

(a)

(b)

(c)

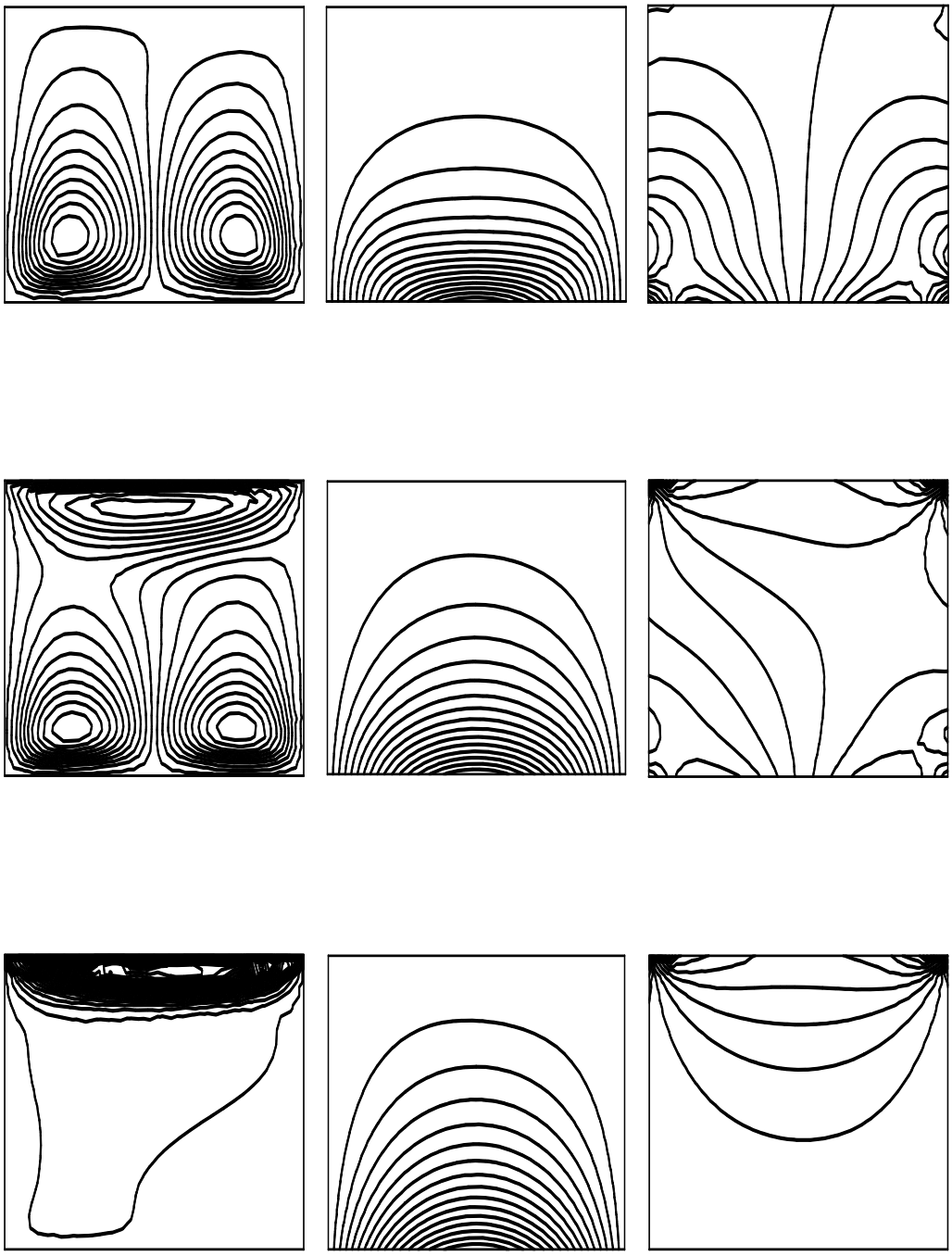

Figure 4.4: Streamlines, isotherms and microrotations for $\mathrm{Ha} = 30, \mathrm{Pr} = 7.2, \mathrm{Gr} = 10^5$ and **(a)** $\mathrm{Re} = 1$ **(b)** $\mathrm{Re} = 10$ **(c)** $\mathrm{Re} = 100$

Streamlines Isotherms Microrotations

(a)

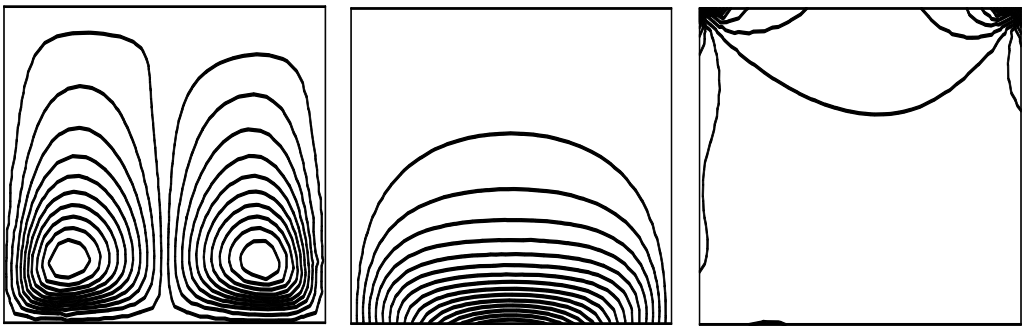

(b)

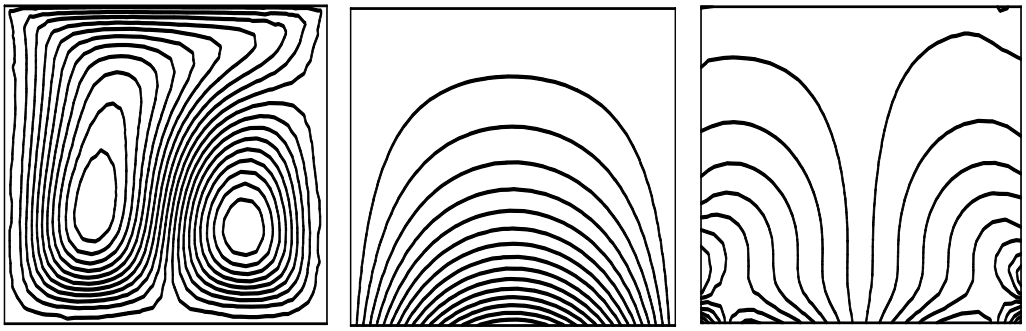

(c)

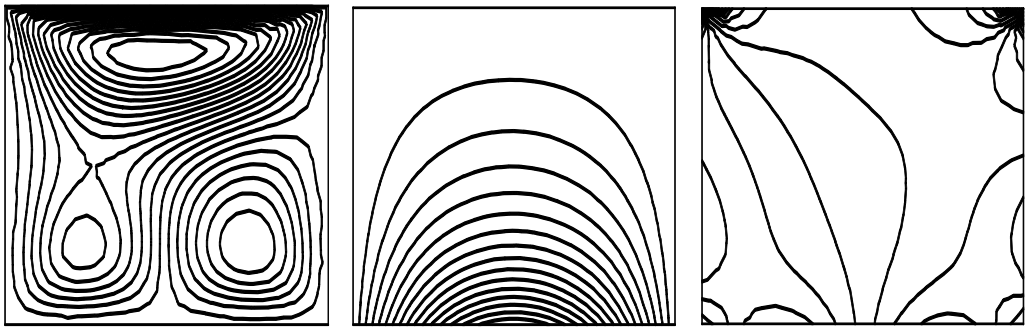

Figure 4.5 (a-c): Streamlines, isotherms and microrotations for $Re = 1, Ha = 30, Pr = 7.2, Gr = 10^5$ and **(a)** $R = 0$ **(b)** $R = 10$ **(c)** $R = 100$

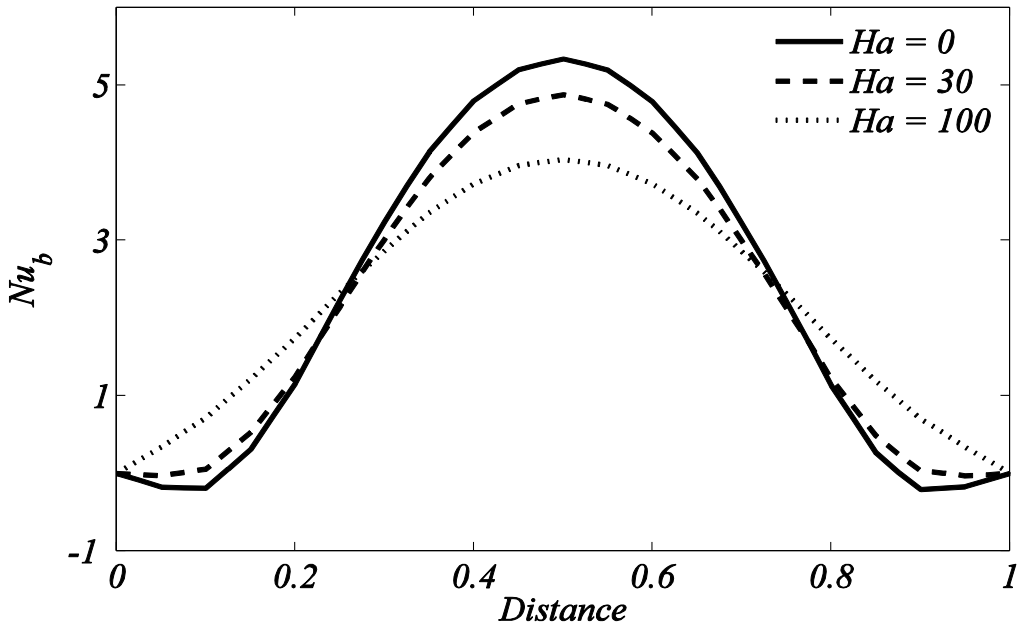

(a)

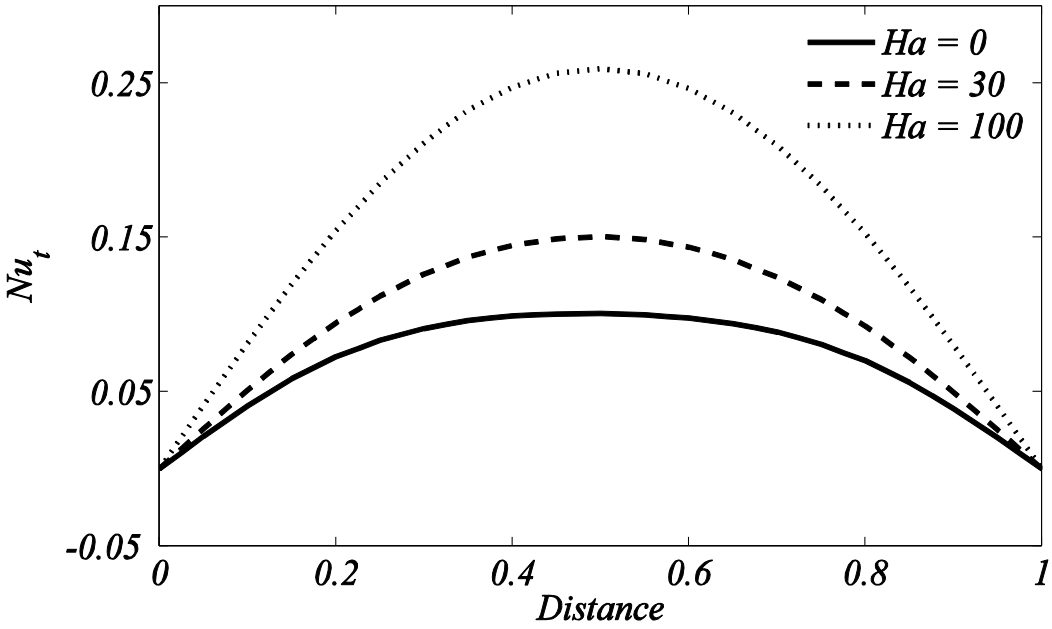

(b)

Figure 4.6: Local Nusselt number against different values of Hartmann number along **(a)** Bottom wall **(b)** Top wall

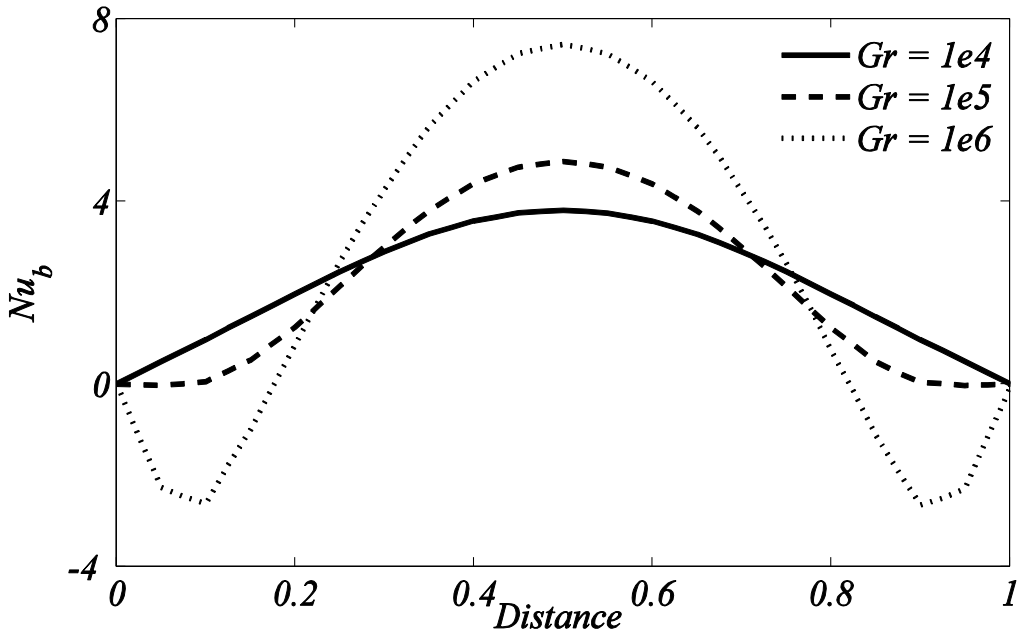

(a)

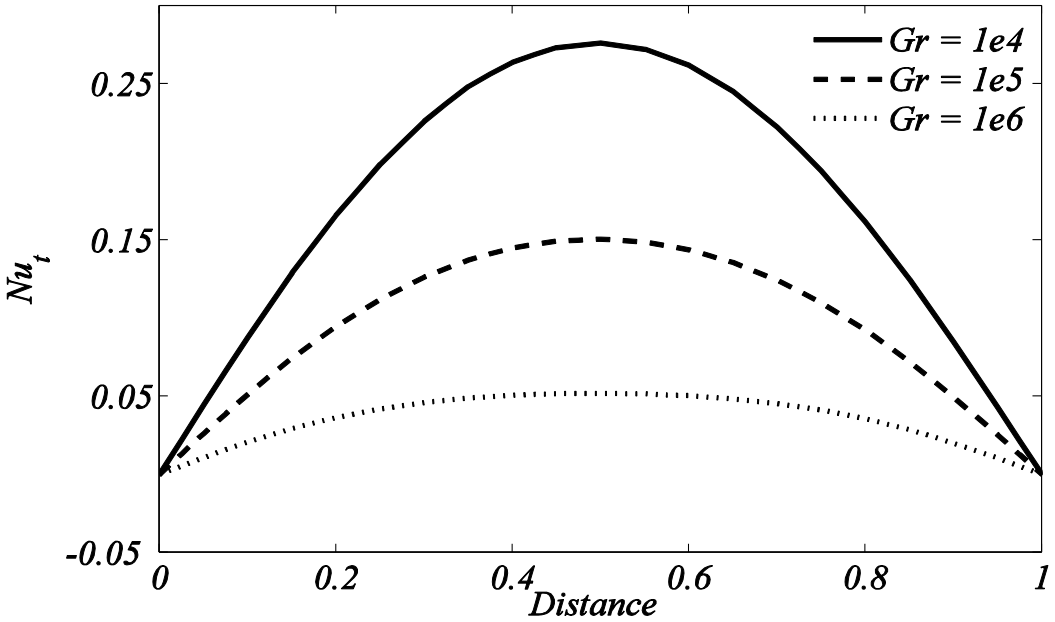

(b)

Figure 4.7: Local Nusselt number against various values of *Gr* along **(a)** Bottom wall **(b)** Top wall

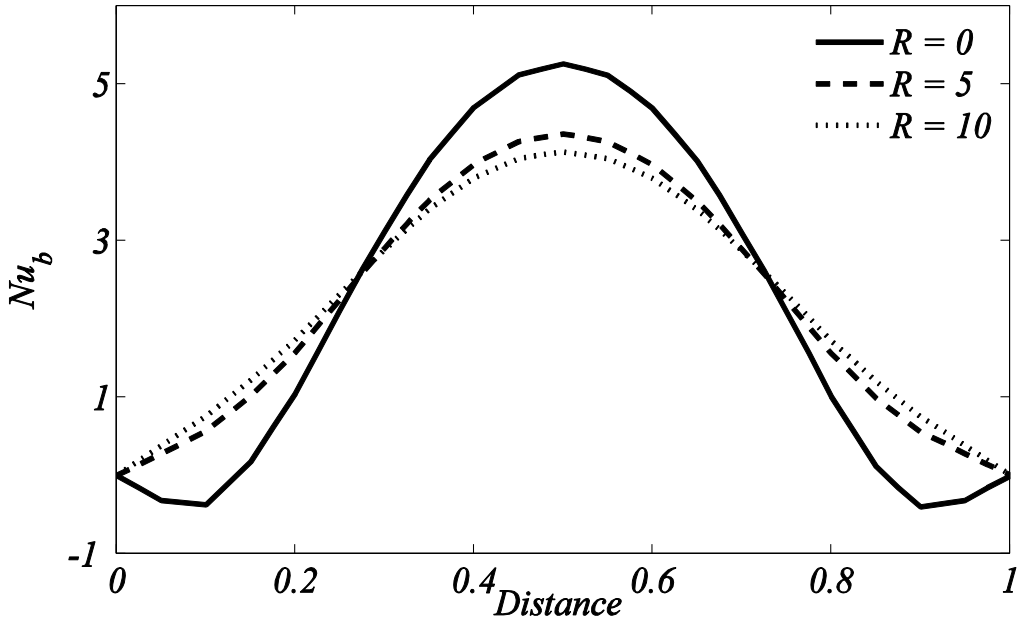

(a)

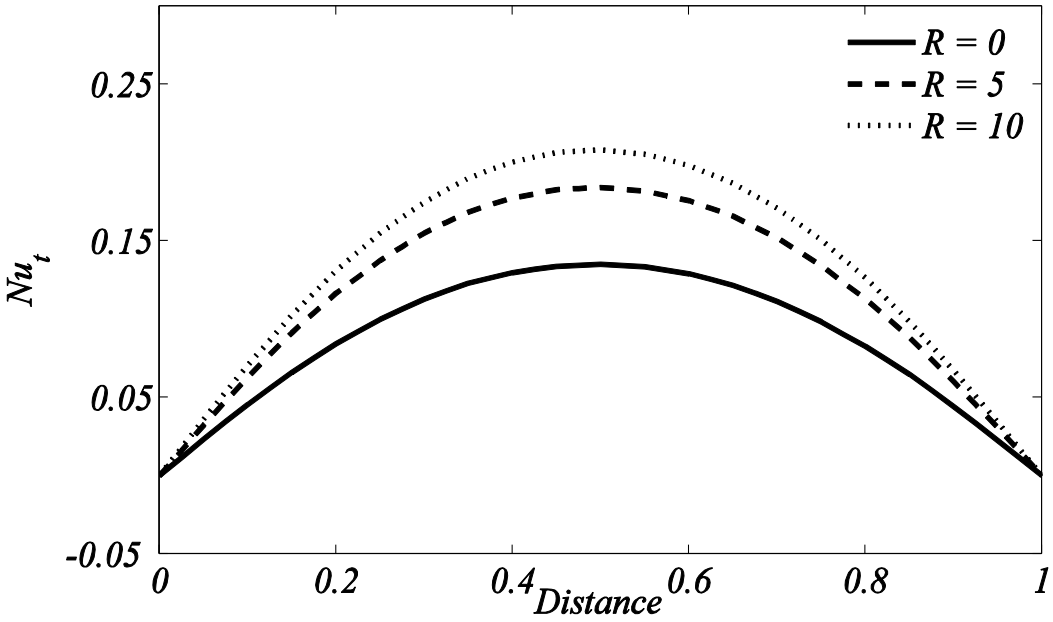

(b)

Figure 4.8: Local Nusselt number against various values of microrotation parameter along **(a)** Bottom wall **(b)** Top wall

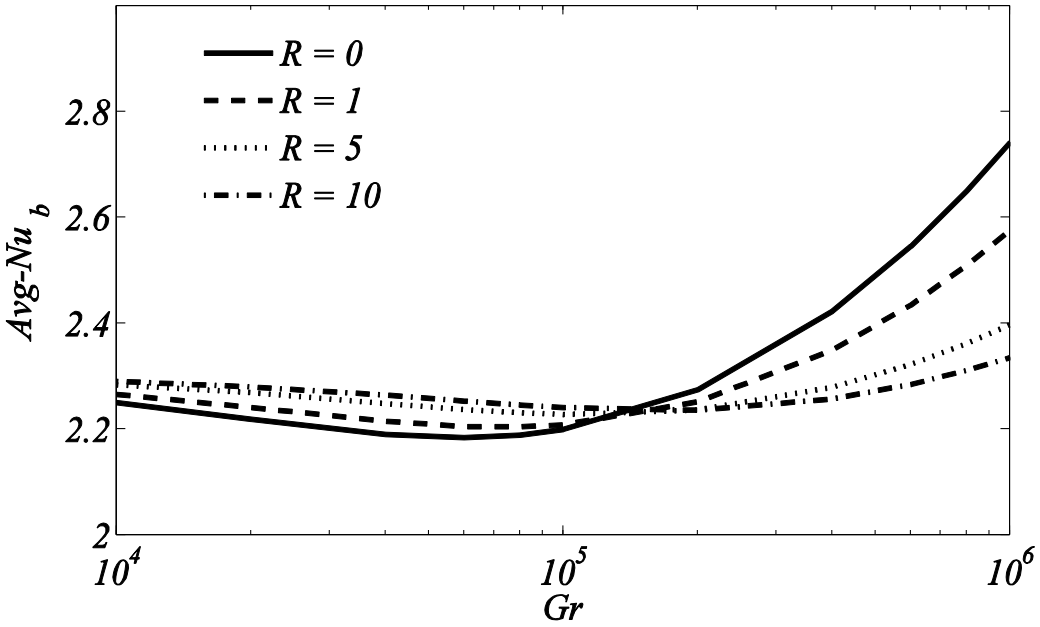

(a)

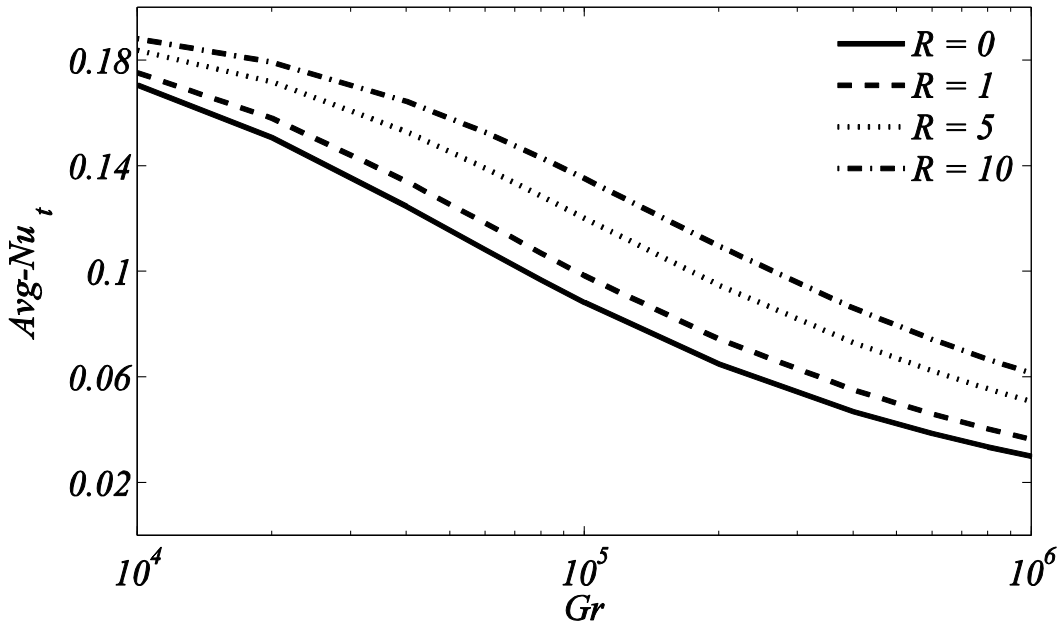

(b)

Figure 4.9: Average Nusselt number for Grashof number against different values of microrotations number along **(a)** Bottom wall **(b)** Top wall

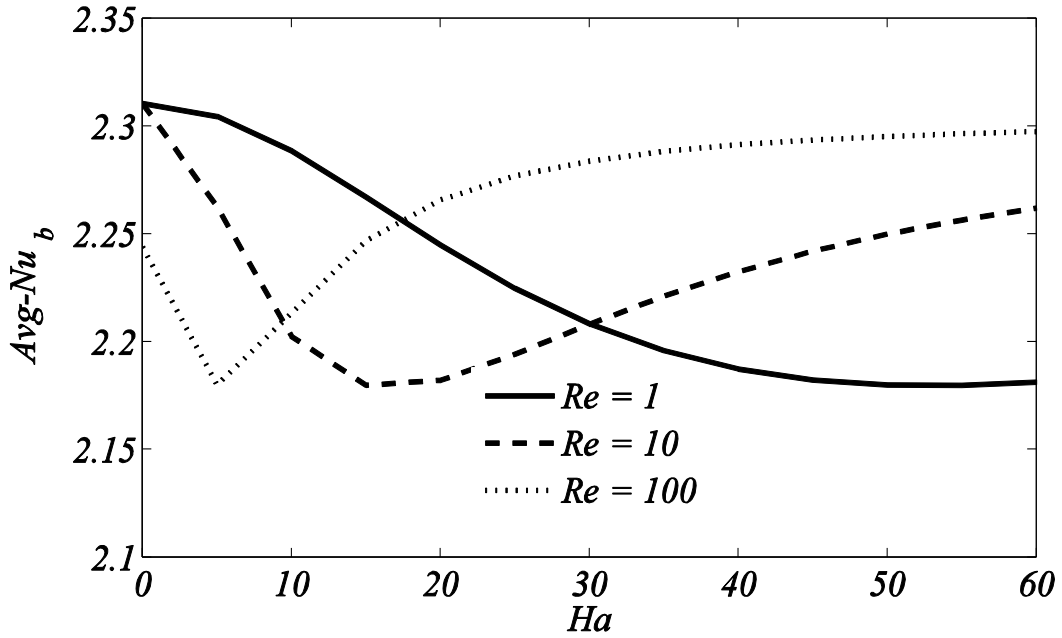

(a)

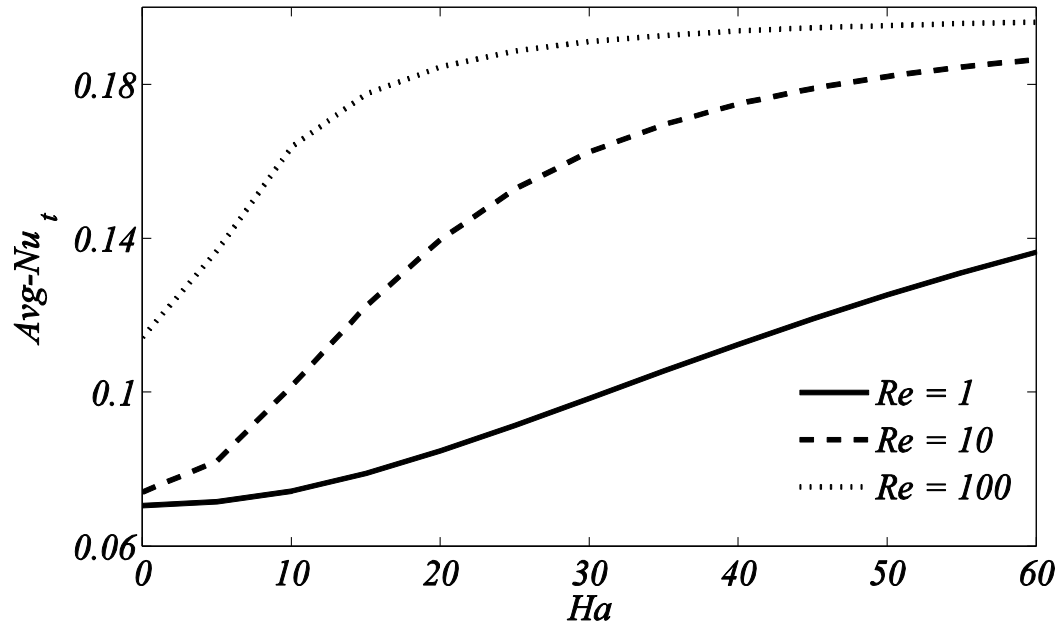

(b)

Figure 4.10: Average Nusselt number for Hartmann number against different values of Reynolds number along **(a)** Bottom wall **(b)** Top wall

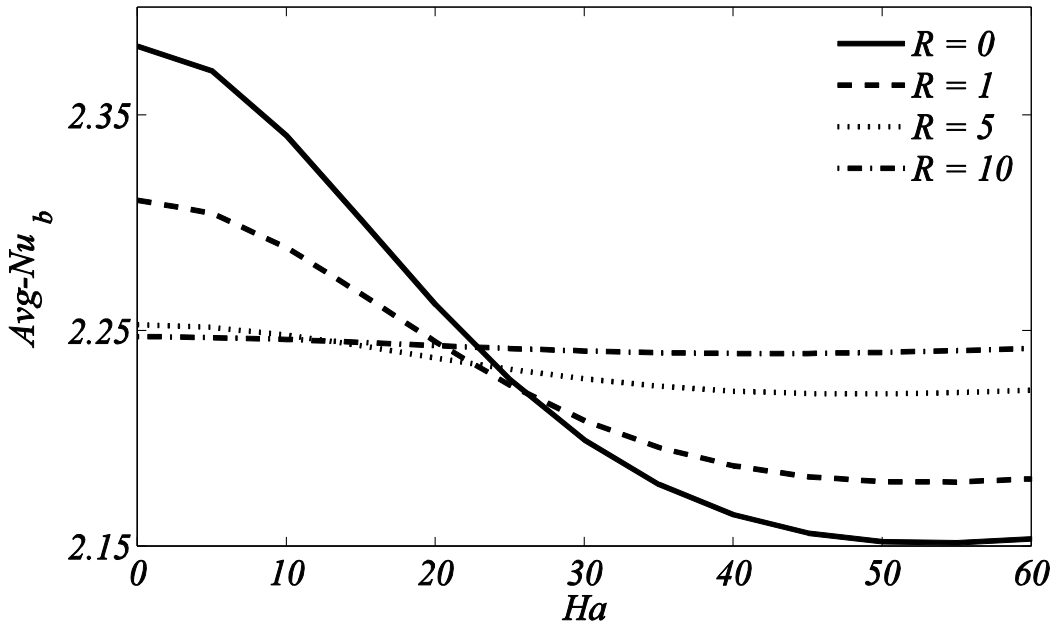

(a)

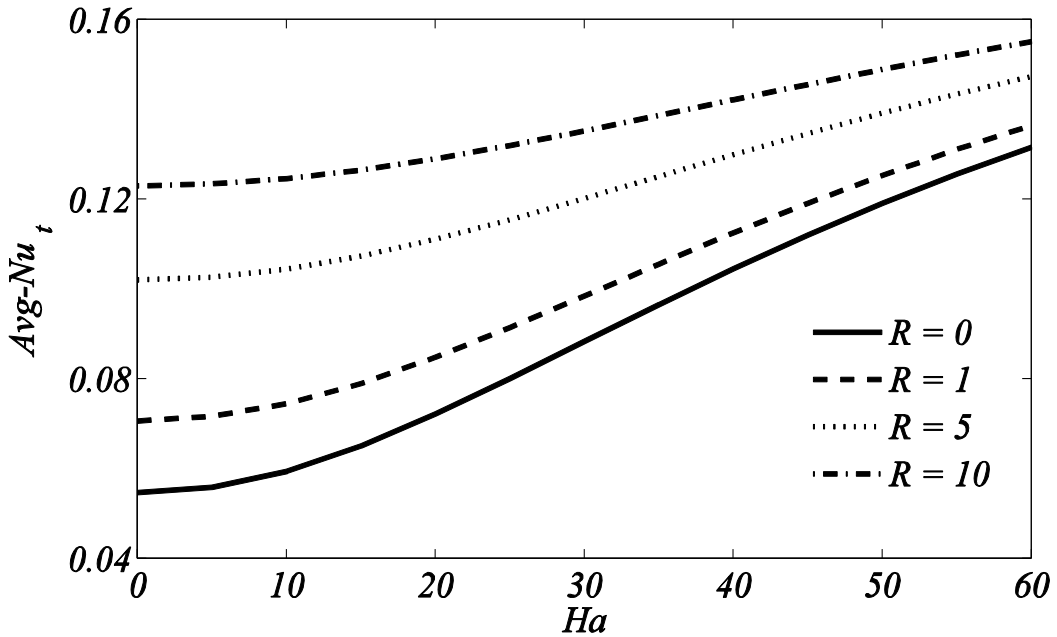

(a)

Figure 4.11: Average Nusselt number for Hartmann number against different values of micropolar parameter along **(a)** Bottom wall **(b)** Top wall

4.4 Conclusions

Present investigation contains numerical simulations for MHD mixed convective flow through micropolar fluid contained in a lid-driven square cavity subject to a uniform horizontal magnetic field when heat is supplied non-uniformly from bottom wall of a cavity. Equations governing the flow problem are modelled using laws of conservation of mass, linear and angular momentums and energy. Developed equations are first subject to penalty function to eliminate pressure term and then Galerkin weighted residual technique is applied to reduced equations which transform to a system of nonlinear algebraic equations. Afterwards, Newton Raphson method has been evoked to obtain the final solution of reduced nonlinear algebraic system. Computed effects are represented in the shape of streamline circulations, isotherms, isothermlines of microrotations, heat transfer coefficient (*Nu)* and overall heat transfer rate for wide range of governing parameters

Our computations reveal that the strength of streamline circulations and microrotations gets increased with increase in Grashof number where increase in micropolar parameter, Hartmann and Reynolds number decreases the strength of circulations and isolines of microrotations. Convection heat transfer regimes are found dominant in the enclosure for large Gr and small Re, Ha and *R*. Along bottom wall, Nusselt numer (Nu*)* is observed to decrease due to increase in Grashof number while increase in micropolar parameter, Hartmann and Reynolds number reduces the heat transfer rate in the cavity while opposite behaviour of *Nu* is seen along top wall for all parameters. Overall heat transfer rate along bottom wall is noticed to decrease with escalation in Reynolds number, Hartmann number and micropolar parameter while augmentation in Grashof number increases Average Nusselt number along bottom wall where opposite behavior of average Nu is observed along top horizontal wall of the enclosure. Prominent effects of moving lid are seen for small Grashof number and for large Reynolds and Hartmann numbers.

Chapter 5

Heat Transfer through Hydromagnetic Ferrofluid inside a Square Cavity with Heated Obstacle

This chapter comprises the numerical simulations of free convective heat transfer through ferrofluid contained in a square cavity affected by external magnetic field when a heated square block with different aspect ratios ($0.25 \leq A/H \leq 0.5$) is placed at the centre of enclosure. Vertical boundaries of enclosure are assumed insulated, top wall is taken cold while bottom wall is heated uniformly. The square obstacle is present at the centre of cavity which also serves as heat source in fluid. The mathematical model is presented in the form of nonlinear PDE's, which are simplified with the help of Galerkin finite element method. Results are shown against wide ranges of physical parameters like Prandtl, Rayleigh and Hartmann numbers etc. The heat transfer and fluid flow structures are noticed to be significantly dependent on strength of magnetic field, Rayleigh number and concentration of ferroparticles present in the base fluid.

5.1 Problem Formulation

A geometrical representation of the square cavity which is considered in this investigation is presented in **Figure 5.1**. The bottom boundary of enclosure is taken at a constant hot temperature T_h while top boundary is considered at cold temperature T_c, whereas side walls of the cavity are maintained adiabatic. A heated square block with different aspect ratios ($0.25 \leq A/H \leq 0.5$) is placed at the centre of the square enclosure as presented in **Figure 5.1**. Gravitational force vector is supposed to be acting along negative $y-$axis. All thermo-physical characteristics of fluid are assumed to be constant excluding density and Boussinesq approximation (Gray and Giorgini (1976)) is applied for the density variation due to temperature dependence of ferrofluid in the buoyancy term. The entire enclosure carries a mixture of base fluid (water) and nano-sized cobalt ferromagnetic particles. The ferromagnetic fluid is considered incompressible and laminar in this study. Thermo-physical properties of nanoscale ferromagnetic particles are presented in **Table 5.1**. Furthermore, magnetic force with magnitude B_0 is acting along negative $x-$direction. Here induced

magnetic field has been ignored being sufficiently small in comparison to applied magnetic field B_0 under low-R_m approximation (Davidson (2001))

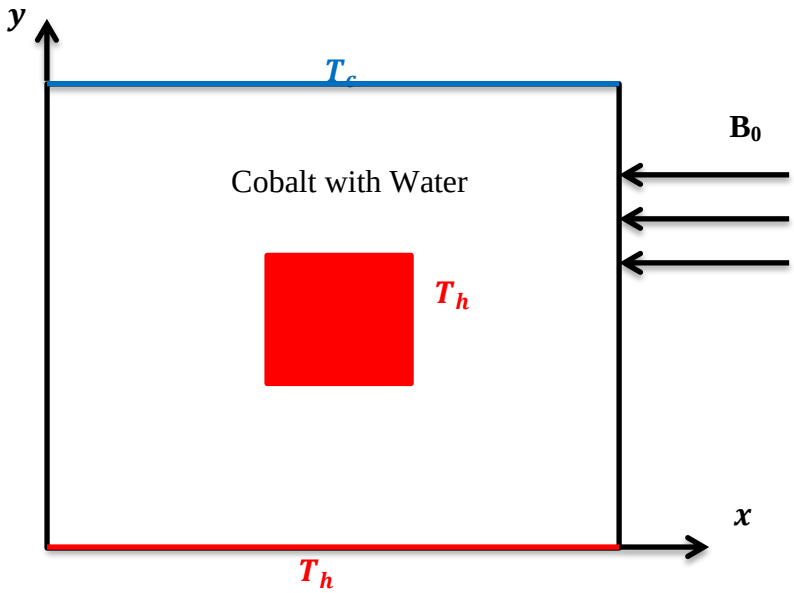

Figure 5.1: Geometrical representation of the present problem

Assuming the boundaries of container be electrically insulated with no Hall effects, the damping factor $-{B_0}^2 v$ represents the total electromagnetic force; here v is vertical velocity component. Therefore, Lorentz force is a function of velocity component v. Subject to above described assumptions, the equations describing the heat and fluid flow for present investigation in the absence of viscous dissipation are expressed as follows:

$$u_x + v_y = 0, \tag{5.1}$$

$$uu_x + vu_y = -\frac{1}{\rho_{ff}} p_x + \frac{\mu_{ff}}{\rho_{ff}} \left(u_{xx} + u_{yy}\right), \tag{5.2}$$

$$uv_x + vv_y = -\frac{1}{\rho_{ff}} p_y + \frac{\mu_{ff}}{\rho_{ff}} \left(v_{xx} + v_{yy}\right) + \frac{g(\rho\beta)_{ff}}{\rho_{ff}} (T - T_c) - \frac{\sigma_{ff} B_0^2}{\rho_{ff}} v, \tag{5.3}$$

$$uT_x + vT_y = \alpha_{ff} \left(T_{xx} + T_{yy}\right). \tag{5.4}$$

The assumed boundary conditions

$$u = v = 0, T = T_h \text{ (at lower horizontal side and heated square block)},$$

$$u = v = 0, T = T_c \text{ (at upper horizontal side)},$$

$$u = v = 0, \frac{\partial T}{\partial x} = 0 \text{ (at vertical sides)}, \tag{5.5}$$

here u, v are velocity components along horizontal and vertical axis respectively, p represents the pressure, ρ_{ff} be the density and μ_{ff} dynamic viscosity of ferrofluid. The following dimensionless variables are defined to transform the given problem into dimensionless form:

$$X=\frac{x}{H}, Y=\frac{y}{H}, U=\frac{uH}{\alpha_f}, V=\frac{vH}{\alpha_f}, P=\frac{pH^2}{\rho_{ff}{\alpha_f}^2}, \theta=\frac{T-T_c}{T_h-T_c}, Pr=\frac{\nu_f}{\alpha_f}, Ra=$$

$$\frac{g\beta_f H^3(T_h-T_c)Pr}{{\nu_f}^2}, Ha^2=\frac{\sigma_f {B_o}^2 H^2}{\mu_f}. \quad (5.6)$$

Above transformations are used in Eqs. (5.2)-(5.4), we get

$$UU_X+VU_Y=-P_X+\frac{\mu_{ff}}{\rho_{ff}\alpha_f}(U_{XX}+U_{YY}), \quad (5.7)$$

$$UV_X+VV_Y=-P_Y+\frac{\mu_{ff}}{\rho_{ff}\alpha_f}(V_{XX}+V_{YY})+\frac{\beta_{ff}}{\beta_f}RaPr\theta-\frac{\rho_f\chi\sigma_{ff}}{\rho_{ff}\sigma_f}Ha^2PrV, \quad (5.8)$$

$$U\theta_X+V\theta_Y=\frac{\alpha_{ff}}{\alpha_f}(\theta_{XX}+\theta_{YY}). \quad (5.9)$$

The boundary conditions of the problems take non-dimensional form such as:

$U=V=0, \theta=1$ (at bottom horizontal side and heated square block),

$U=0=V, \theta=0$ (at top horizontal side),

$U=V=0, \frac{\partial\theta}{\partial X}=0$ (at vertical sides). (5.10)

Here Pr, Ha and Ra represents Prandtl, Hartmann and Rayleigh numbers respectively, *U*, *V* are dimensionless velocity components and θ shows non-dimensional temperature. Where

$$\mu_{ff}=\frac{\mu_f}{(1-\phi)^{2.5}}, \left(\rho c_p\right)_{ff}=(1-\phi)\left(\rho c_p\right)_f+\phi\left(\rho c_p\right)_s,$$

$$\rho_{ff}=(1-\phi)\rho_f+\phi\rho_s, \sigma_{ff}=\sigma_f\left(1+\frac{3\left(\frac{\sigma_s}{\sigma_f}-1\right)\phi}{\left(\frac{\sigma_s}{\sigma_f}+2\right)-\left(\frac{\sigma_s}{\sigma_f}-1\right)\phi}\right),$$

$$\beta_{ff}=(1-\phi)\beta_f+\phi\beta_s,$$

$$\alpha_{ff}=\frac{k_{ff}}{\left(\rho c_p\right)_{ff}}, \frac{k_{ff}}{k_f}=\frac{\left(k_s+2k_f\right)-2\phi\left(k_f-k_s\right)}{\left(k_s+2k_f\right)+\phi\left(k_f-k_s\right)}. \quad (5.11)$$

The heat transfer rate (Nu) and overall heat transfer rate $\left(\overline{\mathrm{Nu}}\right)$for horizontal walls is defined as follows:

$$\mathrm{Nu_h}=\frac{k_{ff}}{k_f}\left(-\sum_{i=1}^{6}\theta_i\frac{\partial\phi_i}{\partial Y}\right), \quad (5.12)$$

$$\overline{\mathrm{Nu_h}}=\frac{\int_0^1 \mathrm{Nu_h}dX}{\int_0^1 dX}=\int_0^1 \mathrm{Nu_h}dX. \quad (5.13)$$

5.2 Grid Independence Test

For the purpose of developing grid independent solution of the discussed problem, the numerical values of the computed average Nusselt number along top wall is demonstrated through **Table 5.2** against different refinement levels of non-uniform initial mesh. It has been noticed that when number of elements are increased or by increasing the refinement level, the percentage error of the solution with the solution

at previous refinement level is decreased. It is as minimum as 1% at the fourth refinement level, therefore throughout the study, third refinement level is used for solution with 1776 number of 6-nodal triangular elements.

5.3 Validation

Once the grid independence is achieved, the code has been further authenticated by making a comparison of computed results with that of (Ho et al. (2010)). He carried out an experimental study on energy transfer through free convection within Al_2O_3-water nanofluid contained in square container. **Table 5.3** shows the values obtained in experimental study through an explicit relation derived by (Ho et al. (2010)) for average Nusselt number and result computed by our code for different concentrations of nano-particles. Our results are found in a great agreement with the experimental findings achieved by (Ho et al. (2010)) and that gives us the confidence about the accuracy of developed code for solution.

5.4 Results and Discussions

This section contains the numerical results which are obtained by using Galerkin weighted residual technique. The comprehensive procedure related to Galerkin weighted residual method has been discussed in chapter 2. Numerical simulations for free convective flow via ferrofluid confined in a square domain with cold upper wall, insulated vertical walls and constant temperature profile at bottom wall. The heat is also provided through a square shaped block with different aspect ratios (i.e. $0.25 \leq A/H \leq 0.5$) placed at the centre of enclosure. Obtained numerical results have been presented in the form of isotherms contours, streamline contours, heat transfer and overall heat transfer rates for different values of involved physical parameters including Rayleigh number ($10^5 < Ra < 10^7$), Prandtl number $Pr = 0.72$, solid volume fraction of nanoscale ferromagnetic particles ($0.0 < \phi < 0.06$) and Hartmann number ($0 < Ha < 60$).

Figure 5.2 (a, b) presents the influence of *Ha* on the flow and heat patterns for $Ra = 10^5$, $Pr = 0.062$, $Ar = 0.25$, $\phi = 0.015$. Since bottom wall of square enclosure is provided with uniform heat and vertical side walls are taken adiabatic therefore fluid present near the centre of bottom wall becomes less dense due to high temperature at the wall and moves upward along the central vertical line around the blockage placed and comes back to lower region along vertical boundaries making two symmetric rolls of circulation, one counter-clockwise and another clockwise

rotation. Here counter-clockwise circulations are taken positive while clockwise circulations are considered negative. The direction of considered magnetic field use to play a dynamic role in transfer of heat and maximum heat flow rate has been found when the magnetic force is assumed parallel to thermal gradient.

In left column of **Figure 5.2 (a, b)** streamline are shown for varying Hartmann number $Ha = 0$ and $Ha = 60$. It is noticed that introducing magnetic field to the flow causes weaker streamline circulations in comparison of the flow without magnetic force. The greatest value of stream function is 0.3 in case of absence of MHD and 0.12 in the presence of MHD. The adverse effects of augmentation in magnetic field strength is caused by the fact that, increase in value of Ha results into a stronger induced magnetic field which causes increase in Lorentz force acting on the flow regime. Consequently, strength of flow current is decreased due to increase in the Lorentz force and ferrofluid, having magnetic particles bears high magnetic susceptibility gets intensively influenced by magnetic field. In right column of **Figure 5.2 (a, b)**, isotherms contours are displayed for varying $Ha = 0$ and 60 at $Ra = 10^5$. It has been observed that the thermal boundary layer is developing as isotherm contours are seen to be parallel to top boundary. These isotherms are noticed to be nonlinear in the centre of a cavity between square blockage and vertical side walls. Furthermore, introduction of magnetic field results into the increase of temperature in flow field.

Results in **Figure 5.3 (a-c)** are shown to analyse the effects of Rayleigh number on heat and fluid flow structures in the presence of MHD at $Ha = 60$. Left column depicts the simulations of streamline circulations for varying Rayleigh number ($Ra = 10^5, 10^6$ and 10^7 respectively). It has been noticed that two symmetric eddies (one clockwise and one counter-clockwise) are formed in the enclosure. Since the terms of Rayleigh number and Hartmann number have opposite signs in governing equation therefore these parameters have opposite effects on flow behavior. Furthermore, the heat and fluid flow structures are noted to get influenced more significantly by Rayleigh number in comparison to Hartmann number. Streamlines are noticed to have higher values of stream function as result of improved thermal conductivity of fluid due to presence of ferroparticles in the fluid. As consequence of the dominance of convection regime for large *Ra* stronger streamline circulations is observed and for large Rayleigh numbers circulation rolls get stretched in the region

between central blockage and vertical boundaries due to thermal buoyant force generated by heated walls. Magnitudes of streamline circulations are 0.12, 3.6 and 17.6 for Rayleigh number 10^5, 10^6 and 10^7 respectively. Right column of **Figure 5.3 (a-c)** isotherms are shown against various Rayleigh numbers when $Ha = 60$. It has been observed that the isotherms appear smooth indicating conduction dominant regime inside the cavity for comparatively small Rayleigh number ($Ra = 10^5$), while increase in Rayleigh number causes distortion in isotherms showing better convection scenario in the enclosure. Parallel isotherms near upper wall of the cavity indicate the development of thermal boundary layer near top wall of the enclosure for all Rayleigh number.

Influence of aspect ratio Ar on the thermal and flow fields are shown in **Figure 5.4 (a, b)**, when $Ra = 10^6$ considering that there is no magnetic field. It has been observed that increase in aspect ratio causes dominance of conduction regime inside the cavity and isotherms are found clustered near upper wall for $Ar = 0.5$ in the middle of enclosure while for $Ar = 0.25$ the isotherms are distributed non-uniformly throughout the cavity showing better convection in the enclosure. The circulation vortices appears to be compressed along the vertical sides and centres of circulations are moved near upper left and right corners, however magnitude of rotation is reduced considerably when aspect ratio is augmented. Greatest values of stream function are 7.7 and 1.3 for $Ar = 0.025$ and 0.5 respectively.

Figure 5.5 (a, b) contains plots for Nusselt numbers along horizontal walls for increasing values of horizontal distance along *x*-axis. It has been noticed that the local Nusselt number is maximum at the edges of lower horizontal boundary for the reason of temperature singularity occurring at these corners. Reduction in Nusselt number is seen while moving towards centre of bottom wall from edges and achieves lowest value at the centre of bottom wall, whereas surge of *Ha* results into reduction of heat flow rate along bottom wall. Opposite to this, local heat flow rate has been noticed to have minimum value at boundaries of cold top wall and it increases while moving inward achieving maximum value at the middle of the top wall. Furthermore, a better transfer of heat rate is seen in the absence of MHD effects ($Ha = 0$) while introducing MHD reduces heat transfer rate considerably. Furthermore, local Nusselt number is seen to attenuate with increasing strength of magnetic field along top wall

except for the region $0.25 < \text{distance} < 0.73$ where increase in Ha increases the heat flow rate.

Figure 5.6 (a, b) represents the effects of Rayleigh number on heat flow rate along horizontal boundaries of the cavity. It is evident in figure that heat flow rate first increases moving inward from both edges to 2 units of distance and then it decreases attaining minima at the middle of bottom wall. Increasing Rayleigh number causes escalation in heat flow rate for any fixed *X* whereas for comparatively small Rayleigh number, rate of flow of heat is noted to be constant against both upper and lower horizontal walls. Along top wall Nu is seen to increase moving inward from both ends and attains its maximum value at the center of the top wall.

Figure 5.7 (a, b) compares the local Nusselt numbers for plain fluid (fluid without ferroparticles) and ferrofluid at bottom and upper walls. It is seen that along hot bottom wall heat transfer rates are similar for both plain and ferrofluid except minor difference as shown in **Figure 5.7 (a)**, while along cold top wall, Nusselt number is significantly high in case of ferrofluid in comparison to that of base fluid as addition of ferroparticles to the plain fluid causes augmentation in thermal conductivity of fluid causing in higher Nusselt number. On the other hand, value of *Nu* decreases moving inward from both ends along bottom wall and achieves minimum value at centre of bottom wall while Nu rises moving inwards from both ends of top wall and achieves maximum value at middle of the upper wall.

Figures 5.8 to **5.10** show the overall heat flow rate $\overline{\text{Nu}}$ against pertinent flow parameters for different values of Ha. It may be seen in **Figure 5.8 (a, b)** that when Hartmann number is increased, $\overline{\text{Nu}}$ is reduced along both lower and upper boundaries due to decrease in kinetic energy resulting from increase in Lorentz force but the rate of decrease is very slow along top wall as compared to that of bottom wall because of opposite temperature profiles present at two walls. Furthermore intensification of ferromagnetic particles causes increase in the average heat flow rate at both lower and upper boundaries. Augmentation in the average heat flow rate against concentration of ferromagnetic particles is more prominent for stronger magnetic field. This effect is because of higher suppression of buoyant flow of ferrofluid when concentration of particles is higher. The overall heat flow rate escalates proportional to increase in solid volume fraction against smaller Hartmann number.

Table 5.1: Thermo-physical properties of ferromagnetic particles

	Base fluid (Water)	Cobalt
$C_0(J/kgK)$	4179	420
$\rho(kg/m^3)$	997.1	8900
$K(W/mK)$	0.613	100
$\beta(1/K)$	21×10^{-5}	1.3×10^{-5}
σ(W/m.K)	0.05	1.602×10^{7}

Table 5.2: Overall heat transfer rate along top wall aainst different mesh sizes

Refinements	Number of Elements	$\overline{\mathrm{Nu}_t}$	%Error
1st	111	2.4040	-
2nd	444	2.3941	0.4
3rd	1776	2.3893	0.2
4th	7104	2.3869	0.1

Table 5.3: Average Nusselt numbers for comparison between results obtained by (Ho et al. (2010)) and results obtained by our developed code

%c_v	$\overline{\mathrm{Nu}_{nf}}$ (Ho et al (2010))	$\overline{\mathrm{Nu}_{nf}}$(Present study)	%Error
1	32.2037	32.0903	0.35
2	31.0905	30.9078	0.58
3	29.0769	28.8528	0.77

Streamlines Isotherms

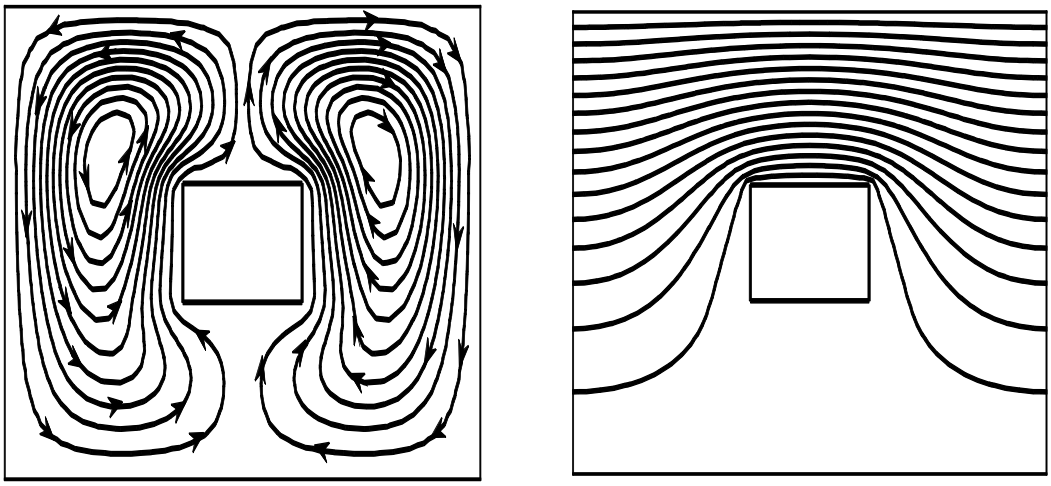

(a)

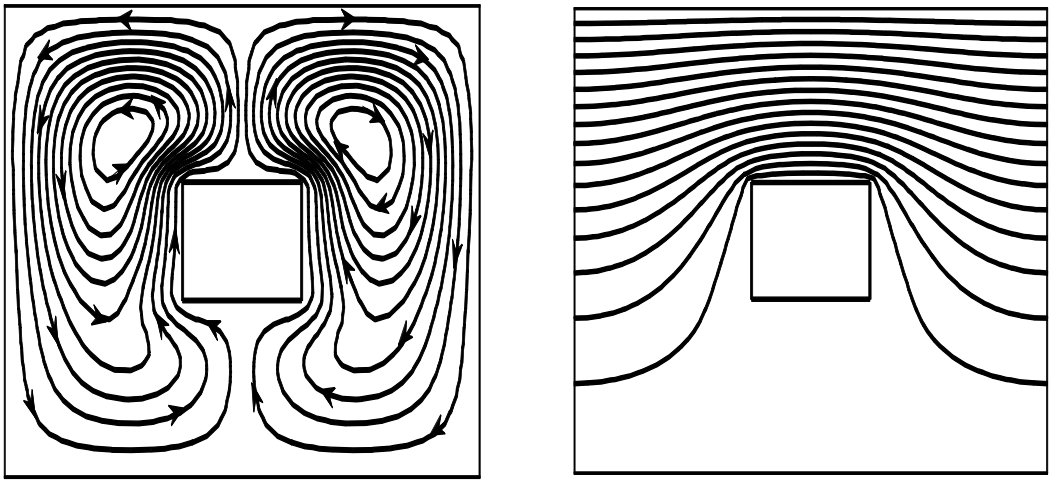

(b)

Figure 5.2: Isotherms and Streamline contours against $\mathrm{Ra} = 10^5, \mathrm{Pr} = 0.72,$ $\phi = 0.015$ **(a)** $\mathrm{Ha} = 0$ and **(b)** $\mathrm{Ha} = 60$

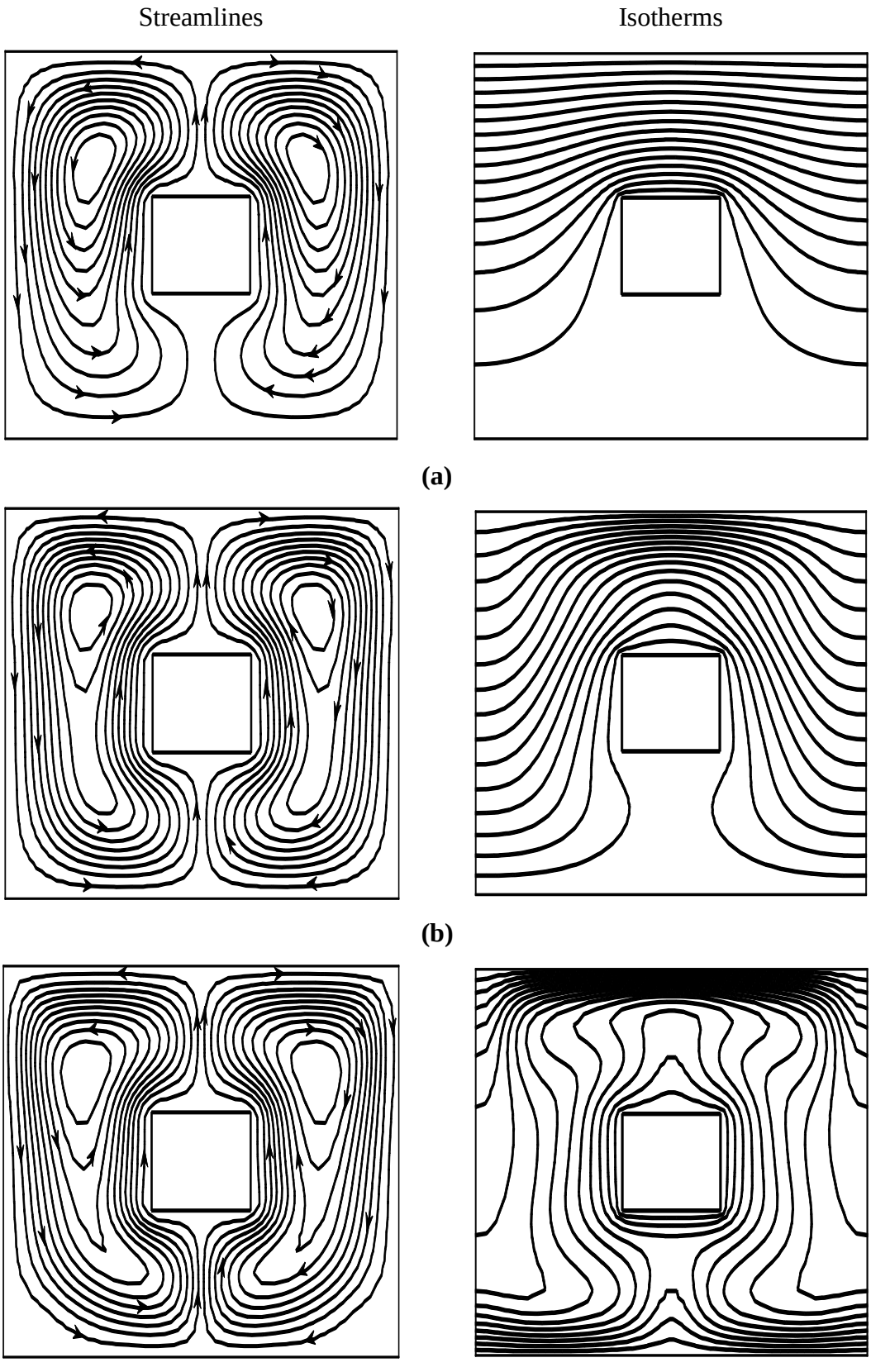

Figure 5.3: Isotherms and Streamline contours against $\mathrm{Ha} = 60, \mathrm{Pr} = 0.72, \phi = 0.015$ **(a)** $\mathrm{Ra} = 10^5$, **(b)** $\mathrm{Ra} = 10^6$ and **(c)** $\mathrm{Ra} = 10^7$

Streamlines Isotherms

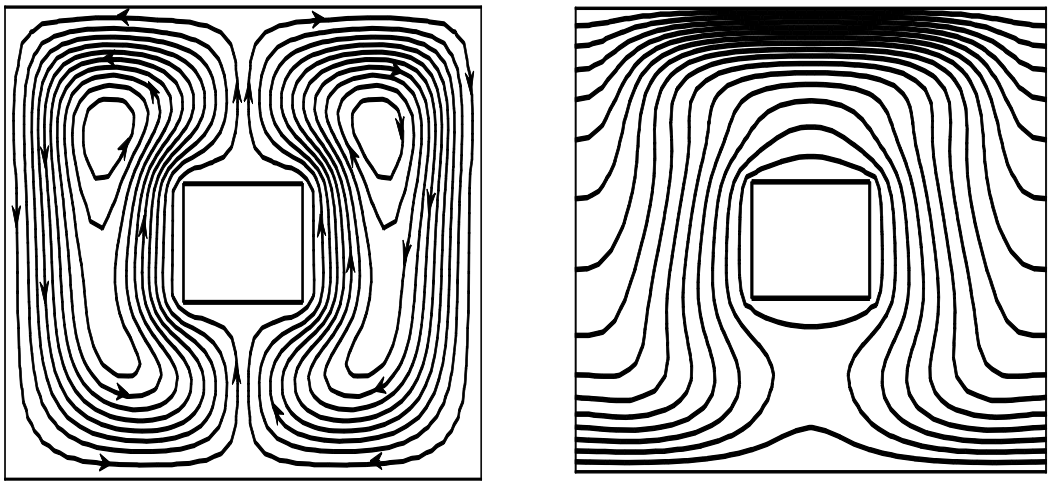

(a)

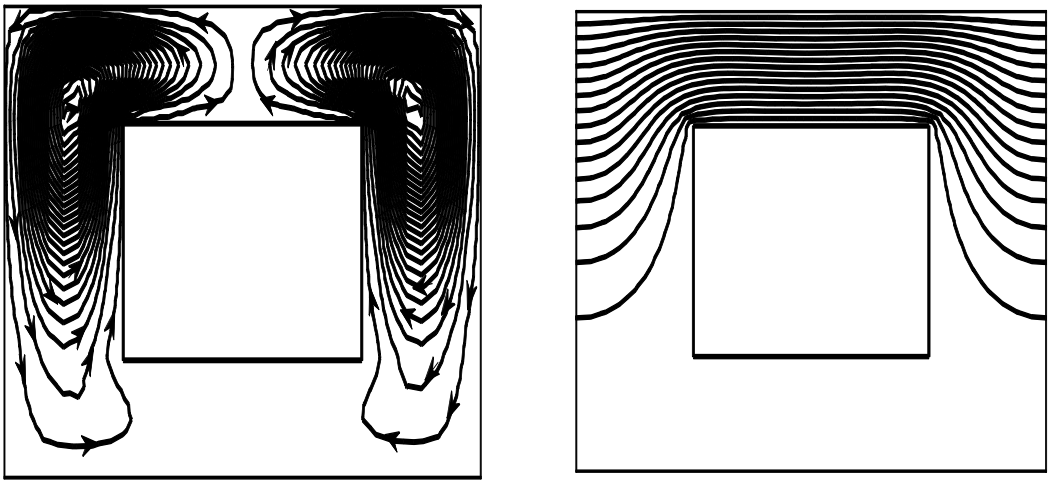

(b)

Figure 5.4: Isotherms and Streamline contours against $\mathrm{Ra} = 10^6, \mathrm{Pr} = 0.72, \phi = 0.015, \mathrm{Ha} = 0$ **(a)** $Ar = 0.25$ and **(b)** $Ar = 0.5$

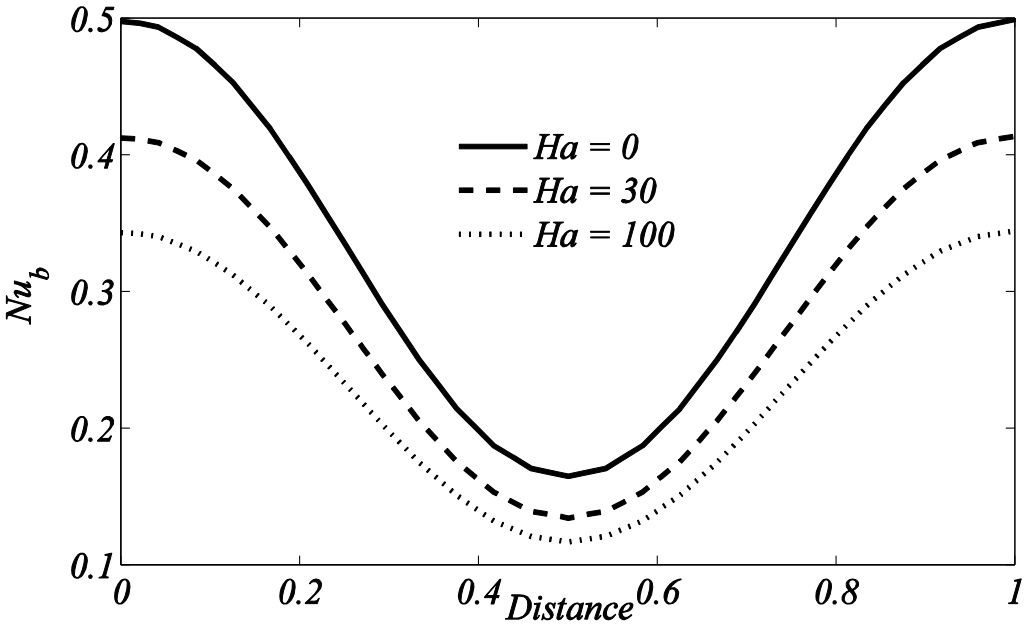

(a)

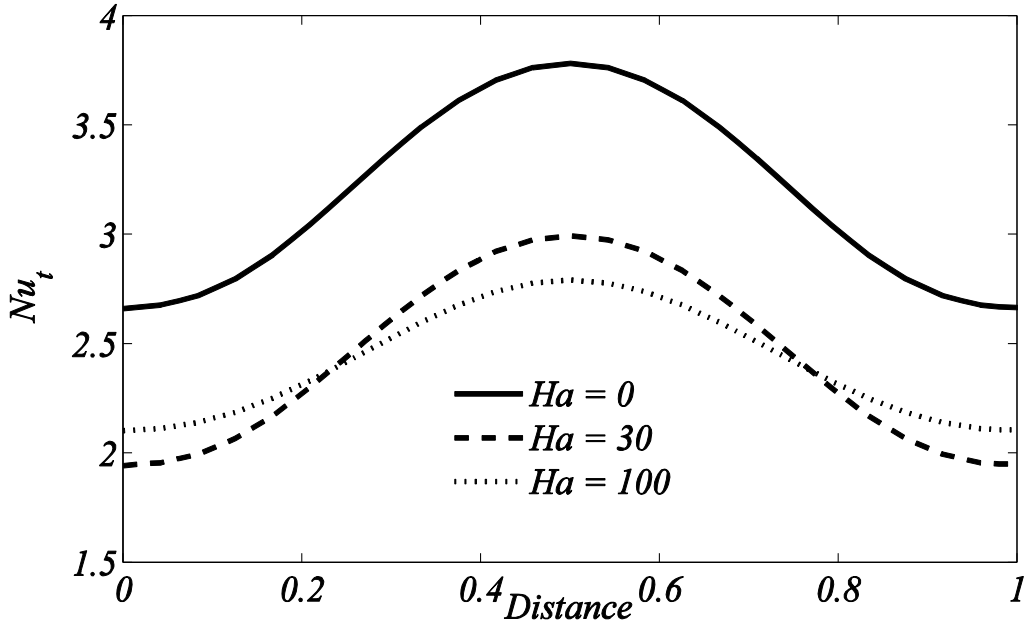

(b)

Figure 5.5 (a, b): Nusselt number against distance along X −axis for different *Ha* against **(a)** lower boundary **(b)** upper boundary

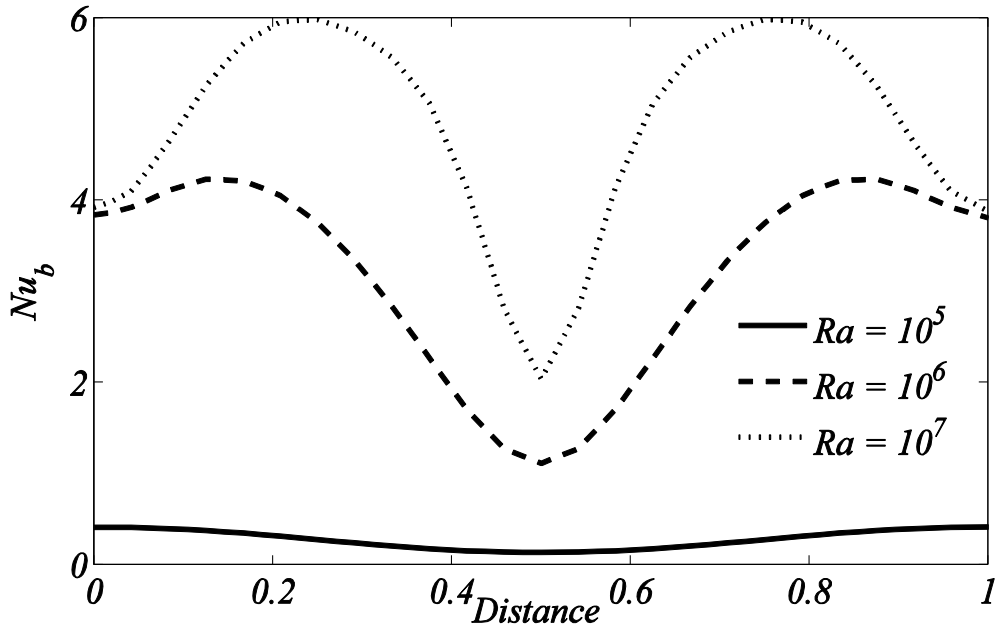

(a)

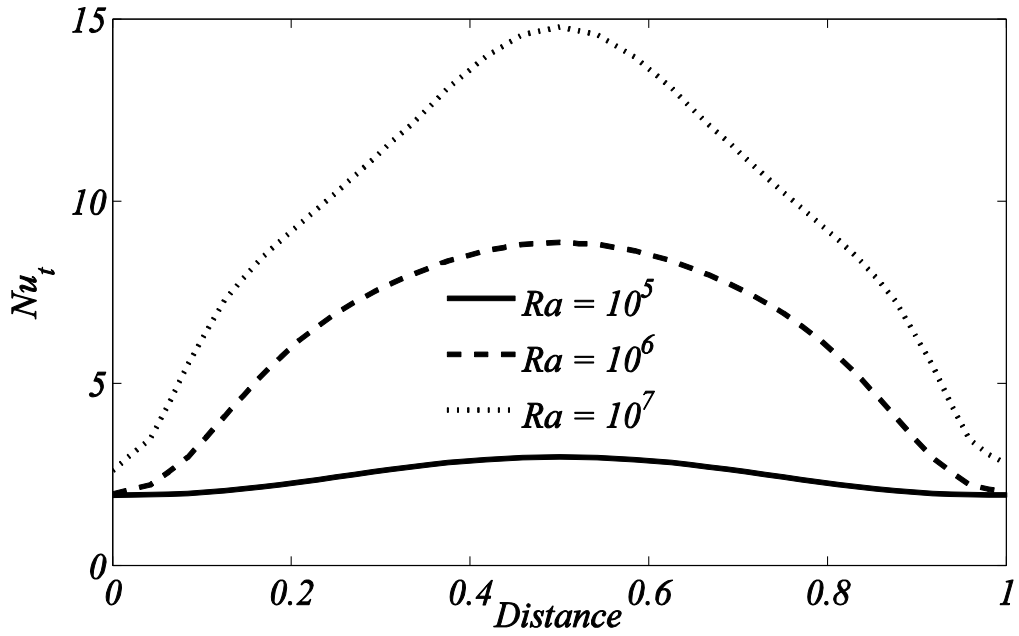

(b)

Figure 5.6: Nusselt number against distance along X −axis for various values of Rayleigh number along **(a)** bottom wall **(b)** top wall

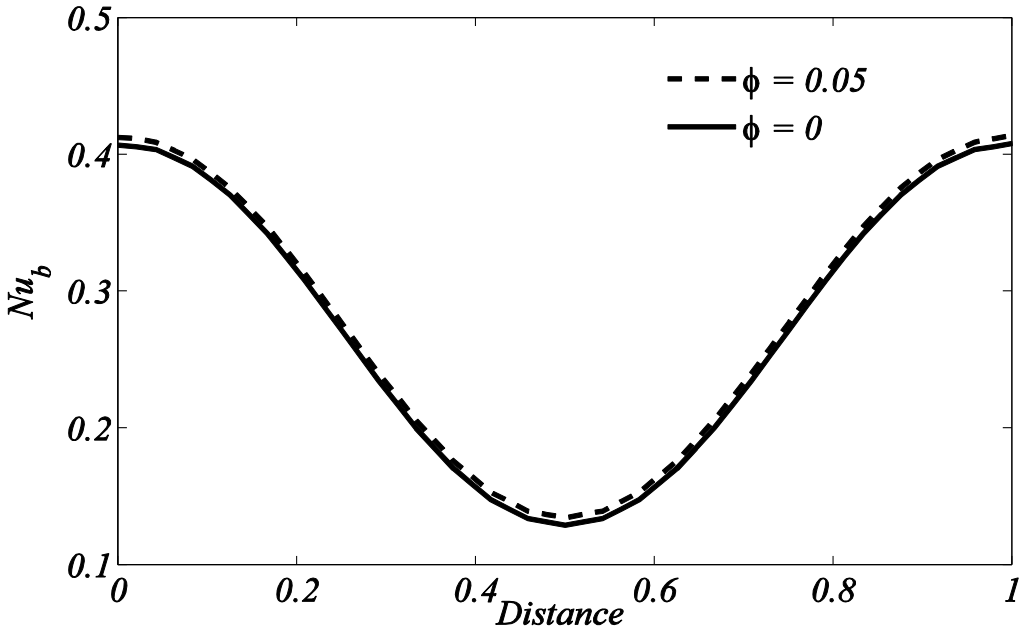

(a)

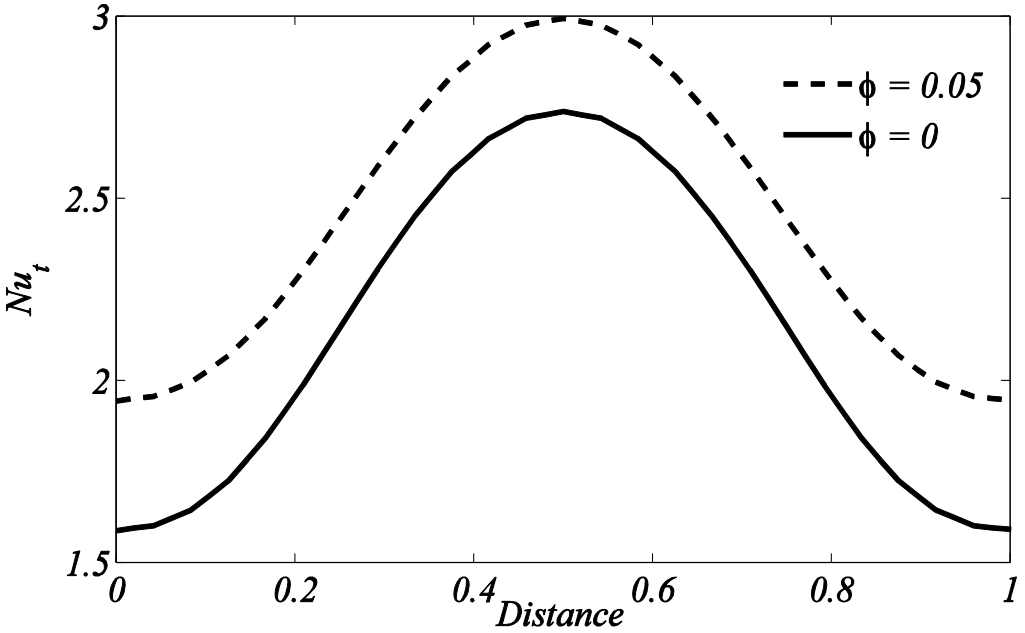

(b)

Figure 5.7: Nusselt number against distance along X −axis for base fluid and ferrofluid against **(a)** lower boundary **(b)** upper boundary

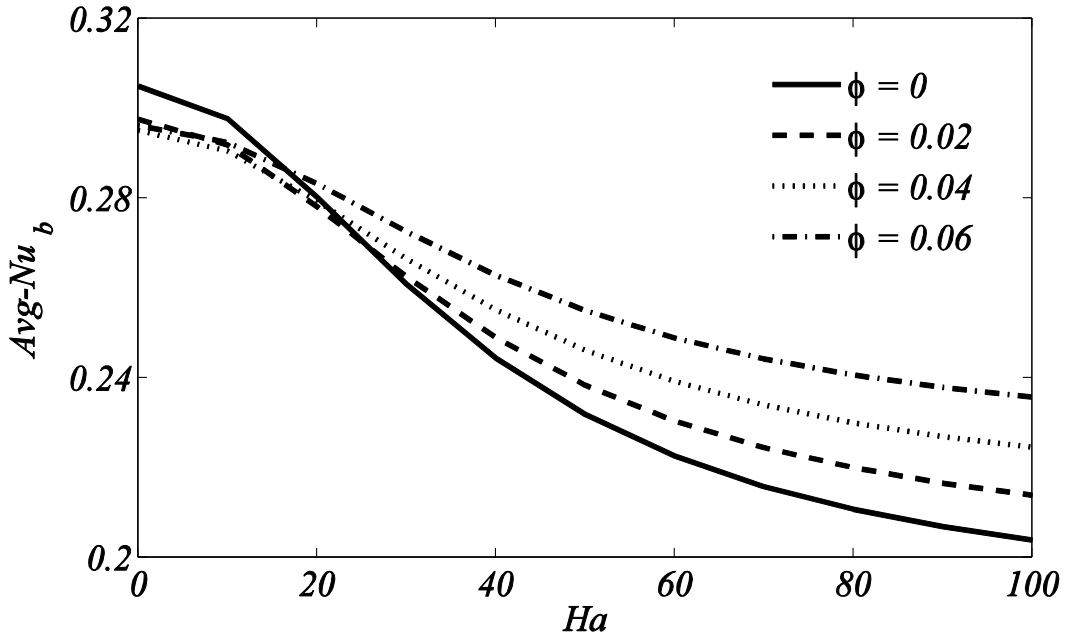

(a)

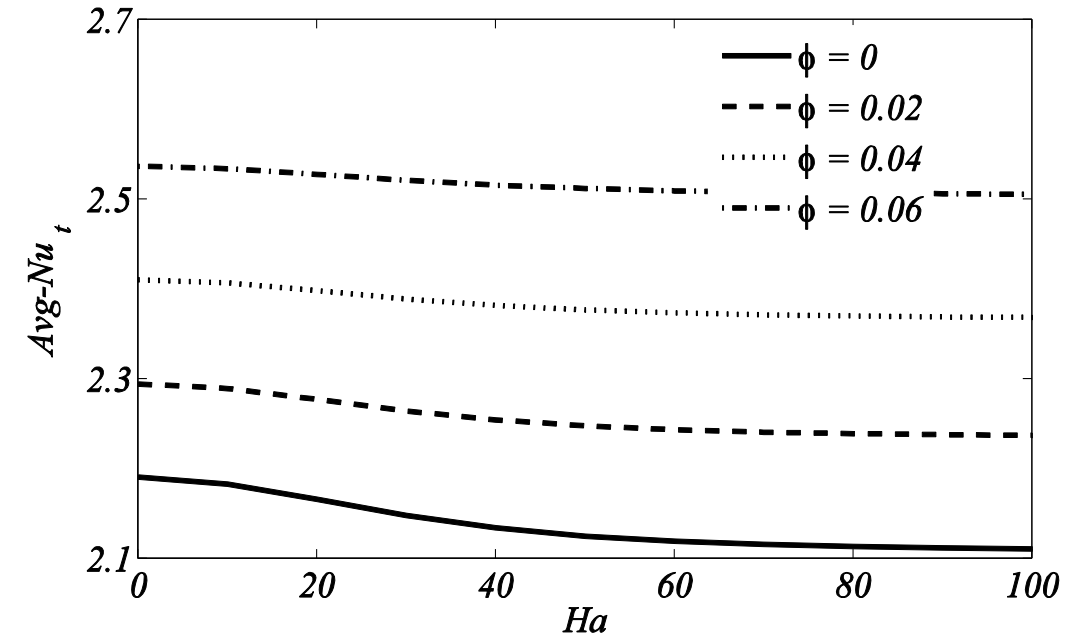

(b)

Figure 5.8: $\overline{\mathrm{Nu}}$ against Hartmann number for different ϕ along **(a)** lower boundary **(b)** upper boundary

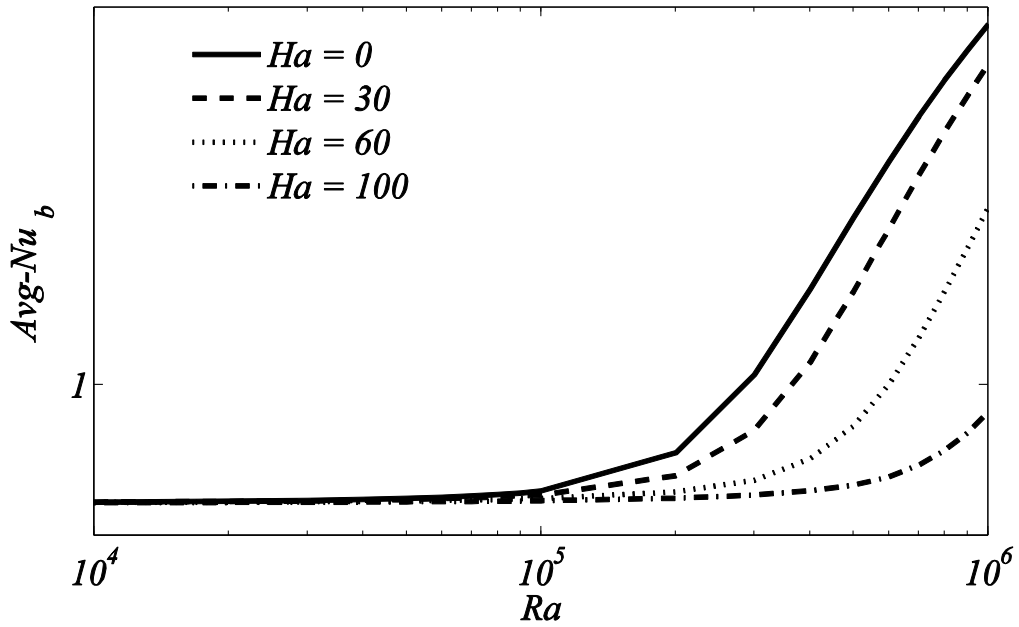

(a)

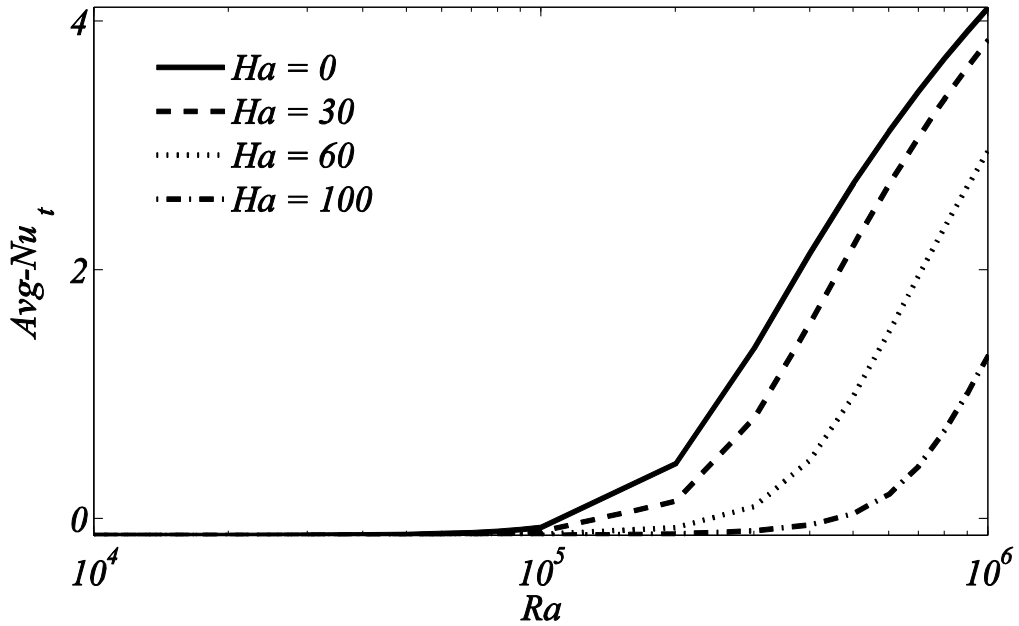

(b)

Figure 5.9: $\overline{\mathrm{Nu}}$ against Rayleigh number for different Ha along **(a)** lower boundary **(b)** upper boundary

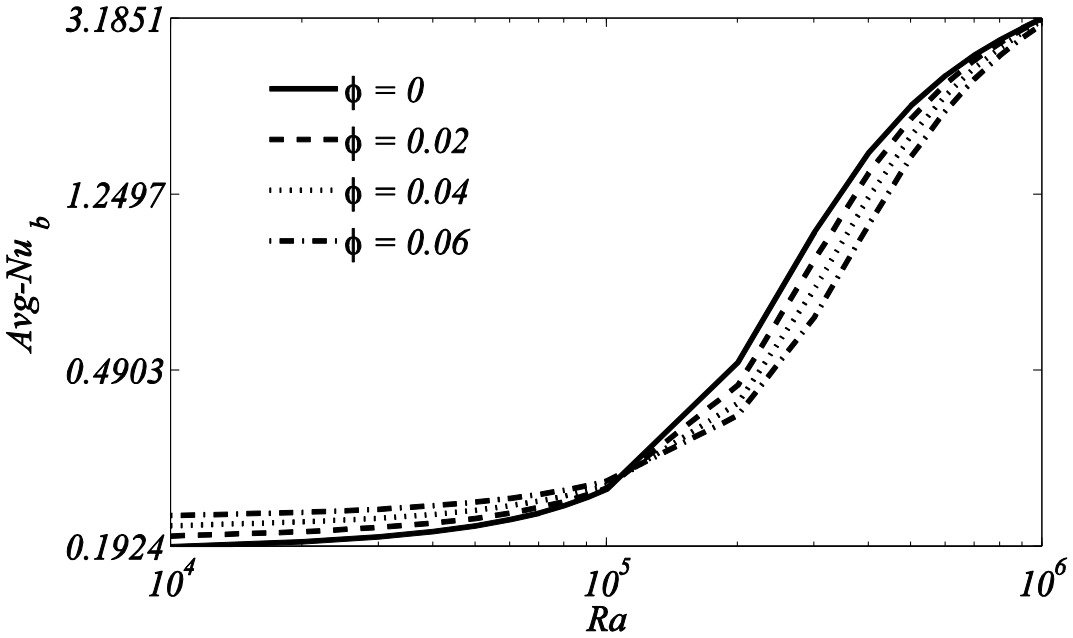

(a)

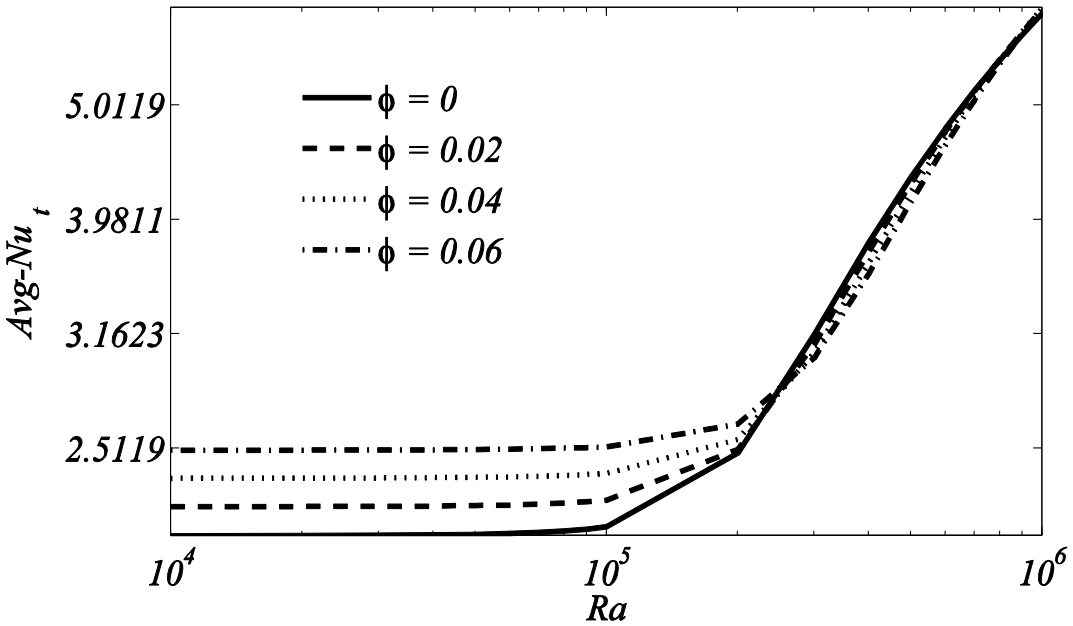

(b)

Figure 5.10: $\overline{\mathrm{Nu}}$ against Rayleigh number for different ϕ along **(a)** lower boundary **(b)** upper boundary

Figure 5.9 (a, b) depicts the combined effects of Hartmann and Rayleigh numbers on the Average Nusselt number along lower and upper boundaries of the container. It has been noticed that average heat flow rate gets insignificantly affected by Hartmann number when Rayleigh number is comparatively small i.e. for $Ra < 10^5$ while against higher Ra, Hartmann number influences the overall heat transfer rate significantly. The decay in overall heat flow rate against increasing Ha (as shown in **Figure 5.9**) is due to the increase in the strength of Lorentz force that causes attenuation in strength of low current in the container. Whereas against any fixed Hartmann number, $\overline{\mathrm{Nu}}$ appears constant for smaller values of Ra while afterwards $\overline{\mathrm{Nu}}$ is seen to rise with escalation in Rayleigh number.

The combine effect of Ra and concentration of solid particles on average heat flow rate are presented in **Figure 5.10 (a, b)**. It is investigated that up to certain values of Rayleigh number ($Ra < 10^5$ for bottom wall and $Ra < 4 \times 10^5$ for top wall) the increase in the concentration of ferroparticles escalates the overall heat flow rate in container owing the fact that addition of ferroparticles rises the conductivity of ferrofluid and that is responsible for increased heat flow rate exchanged among heated boundary and ferrofluid. Whereas $\overline{Nu}$ is found to be a decreasing function of solid volume fraction of ferroparticles afterwards the above mentioned values of Rayleigh number. Opposite to this average heat transfer rate is seen to escalate with augmentation in Rayleigh number against any fixed solid volume fraction of ferroparticles, however this increase is significantly sharp after the above reffered values of Rayleigh number.

5.5 Conclusions

In this chapter, we discussed the numerical simulations to investigate two dimensional laminar flow of ferrofluid though a square enclosure considering uniform horizontal magnetic field where lower boundary is provided constant heat, top wall is taken cold, vertical side walls are insulated perfectly and a heated square blockage is placed with different aspect ratios ($0.25 \leq A/H \leq 0.5$) at the centre of cavity. The solution of momentum, energy and mass conservation equations governing the flow problem is obtained using Galerkin weighted residual technique and resulting nonlinear algebraic system is subjected to Newton's method. Results are shown against various ranges of solid volume fraction of nanoscale ferromagnetic particles, Prandtl, Rayleigh and Hartmann numbers.

It is observed that the intensification of strength of magnetic field weakens the strength of streamlines circulation and conduction regime is dominant in container for all Ha when Rayleigh number is taken small. Upsurge in Ra results in escalation of strength of streamline circulations while isotherms become highly distorted showing convection dominant regime in cavity for large Rayleigh numbers. Heat flow rate of ferrofluid is greater than that of plain fluid and increase in aspect ratio of square blockage reduces the magnitude of streamline circulations.

Chapter 6

Thermal Energy of Hydromagnetic Ferrofluid Flow in a Square Cavity with Adiabatic Block

The present chapter contains computational results for mixed convective energy flow in cobalt-based ferrofluid enclosed in a two-sided lid-driven container provided heat from left vertical moving boundary under MHD effects influenced by a source of heat generation/absorption when a square adiabatic block of different aspect ratios is located at the centre of the square container. The governing equations describing the heat transfer and fluid flow are exposed to penalty method first and after that reduced equations are simplified by Galerkin technique. The governing flow parameters are the concentration of nano-scale ferromagnetic particles $(0.0 < \phi < 0.1)$, Reynolds number $(50 < Re < 200)$, Richardson number $(0.1 < Ri < 100)$, Hartmann number $(0 < Ha < 100)$ and heat generation/absorption coefficient $(-10 < Q < 10)$. The results of present investigation shows that the enhancements in heat transport occur due to presence of the block up to the certain block size. Streamlines recirculation cells suppressed and augmentation in heat transfer is remarkably high due to presence of an adiabatic block. The results also display that the arrangements of fluid and energy flows are significantly depends on the concentration of nano-scale solid ferromagnetic particles, heat generation/absorption coefficient, Richardson, Reynolds and Hartmann numbers.

6.1 Geometrical Configuration and Governing Equations

A geometrical representation of the square cavity which is considered in this investigation is presented in **Figure 6.1**. The width and length of the square container is represented by L and height of a container is supposed to be long enough so the investigation can be considered as two dimensional. It is assumed that vertical walls of the container are oscillating in their own plane in upward and downward directions respectively with the same speed V_0 while rest of the walls is in static position. Side left and right walls of square container are maintained at a high and low temperature T_h and T_c respectively whereas the top and bottom walls are considered thermally insulated. An adiabatic square block with different aspect ratios is placed at the centre of the cavity which is used to modify the process of energy transport. The entire

enclosure carries a mixture of base fluid (water) and nano-sized cobalt ferromagnetic particles. The ferromagnetic fluid is considered as incompressible, steady and laminar in this study. The gravitational force is considered to act along negative y −direction. By imposing the Boussinique approximation, a physical factor appears as a result of the density change in the momentum equation, where all other physical properties are supposed to be constant except for the density as a function of temperature. Moreover a uniform magnetic field is applied parallel to horizontal walls of the cavity. Here induced magnetic field has been ignored being sufficiently small in comparison of applied magnetic field B_0 under low-R_m approximation (Davidson (2001)). Considering all boundaries of the container to be electrically insulated without Hall effects, magnetic term can be simplified to a restraining factor $-{B_0}^2 v$ (Garandet et al. (1992)). Therefore, electromagnetic force is a function of velocity component (v) normal to magnetic field.

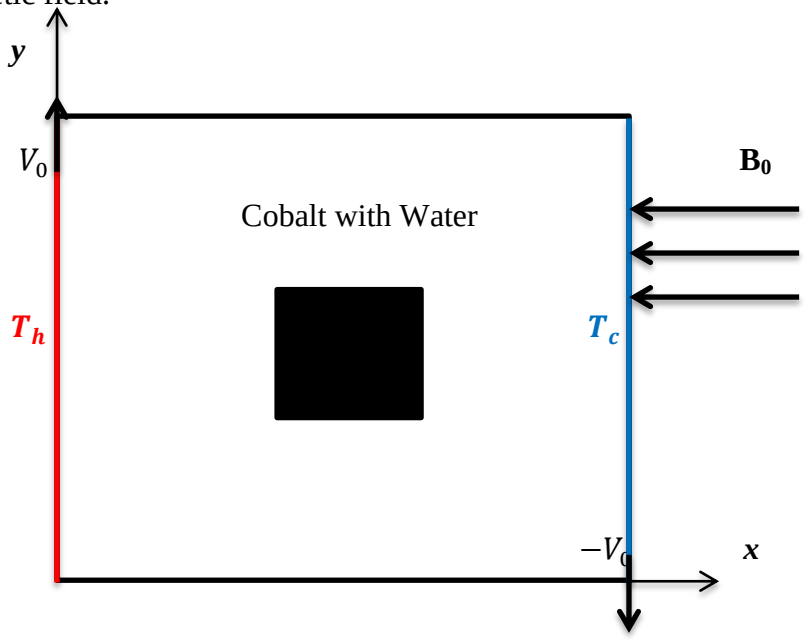

Figure 6.1: Geometrical representation of the present problem

By considering above assumptions and in the absence of viscous dissipation, equations describing the fluid and heat flows may be expressed in the following form:

$$u_x + v_y = 0, \tag{6.1}$$

$$uu_x + vu_y = -\frac{1}{\rho_{ff}} p_x + \frac{\mu_{ff}}{\rho_{ff}} \left(u_{xx} + u_{yy}\right), \tag{6.2}$$

$$uv_x + vv_y = -\frac{1}{\rho_{ff}} p_y + \frac{\mu_{ff}}{\rho_{ff}} \left(v_{xx} + v_{yy}\right) + \frac{g(\rho\beta)_{ff}}{\rho_{ff}} (T - T_c) - \frac{\sigma_{ff} B_o^2}{\rho_{ff}} v, \tag{6.3}$$

$$uT_x + vT_y = \frac{\alpha_{ff}}{(\rho C_p)_{ff}}\left(T_{xx} + T_{yy}\right) + \frac{Q_o}{(\rho C_p)_{ff}}(T - T_c) \tag{6.4}$$

subject to the following boundary conditions

$$u = 0, v = 0, \frac{\partial T}{\partial x} = 0 \text{ if } 0 \le x \le L \text{ and } y = 0,$$

$$u = 0, v = 0, \frac{\partial T}{\partial x} = 0 \text{ if } 0 \le x \le L \text{ and } y = L,$$

$$u = 0, v = V_0, T = T_h \text{ if } 0 \le y \le L \text{ and } x = 0,$$

$$u = 0, v = -V_0, T = T_c \text{ if } 0 \le y \le L \text{ and } x =, \tag{6.5}$$

where *u*, *v* represents velocity components in cartesian coordinates system, *p* be the modified pressure, ρ_{ff} and μ_{ff} are ferrofluid 's density and dynamic viscosity. The definitions of non-dimensional variables and parameters incorporated to derive the dimensionless form of Eqs. (6.1)-(6.5) are as follows:

$$(X, Y) = \left(\frac{x}{L}, \frac{y}{L}\right), (U, V) = \left(\frac{u}{V_0}, \frac{v}{V_0}\right), P = \frac{p}{\rho_{ff}{V_0}^2}, \theta = \frac{T - T_c}{T_h - T_c}, Pr = \frac{\nu_f}{\alpha_f}, Gr = \frac{g\beta_f L^3 \Delta T}{{\nu_f}^2}, Re = \frac{\rho_f V_0 L}{\mu_f}, Ri = \frac{Gr}{Re^2}, Ha^2 = \frac{\sigma_f {B_o}^2 H^2}{\mu_f}. \tag{6.6}$$

Above transformation is used in Eqs. (6.2)-(6.4), to get

$$U_X + V_Y = 0, \tag{6.7}$$

$$UU_X + VU_Y = -P_X + \frac{1}{Re}\frac{\mu_{ff}\rho_f}{\rho_{ff}\mu_f}(U_{XX} + U_{YY}), \tag{6.8}$$

$$UV_X + VV_Y = -P_Y + \frac{1}{Re}\frac{\mu_{ff}\rho_f}{\rho_{ff}\mu_f}(V_{XX} + V_{YY}) + \frac{(\rho\beta)_{ff}}{\rho_f\beta_f\rho_{ff}}Ri\theta - \frac{\rho_f\chi\sigma_{ff}}{\rho_{ff}\sigma_f}\frac{Ha^2}{Re}V, \tag{6.9}$$

$$U\theta_X + V\theta_Y = \frac{1}{RePr}\frac{\alpha_{ff}}{\alpha_f}(\theta_{XX} + \theta_{YY}) + \frac{1}{RePr}\frac{\alpha_{ff}}{\alpha_f}Q\theta. \tag{6.10}$$

The reduced boundary conditions are expressed in non-dimensional from as:

$$U = 0, V = 1, \theta = 1 \text{ if } 0 \le Y \le 1 \text{ and } X = 0,$$

$$U = 0, V = -1, \theta = 0 \text{ if } 0 \le Y \le 1 \text{ and } X = 1.$$

$$U = 0, V = 0, \frac{\partial\theta}{\partial Y} = 0 \text{ if } 0 \le X \le 1 \text{ and } Y = 0,$$

$$U = 0, V = 0, \frac{\partial\theta}{\partial Y} = 0 \text{ if } 0 \le X \le 1 \text{ and } Y =, \tag{6.11}$$

where Pr, Gr, Re, Ri and Ha represents the Prandtl, Grashof, Reynolds, Richardson and Hartmann numbers respectively. *U* and *V* are dimensionless velocity components, θ shows non-dimensional temperature and **Table 6.1** represents the properties of ferrofluid.

The heat flow rate (Nu) and average heat flow rate $(\overline{\text{Nu}})$for veritcal walls is defined as follows:

$$\mathrm{Nu_v} = \frac{k_{ff}}{k_f}\left(-\sum_{i=1}^{6}\theta_i \frac{\partial \phi_i}{\partial Y}\right) \tag{6.12}$$

$$\overline{\mathrm{Nu_v}} = \frac{\int_0^1 \mathrm{Nu_v} dY}{\int_0^1 dY} = \int_0^1 \mathrm{Nu_v} dY. \tag{6.13}$$

6.2 Results and Discussions

The objective of present study is to obtain the numerical results for combined convection heat transfer through ferrofluid contained in a square container with constant temperature profile at left moving lid, cold right moving lid and insulated both horizontal walls in the presence of an adiabatic square blockage with various aspect ratios placed at middle of the cavity. The obtained results have been presented in the form of streamline contours, isotherm contours, Nusselt number and average Nusselt number against different ranges of the involved physical parameters including Richardson number $(0.1 < Ri < 200)$, Reynolds number $(50 < Re < 200)$, solid volume fraction of ferromagnetic particles $(0.0 < \phi < 0.1)$, coefficient of heat generation or absorption $(-10 < Q < 10)$ and Hartmann number $(0 < Ha < 100)$. The selected ranges for the governing flow parameters involved in the flow problem (Reynolds, Grashof and Richardson numbers) represents the three flow regimes namely, free convection when $Ri \to \infty$, forced convection when $Ri \to 0$ and mixed convection when $Ri = 1$.

The effects of Hartmann number and adiabatic block on the fluid flow and heat flow structure have been presented in **Figure 6.2** and **Figure 6.3** respectively. It should be noted that Prandtl number, Richardson number, Reynolds number, solid volume fractions of nanoparticles and heat generation coefficient are fixed at $7.2, 1, 200, 0.1$ and 1 respectively. Mixed convection is caused by the motion of side walls and by the influence of the buoyancy-induced flow at $\mathrm{Re} = 200$ and $\mathrm{Ri} = 1$ as shown in **Figure 6.2 (a)**. The fluid present near the heat source rises and flows down along with cold wall forming primary clockwise circulations within the enclosure when there is no block present as shown in figure. The strength of circulation of stream function in the central region of the enclosure reduces due to augmentation in block size. In the presence of block, the primary clockwise circulation cells of stream function are divided into two small vortices and secondary counter-clockwise circulation cells are also found near the central region of upper and lower horizontal walls of the cavity. On the other hand, augmentation in strength of magnetic force causes reduction in the magnitude of the stream function and flow becomes weaker. In general, influence of

magnetic force suppresses the flowing fluid structure due to the retarding effects of Lorentz force. Therefore, reduction in energy transport and fluid flow is expected for large values of Hartmann number. The influence of magnetic force and adiabatic block on heat flow in terms of isotherm lines is presented in **Figure 6.3**. Originating heat flow from the heated wall and rises up via top region of the enclosure isotherm lines reaches to the right cold wall where heat is released out finally with non-uniform decreasing rate along cold right wall of the cavity. The insulating block is a complete barrier to energy transport and significantly affects the temperature field. The presence of the insulating block destroys some contours of the isotherm because it acts as an internal flow boundary. The end of the isothermal profile on the surface of the block significantly changes the position of the isotherms compared to the case when block is not present. The end-to-end isotherm lines between the two side walls establish energy transport between the source and the heat sink. Furthermore, increase in magnetic force decreases the strength of isotherm lines and makes the flow smoother as compared to the case which has no magnetic force.

Figures 6.4 and **6.5** depict the influence of centred block and Richardson number on fluid flow and energy transport arrangements while the other pertinent parameters are kept fixed at $\mathrm{Re} = 200$, $\mathrm{Ha} = 30$ and $\mathrm{Pr} = 7.2$. From Eq. (6.3), it can be noticed that the sign of Ri is opposite to the sign of Ha in source terms which means that they have opposite effects on flow regime. As expected, due to heated left vertical lid and cold right vertical lid of square container, flowing fluid rise up through the heated portion and flow down along the cold side developing circulation cells inside enclosure. **Figure 6.4 (a)** reveals that the motion of the side walls causing forced convection flow at $\mathrm{Ri} = 0.1$, as buoyancy driven flow becomes weaker. Furthermore, flowing fluid near the left heated wall rises in upward direction and fluid present near the cold right wall compresses in downward direction due to motion of the lids and forced convection regimes are found dominant at the corners of the cavity. Streamlines are compressed and primary circulation cells have been divided into two parts due to presence of the block as shown in **Figure 6.4 (a)**. As block size increases, the circulations strength of vortices in the central region of the cavity decreases due to the fact that the block reduces the effective volume of the fluid present in the cavity. Primary circulation cells are compressed towards the moving walls and secondary circulation cells are also observed near the top and bottom insulating walls of the

cavity. When Richardson number rises to 1 (**Figure 6.4 (b)**), the flow field is categorized by mixed convection dominant regime. The shape of the streamline circulation cells (**Figure 6.4 (b)** without block) mainly depends upon the values of Richardson number. The streamline circulation cells are found as stretched in elliptical shape at the comparable significance of natural and forced convection. Further increase in Richardson number upto 100 (**Figure 6.4 (c)**) leads to natural convection dominant regime as the forced convection flow is very weak, the buoyancy driven flow is generated due to the influence of the gravitational force and high temperature difference. The magnitude of the streamline circulation becomes very high which results into strong circulations and dominance of the natural convection. For the case of isotherm lines (**Figure 6.5**), aggregation of isotherms indicating a high temperature gradient occurs near the lower left corner and at the upper right corner. As mentioned earlier, the insulation module affects the isotherms. It is observed from **Figure 6.5** that the isotherms are moving towards adiabatic block present in the cavity as if they were pulled or attracted. The adiabatic block attempts to maintain the same thermal state as imposed on cavity walls.

Figure 6.6 shows heat transfer coefficient *Nu* against various values of Hartmann number along vertical moving walls. It has been noticed that heat transfer rate is maximum at the bottom edge of left heated moving lid where it reduces sharply while moving inwards and becomes minimum near the region of upper adiabatic wall. Contrary to case of cold moving right wall heat transfer rate achieved the maximum value near the upper wall of a cavity and it reduces with distance *Y* along the vertical right wall and reaches to its minimum value near the bottom of the right cold wall. Furthermore, increase in Hartmann number has significant effects on heat transfer rate along heated lid as shown in **Figure 6.6 (a)**. Along both moving walls reduction in heat transfer rate is seen with increase in Hartmann number. Augmentation in Hartmann number causes stronger magnetic field, which results in a Lorentz force acting on a flow field. This force reduces the intensity of fluid flowing in a cavity.

Figure 6.7 presents the effects of Richardson number on the heat transfer rate of heated and cold moving walls in opposite direction. It has been observed that Nusselt number is maximum near bottom region of left heated moving wall and it decreases to its minimum value near upper region of heated wall as shown in **Figure 6.7 (a)**. Opposite to this in the case of cold moving wall heat transfer rate achieved its maximum value in upper region of the right cold wall and it decreases slowly to its

minimum value near bottom region of this wall as presented in **Figure 6.7 (b)**. It has also been noticed that heat transfer rate increases with increase in the values of Richardson number, which also indicates that heat transfer rate is maximum in the case of natural convection and it is minimum in the case of forced convection for both heated and cold moving walls as presented in **Figure 6.7**.

Figure 6.8 contains graphs for local Nusselt number along both moving walls against various values of Reynolds number. It has been noted that heat transfer rate along heated wall is maximum in the lower segment of heated wall and then it reduces to its minimum value at the top of it. Opposite to this, heat transfer rate is maximum at the upper region of the cold wall, after that it reduces to meet its minimum value at the lower segment of cavity as shown in **Figure 6.8 (a, b)**. It has also been noticed that escalation in Reynolds number causes enhancement in Nusselt number significantly along heated and cold moving walls.

Figure 6.9 describes the linear trends of average Nusselt number along moving vertical lids. It is seen through figure that overall heat transfer rate reduces with augmentation in Hartmann number and there is a slight enhancement in overall heat transfer rate due augmentation in Richardson number along left heated wall as presented in **Figure 6.9 (a)**. Average Nusselt number along moving cold right wall also decreases with increase in Hartmann number. It can also be observed that there is approximately uniform distribution of average Nusselt number within the cavity.

Figure 6.10 represents the overall heat transfer rate along left heated and right cold vertical moving lids against Hartmann number for different values of nano-scale ferromagnetic particles. It has been observed that augmentation in solid volume fraction causes reduction in overall heat transfer rate and increasing the strength of magnetic field also reduces average Nusselt number along heated lid and this rate of decrease is more significant when $Ha > 10$. Average Nusselt number is maximum in the absence of magnetic field and then it decreases monotonically under the influence of magnetic field to its minimum value as shown in **Figure 6.10 (a)**. Similar behavior can be observed for the case of right moving cold lid.

Figure 6.11 contains curves for average heat transfer rate along left heated lid and right cold lid against heat generation/absorption coefficient for various values of nano-scale ferromagnetic particles. It is observed that at $Q = -10$, the addition of nano-scale ferromagnetic particles slightly increases overall heat transfer rate. Whereas, by enhancing the values of heat source/sink coefficient Q the average

Nusselt number becomes significant along heated wall as shown in **Figure 6.11 (a)**. Furthermore, overall heat transfer rate is found to be more significant as compared to the case of heated wall. It has also been observed that for the case of heat absorption i.e. $Q < 0$, overall heat transfer rate is observed as an increasing function. Contrary to this for the case of heat generation i.e. $Q > 0$, overall heat transfer rate is found to be a decreasing function.

Figure 6.12 shows the graphs for average Nusselt number along both moving walls against Richardson number for various values of nano-scale ferromagnetic particles. It is shown through figure that for small value of Richardson number, addition of the nano-scale ferromagnetic particles slightly reduces the overall heat transfer rate along heated wall. Whereas, for the case of cold wall, this increment in overall heat transfer rate is more significant as compared to heated wall. While by increasing the values of Richardson number overall heat transfer rate is found to be an increasing function. Throughout the entire domain of Richardson number, average Nusselt number of base fluid is higher as compared to ferrofluid. From figure it is revealed that the use of nano-scale ferromagnetic particles provide better results in heat transfer than that of base fluid.

Figure 6.13 contains the graphs for overall heat transfer rate for Hartmann number against various values of Reynolds number along both heated and cold moving walls. From figure, it has been noticed that at $\mathrm{Ha} = 0$, increase in values of Reynolds number results into an augmentation in overall heat transfer rate along both heated and cold moving walls. Furthermore, for the range of $Ha < 40$ for the case of $Re = 50$, overall heat transfer rate decreases and after $Ha = 40$ it becomes uniform. For other two cases i.e. $Re = 100$ and $Re = 200$, average temperature gradient decreases sharply for certain range i.e. $Ha < 40$ and after that decrease is slight. Augmentation in Reynolds number causes enhancement in average temperature gradient along both heated and cold moving walls as shown in **Figure 6.13**.

Table 6.1: Applied formulation of nanofluid properties

Ferrofluid Properties	Applied Model
Dynamic viscosity	$\mu_{ff} = \frac{\mu_f}{(1-\phi)^{2.5}}$
Heat capacitance	$(\rho c_p)_{ff} = (1-\phi)(\rho c_p)_f + \phi(\rho c_p)_s$
Density	$\rho_{ff} = (1-\phi)\rho_f + \phi\rho_s$
Thermal expansion coefficient	$(\rho\beta)_{ff} = (1-\phi)(\rho\beta)_f + \phi(\rho\beta)_s$
Thermal conductivity	$\frac{k_{ff}}{k_f} = \frac{(k_s+2k_f)-2\phi(k_f-k_s)}{(k_s+2k_f)+\phi(k_f-k_s)}$
Thermal diffusivity	$\alpha_{ff} = \frac{k_{ff}}{(\rho c_p)_{ff}}$
Electrical conductivity	$\sigma_{ff} = \sigma_f\left(1 + \frac{3\left(\frac{\sigma_s}{\sigma_f}-1\right)\phi}{\left(\frac{\sigma_s}{\sigma_f}+2\right)-\left(\frac{\sigma_s}{\sigma_f}-1\right)\phi}\right)$

Table 6.2: Overall heat transfer rate along heated wall for block sizes $(0 - 0.8)$

Re	Ri	$\overline{\mathrm{Nu_L}}$									
		No Block	A_1	A_2	A_3	A_4	A_5	A_6	A_7	A_8	A_9
50	0.1	7.856	7.857	7.858	7.835	7.743	7.548	7.235	6.830	6.384	5.932
	1	8.074	8.077	8.083	8.087	8.033	7.861	7.523	7.032	6.484	5.964
	10	8.945	8.951	8.968	9.021	9.066	9.056	8.897	8.382	7.367	6.280
	100	11.240	11.245	11.261	11.308	11.365	11.422	11.454	11.402	10.940	8.771
100	0.1	14.158	14.165	14.187	14.259	14.279	14.130	13.717	13.019	12.144	11.233
	1	14.340	14.347	14.372	14.454	14.523	14.487	14.219	13.550	12.488	11.355
	10	15.644	15.653	15.676	15.748	15.836	15.911	15.917	15.718	14.818	12.612
	100	18.944	18.947	18.959	19.002	19.102	19.148	19.192	19.231	19.128	17.927
200	0.1	21.765	21.766	21.779	21.867	22.125	22.384	22.325	21.616	20.141	18.319
	1	22.086	22.095	22.128	22.263	22.456	22.628	22.661	22.299	21.019	18.756
	10	23.834	23.843	23.765	23.830	23.908	23.999	24.090	24.108	23.771	21.678
	100	28.511	28.514	28.524	28.556	28.606	28.665	28.665	28.704	28.803	28.399

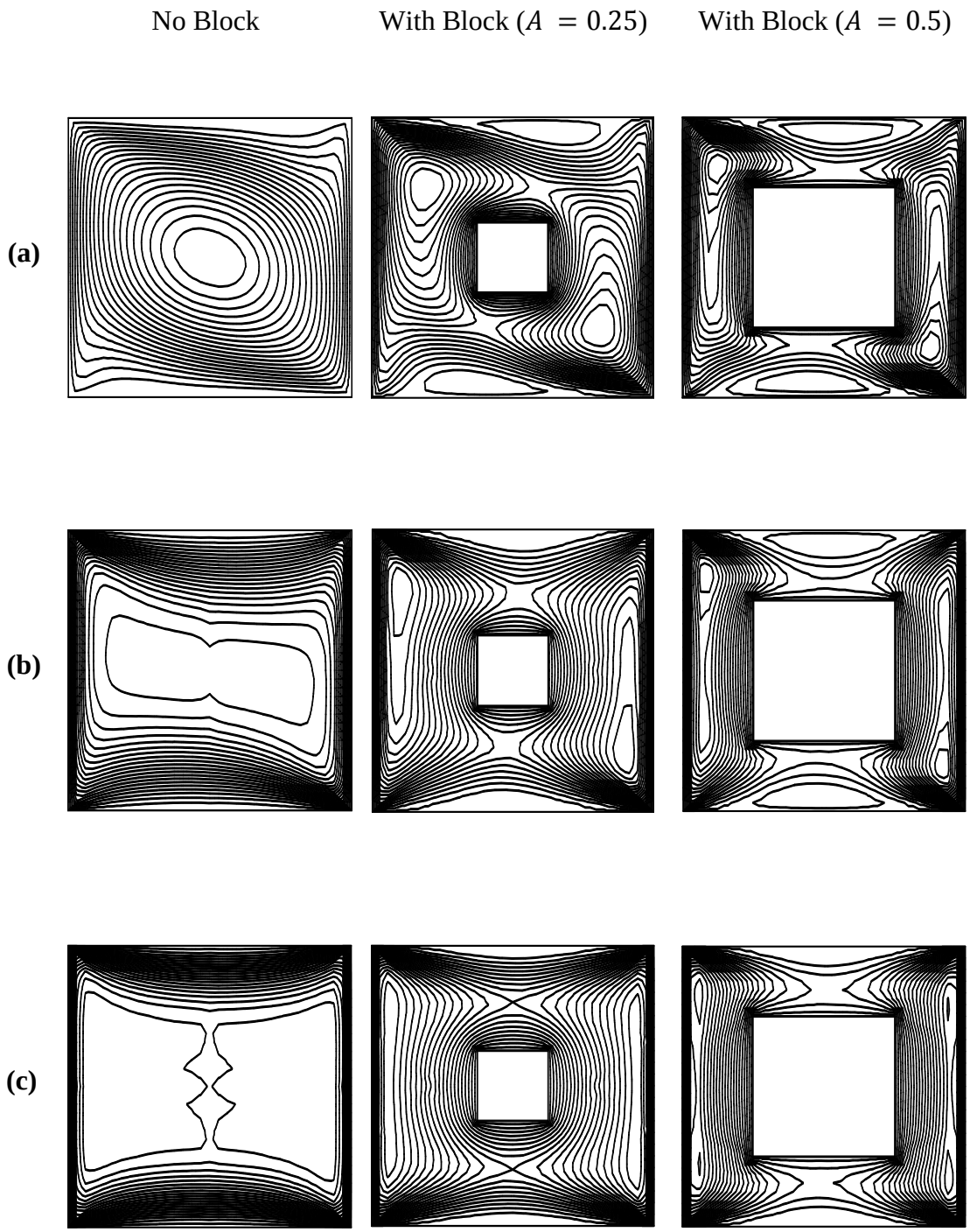

Figure 6.2: Contours of stream function against $\mathrm{Re} = 200,\ \mathrm{Ri} = 1, \mathrm{Pr} = 7.2$ and **(a)** $\mathrm{Ha} = 0$ **(b)** $\mathrm{Ha} = 30$ **(c)** $\mathrm{Ha} = 60$

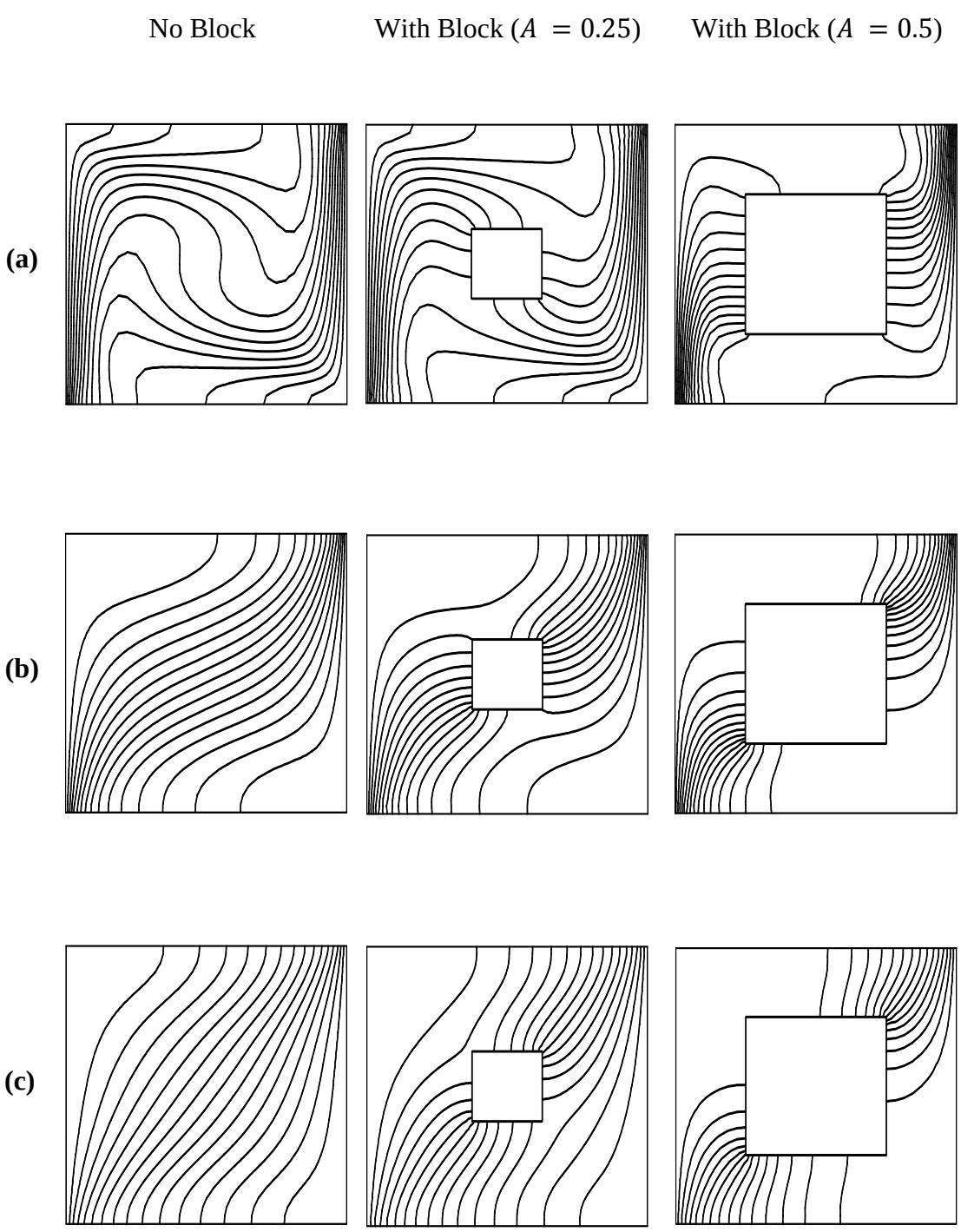

Figure 6.3: Isothermlines against $\mathrm{Re} = 200, \mathrm{Ri} = 1, \mathrm{Pr} = 7.2$ and **(a)** $\mathrm{Ha} = 0$ **(b)** $\mathrm{Ha} = 30$ **(c)** $\mathrm{Ha} = 60$

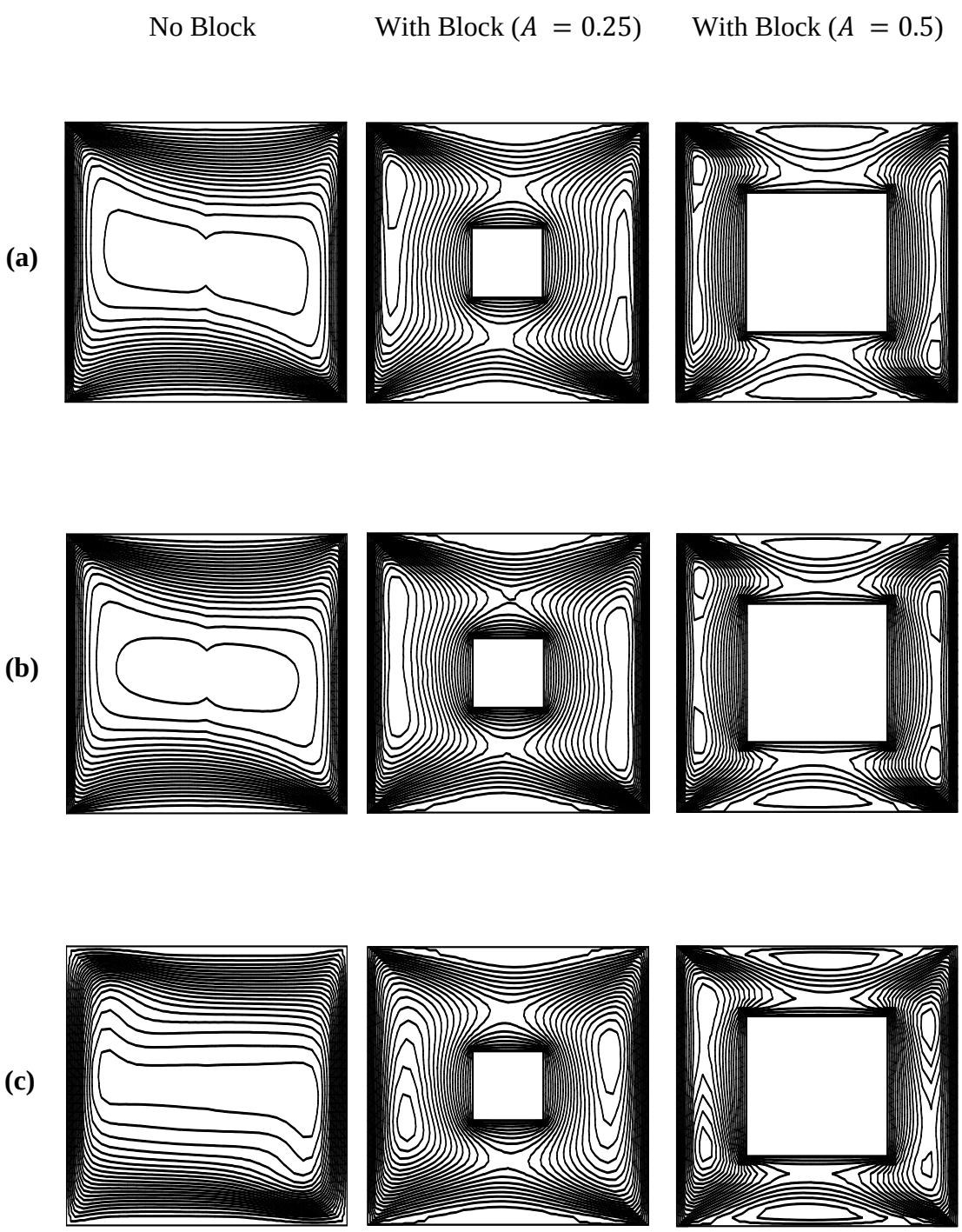

Figure 6.4: Contours of stream function against $\mathrm{Re} = 200, \mathrm{Ha} = 30, \mathrm{Pr} = 7.2$ and **(a)** $\mathrm{Ri} = 0.01$ **(b)** $\mathrm{Ri} = 1$ **(c)** $\mathrm{Ri} = 100$

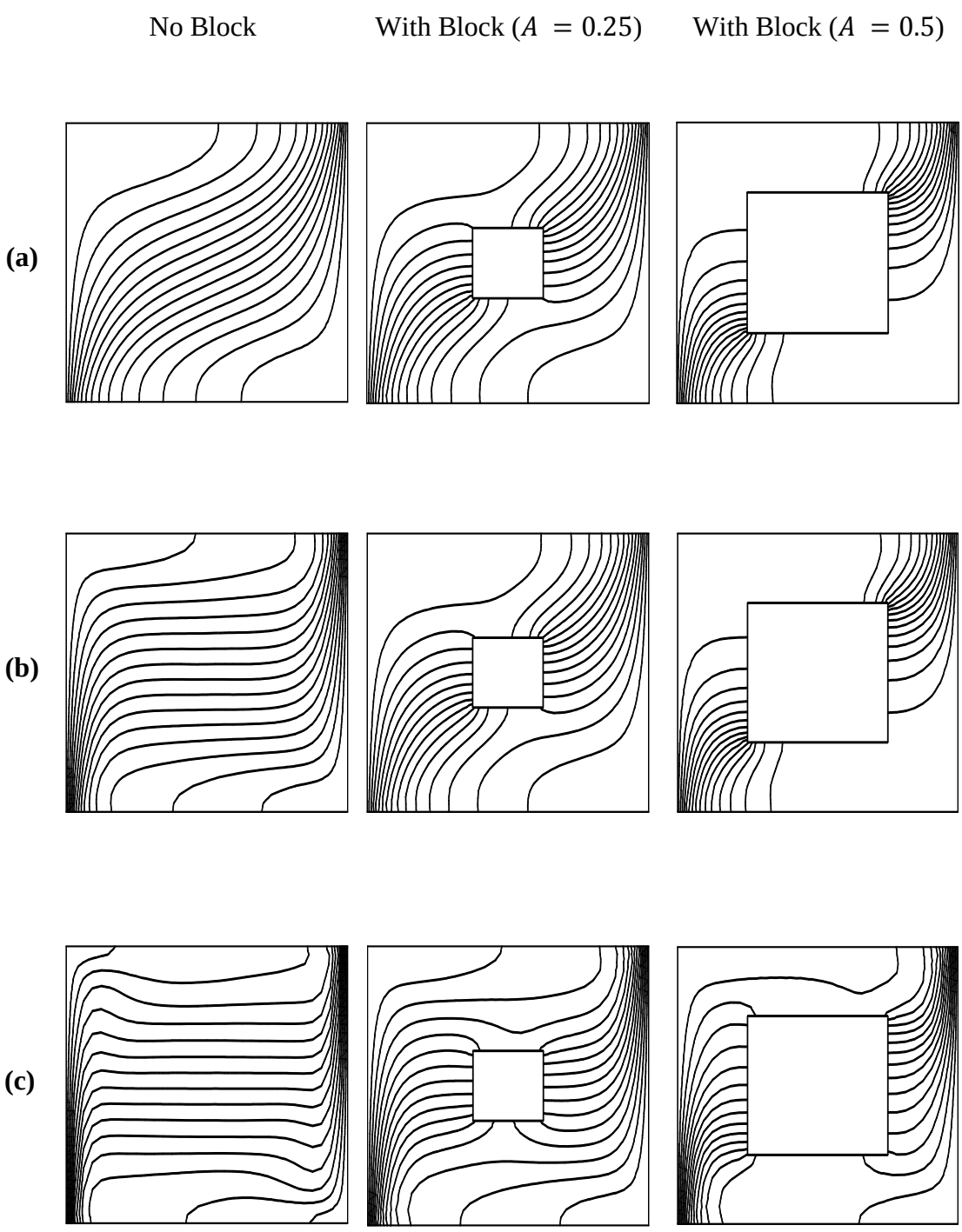

Figure 6.5: Isothermlines against $\mathrm{Re} = 200, \mathrm{Ha} = 30, \mathrm{Pr} = 7.2$ and **(a)** $\mathrm{Ri} = 0.01$ **(b)** $\mathrm{Ri} = 1$ **(c)** $\mathrm{Ri} = 100$

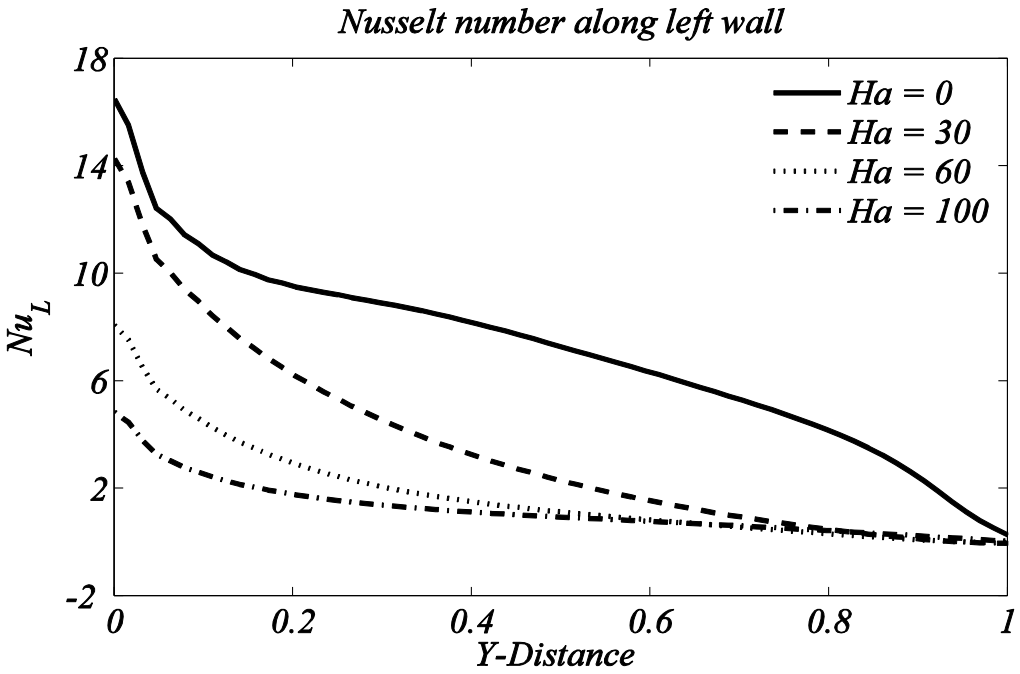

(a)

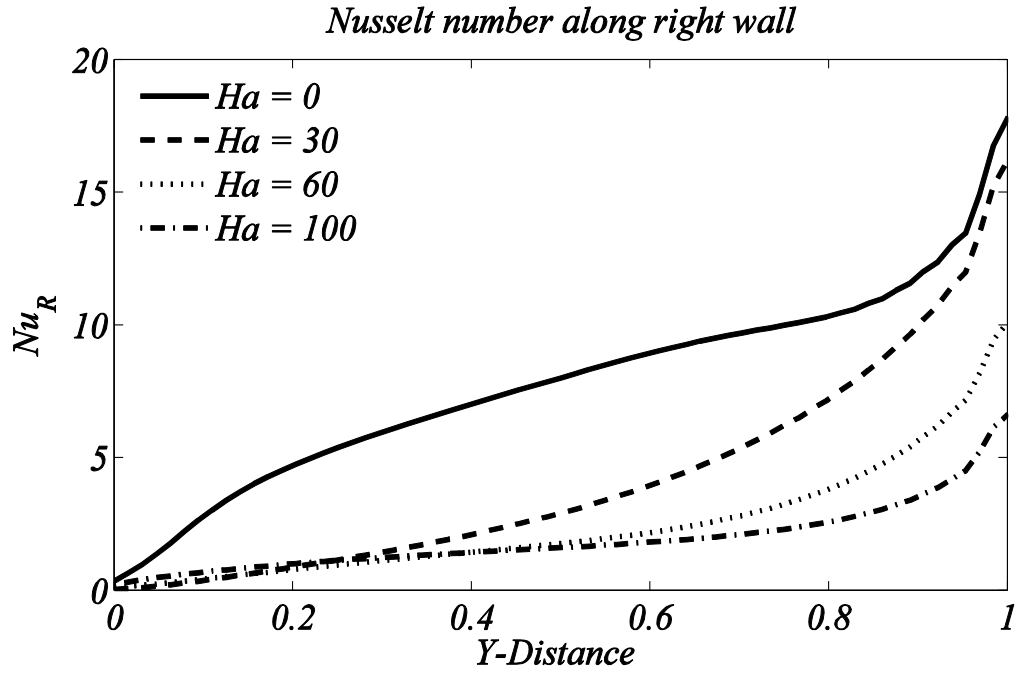

(b)

Figure 6.6: Local heat transfer rate for various values of Hartmann number along **(a)** Left heated wall **(b)** Right cold wall

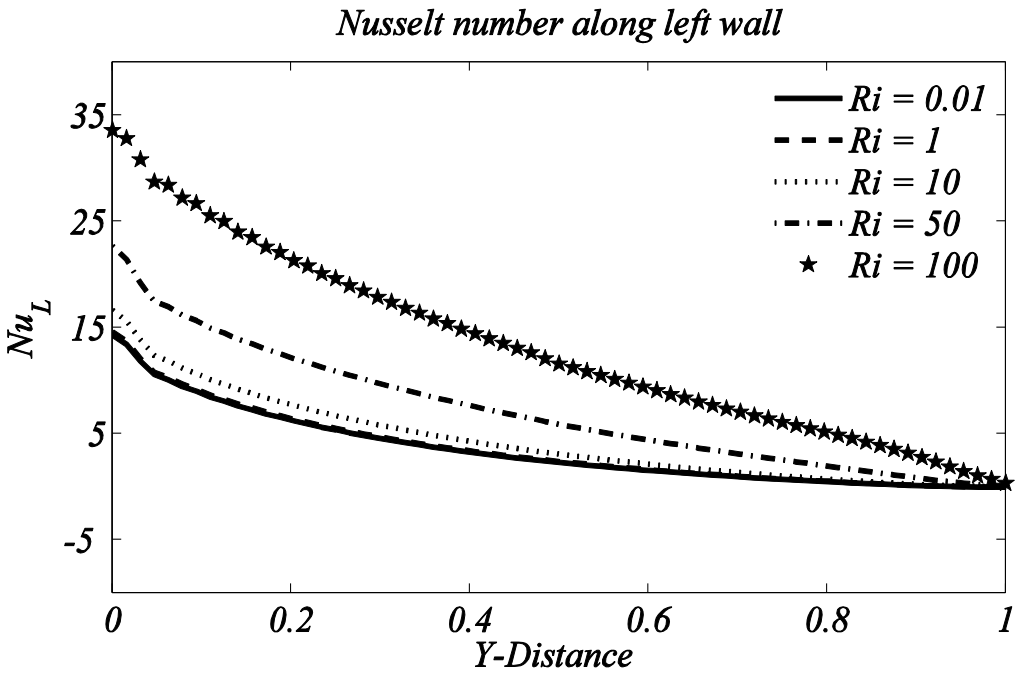

(a)

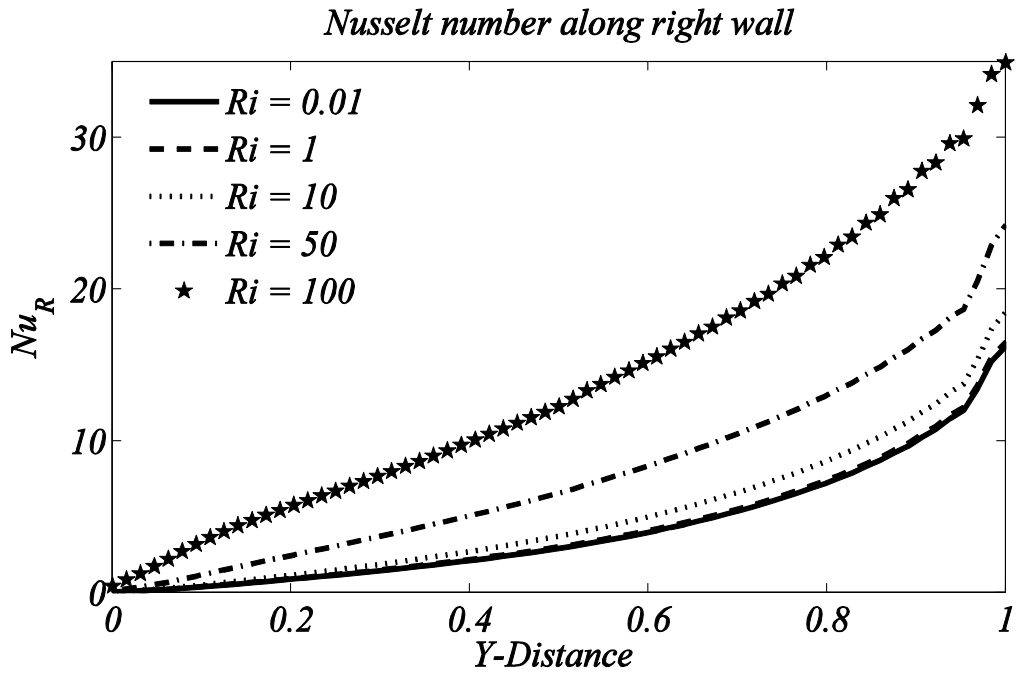

(b)

Figure 6.7: Local heat transfer rate for various values of Richardson number along **(a)** Left heated wall **(b)** Right cold wall

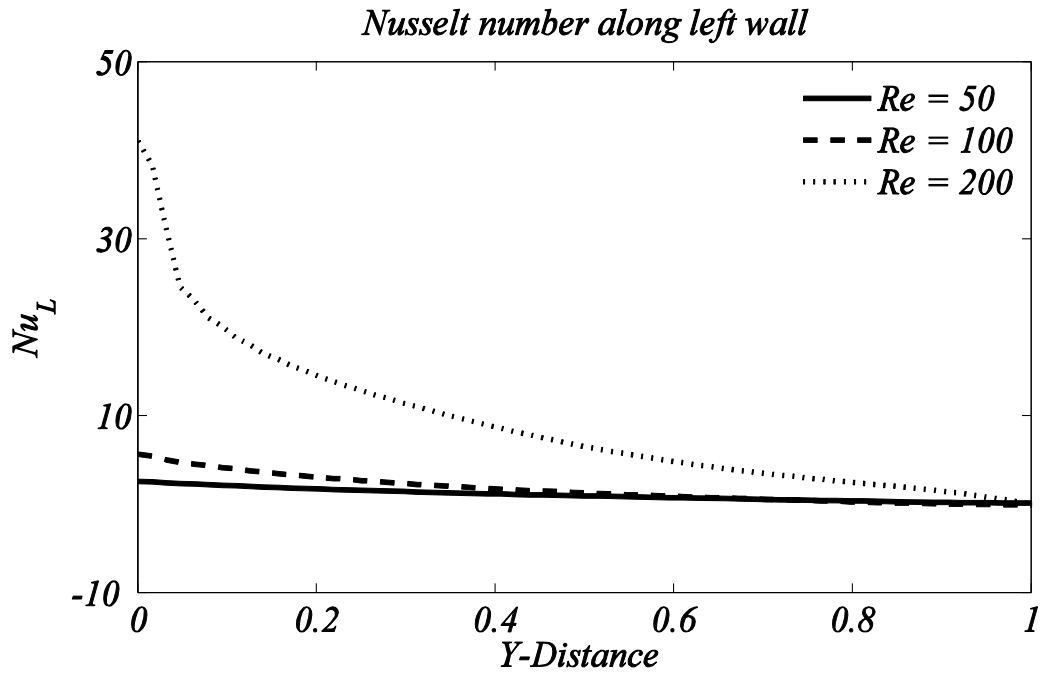

(a)

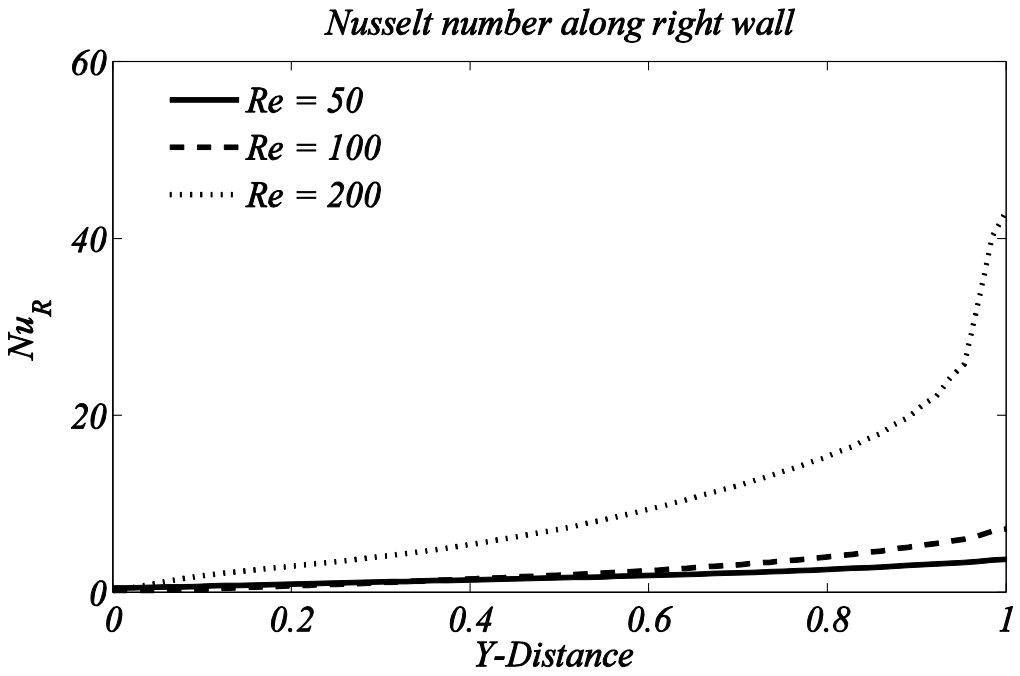

(b)

Figure 6.8: Local heat transfer rate for various values of Reynolds number along **(a)** Left heated wall **(b)** Right cold wall

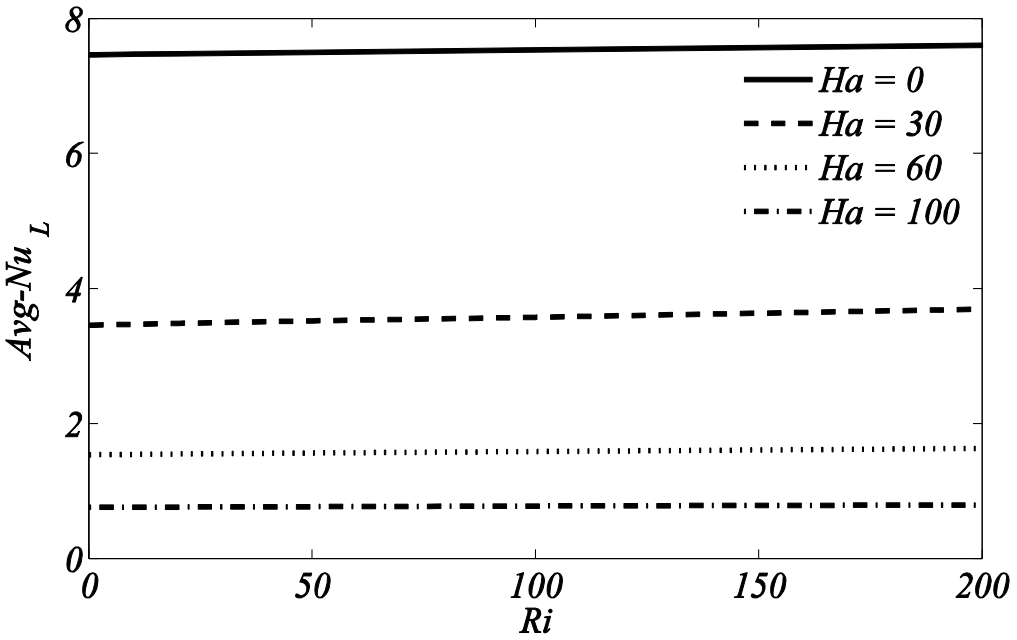

(a)

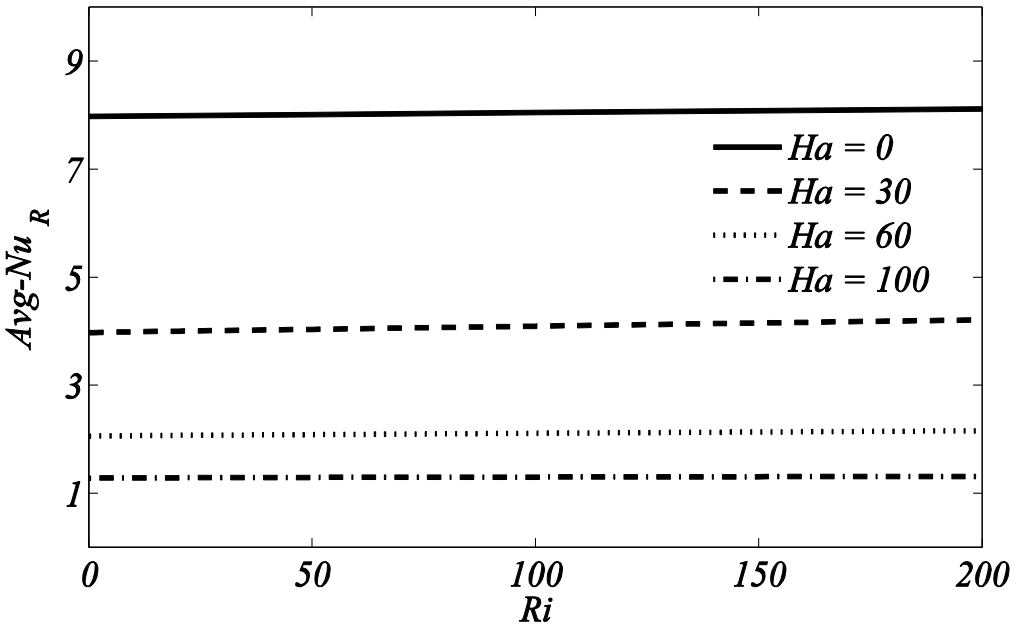

(b)

Figure 6.9: Overall heat transfer rate for various values of Hartmann number against Richarson number along **(a)** Left heated wall **(b)** Right cold wall

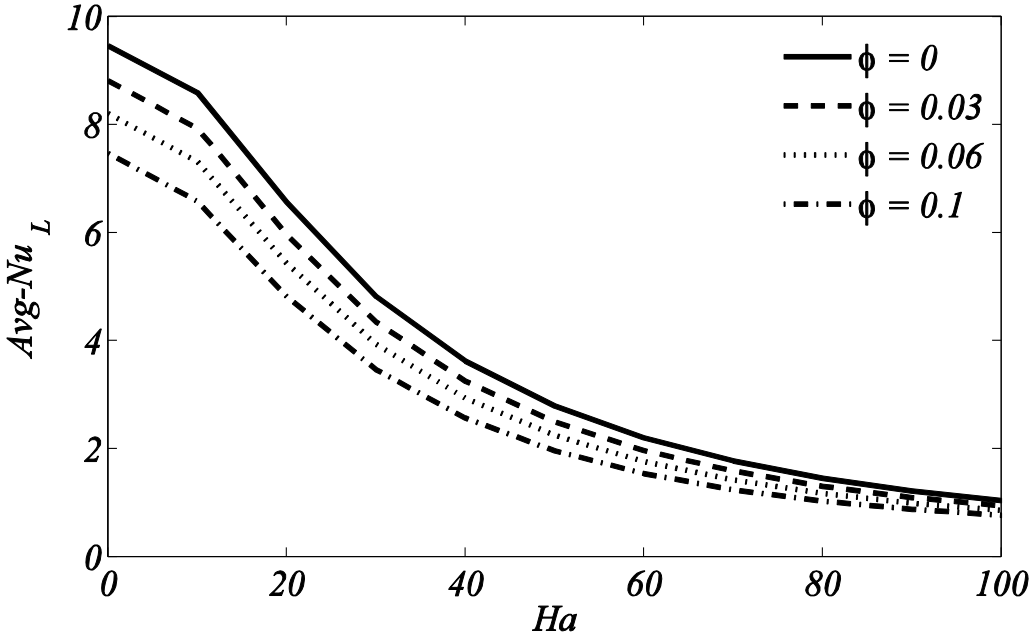

(a)

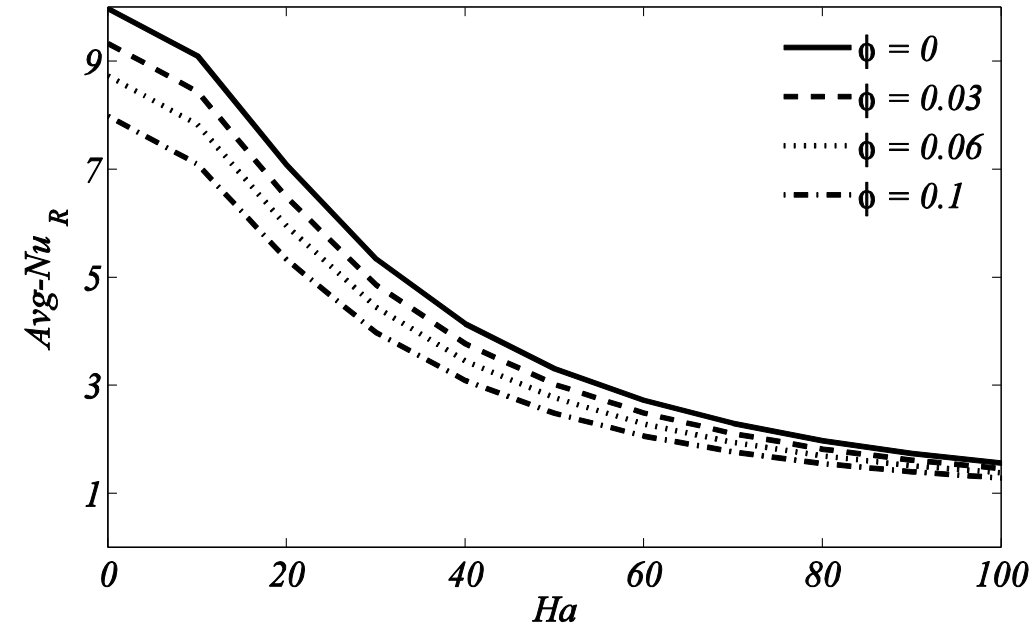

(b)

Figure 6.10: Overall heat transfer rate against Hartmann number for various values nano-scale ferromagnetic particles along **(a)** Left heated wall **(b)** Right cold wall

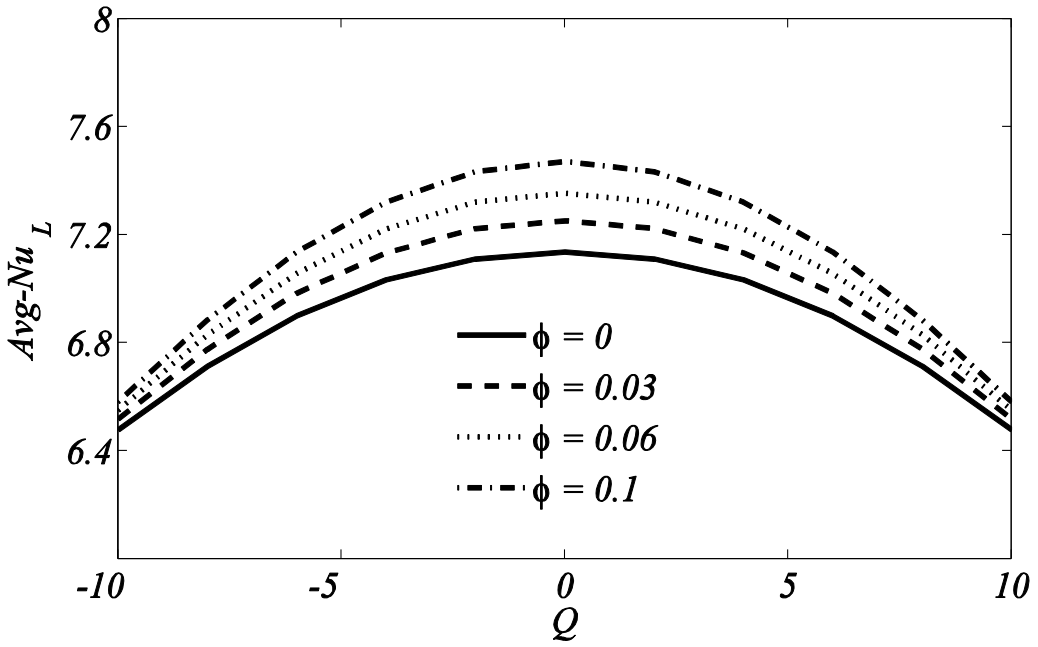

(a)

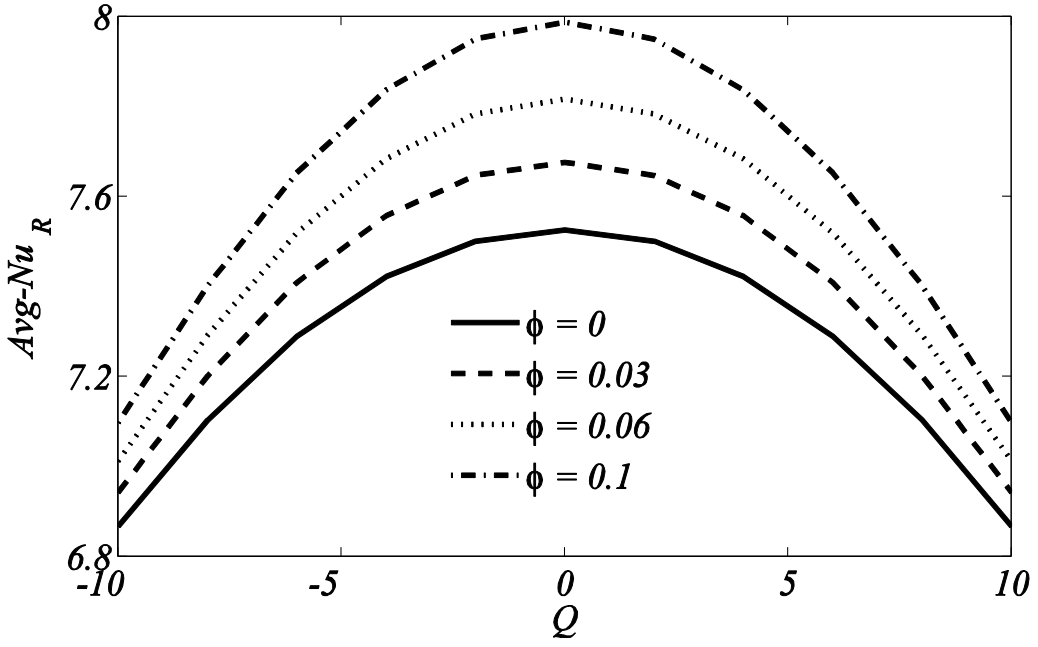

(b)

Figure 6.11: Overall heat transfer rate against heat generation/absorption coefficient for various nano-scale ferromagnetic particles along **(a)** Left heated wall **(b)** Right cold wall

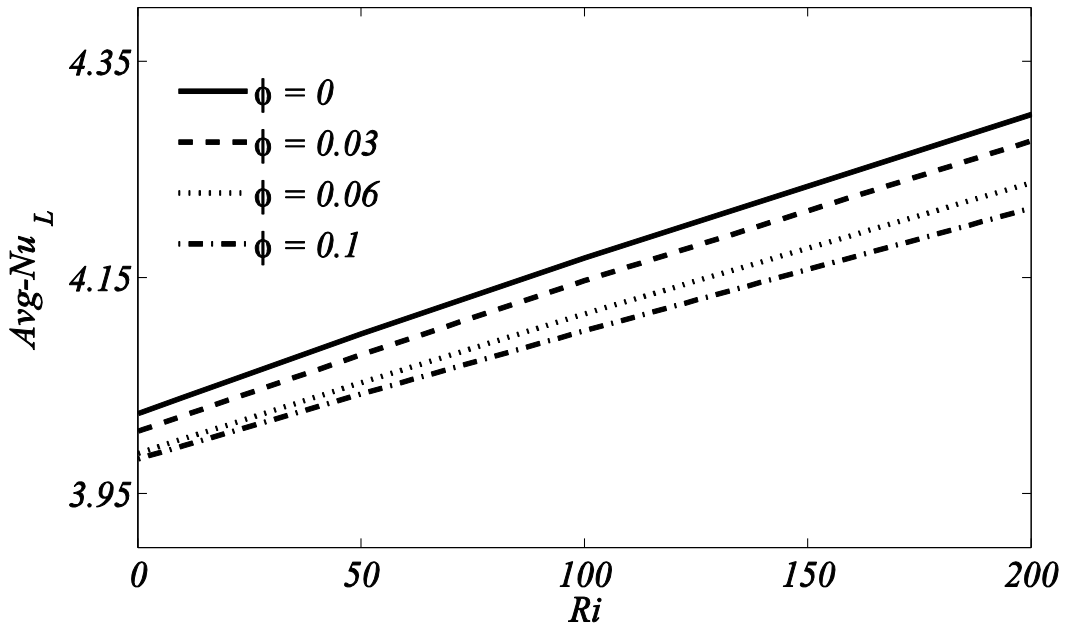

(a)

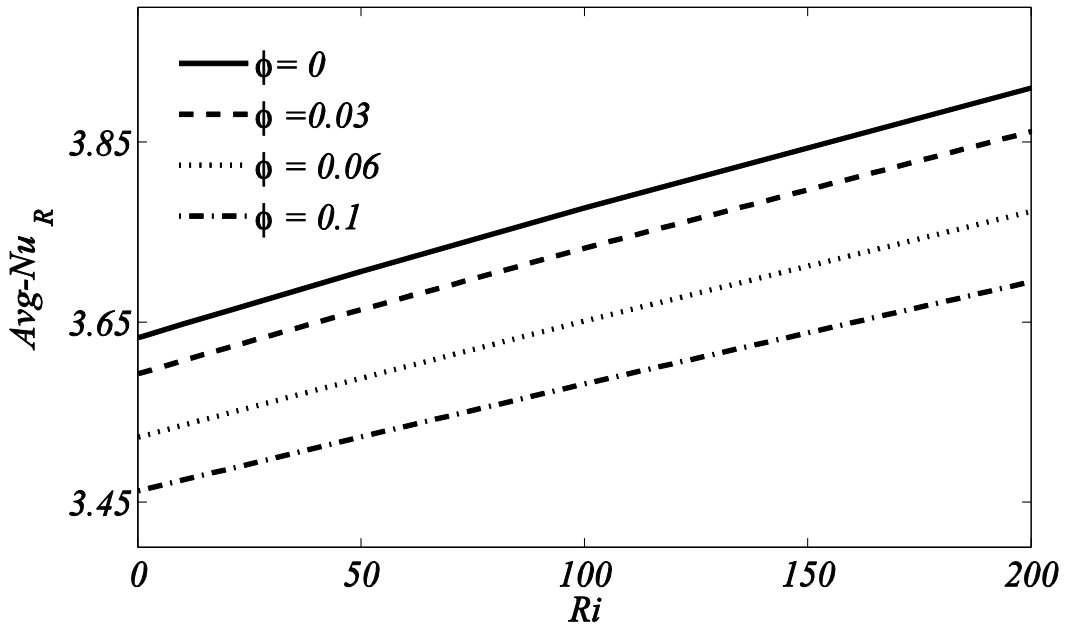

(b)

Figure 6.12: Overall heat transfer rate against Richardson number for different values of nano-scale ferromagnetic particles along **(a)** Left heated wall **(b)** Right cold wall

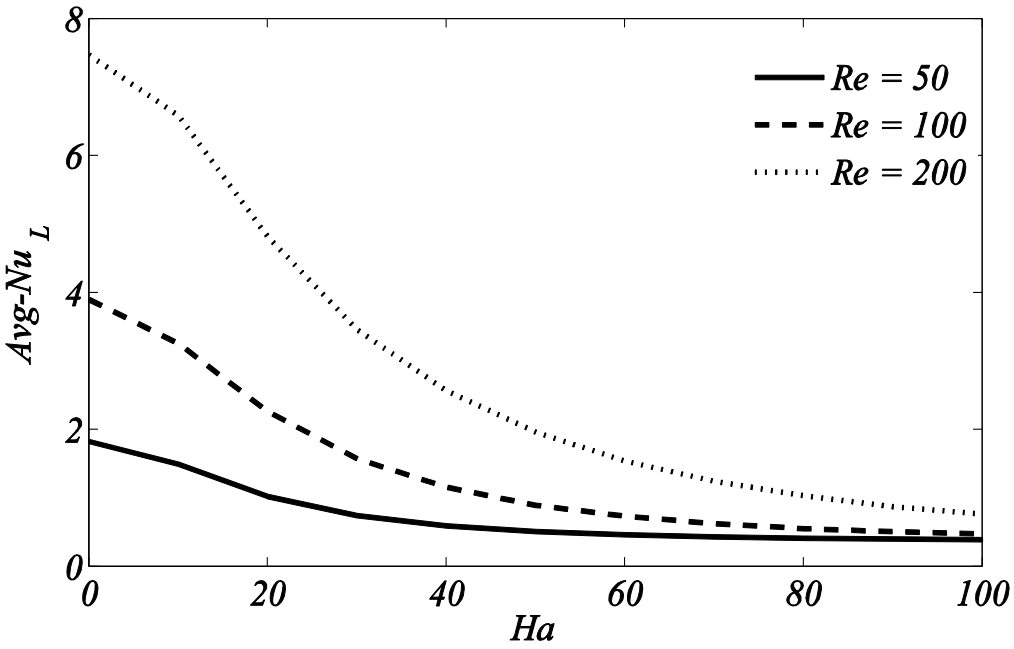

(a)

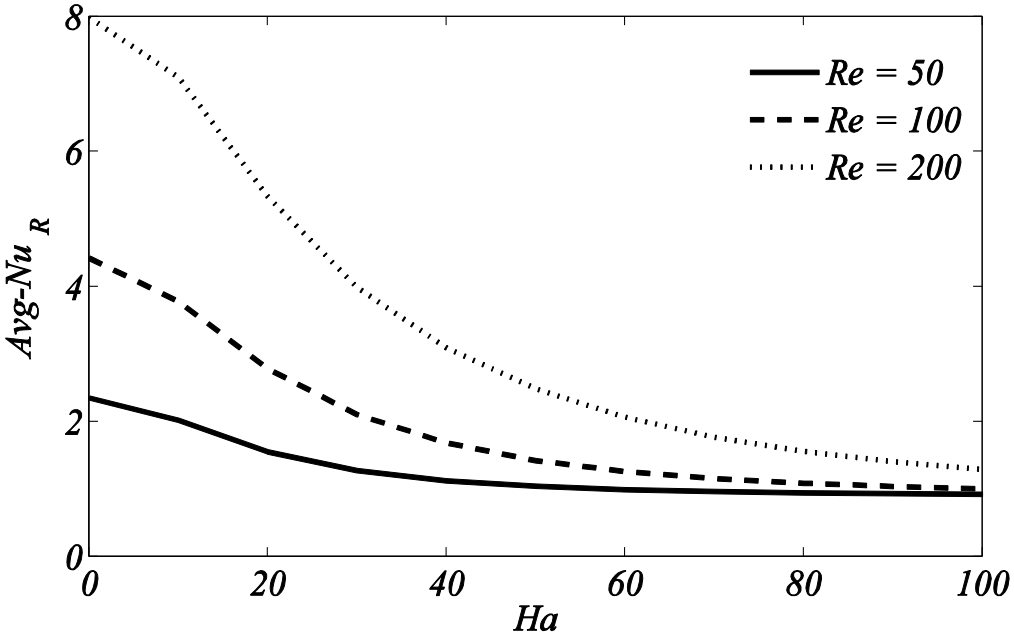

(b)

Figure 6.13: Overall heat transfer rate against Hartmann number for different values of Reynolds number along **(a)** Left heated wall **(b)** Right cold wall

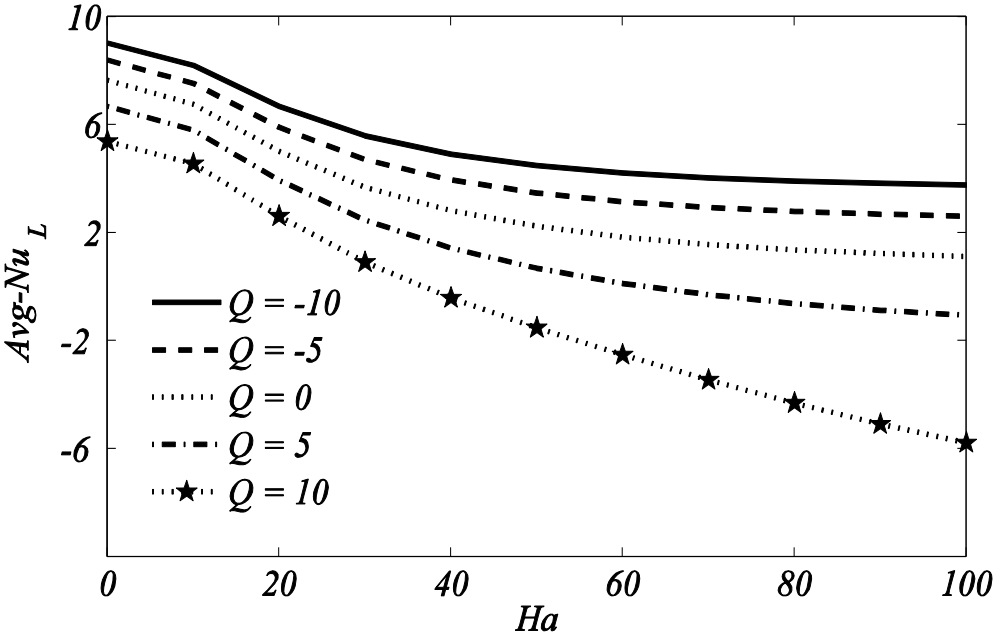

(a)

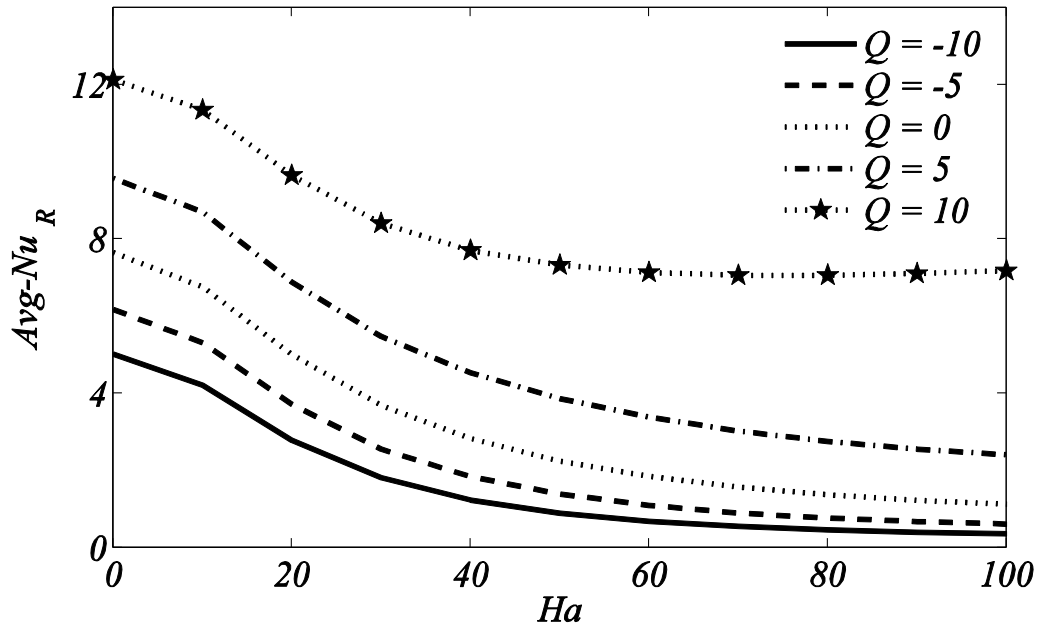

(b)

Figure 6.14: Overall heat transfer rate for different values of heat generation/absorption coefficient against Hartmann number along **(a)** Left heated wall **(b)** Right cold wall

Figure 6.14 shows the effects of Hartmann number and coefficient of heat generation/absorption on average temperature gradient along heated and cold moving walls. In general, magnetic field causes reduction in average temperature gradient. It is noted from the figure that for the case of heat absorption i.e. $Q < 0$, average Nusselt number is high and influence of magnetic field is small which represents a slight reduction in overall heat transfer rate. Opposite to this, for the case of heat generation i.e. $Q > 0$, both heat generation and magnetic field causes reduction in average temperature gradient which indicates that the large values of Hartmann number reduces the overall heat transfer rate significantly. It is also noticed that average Nusselt number is a decreasing function of Hartmann number along the left heated moving wall as shown in **Figure 6.14 (a)**. Contrary to this, overall heat transfer rate is an increasing function along the right cold moving wall as it is decreasing with increasing in the values of heat generation/absorption coefficient as shown in **Figure 6.14 (b)**. Furthermore, the average temperature gradient in the presence and absence of block for $\mathrm{Ri} = 0.1 - 100$ and $\mathrm{Re} = 50 - 200$ are presented in **Table 6.2**.

6.3 Conclusions

Our computation reveals that the heat transfer process can be controlled with the help of an adiabatic block. It is investigated that block present with different aspect ratios severely affects the Nusselt number which depends upon the motion of the moving lid, Re, Ri and Ha. Augmentation in heat transfer up to a certain size of adiabatic block is noticed and further increase in block size causes reduction in heat transfer. Heat flow from left heated moving lid to the right cold moving lid is happened through well-defined energy transport phenomenon represented by the isotherm lines. In general, streamlines recirculation cells are strongly suppressed due to presence of an adiabatic square blockage. Heat transfer in the presence of block shows an improve trends for the range of $\mathrm{Ri} = 0.1 - 100$ and $\mathrm{Re} = 50 - 200$ except for some exceptions. Convection heat transfer regime is found dominant in the enclosure for large Richardson number and small Hartmann and Reynolds numbers. Along both left and right moving walls, heat transfer rate is noted to reduce with augmentation in Hartmann number while enhancement in Nusselt number has been observed for increase in the values of Reynolds and Richardson numbers. Average temperature gradient reduces with increase in Hartmann, Richardson numbers and solid volume

fraction along both moving walls of a cavity. Augmentation in average temperature gradient is seen for the cases of heat generation/absorption coefficient with nano-scale ferromagnetic particles, Reynolds number and Hartmann number. It has also been observed that average temperature gradient along left hot wall reduces with augmentation in heat generation/absorption coefficient and Hartmann number. Opposite to this, enhancement in average temperature gradient is seen due to increase in heat generation/absorption coefficient along right cold wall. Prominent effects of moving lid are seen for small Richardson number and for large Reynolds and Hartmann number.

Chapter 7

Heat Transfer in Flow of Nanofluid through Entrapped Porous Triangular Cavities

In this chapter, Numerical simulations are carried out for free convective heat transfer through nanofluid saturated in entrapped triangular cavities enclosing porous medium has been discussed. Inclined walls of cavities are taken cold while horizontal walls are assumed to be heated uniformly. Numerical results obtained are shown in the form of flow patterns, isotherms, temperature gradient and average temperature gradient for wide range of physical parameters including solid volume fraction, porosity parameter, Darcy, Prandtl and Rayleigh numbers.

Most of results presented in this chapter are obtained using nanoparticles of copper because the combination of water-Cu nonofluid returns better heat transfer rate as compare to other combinations (Al_2O_3 and TiO_2). This investigation shows that the Darcy and Rayleigh numbers produce noticeable effects on flow patterns and temperature distribution in both cavities. Increasing Darcy and Rayleigh numbers increase the strength of streamline circulations. Similarly, overall heat transfer rate $\overline{\mathrm{Nu}}$ along the inclined walls of lower triangular enclosure is found increasing function of Rayleigh and Darcy numbers. Further it is seen that the local heat transfer rate Nu is maximum at the edges of horizontal boundaries of the cavities and it decreases while moving toward centre from edges.

7.1 Problem Formulation

Configuration considered in this investigation consists of laminar, steady state, two dimensional natural convective fluid flows within two entrapped triangular porous cavities as presented in **Figure 7.1**. The porous medium enclosed in two entrapped triangular cavities is full of nanofluid composed of a combination of H_2O and Cu spherical nanoparticles. It is supposed that the inclined and horizontal walls of the cavities are maintained at uniform temperatures T_c (cold) and T_h (hot) respectively. With the help of Boussinesq approximation (Gray and Giorgini (1976)), variation in the density of fluid with respect to temperature of fluid accounts for a body force term within governing Naver-Stokes equation. Furthermore, the temperature of fluid and solid sections in the porous region is equal and therefore Local Thermal Equilibrium

(LTE) is applicable in this study (Nield and Bejan (2006)). The fluid is considered to be Newtonian, viscous and incompressible. Furthermore, there is no slip between base fluid and particles of nanofluid. **Table 7.1** shows the thermo-physical properties of water and nanofluid.

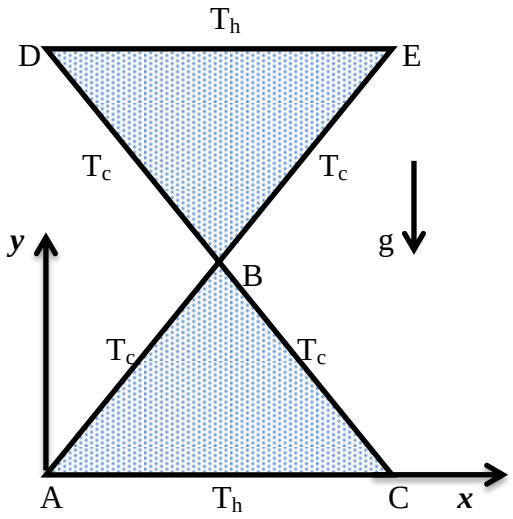

Figure 7.1: Geometrical description of the problem

Under the above suppositions and by using the laws of conservation of mass, momentum and energy, the governing equations of the current problem might be expressed in dimensional form as:

$$u_x + v_y = 0, \tag{7.1}$$

$$uu_x + vu_y = -\frac{\varepsilon}{\rho_{nf}} p_x + \frac{\mu_{nf}\varepsilon}{\rho_{nf}}\left(u_{xx} + u_{yy}\right) - \varepsilon^2 \frac{\mu_{nf} u}{\rho_{nf} K}, \tag{7.2}$$

$$uv_x + vv_y = -\frac{\varepsilon}{\rho_{nf}} p_y + \frac{\mu_{nf}\varepsilon}{\rho_{nf}}\left(v_{xx} + v_{yy}\right) + \frac{g(\rho\beta)_{nf}\varepsilon^2}{\rho_{nf}}(T - T_c) - \varepsilon^2 \frac{\mu_{nf} v}{\rho_{nf} K}, \tag{7.3}$$

$$uT_x + vT_y = \alpha_{nf}\left(T_{xx} + T_{yy}\right). \tag{7.4}$$

where u and v be the components of velocity along x and y axis respectively, p be the pressure, ε is the porosity of the medium and it is supposed to be constant ($\varepsilon = 0.4$). The following non-dimensional variables are introduced to non-dimensionalize equations governing the boundary value problem (7.1)–(7.4).

$$X = \frac{x}{L}, Y = \frac{y}{L}, U = \frac{uL}{\alpha_f}, V = \frac{vL}{\alpha_f}, P = \frac{pL^2}{\rho_{nf}{\alpha_f}^2}, \theta = \frac{T - T_c}{T_h - T_c}, \mathrm{Pr} = \frac{\nu_f}{\alpha_f}, \mathrm{Ra} = \frac{g\beta_f L^3 (T_h - T_c)\mathrm{Pr}}{{\nu_f}^2}, \mathrm{Da} = \frac{K}{L^2}. \tag{7.5}$$

We get the following non-dimensional form as:

$$UU_X + VU_Y = -\varepsilon P_X + \frac{\varepsilon\mu_{nf}}{\rho_{nf}\alpha_f}(U_{XX} + U_{YY}) - \varepsilon^2 \frac{\mu_{nf} U}{\rho_{nf}\alpha_f Da}, \tag{7.6}$$

$$UV_X + VV_Y = -\varepsilon P_Y + \frac{\varepsilon \mu_{nf}}{\rho_{nf}\alpha_f}(V_{XX} + V_{YY}) + \varepsilon^2 \frac{(\rho\beta)_{nf}}{\rho_{nf}\beta_f} RaPr\theta - \varepsilon^2 \frac{\mu_{nf} V}{\rho_{nf}\alpha_f Da}, \quad (7.7)$$

$$U\theta_X + V\theta_Y = \frac{\alpha_{nf}}{\alpha_f}(\theta_{XX} + \theta_{YY}). \quad (7.8)$$

The dimensionless boundary conditions in the form of velocities U, V and temperature θ are as follows:

$$U = V = 0, \theta = 0 \text{ at } Y = 0 \text{ and } 0 \le X \le 2,$$
$$U = V = 0, \theta = 0 \text{ at } Y = 0 \text{ and } 0 \le X \le 2,$$
$$U = 0 = V, \theta = 0 \text{ at } Y - X = 0 \text{ and } 0 \le X, Y \le 2,$$
$$U = V = 0, \theta = 0 \text{ at } Y + X = 2 \text{ and } 0 \le X, Y \le 2. \quad (7.9)$$

The dimensionless heat transfer coefficient Nu may be computed for heat transfer analysis in free convection flow in an enclosure. The local Nusselt number for lower and upper triangle can be expressed in the form of temperature field as

(a) Entrapped lower triangle

$$\mathrm{Nu_h} = \frac{k_{nf}}{k_f}\left(\sum_{i=1}^{6} \theta_i \frac{\partial \phi_i}{\partial Y}\right),$$
$$\mathrm{Nu_l} = \frac{k_{nf}}{k_f}\left(\sum_{i=1}^{6} \theta_i \left(\frac{1}{\sqrt{2}}\frac{\partial \phi_i}{\partial X} - \frac{1}{\sqrt{2}}\frac{\partial \phi_i}{\partial Y}\right)\right),$$
$$\mathrm{Nu_r} = \frac{k_{nf}}{k_f}\left(\sum_{i=1}^{6} \theta_i \left(\frac{-1}{\sqrt{2}}\frac{\partial \phi_i}{\partial X} - \frac{1}{\sqrt{2}}\frac{\partial \phi_i}{\partial Y}\right)\right). \quad (7.10)$$

(b) Entrapped upper triangle

$$\mathrm{Nu_h} = \frac{k_{nf}}{k_f}\left(-\sum_{i=1}^{6} \theta_i \frac{\partial \phi_i}{\partial Y}\right),$$
$$\mathrm{Nu_l} = \frac{k_{nf}}{k_f}\left(\sum_{i=1}^{6} \theta_i \left(\frac{1}{\sqrt{2}}\frac{\partial \phi_i}{\partial X} + \frac{1}{\sqrt{2}}\frac{\partial \phi_i}{\partial Y}\right)\right),$$
$$\mathrm{Nu_r} = \frac{k_{nf}}{k_f}\left(\sum_{i=1}^{6} \theta_i \left(\frac{-1}{\sqrt{2}}\frac{\partial \phi_i}{\partial X} + \frac{1}{\sqrt{2}}\frac{\partial \phi_i}{\partial Y}\right)\right). \quad (7.11)$$

The overall heat transfer rate $\overline{\mathrm{Nu}}$ is computed by integrating Eqs. (7.10) and (7.11) for the horizontal and inclined walls as follows

$$\overline{\mathrm{Nu_h}} = \frac{\int_0^2 \mathrm{Nu_h} dx}{X|_0^2} = \frac{1}{2}\int_0^2 \mathrm{Nu_h} dX \text{ and } \overline{\mathrm{Nu_l}} = \overline{\mathrm{Nu_r}} = \frac{1}{\sqrt{2}}\int_0^{\sqrt{2}} \mathrm{Nu_l} dS. \quad (7.12)$$

7.2 Results and Discussions

This section contains numerical results and their analysis for free convection through permeable entrapped triangular cavities filled with nanofluid when inclined and horizontal walls are maintained at uniform cold and hot temperatures respectively. The results are obtained and shown in terms of graphs for streamline contours, isotherm contours, heat transfer rate Nu and overall heat transfer rate $\overline{\mathrm{Nu}}$ for wide range of involved physical parameters like Darcy number ($10^{-5} \le \mathrm{Da} \le 10^{-3}$) and Rayleigh number ($10^4 \le \mathrm{Ra} \le 10^7$), while Prandtl number, porosity ε and Solid volume fraction ϕ are fixed at 6.2, 0.4 and 0.1 respectively.

Figure 7.2 (a-c) shows the graphs for streamline circulations and isotherms contours at $Pr = 6.2,\ Da = 10^{-4},\ \phi = 0.1,\ \varepsilon = 0.4$ and $10^5 \leq Ra \leq 10^7$. It is evident from this figure that there are significant effects of Raylegh number on flow patterns and heat transfer in the cavity. It is noted that near the centre of bottom wall of lower triangle, fluid rises up and after reaching to the top of lower triangle it comes down along inclined walls forming two symmetric rolls of clockwise and counter-clockwise circulations. Similarly two symmetric rolls of concentric circulations are seen in upper triangle also. Here positive values are used to show the heights of counterclockwise circulation contours and negative values are used to show the heights of clockwise circulation contours. Furthermore, the increase in Rayleigh number causes increase in the strength of both (clockwise and anticlockwise) circulations where the strength of circulation is increased more significantly in the lower triangle with increase in Rayleigh number as compare to that in upper triangle. The magnitude of maximum values of streamline contours $|\psi|_{max}$are $0.15, 1$ and 4 in upper triangle, $0.15, 3$ and 18 in lower triangle for Ra $= 10^5$, 10^6 and 10^7 respectively as shown in **Figure 7.2 (a-c)**. On the other hand, isotherm contours for small Rayleigh number appears to be smooth and monotonic showing conduction dominant regime as shown in **Figure 7.2 (a)**. When Rayleigh number is increased to 10^6 isotherms in lower triangle starts stretching upward to top and isotherms in upper triangle gets compressed slightly to top horizontal wall of upper triangle. Increasing Rayleigh number further to 10^7 results into deformed isotherms in lower triangle showing convection dominant effects and a plume like flow pattern is formed in lower triangle where stratification of isotherms is seen near top horizontal wall of upper triangle due to which there were less significant effects on streamline circulation in upper triangle as compared to the effects on streamline circulation in lower triangle.

Figure 7.3 shows the graphs for streamline circulation and isotherms contours for two values of Darcy number $Da = 10^{-3}$ and $Da = 10^{-5}$ respectively where Ra, Pr, porosity ε and solid volume fraction ϕ are fixed at 10^5, $6.2, 0.4$ and 0.1 respectively. It is noticed that increase in Darcy number results in stronger streamline circulations in both clockwise and anticlockwise directions and change in the values of Darcy number affects circulation contours in lower triangle more prominently. Magnitude of highest value of streamline $|\psi|_{max}$ is noted to be 0.015 and 0.7 in upper triangle and 0.015 & 1.5 in lower triangle for Da $= 10^{-3}$ and 10^{-5} respectively as shown in

Figure 7.3. On the other hand, an isotherm seems to be symmetric about vertical line passing through the centre of horizontal walls of upper and lower triangles. It is seen that for small value of Darcy number, isotherms are smooth and monotonically distributed in the enclosure and when Darcy number is decreased to 10^{-5} isotherms appears to be slightly pushed upward from near the centre of bottom wall in lower triangle while in upper triangle isotherms are compressed a little towards top wall in upper triangle.

Figure 7.4 contains the graphs for local Nusselt numbers along horizontal and inclined walls of enclosure against increasing values of distance for three different Rayleigh number $Ra = 10^5$, 10^6 and 10^7 respectively where Prandtl number Pr, Darcy number *Da*, Porosity ε and solid volume fraction ϕ are fixed at 6.2, 10^{-4}, 0.4 and 0.1. Since horizontal walls of both, upper and lower triangular cavities are considered at a constant temperature ($\theta = 1$) while inclined walls are taken cold therefore, there appears a jump type discontinuity at the vertices of horizontal walls of upper and lower triangular cavities. It is due to the fact that the two walls coinciding at these vertices are at different temperature. This discontinuity has been given special attention and is dealt according to (Ganzarolli and Milanez (1995)). Temperature at these corners nodes is taken to be the average temperature of horizontal and corresponding side walls. However, the adjacent nodes are taken at corresponding boundary wall temperature to avoid singularity. In left column of **Figure 7.4 (a)**, symmetric distribution of local Nusselt numbers has been observed along the top horizontal wall of upper triangle and value of Nusselt number *Nu* is noticed to be maximum at both edges of the horizontal wall due to the singularity appearing at these vertices. While moving toward centre from there corners, Nusselt number decreases and attains minimum value at the centre of horizontal wall. Furthermore increasing Rayleigh number increases local Nusselt numbers monotonically for a fixed value of Distance X near the central area ($0.3 \leq X \leq 1.7$) of horizontal wall and Nu is straight horizontal line in this region for a fixed value of $Ra = 10^7$, where Nusselt numbers for other Rayleigh numbers coincide for $X \leq 0.3$ and $1.7 \leq X$. Similarly for the lower triangle, local Nusselt number is observed maximum at edges of horizontal bottom wall due to the singularity there and it decreases while moving toward centre from the corner edges and attains its minimum value at the centre of horizontal wall,

while for a fixed value of distance X local Nusselt number Nu increases with increasing values of Rayleigh number as shown in right column of **Figure 7.4 (a)**.

Figure 7.4 (b) shows local Nusselt numbers along inclined side walls of triangular cavities. Since both inclined walls are taken cold (at the same temperature), therefore curves for both inclined wall are identical and thus we had shown Nusselt number along any side wall of each triangular enclosure. It is observed that local Nusselt number $\mathrm{Nu_s}$ increases slowly when distance is increased along inclined walls of upper triangular cavity upto 1.8 but $\mathrm{Nu_s}$ increases significantly sharp for $X > 1.8$. However, increasing Rayleigh number increases Nu_s non-significantly up to $X = 1.6$ and contrarily Nu_s decreases with increase in Ra afterwards as shown in left column of **Figure 7.4 (b)**. While in lower triangular cavity, Nu_s decreases sharply upto distance $= 0.1$ and afterwards it changes slowly with increase in distance for $Ra = 10^5$ and 10^6, but for $\mathrm{Ra} = 10^7$ Nu_s increases in the region $0.1 < X < 1.2$ and then it decreases afterwards.

Figure 7.5 depicts the graphs for average Nusselt numbers along horizontal and inclined walls of upper and lower triangular enclosures against Darcy number Da for various values of porosity ε by keeping other parameters fixed. It is seen from left column of **Figure 7.5 (a)** for the upper triangle that the overall heat transfer rate along horizontal wall $\overline{\mathrm{Nu_h}}$ first decreases slightly and then increases with increase in Darcy number Da where for a fixed value of Da, overall heat transfer rate $\overline{\mathrm{Nu_h}}$ decreases with increase in porosity ε along left half of upper horizontal wall while reverse behavior is seen along right half of this wall. Whereas for lower triangle, overall heat transfer rate $\overline{\mathrm{Nu_h}}$ along horizontal wall increases with increase in Darcy number Da and for a fixed value of Da, $\overline{\mathrm{Nu_h}}$ increase with increase in porosity parameter ε as shown in right column of **Figure 7.5 (a)**. In left column of **Figure 7.5 (b)**, similar behavior of overall heat transfer rate is seen along inclined side walls of lower triangular enclosure while along the side walls of upper cavity, overall heat transfer rate is observed to increase upto $\mathrm{Da} = 0.2 \times 10^{-3}$ and then decreases afterwards with increase in Darcy number where increasing values of porosity parameter ε increases the overall heat transfer rate $\overline{\mathrm{Nu_s}}$ against the entire range of Darcy parameter.

Figure 7.6 (a) shows the plots for average Nusselt numbers using combination of water to different nanoparticle including Cu, TiO_2 and Al_2O_3 with water as base fluid against increasing values of solid volume fraction ϕ. It has been evidently seen in the

figure that increasing solid volume fraction increases the heat transfer rate and comparatively highest heat transfer rate is returned with copper (Cu) nano particles. **Figure 7.6 (b)** shows the ratio effect of average Nusselt number with different nano particles to the average Nusselt number with Cu nano particles $\overline{\mathrm{Nu}}/\overline{\mathrm{Nu}_{\mathrm{C}}}$ against volume fraction parameter and it is found that the quantitative effects of solid volume fraction ϕ on the ratio $\overline{\mathrm{Nu}}/\overline{\mathrm{Nu}_{\mathrm{C}}}$ are maximum for the case of water-Cu nonofluid.

Figure 7.7 shows the effect of overall heat transfer rate along horizontal and inclined walls of upper and lower enclosures against Rayleigh number for various values of solid volume fraction ϕ. It has been noticed that along top horizontal wall of upper cavity and inclined walls of lower cavity, average Nusselt numbers increase with increase Rayleigh number. While for a fixed value of Ra, increase in average Nusselt numbers is observed with increase in the value of solid volume fraction. Similarly increase in Rayleigh number increases average Nusselt number along bottom wall of lower cavity and along inclined walls of upper cavity while for a fixed value of Ra, average Nusselt number is observed to increase with increase in the value of ϕ.

Table 7.1: Thermo-physical properties of pure water and nanoparticles

Physical Properties	water	TiO_2	Al_2O_3	Cu
$C_p(J/kgK)$	4179	686.2	765	385
$\rho(kg/m^3)$	997.1	4250	3970	8933
$K(W/mK)$	0.613	8.9538	40	400
$\beta(1/K)$	21×10^{-5}	0.9×10^{-5}	0.85×10^{-5}	1.67×10^{-5}
$\alpha(m^2/s)$	1.47×10^{-7}	30.7×10^{-7}	131.7×10^{-7}	57.45×10^{-7}

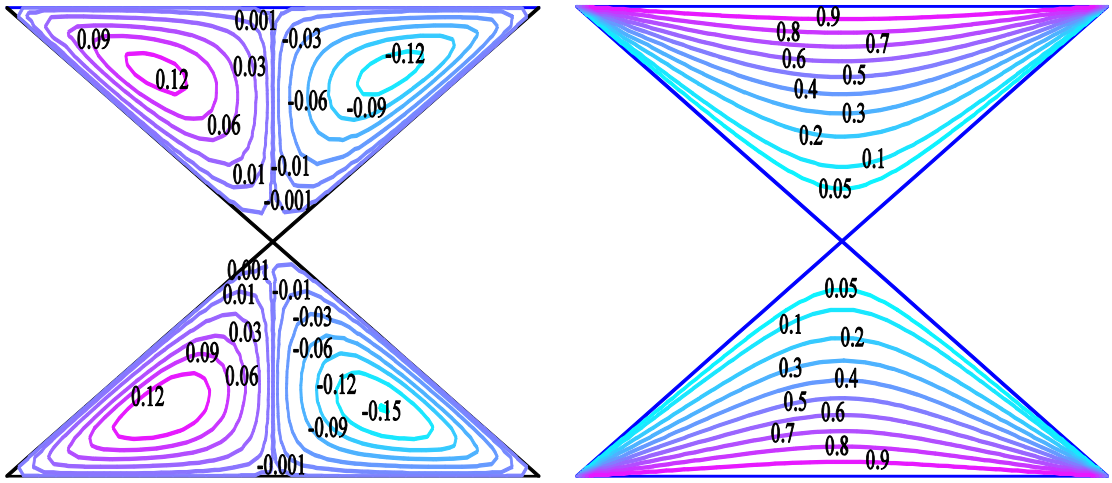

(a)

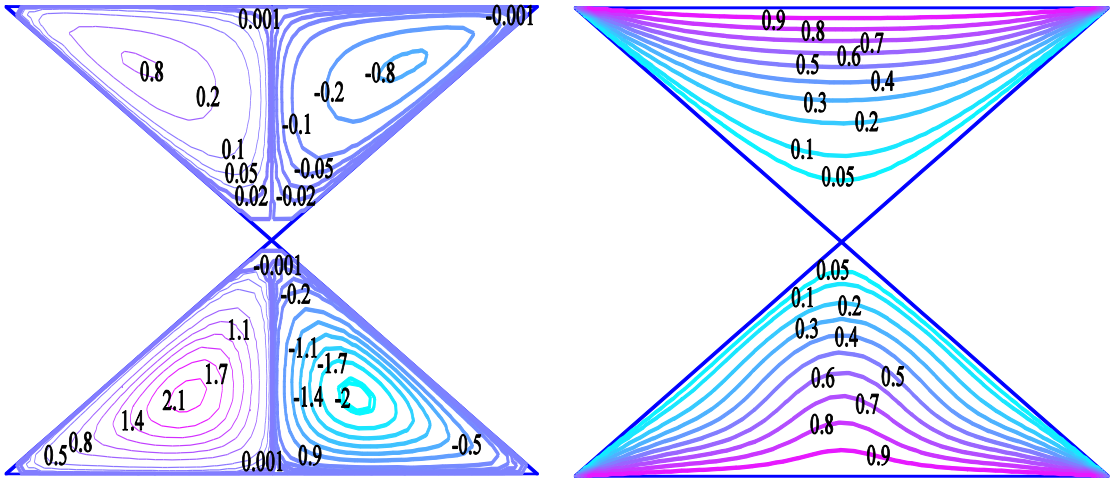

(b)

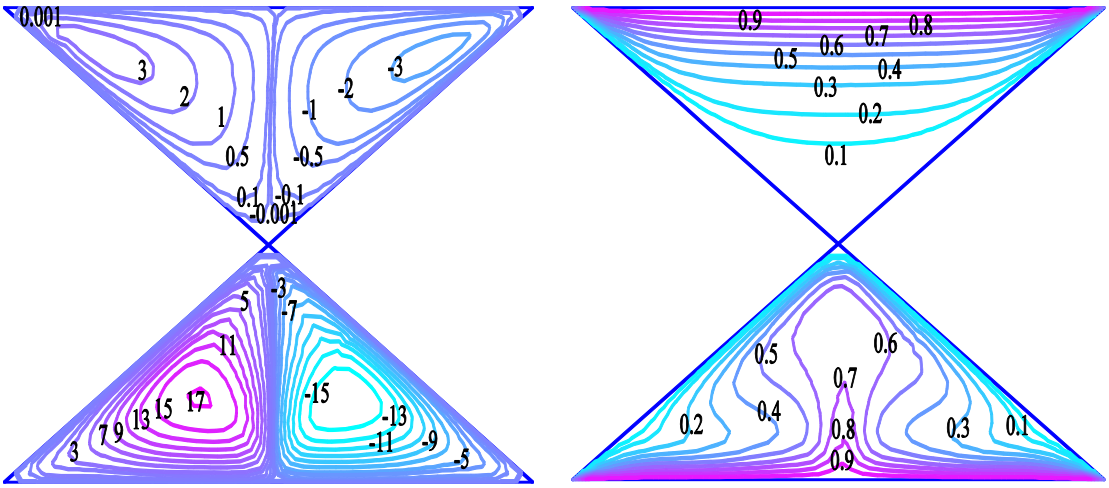

(c)

Figure 7.2: Streamline and isotherms contours for $\mathrm{Da} = 10^{-4}, \mathrm{Pr} = 6.2, \phi = 0.1,$ $\varepsilon = 0.4$ and **(a)** $\mathrm{Ra} = 10^{5}$, **(b)** $\mathrm{Ra} = 10^{6}$, **(c)** $\mathrm{Ra} = 10^{7}$

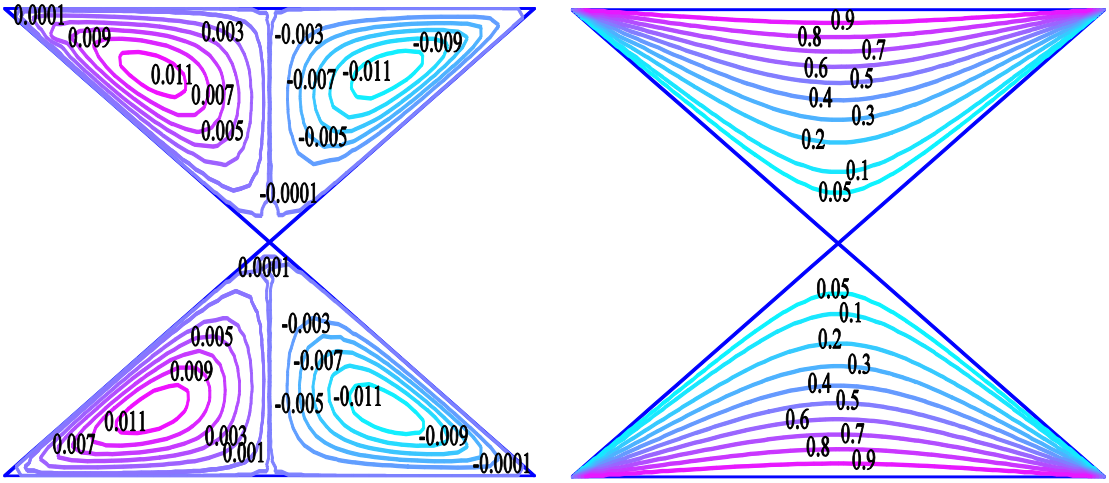

(a)

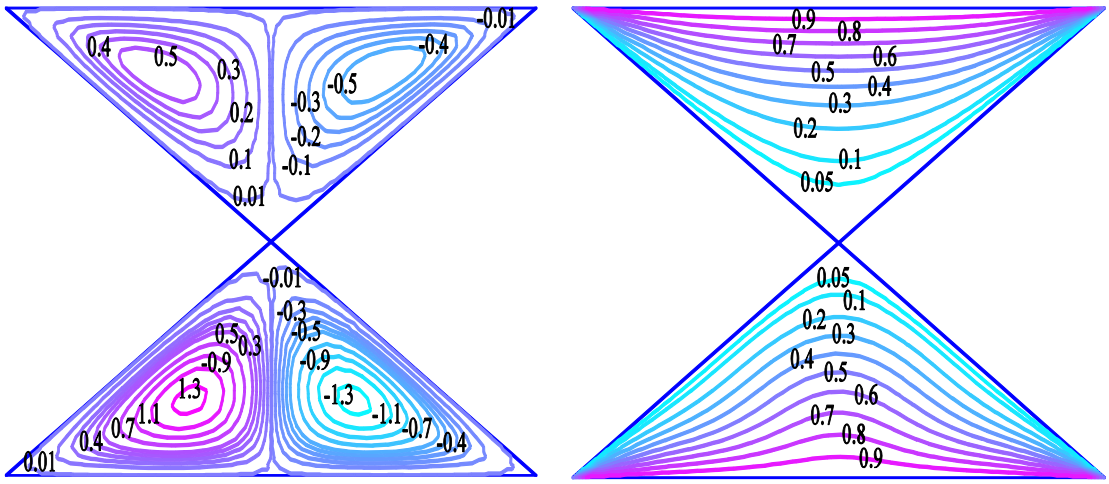

(b)

Figure 7.3: Isotherms and streamline contours for $\mathrm{Ra} = 10^5, \mathrm{Pr} = 6.2, \phi = 0.1,\ \varepsilon = 0.4$ and **(a)** $\mathrm{Da} = 10^{-3}$, **(b)** $\mathrm{Da} = 10^{-5}$

Upper Triangle Lower Triangle

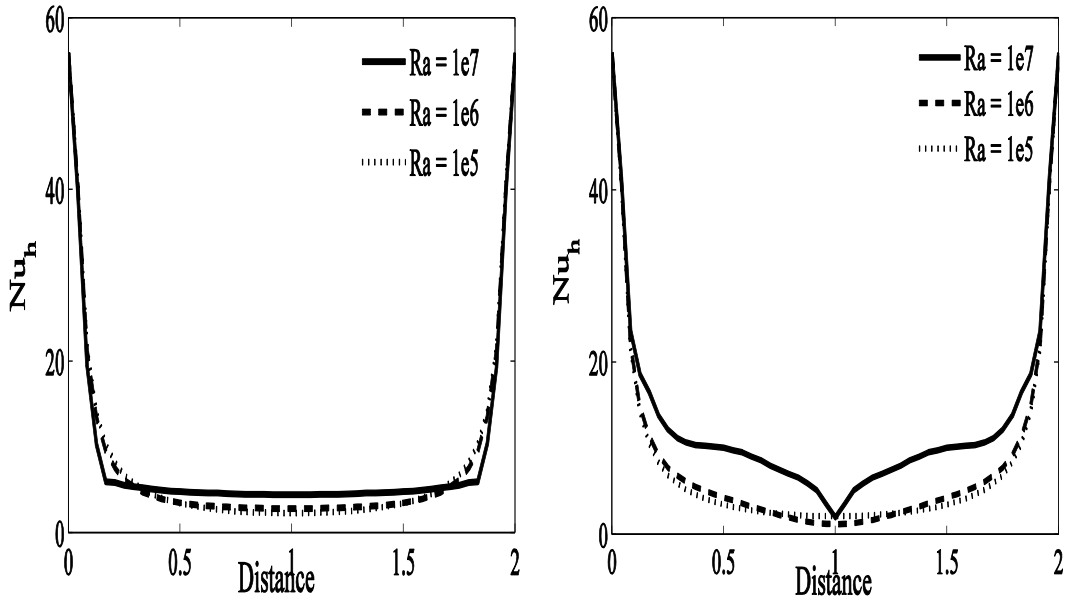

(a)

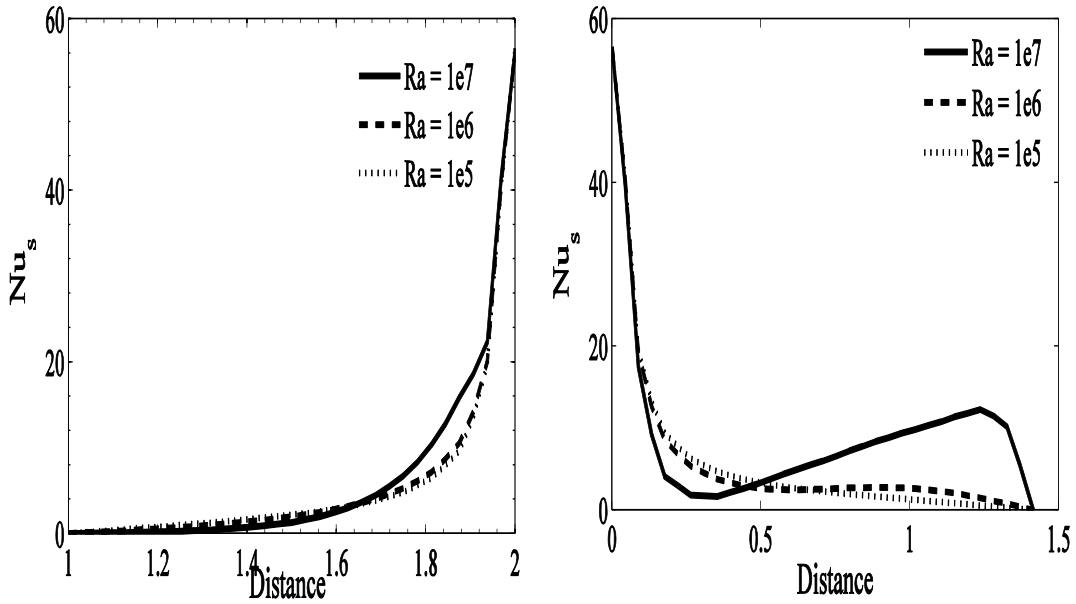

(b)

Figure 7.4: Nusselt number against distance for different values of Ra, where $\mathrm{Da} = 10^{-4}, \mathrm{Pr} = 6.2, \phi = 0.1,\ \varepsilon = 0.4$ and **(a)** Horizontal wall, **(b)** Inclined side walls

Upper Triangle Lower Triangle

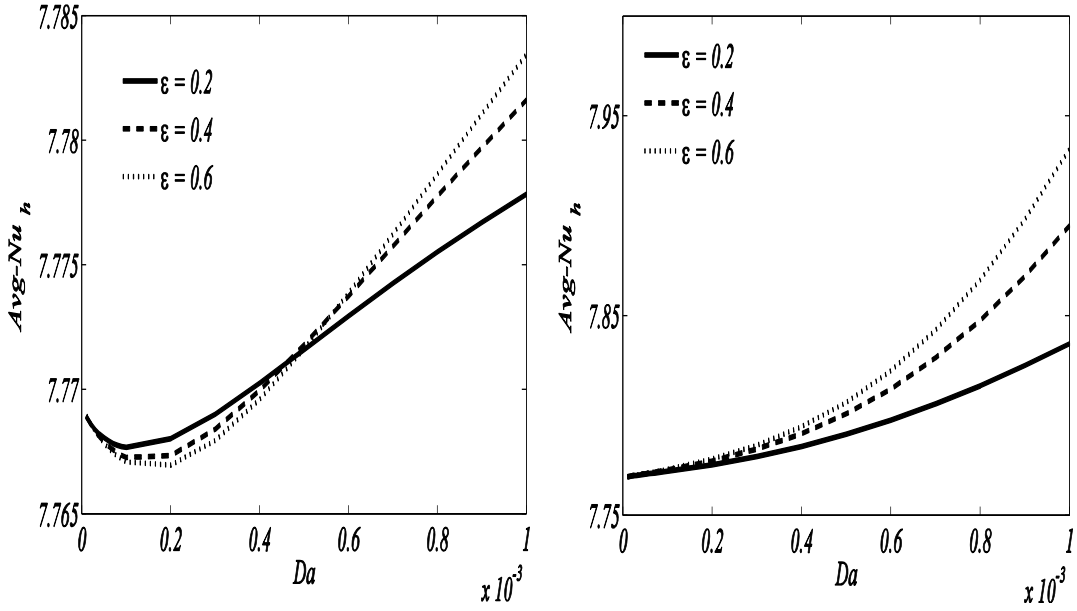

(a)

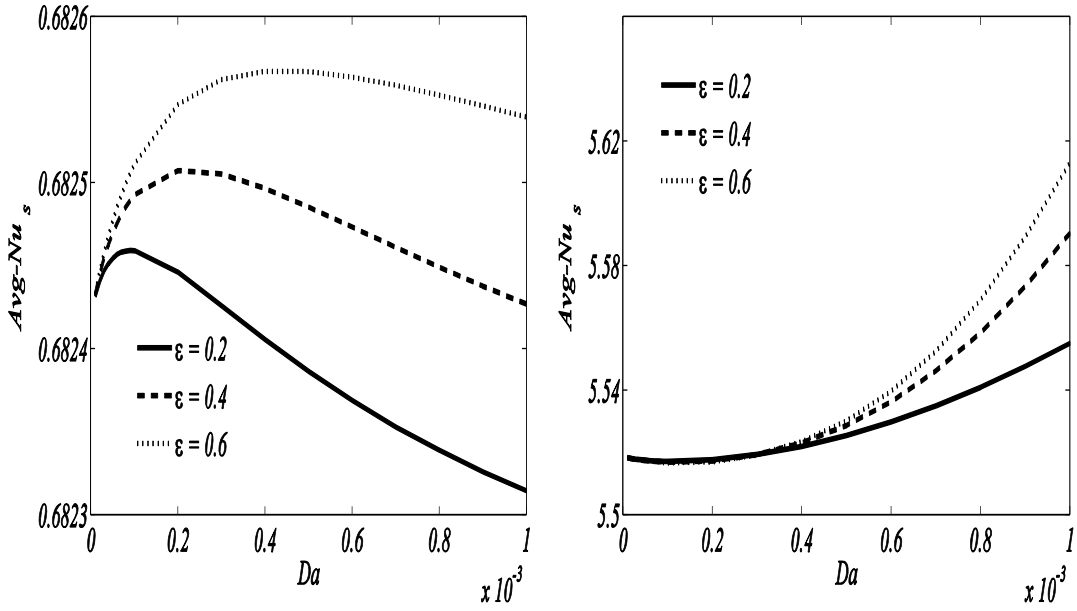

(b)

Figure 7.5: Overall heat transfer rate against Da for various values of porosity **(a)** Horizontal wall, **(b)** Inclined side walls where for $\mathrm{Ra} = 10^5, \mathrm{Pr} = 6.2, \phi = 0.1$

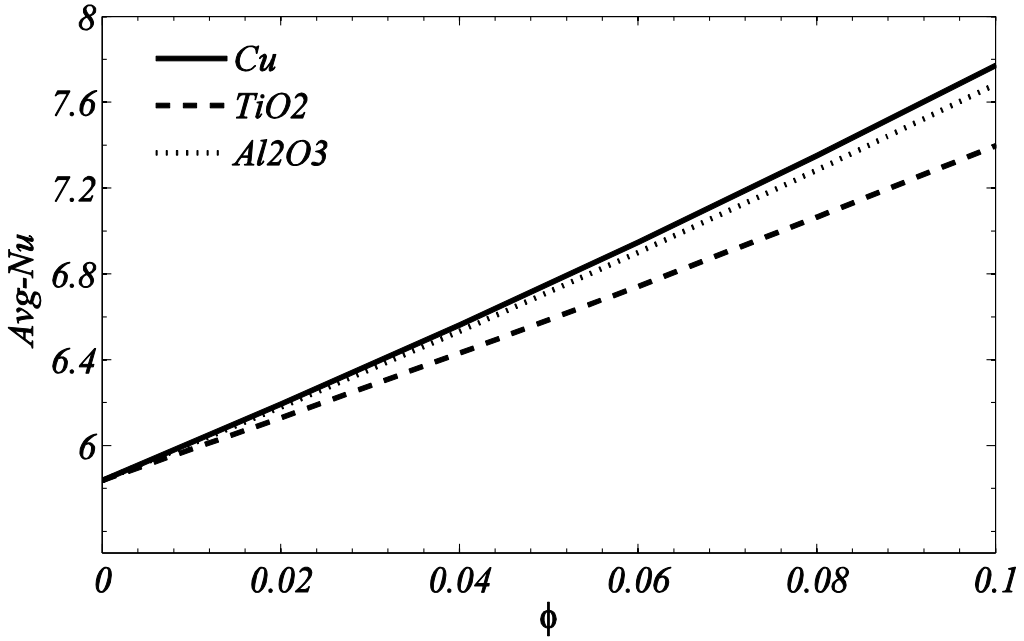

(a)

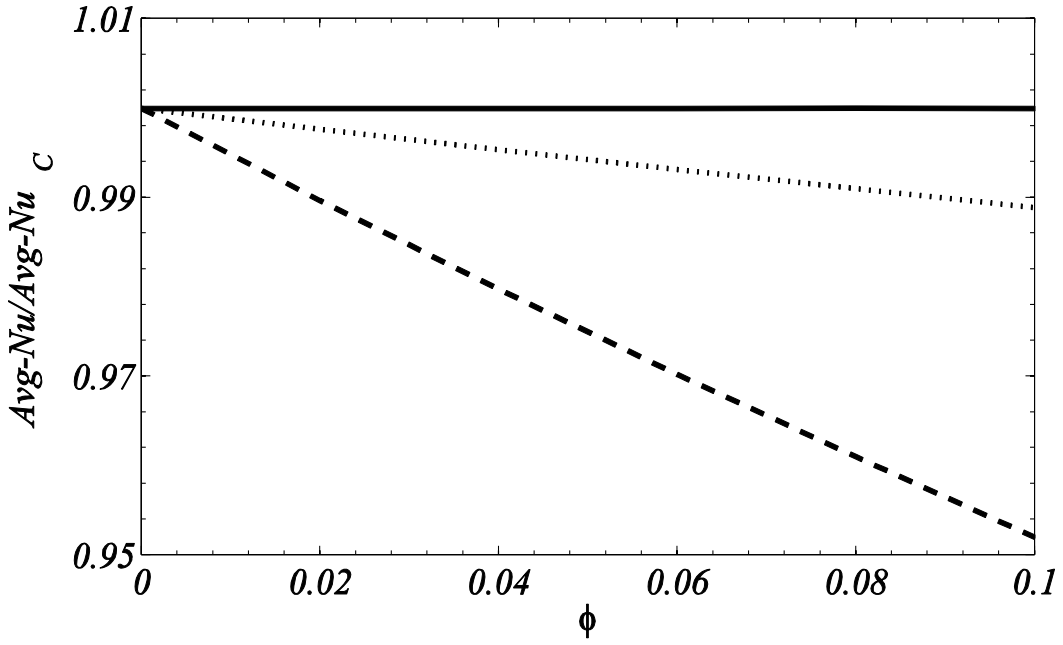

(b)

Figure 7.6: (a) Overall heat transfer rate ($\overline{\mathrm{Nu}}$) and **(b)** ratio of overall heat transfer rate to overall heat transfer rate with water-Cu nanoparticles ($\overline{\mathrm{Nu}}/\overline{\mathrm{Nu}}_c$) against solid volume fraction ϕ for different nanoparticles

Upper Triangle Lower Triangle

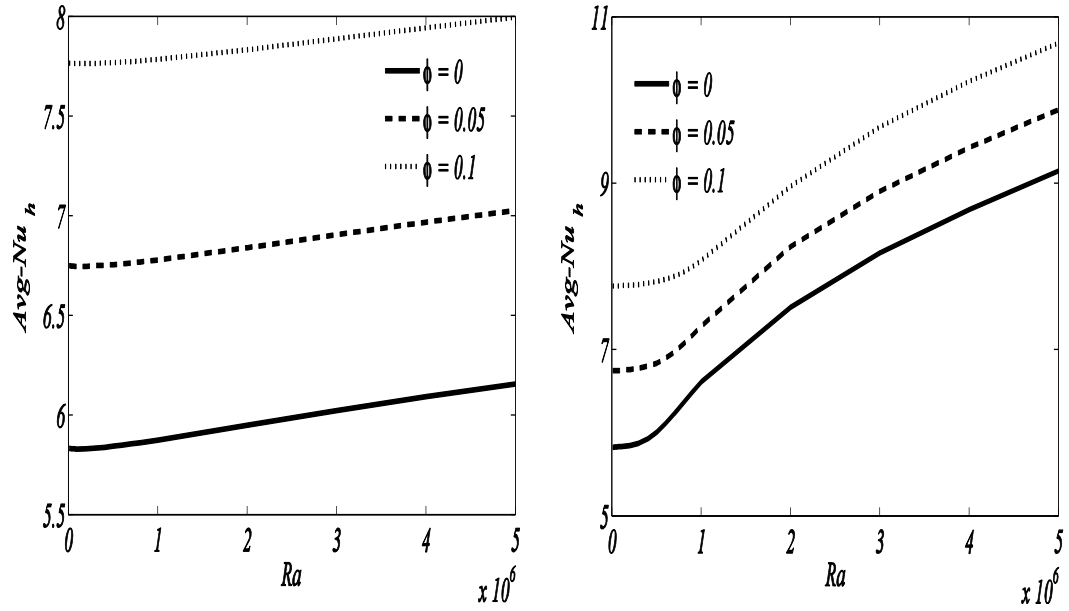

(a)

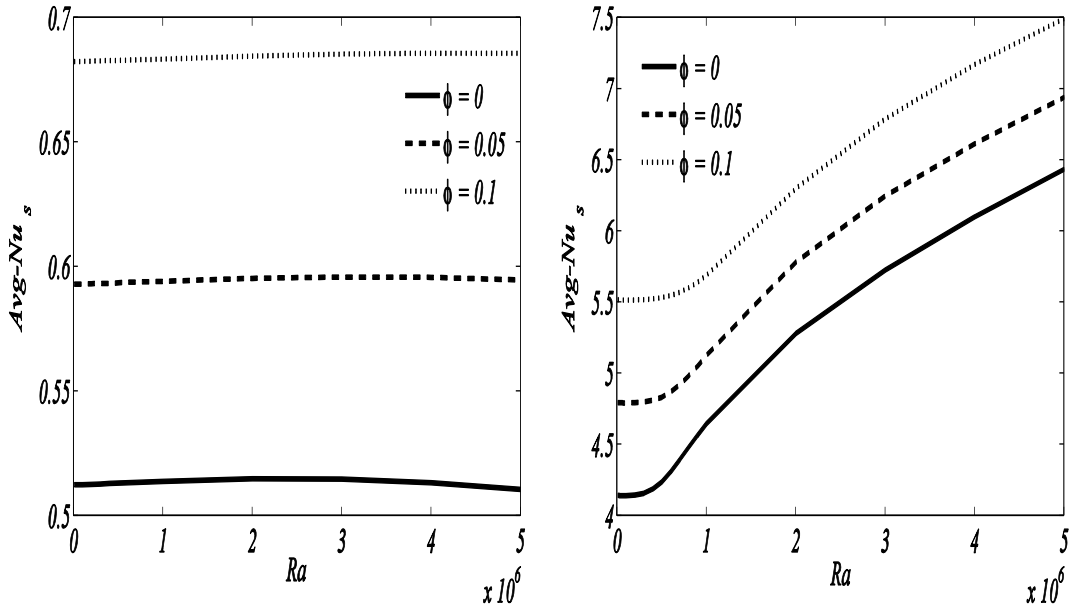

(b)

Figure 7.7: Overall heat transfer rate ($\overline{\mathrm{Nu}}$) against Ra for various values of solid volume frction **(a)** Horizontal wall, **(b)** Inclined side walls where for $\mathrm{Da} = 10^{-4}, \mathrm{Pr} = 6.2,\ \varepsilon = 0.4$

7.3 Conclusions

This chapter deals with natural convection through water-Cu nanofluid saturated in porous medium filled in entrapped triangular cavities, when inclined walls of cavities are considered cold and horizontal walls are taken at constant temperature. We first applied penalty method to the governing momentum equations to eliminate pressure terms and then reduced momentum equations along with energy equation are solved using Galerkin weighted residual technique of finite element method. As a result we get a system of nonlinear algebraic equations which is solved iteratively using Newton- Raphsom method. Numerical results are obtained for wide range physical parameters including Rayleigh number *Ra*, Darcy number *Da*, Prandtl number *Pr*, Porosity parameter ε and Solid volume fraction ϕ.

Obtained results revealed that increase in Rayleigh number increases the strength of clockwise and counter clockwise streamline circulation in both the upper and lower triangular cavities. It is noted that more significant effects of Rayleigh number are observed in lower cavity. For small Ra, conduction regime is dominant while for large value of Rayleigh number heat transfers through convection and isotherms are observed to form plume like flow. Similarly increasing Darcy number also increases the strength of streamline circulations and it increases comparatively more sharply in lower triangular enclosure then that of upper enclosure. Furthermore average Nusselt number is found to be an increasing function of Da along the inclined and horizontal walls of lower cavity. Where along horizontal wall of upper cavity, $\overline{\mathrm{Nu}_h}$ increases and along inclined walls $\overline{\mathrm{Nu}_s}$ decreases with increase in Da. Local Nusselt number decreases with increase in distance along inclined wall of lower cavity. On the other hand water-Cu nonofluid is observed to returns better heat transfer rate comparison to that of water-TiO_2 and water-Al_2O_3 nanofluids.

Chapter 8

Heat Transfer in Hydromagnetic Flow of Micropolar Nanofluid through Entrapped Triangular Cavities

The present chapter conveys numerical computation for mixed convection heat transfer through entrapped triangular enclosures saturated with a micropolar nanofluid. The horizontal upper and lower walls of the enclosures are moving with uniform velocity and these are subjected to uniform heat however inclined walls are kept cold. Equations describing the flow are first subjected to the penalty function and then resultant equations are simplified with the help of Galerkin variational method of finite element analysis. The pertinent flow parameters with their ranges under discussion are solid volume fraction $(0.0 < \phi < 0.1)$, Hartmann number $(0 < \mathrm{Ha} < 100)$, Richardson number $(0.1 < \mathrm{Ri} < 50)$, Reynolds number $(1 < \mathrm{Re} < 100)$, microrotation coefficient $(0 < K < 10)$ and heat source/sink coefficient $(-10 < Q < 10)$. The results of the present investigation show that the structures of heat flow are dependant significantly upon heat generation/absorption coefficient, solid volume fraction of nanoparticles, microrotation parameter, Reynolds, Hartmann and Richardson numbers. Effects of moving walls are more prominent for small values of Hartmann number, large values of microrotaion parameter and Richardson number. Average temperature gradient is remarkably high for small values of Hartmann number against bottom wall and large values of Hartmann number against top wall. Obtained solutions are illustrated through graphs of isotherms, local and average heat transfer rates.

8.1 Problem Formulation

The present configuration of flow problem consists of two entrapped triangular cavities filled with incompressible laminar micropolar nanofluid and magnetic field is applied in the direction parallel to horizontal axis. It is supposed that the top and bottom horizontal lids are moving with uniform velocity U_0. Furthermore, horizontal top and bottom lids of enclosure are subjected to heated uniformly where both inclined walls are taken cold as shown in **Figure 8.1**. The fluid within entrapped triangular cavities is micropolar water based nanofluid filled with solid spherical nanoparticles of Cu. Nanofluid is considered to be incompressible and the flow is

supposed to be steady, laminar and two dimensional. The particles of nanofluid are assumed to be in thermal equilibrium within base fluid. Furthermore, there is no slip between base fluid and particles of nanofluid. Fluid's density is considered to be function of temperature and the density variation causes a body force term in governing expressions after applying Boussinesq approximation (Gray and Giorgini (1976)). It is further supposed that magnetic field **B** with constant magnitude B_0 is applied along direction parallel to $x-$axis. In this study, viscous, radiation and joule heating effects are neglected with no Hall effects and induced magnetic field is also ignored being very small as compared to B_0 under low-R_m approximation (Davidson (2001)).

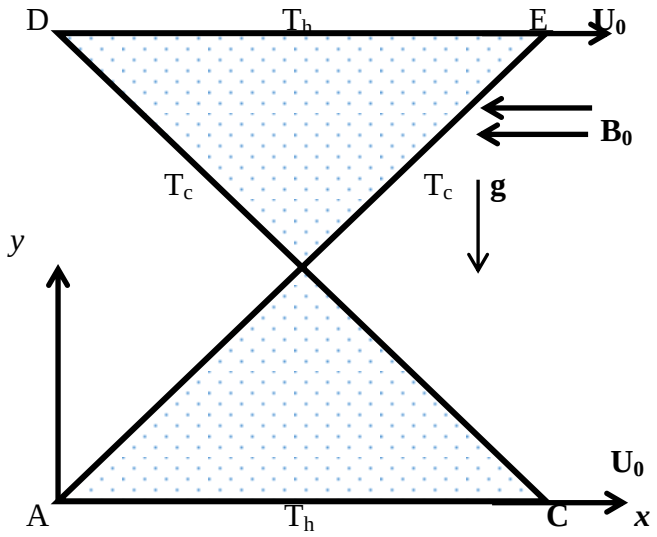

Figure 8.1: Graphical representation of the flow domain

Under these assumptions, governing conservation of mass, linear momentum, angular momentum and energy balance equations are modeled in dimensionless form as:

$$U_X + V_Y = 0, \tag{8.1}$$

$$UU_X + VU_Y = -P_X + \frac{1}{Re}\left(\frac{\rho}{\rho_{nf}}\right)\left(\frac{\mu_{nf}}{\mu} + K\right)(U_{XX} + U_{YY}) + \frac{K}{Re}\left(\frac{\rho}{\rho_{nf}}\right)N_Y, \tag{8.2}$$

$$UV_X + VV_Y = -P_Y + \frac{1}{Re}\left(\frac{\rho}{\rho_{nf}}\right)\left(\frac{\mu_{nf}}{\mu} + K\right)(V_{XX} + V_{YY}) + Ri\frac{(\rho\beta)_{nf}}{\rho_{nf}\beta_f}\theta + \frac{\rho_f\sigma_{nf}Ha^2V}{\rho_{nf}\sigma_f} - \frac{K}{Re}\left(\frac{\rho}{\rho_{nf}}\right)N_X, \tag{8.3}$$

$$UN_X + VN_Y = \frac{1}{Re}\left(\frac{\rho}{\rho_{nf}}\right)\left(\frac{\mu_{nf}}{\mu} + \frac{K}{2}\right)(N_{XX} + N_{YY}) - \frac{K}{Re}\left(\frac{\rho}{\rho_{nf}}\right)(2N + U_Y - V_X), \tag{8.4}$$

$$U\theta_X + V\theta_Y = \frac{1}{RePr}\left(\frac{\alpha_{nf}}{\alpha}\right)(\theta_{XX} + \theta_{YY}) + \frac{1}{RePr}\left(\frac{\alpha_{nf}}{\alpha}\right)q\theta. \tag{8.5}$$

The boundary conditions of the governing flow problem in dimensionless form are expressed as:

$U = 1, V = 0, \theta = 0,$ and $N = 0$ at $Y = 0$ and $0 \leq X \leq 2,$

$U = 1, V = 0, \theta = 0$ and $N = 0$ at $Y = 2$ and $0 \leq X \leq 2,$

$U = 0 = V, \theta = 0$ and $N = 0$ at $Y - X = 0$ and $0 \leq X, Y \leq 2,$

$U = V = 0, \theta = 0$ and $N = 0$ at $Y + X = 2$ and $0 \leq X, Y \leq 2.$ (8.6)

The dimensionless heat transfer coefficient Nu may be computed for heat transfer analysis in free convection flow in an enclosure. The Nusselt number can be expressed in the form of temperature field as

$$\mathrm{Nu} = -\frac{k_{nf}}{k_f}\left(\frac{\partial \theta}{\partial \eta}\right), \tag{8.7}$$

where η represents the direction normal to the plane.

The average Nusselt numer $\overline{\mathrm{Nu}}$ is computed by integrating Eq. (8.7) as follows

$$\overline{\mathrm{Nu}} = \frac{\int_0^2 \mathrm{Nu_h} dx}{X|_0^2} = \frac{1}{2}\int_0^2 \mathrm{Nu} dX. \tag{8.8}$$

8.2 Results and Discussions

This portion contains the results for mixed convective flow through two entrapped triangular enclosures containing micropolar nanofluid in the presence of horizontal external magnetic field when horizontal walls are provided with uniform heating while inclined walls are considered cold. The effects are represented in the shape of plots for isotherms, heat transfer rate and average Nusselt number for wide-ranging pertinent flow parameters including heat generation coefficient, Reynolds number, Richardson number, Hartmann number and microrotation coefficient etc.

Figure 8.2 includes the plots of isotherm contours for varying values of Hartmann number where $\mathrm{Ri}, \mathrm{Re}, K$ and Q are fixed at $0.01, 10, 1$ and 1 respectively. It is observed that a surge in the strength of Lorentz force causes attenuation in the gradient of temperature within the cavity which is consequence of low currents due to enhanced magnetic strength. The isotherm contours gets straighten near the horizontal sides of an enclosure indicating the development of thermal boundary layer for large values of Hartmann number. Furthermore, smooth and monotonic isotherms against large Ha are due to the dominance of conduction regime inside entrapped enclosures.

Figure 8.3 shows the local heat transfer rates for varying Hartmann number where $\mathrm{Ri}, \mathrm{Re}, K$ and Q are fixed at $0.01, 10, 1$ and 1 respectively. Figure reveals that along bottom wall of the enclosure, heat transfer rate increases with increase in the values of Hartmann number upto a certain value of distance and afterwards behavior of Nusselt number gets reversed. Similarly the magnitude of heat flow rate decreases due to

increase in strength of magnetic field upto certain distance along top wall and afterwards reversed behavior of heat transfer rate is observed along top wall of the enclosure. **Figure 8.4** illustrate the influence of variation in *K* on the heat flow structures in the entrapped cavities where values of *Ri, Re, Ha* and *Q* are fixed at *0.01, 10, 30* and *1* respectively. The isotherm contours are noted to be smooth and monotonic for smaller values of K showing the dominance of conduction regime within the enclosure while increase in the value of *K* escalates influence of convection inside the cavity. The straightened isotherm contours near the upper and lower walls of the enclosure indicate the development of thermal boundary layer near these boundaries. **Figure 8.5** depicts the effects of variation of K upon the heat flow rates along lower and upper horizontal walls of entrapped cavities. These graphs reveals that heat transfer rate is maximum at the edges of the lower horizontal wall and it attenuates non-symmetrically while moving inward from corners of the boundary and this non-symmetric reduction is due to motion of wall whereas reverse behavior of heat transfer rate is seen along the upper horizontal wall of the enclosure. No significant effects of change in the value of *K* on the rate of heat transfer along both horizontal boundaries of cavity are observed. **Figure 8.6** illustrate the effects of variation in Richardson number on the heat flow structures where values of *Re, Ha, K* and *Q* are fixed at *10, 30, 1* and *1* respectively. Increase in the value or Richardson number increases the heights of isotherm contours which indicate that convection heat transfer regime gets dominant for that case. Whereas this nonlinear behavior of isotherms near the horizontal walls of entrapped cavities corresponds to the motion of these walls. **Figure 8.7** examines the nature of heat flow rates against horizontal boundaries of cavity for different values of Richardson number where the other pertinent parameters are kept fixed. It is noticed that heat flow rate is maximum at the edges of the lower wall and it reduces non-symmetrically while moving inward from corners of the wall and this non-symmetric reduction is due to motion of wall whereas reverse behavior of heat flow rate is observed along the upper wall of the cavity. The straightened isotherm contours near the upper and lower walls of an enclosure indicate the development of thermal boundary layer near these boundaries. **Figure 8.8** corresponds to the effects of average heat flow rates along bottom and top boundaries for various values of solid volume fraction of solid particles and strength of magnetic field where values of $Q, K,$ Re and Ri are fixed at $1,1,10$ and 0.01 respectively. It has been noticed that increase in the values of solid volume fraction increases the overall

heat transfer rate along lower wall and increasing strength of magnetic field reduces average Nusselt number along lower wall of the enclosure whereas along upper wall of enclosure reverse behavior of overall heat flow rate is noted for both Hartmann number and solid volume fraction. **Figure 8.9** expresses the influence of varying solid volume fraction and Q on overall heat transfer rate along bottom and top boundaries where values of $\mathrm{Ri}, \mathrm{Re}, K$ and Ha are fixed at $0.01, 10, 1$ and 30 respectively. It has been seen through graphs that with increase in heat generation coefficient, the overall heat flow rate decreases along lower wall and increase in the concentration of solid particles causes increase in overall heat flow rate along lower wall, whereas along upper boundary, opposite behavior of overall heat transfer rate is observed for both heat generation coefficient and solid volume fraction. **Figure 8.10** shows the behaviour of overall heat transfer rate along horizontal boundaries for varying Hartmann number and heat generation coefficient where values of K, Re and Ri are fixed at $1, 10$ and 0.01 respectively. It is noticed that overall heat flow rates attenuates with augmentation in both Q and Ha along the bottom wall of container whereas along top wall of the enclosure increase in heat generation coefficient and strength of magnetic field results in escalation of average Nusselt number. **Figure 8.11** contains the graphs for average Nusselt number against variation in strength of magnetic field for different values of Reynolds number where Richardson number, coefficient of heat generation and microrotation coefficient are fixed at $0.01, 1$ and 1 respectively. Along bottom wall, average heat flow rate is noted to decrease with increase in Hartmann number and rate of this decrease is significant for large Reynolds number whereas augmentation in Reynolds number escalates over all heat flow rate for any fixed value of Ha. Along top wall, opposite behaviorin average heat transfer rate is noted against both Reynolds and Hartmann numbers.

$\mathrm{Ha} = 0$ $\mathrm{Ha} = 30$

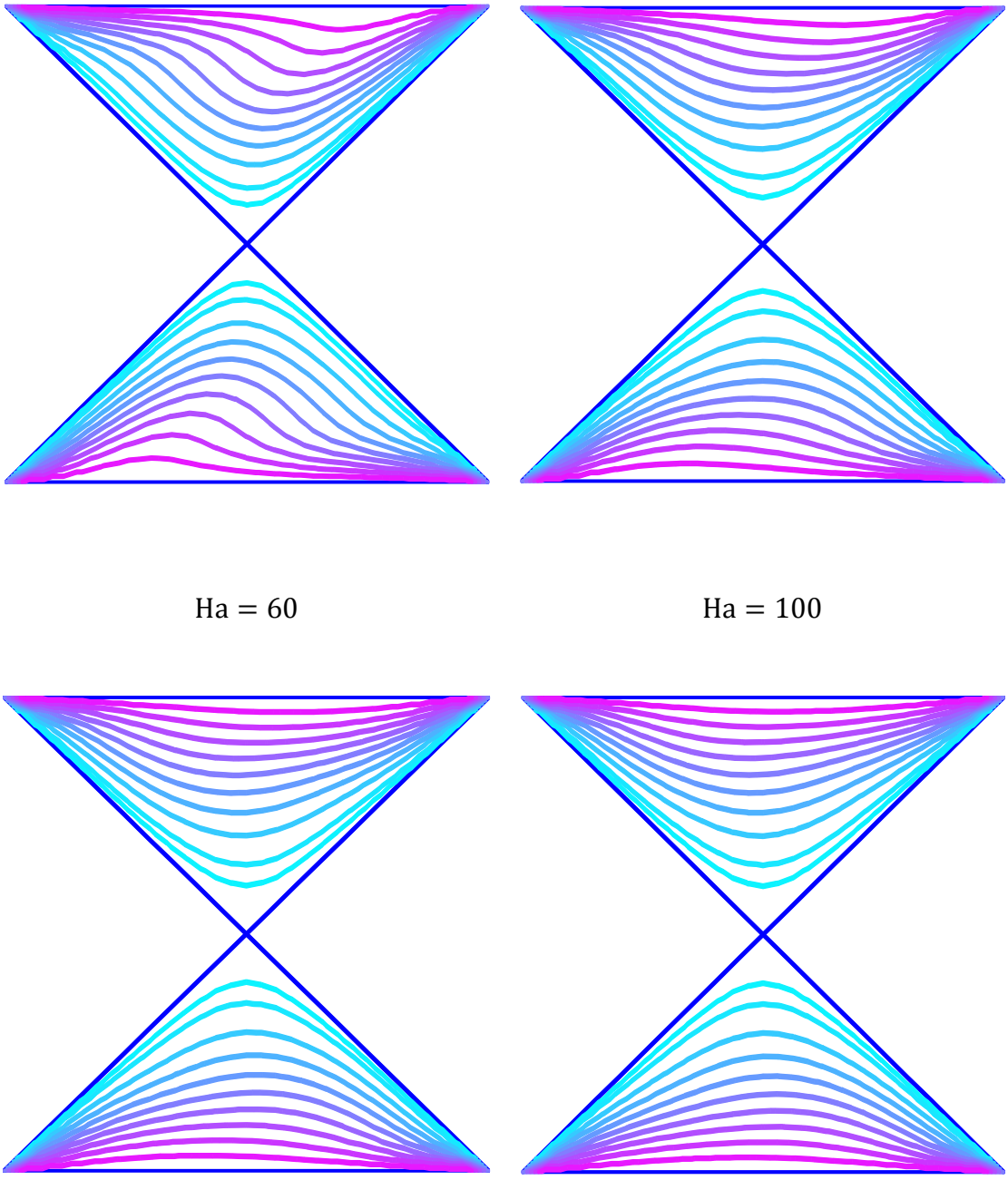

Figure 8.2: Isotherm contours for varying Ha where $\mathrm{Ri} = 0.01, \mathrm{Re} = 10, K = 1$ and $Q = 1$

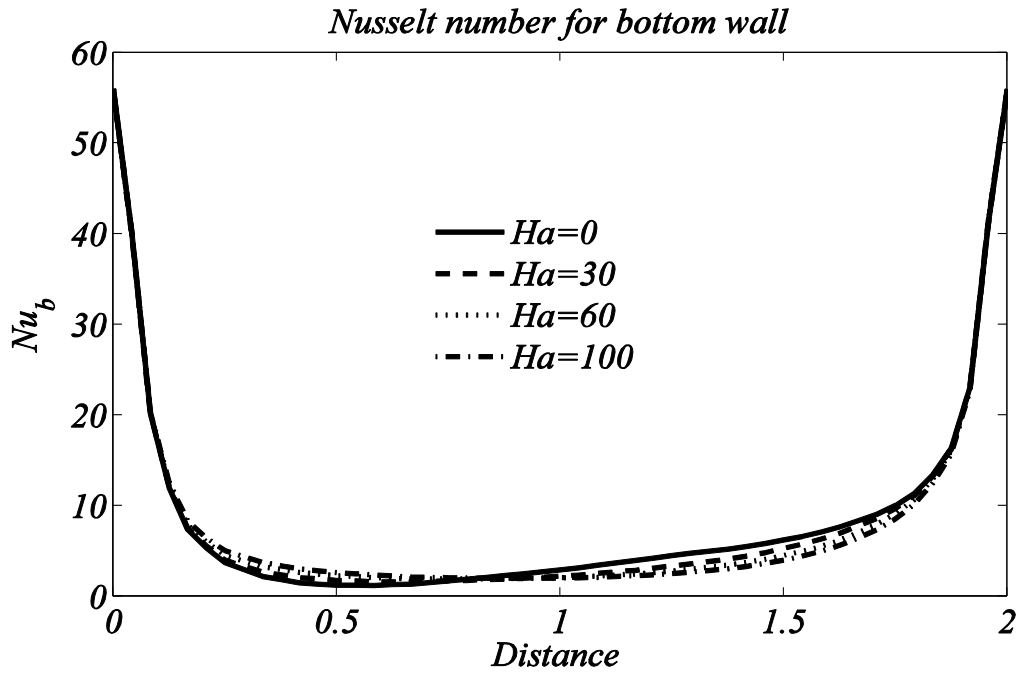

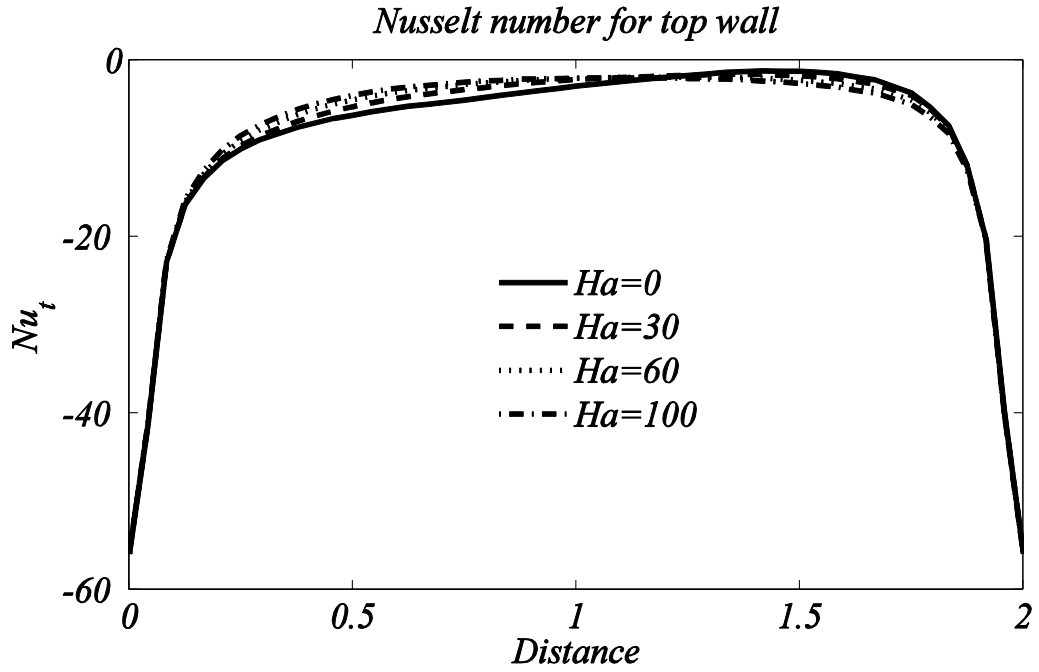

Figure 8.3: Local Nusselt number for varying Ha where $\mathrm{Ri} = 0.01, \mathrm{Re} = 10, K = 1$ and $Q = 1$

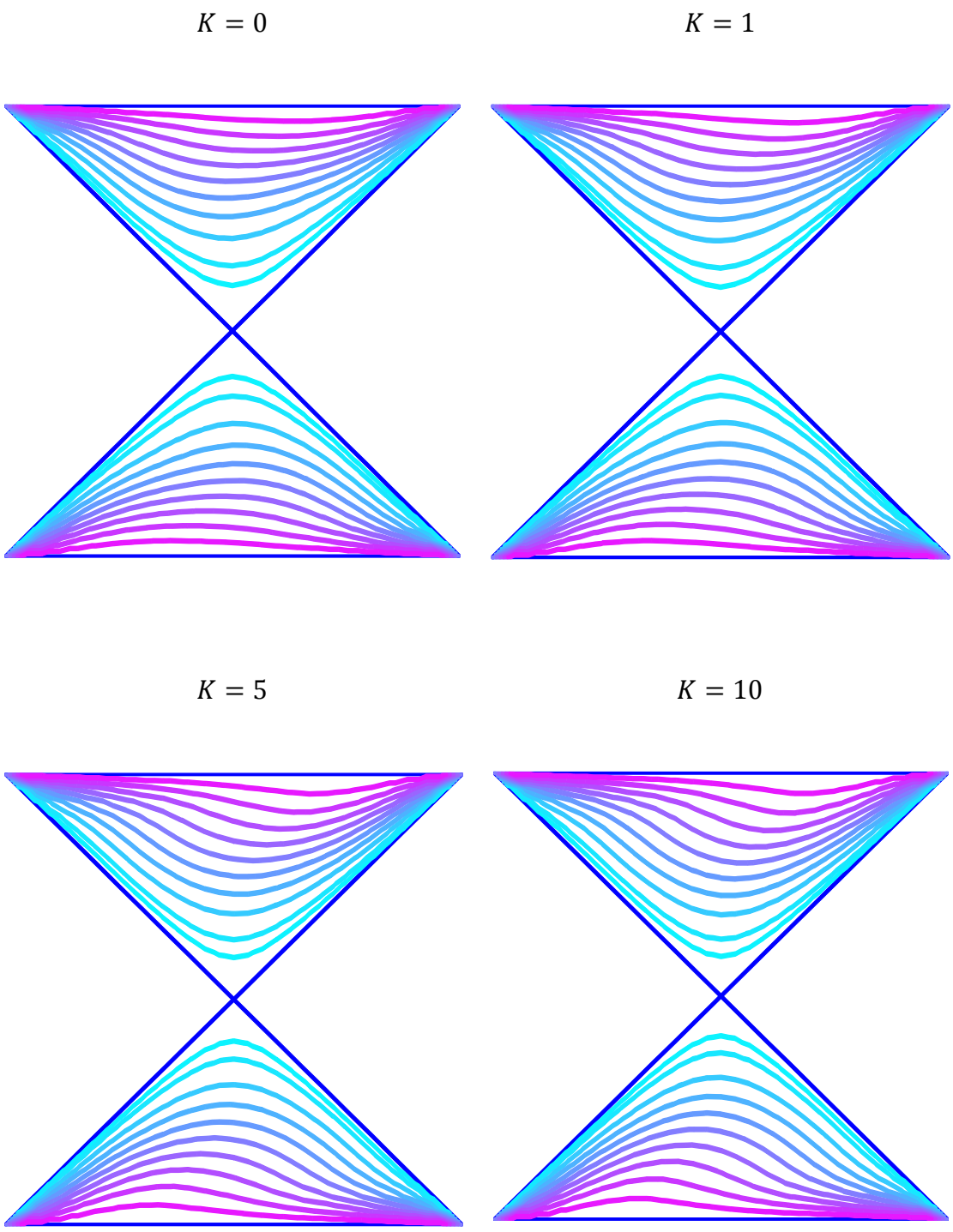

Figure 8.4: Isotherm contours for varying K where $\mathrm{Ri} = 0.01, \mathrm{Re} = 10, \mathrm{Ha} = 30$ and $Q = 1$

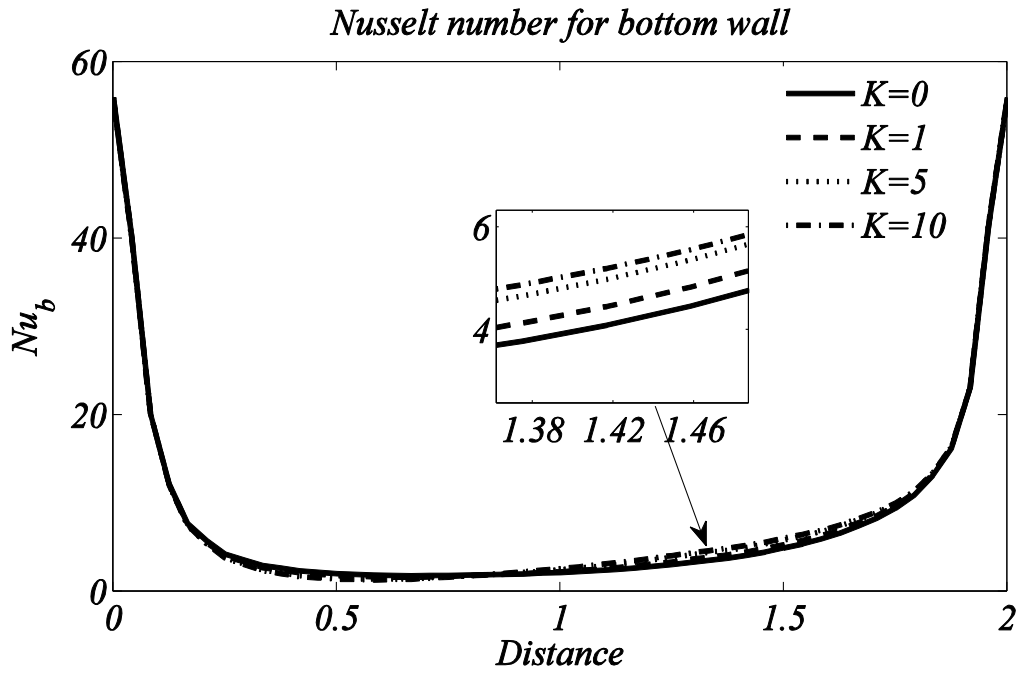

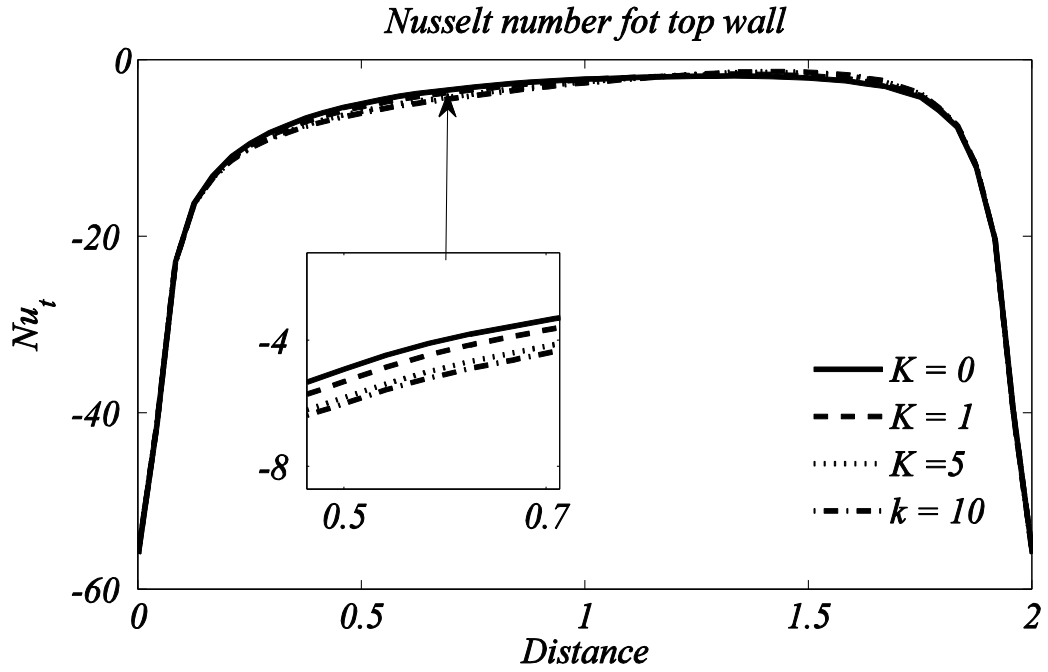

Figure 8.5: Local Nusselt number for varying K where $\mathrm{Ri} = 0.01, \mathrm{Re} = 10, \mathrm{Ha} = 30$ and $Q = 1$

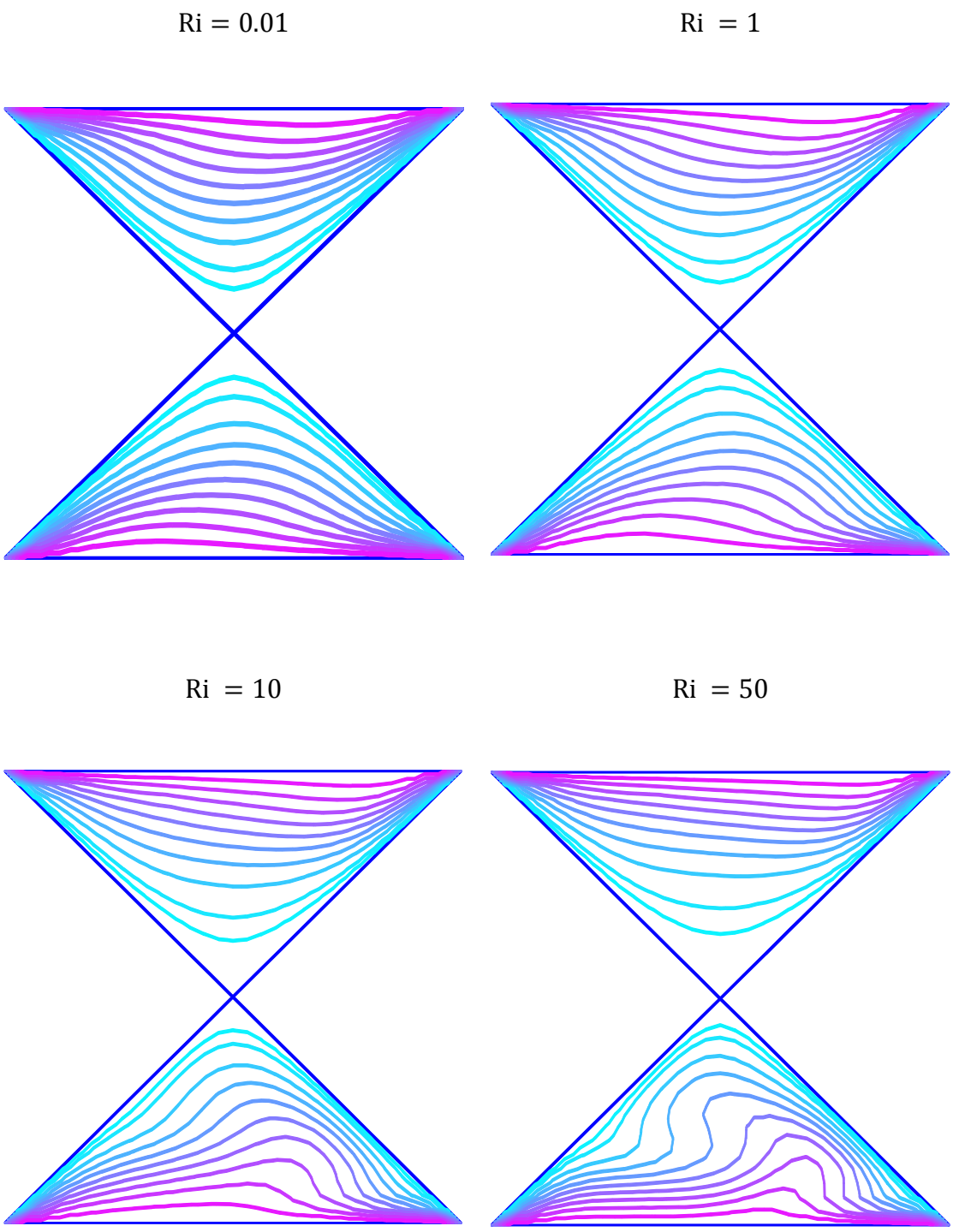

Figure 8.6: Isotherm contours for varying Ri where $K = 1.0, \mathrm{Re} = 10, \mathrm{Ha} = 30$ and $Q = 1$

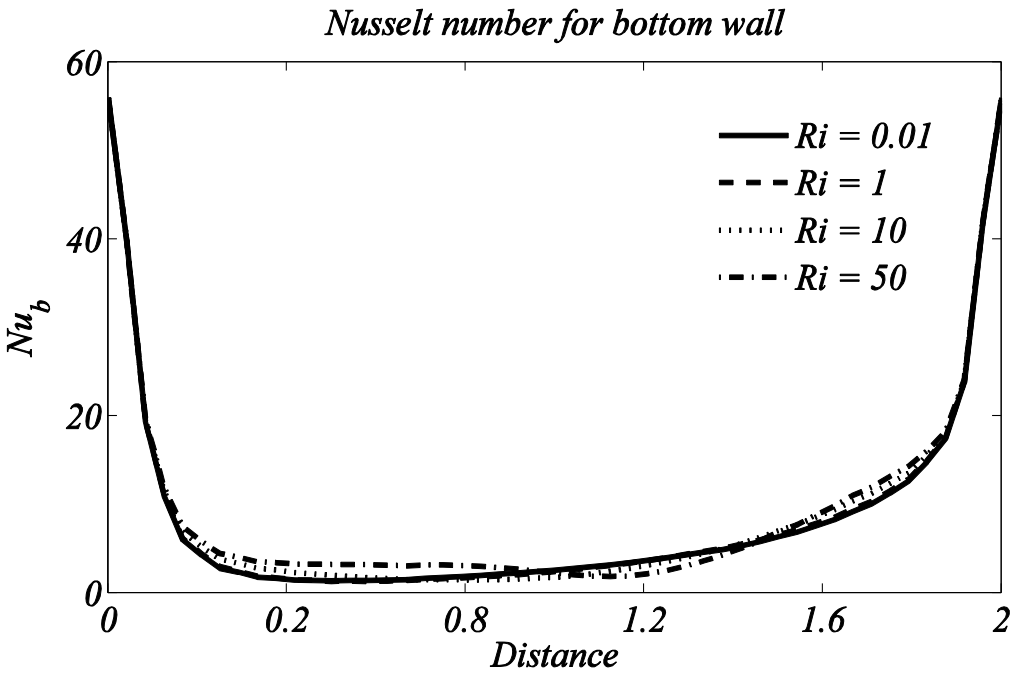

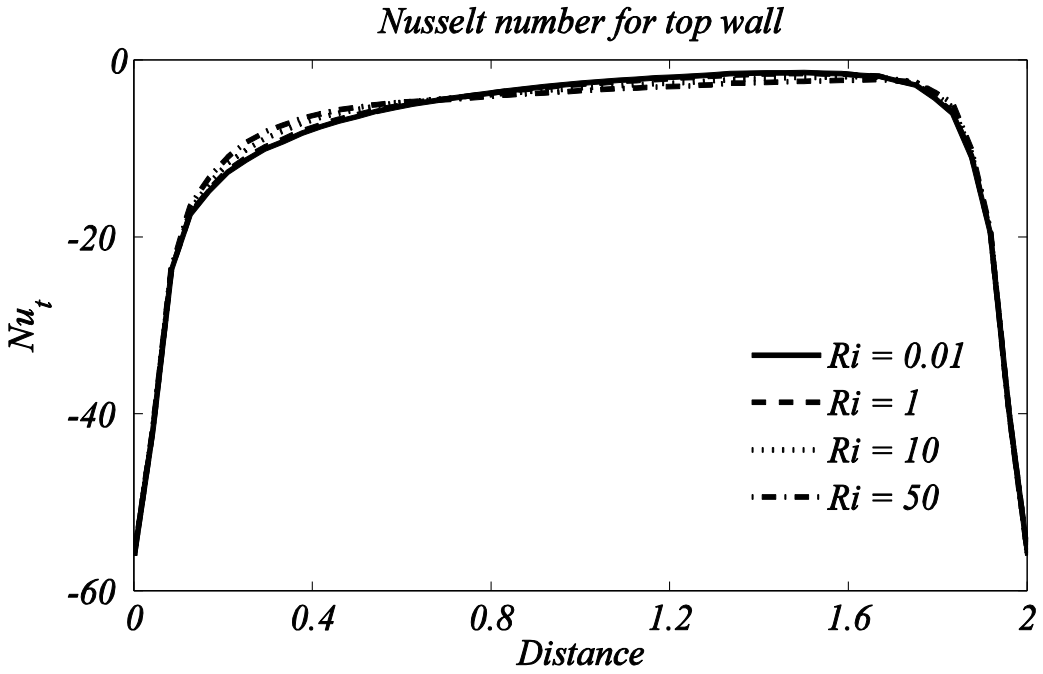

Figure 8.7: Local Nusselt number for varying Ri where $K = 1, \mathrm{Re} = 10, \mathrm{Ha} = 30$ and $Q = 1$

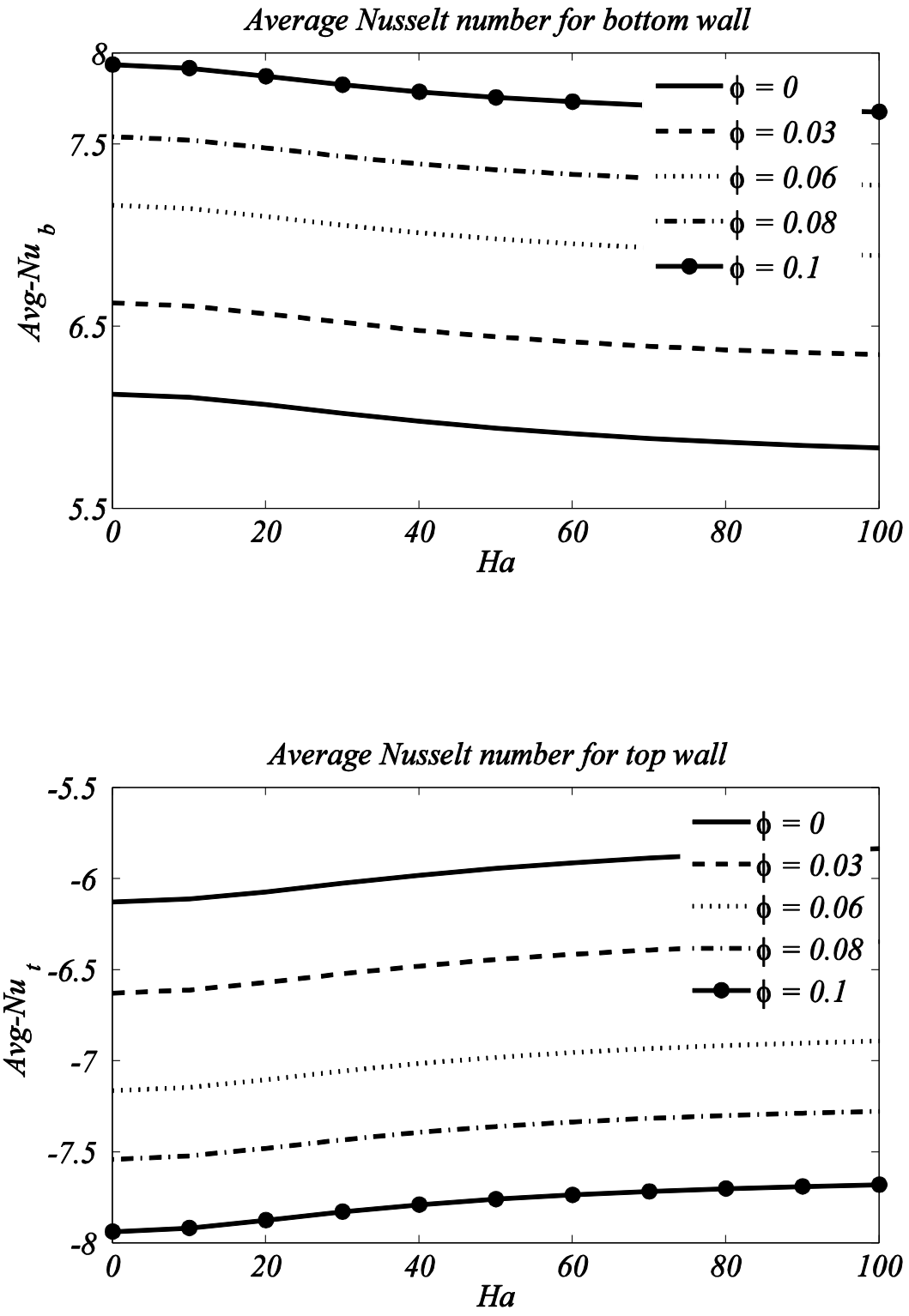

Figure 8.8: Average Nusselt number for varying solid volume fraction and Ha where $\mathrm{Ri} = 0.01, K = 1, \mathrm{Re} = 10$ and $Q = 1$

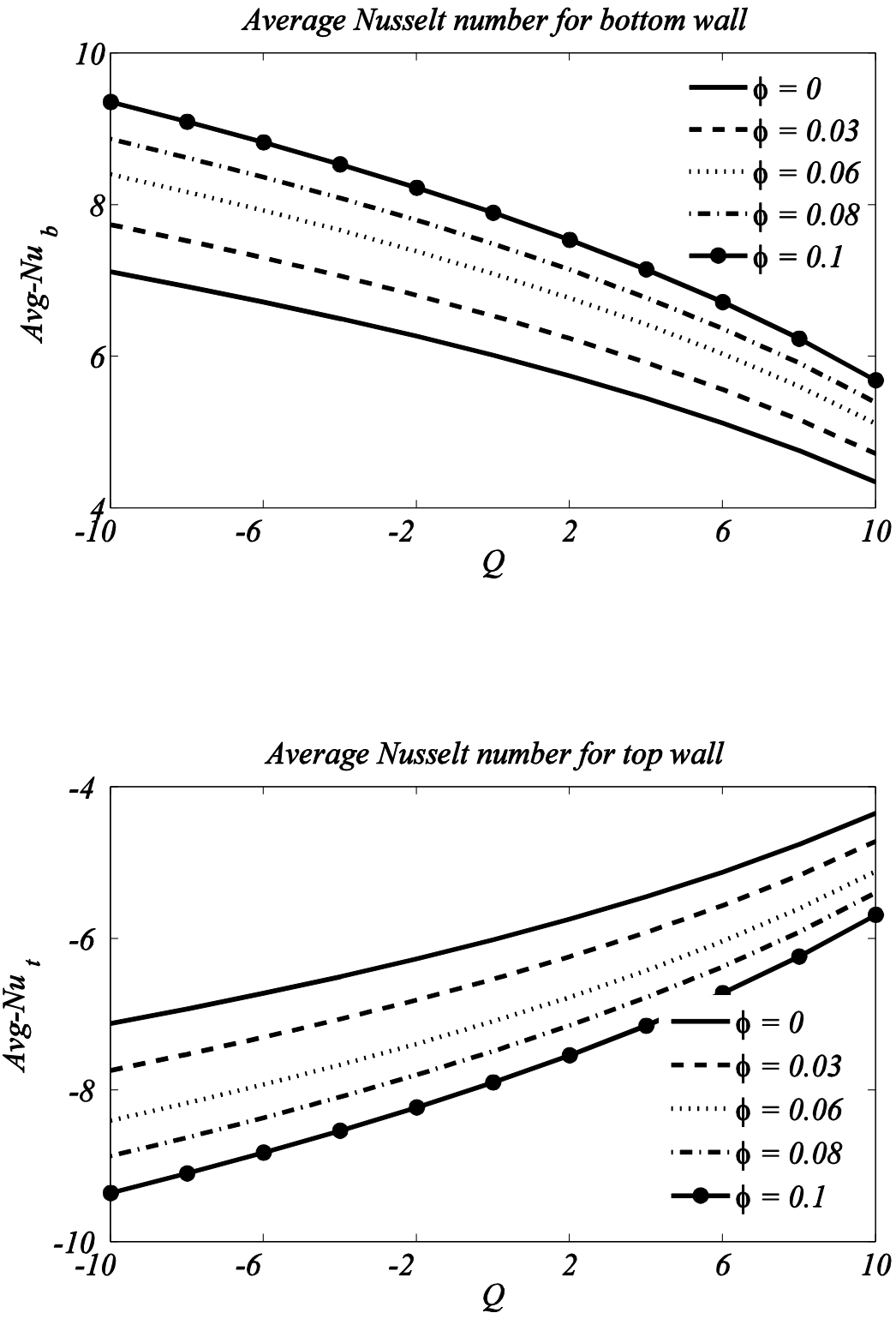

Figure 8.9: Average Nusselt for varying solid volume fraction and Q where Ri $=$ $0.01, K = 1,$ Re $= 10$ and Ha $= 30$

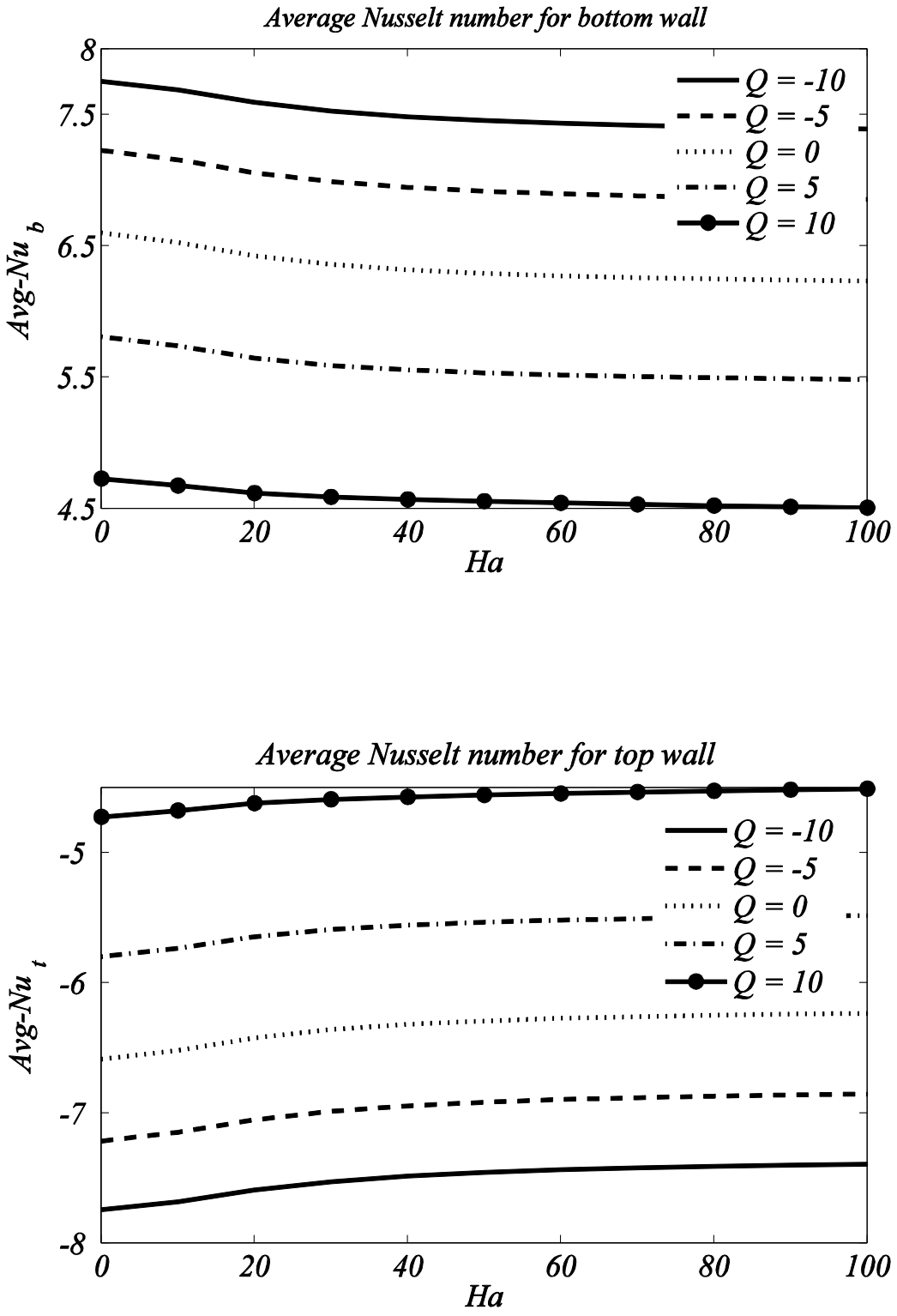

Figure 8.10: Average Nusselt number for varying Q and Ha where Ri $= 0.01, K =$ 1 and Re $= 10$

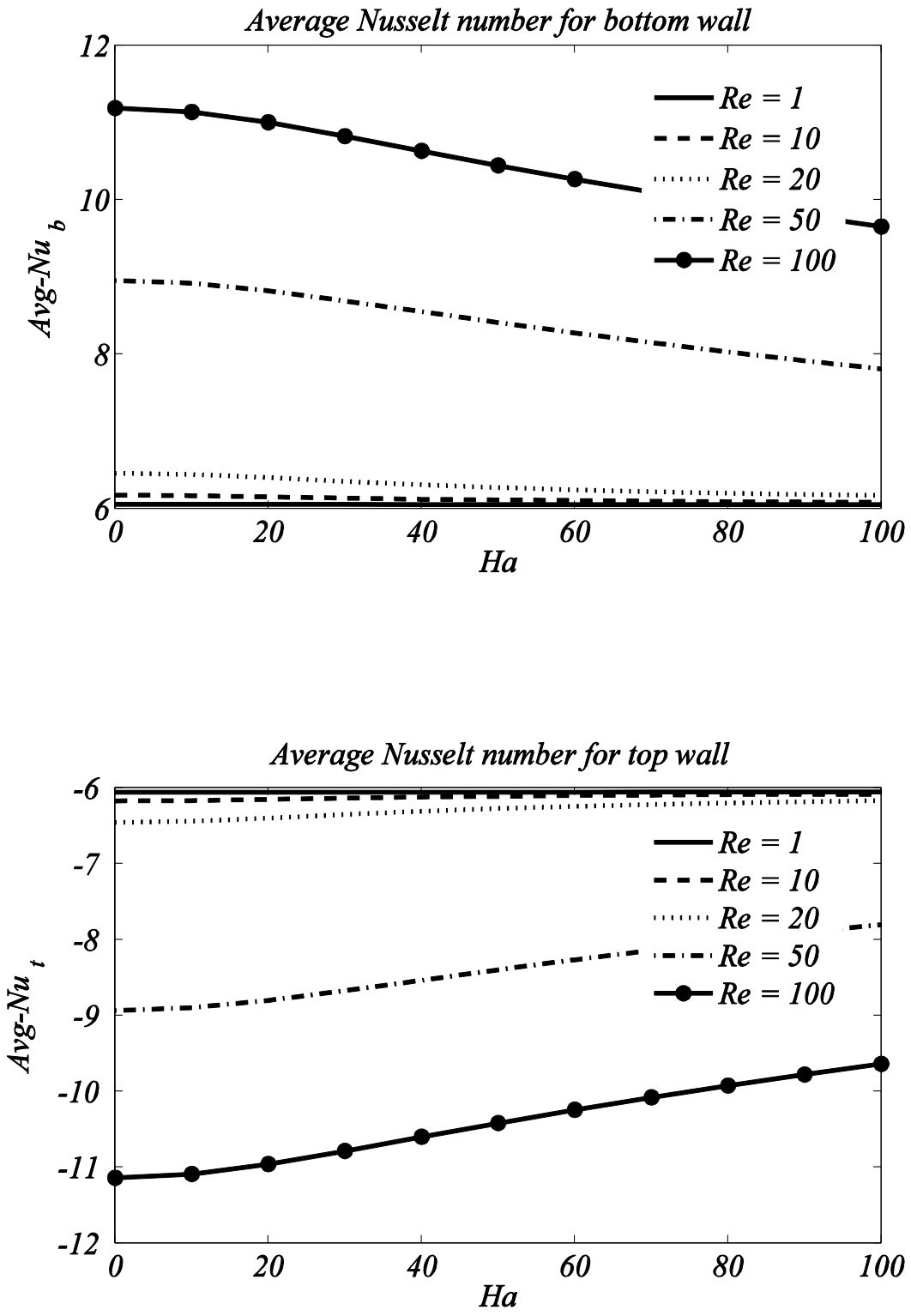

Figure 8.11: Average Nusselt for varying Re and Ha where $Q = 1, K = 1$ and $\mathrm{Ri} = 0.01$

8.3 Conclusions

This investigation comprises numerical study for MHD mixed convective heat flow in entrapped triangular cavities enclosing copper-based micropolar nanofluid in the presence of heat generation/absorption when uniform heat is supplied to both top and bottom oscillating lids of a container while inclined sides are maintained as cold. Equations describing the flow are modelled by using principles related to conservation of mass, linear momentum, angular momentum and energy. Penalty function is employed to eliminate pressure gradient terms from the governing expressions and then reduced equations of linear momentum along with angular momentum and energy equations are subjected to the Galerkin weighted residuals technique which results into a system of nonlinear algebraic expressions and that system is further simplified with the help of Newton Raphson technique to obtain a numerical solution. Obtained numerical results are shown against different values of pertinent flow parameters in the shape of isotherm contours, Nusselt and average Nusselt numbers. Our computations reveal that the transfer of energy process can be controlled through concentration of solid particles. Heat flows from top and bottom moving lids to the cold inclined walls of a cavity through well-defined energy transport phenomenon and is represented by isothermal lines. It is noticed that the augmentation in Hartmann number causes decrease in overall temperature gradient along bottom moving wall of the lower enclosure. Contrary to this, along top moving wall of the upper enclosure, augmentation in Hartmann number results into an enhancement in overall temperature gradient. Conduction regime is dominant for small values of microrotation parameter and large values of Hartmann number and convection regime is dominant for large Richardson number. Augmentation in concentration of solid particles enhances overall temperature gradient along bottom wall whereas overall heat transfer rate decreases along upper wall for large values of solid volume fraction.

References

Abaid-ur-Rehman, (2016), Study of fluid flow within a square cavity by using FEM, MS Dissertation, IIUI, Pakistan

Ahmed, S. E., Mansour, M. A., Hussein, A. K., & Sivasankaran, S. (2016). Mixed convection from a discrete heat source in enclosures with two adjacent moving walls and filled with micropolar nanofluids. Engineering Science and Technology, an International Journal, 19(1), 364-376.

Alloui, Z., & Vasseur, P. (2010). Natural convection in a shallow cavity filled with a micropolar fluid. International Journal of Heat and Mass Transfer, 53(13-14), 2750-2759.

Anandalakshmi, R., & Basak, T. (2011). Heatline analysis for natural convection within porous rhombic cavities with isothermal/nonisothermal hot bottom wall. Industrial & Engineering Chemistry Research, 51(4), 2113-2132.

Anandalakshmi, R., & Basak, T. (2013). Analysis of natural convection via entropy generation approach in porous rhombic enclosures for various thermal aspect ratios. International Journal of Heat and Mass Transfer, 64, 224-244.

Anandalakshmi, R., & Basak, T. (2013). Numerical simulations for the analysis of entropy generation during natural convection in porous rhombic enclosures. Numerical Heat Transfer, Part A: Applications, 63(4), 257-284.

Atalla, N., & Sgard, F. (2015). Finite element and boundary methods in structural acoustics and vibration. CRC Press.

Aydin, O., & Pop, I. (2005). Natural convection from a discrete heater in enclosures filled with a micropolar fluid. International journal of engineering science, 43(19-20), 1409-1418.

Aydın, O., & Pop, I. (2007). Natural convection in a differentially heated enclosure filled with a micropolar fluid. International journal of thermal sciences, 46(10), 963-969.

Aydin, O., Ünal, A., & Ayhan, T. (1999). Natural convection in rectangular enclosures heated from one side and cooled from the ceiling. International Journal of Heat and Mass Transfer, 42(13), 2345-2355.

Aydm, O. (1999). Aiding and opposing mechanisms of mixed convection in a shear- and buoyancy-driven cavity. International communications in heat and mass transfer, 26(7), 1019-1028.

Barletta, A., & Nield, D. A. (2009). Mixed convection with viscous dissipation and pressure work in a lid-driven square enclosure. International journal of heat and mass transfer, 52(19), 4244-4253.

Basak, T., Aravind, G., & Roy, S. (2009). Visualization of heat flow due to natural convection within triangular cavities using Bejan's heatline concept. International Journal of Heat and Mass Transfer, 52(11-12), 2824-2833.

Basak, T., Aravind, G., Roy, S., & Balakrishnan, A. R. (2010). Heatline analysis of heat recovery and thermal transport in materials confined within triangular cavities. International Journal of Heat and Mass Transfer, 53(19-20), 3615-3628.

Basak, T., Roy, S., & Babu, S. K. (2008). Natural convection and flow simulation in differentially heated isosceles triangular enclosures filled with porous medium. Chemical Engineering Science, 63(13), 3328-3340.

Basak, T., Roy, S., & Balakrishnan, A. R. (2006). Effects of thermal boundary conditions on natural convection flows within a square cavity. International Journal of Heat and Mass Transfer, 49(23-24), 4525-4535.

Basak, T., Roy, S., & Thirumalesha, C. (2007). Finite element analysis of natural convection in a triangular enclosure: effects of various thermal boundary conditions. Chemical Engineering Science, 62(9), 2623-2640.

Basak, T., Roy, S., Babu, S. K., & Balakrishnan, A. R. (2008). Finite element analysis of natural convection flow in a isosceles triangular enclosure due to uniform and non-uniform heating at the side walls. International Journal of Heat and Mass Transfer, 51(17-18), 4496-4505.

Basak, T., Roy, S., Ramakrishna, D., & Pop, I. (2010). Visualization of heat transport due to natural convection for hot materials confined within two entrapped porous triangular cavities via heatline concept. International Journal of Heat and Mass Transfer, 53(9-10), 2100-2112.

Basak, T., Roy, S., Ramakrishna, D., & Pop, I. (2010). Visualization of heat transport during natural convection within porous triangular cavities via heatline approach. Numerical Heat Transfer, Part A: Applications, 57(6), 431-452.

Baytas, A. C., & Pop, I. (1999). Free convection in oblique enclosures filled with a porous medium. International Journal of Heat and Mass Transfer, 42(6), 1047-1057.

Bejan, A. (2013). Convection heat transfer. John wiley & sons.

Ben-David, O., Levy, A., Mikhailovich, B., & Azulay, A. (2014). Gallium melting in a rectangular box. interface, 16, 17.

Bhardwaj, S., & Dalal, A. (2013). Analysis of natural convection heat transfer and entropy generation inside porous right-angled triangular enclosure. International Journal of Heat and Mass Transfer, 65, 500-513.

Bhardwaj, S., & Dalal, A. (2015). Effect of undulations on the natural convection heat transfer and entropy generation inside a porous right-angled triangular enclosure. Numerical Heat Transfer, Part A: Applications, 67(9), 972-991.

Bhardwaj, S., Dalal, A., & Pati, S. (2015). Influence of wavy wall and non-uniform heating on natural convection heat transfer and entropy generation inside porous complex enclosure. Energy, 79, 467-481.

Bin Kim, Jae Min Hyun, Ho Sang Kwak, G. (2001). Buoyant convection in a square cavity partially filled with a heat-generating porous medium. Numerical Heat Transfer: Part A: Applications, 40(6), 601-618.

Bourantas, G. C., & Loukopoulos, V. C. (2014). MHD natural-convection flow in an inclined square enclosure filled with a micropolar-nanofluid. International Journal of Heat and Mass Transfer, 79, 930-944.

Braunsfurth, M. G., Skeldon, A. C., Juel, A., Mullin, T., & Riley, D. S. (1997). Free convection in liquid gallium. Journal of Fluid Mechanics, 342, 295-314.

Chamkha, A. J. (2002). Hydromagnetic combined convection flow in a vertical lid-driven cavity with internal heat generation or absorption. Numerical Heat Transfer: Part A: Applications, 41(5), 529-546.

Cheng, T. S., & Liu, W. H. (2014). Effects of cavity inclination on mixed convection heat transfer in lid-driven cavity flows.Computers & Fluids, 100, 108-122.

Chiang, H., & Kleinstreuer, C. (1991). Analysis of passive cooling in a vertical finite channel using a falling liquid film and buoyancy-induced gas-vapor flow. International journal of heat and mass transfer, 34(9), 2339-2349.

Dalal, R., Naylor, D., & Roeleveld, D. (2009). A CFD study of convection in a double glazed window with an enclosed pleated blind. Energy and Buildings, 41(11), 1256-1262.

Das, D., Roy, M., & Basak, T. (2017). Studies on natural convection within enclosures of various (non-square) shapes–A review. International Journal of Heat and Mass Transfer, 106, 356-406.

Davidson, P.A. (2001). An introduction to magnetohydrodynamics, Cambridge University Press, Cambridge.

Dayem, A. M. A. (2006). Experimental and numerical performance of a multi-effect condensation–evaporation solar water distillation system. Energy, 31(14), 2710-2727.

Dhifaoui, B., Jabrallah, S. B., Belghith, A., & Corriou, J. P. (2007). Experimental study of the dynamic behaviour of a porous medium submitted to a wall heat flux in view of thermal energy storage by sensible heat. International journal of thermal sciences, 46(10), 1056-1063.

Du, Z. G., & Bilgen, E. (1992). Natural convection in vertical cavities with internal heat generating porous mediumFreie Konvektion in vertikalen Hohlräumen mit internem, wärmeerzeugenden porösen Medium. Wärme-und Stoffübertragung, 27(3), 149-155.

Eringen, A. C. (1966). Theory of micropolar fluids. Journal of Mathematics and Mechanics, 1-18.

Fusegi, T., & Hyun, J. M. (1994). Laminar and transitional natural convection in an enclosure with complex and realistic conditions. International journal of heat and fluid flow, 15(4), 258-268.

Ganzarolli, M. M., & Milanez, L. F. (1995). Natural convection in rectangular enclosures heated from below and symmetrically cooled from the sides. International Journal of Heat and Mass Transfer, 38(6), 1063-1073.

Garandet, J. P., Alboussiere, T., & Moreau, R. (1992). Buoyancy driven convection in a rectangular enclosure with a transverse magnetic field. International Journal of Heat and Mass Transfer, 35(4), 741-748.

Ghasemi, B., & Aminossadati, S. M. (2010). Periodic natural convection in a nanofluid-filled enclosure with oscillating heat flux. International Journal of Thermal Sciences, 49(1), 1-9.

Ghia, U. K. N. G., Ghia, K. N., & Shin, C. T. (1982). High-Re solutions for incompressible flow using the Navier-Stokes equations and a multigrid method. Journal of computational physics, 48(3), 387-411.

Gibanov, N. S., Sheremet, M. A., & Pop, I. (2016). Free convection in a trapezoidal cavity filled with a micropolar fluid. International Journal of Heat and Mass Transfer, 99, 831-838.

Gibanov, N. S., Sheremet, M. A., & Pop, I. (2016). Natural convection of micropolar fluid in a wavy differentially heated cavity. Journal of Molecular Liquids, 221, 518-525.

Gibanov, N. S., Sheremet, M. A., Oztop, H. F., & Nusier, O. K. (2017). Convective heat transfer of ferrofluid in a lid-driven cavity with a heat-conducting solid backward step under the effect of a variable magnetic field. Numerical Heat Transfer, Part A: Applications, 72(1), 54-67.

Gray, D. D., & Giorgini, A. (1976). The validity of the Boussinesq approximation for liquids and gases. International Journal of Heat and Mass Transfer, 19(5), 545-551.

Guo, G., & Sharif, M. A. (2004). Mixed convection in rectangular cavities at various aspect ratios with moving isothermal sidewalls and constant flux heat source on the bottom wall. International journal of thermal sciences, 43(5), 465-475.

Hannoun, N., Alexiades, V., & Mai, T. Z. (2003). Resolving the controversy over tin and gallium melting in a rectangular cavity heated from the side. Numerical Heat Transfer: Part B: Fundamentals, 44(3), 253-276.

Ho, C. J., Liu, W. K., Chang, Y. S., & Lin, C. C. (2010). Natural convection heat transfer of alumina-water nanofluid in vertical square enclosures: an experimental study. International Journal of Thermal Sciences, 49(8), 1345-1353.

Hoogendoorn, C. J. (1986, August). Natural convection in enclosures. In Proceedings of the 8th International Heat Transfer Conference (Vol. 1, pp. 111-120).

Hossain, M. A., & Wilson, M. (2002). Natural convection flow in a fluid-saturated porous medium enclosed by non-isothermal walls with heat generation. International Journal of Thermal Sciences, 41(5), 447-454.

Hsu, T. H. (1996). Natural convection of micropolar fluids in a rectangular enclosure. International journal of engineering science, 34(4), 407-415.

Hsu, T. H. (2000). Mixed convection in a rectangular enclosure with discrete heat sources. Numerical Heat Transfer: Part A: Applications, 38(6), 627-652.

Hsu, T. H., & Hong, K. Y. (2006). Natural convection of micropolar fluids in an open cavity. Numerical Heat Transfer, Part A: Applications, 50(3), 281-300.

Hsu, T. H., & Hsu, P. T. (1995). Thermal convection of micropolar fluids in a lid-driven cavity. International communications in heat and mass transfer, 22(2), 189-200.

Hsu, T. H., & Wang, S. G. (2000). Mixed convection of micropolar fluids in a cavity. International journal of heat and mass transfer, 43(9), 1563-1572.

Hsu, T. H., Hsu, P. T., & How, S. P. (1997). Mixed convection in a partially divided rectangular enclosure. Numerical Heat Transfer, Part A Applications, 31(6), 655-683.

Hsu, T. H., Hsu, P. T., & Tsai, S. Y. (1997). Natural convection of micropolar fluids in an enclosure with heat sources. International journal of heat and mass transfer, 40(17), 4239-4249.

Hyun, J. M., & Choi, B. S. (1990). Transient natural convection in a parallelogram-shaped enclosure. International Journal of Heat and Fluid Flow, 11(2), 129-134.

Ismael, M. A., Pop, I., & Chamkha, A. J. (2014). Mixed convection in a lid-driven square cavity with partial slip.International Journal of Thermal Sciences, 82, 47-61.

Iyican, L., Bayazitoglu, Y., & Witte, L. C. (1980). An analytical study of natural convective heat transfer within a trapezoidal enclosure. Journal of Heat Transfer, 102(4), 640-647.

Javed, T., Mehmood, Z. & Abbas, Z. (2017). Natural convection in square cavity filled with ferrofluid saturated porous medium in the presence of uniform magnetic field. Physica B: Condensed Matter 506, 122–132.

Jhumur, N. C., & Bhattacharjee, A. (2017). Unsteady MHD Mixed Convection inside L-shaped Enclosure in the Presence of Ferrofluid (Fe3O4). Procedia engineering, 194, 494-501.

Ji, T. H., Kim, S. Y., & Hyun, J. M. (2007). Transient mixed convection in an enclosure driven by a sliding lid. Heat and mass transfer, 43(7), 629.

Joudi, K. A., Hussein, I. A., & Farhan, A. A. (2004). Computational model for a prism shaped storage solar collector with a right triangular cross section. Energy Conversion and Management, 45(3), 391-409.

Kalaiselvam, S., Veerappan, M., Aaron, A. A., & Iniyan, S. (2008). Experimental and analytical investigation of solidification and melting characteristics of PCMs inside cylindrical encapsulation. International Journal of Thermal Sciences, 47(7), 858-874.

Kaluri, R. S., & Basak, T. (2010). Analysis of distributed thermal management policy for energy-efficient processing of materials by natural convection. Energy, 35(12), 5093-5107.

Kaluri, R. S., Anandalakshmi, R., & Basak, T. (2010). Bejan's heatline analysis of natural convection in right-angled triangular enclosures: effects of aspect-ratio and thermal boundary conditions. International Journal of Thermal Sciences, 49(9), 1576-1592.

Kamiyo, O. M., Angeli, D., Barozzi, G. S., Collins, M. W., Olunloyo, V. O. S., & Talabi, S. O. (2010). A comprehensive review of natural convection in triangular enclosures. Applied Mechanics Reviews, 63(6), 060801.

Karyakin, Y. E. (1989). Transient natural convection in prismatic enclosures of arbitrary cross-section. International journal of heat and mass transfer, 32(6), 1095-1103.

Kefayati, G. H. R. (2014). Natural convection of ferrofluid in a linearly heated cavity utilizing LBM. Journal of Molecular Liquids, 191, 1-9.

Kefayati, G. R. (2014). Simulation of ferrofluid heat dissipation effect on natural convection at an inclined cavity filled with kerosene/cobalt utilizing the Lattice Boltzmann method. Numerical Heat Transfer, Part A: Applications, 65(6), 509-530.

Kent, E. F. (2009). Numerical analysis of laminar natural convection in isosceles triangular enclosures for cold base and hot inclined walls. Mechanics Research Communications, 36(4), 497-508.

Kent, E. F., Asmaz, E., & Ozerbay, S. (2007). Laminar natural convection in right triangular enclosures. Heat and Mass Transfer, 44(2), 187.

Koca, A., Oztop, H. F., & Varol, Y. (2007). The effects of Prandtl number on natural convection in triangular enclosures with localized heating from below. International communications in heat and mass transfer, 34(4), 511-519.

Kodah, Z. H., Jarrah, M. A., & Shanshal, N. S. (1999). Thermal characterization of foam–cane (Quseab) as an insulant material. Energy conversion and Management, 40(4), 349-367.

Lage, J. L., & Bejan, A. (1993). The resonance of natural convection in an enclosure heated periodically from the side. International Journal of Heat and Mass Transfer, 36(8), 2027-2038.

Lee, T. S. (1984). Computational and experimental studies of convective fluid motion and heat transfer in inclined non-rectangular enclosures. International journal of heat and fluid flow, 5(1), 29-36.

Mahapatra, S. K., Nanda, P., & Sarkar, A. (2006). Interaction of mixed convection in two-sided lid driven differentially heated square enclosure with radiation in presence of participating medium. Heat and mass transfer, 42(8), 739-757.

Manca, O., Nardini, S., Khanafer, K., & Vafai, K. (2003). Effect of heated wall position on mixed convection in a channel with an open cavity. Numerical Heat Transfer: Part A: Applications, 43(3), 259-282.

Miroshnichenko, I. V., Sheremet, M. A., & Pop, I. (2017). Natural convection in a trapezoidal cavity filled with a micropolar fluid under the effect of a local heat source. International Journal of Mechanical Sciences, 120, 182-189.

Mistry, H., Dey, S., Bishnoi, P., & Castillo, J. L. (2006). Modeling of transient natural convection heat transfer in electric ovens. Applied thermal engineering, 26(17-18), 2448-2456.

Mohamad, A. A., & Viskanta, R. (1991). Transient low Prandtl number fluid convection in a lid-driven cavity. Numerical Heat Transfer, 19(2), 187-205.

Mohamad, A. A., & Viskanta, R. (1994). Flow structures and heat transfer in a lid-driven cavity filled with liquid gallium and heated from below. Experimental thermal and fluid science, 9(3), 309-319.

Mohamad, A. A., & Viskanta, R. (1995). Flow and heat transfer in a lid-driven cavity filled with a stably stratified fluid.Applied mathematical modelling, 19(8), 465-472.

Mojumder, S., Saha, S., Saha, S., & Mamun, M. A. H. (2015). Effect of magnetic field on natural convection in a C-shaped cavity filled with ferrofluid. Procedia Engineering, 105, 96-104.

Moukalled, F., & Darwish, M. (2010). Natural convection heat transfer in a porous rhombic annulus. Numerical Heat Transfer, Part A: Applications, 58(2), 101-124.

Nield, D. A., Bejan, A., & Nield-Bejan... (2006). Convection in porous media (Vol. 3). New York: springer.

Ostrach, S. (1972). Natural convection in enclosures. In Advances in heat transfer (Vol. 8, pp. 161-227). Elsevier.

Ostrach, S. (1988). Natural convection in enclosures. Journal of Heat Transfer, 110(4b), 1175-1190.

Oztop, H. F., & Dagtekin, I. (2004). Mixed convection in two-sided lid-driven differentially heated square cavity. International journal of heat and mass transfer, 47(8), 1761-1769.

Oztop, H. F., Varol, Y., & Pop, I. (2009). Investigation of natural convection in triangular enclosure filled with porous medi saturated with water near 4° C. Energy Conversion and Management, 50(6), 1473-1480.

Payvar, P. (1991). Laminar heat transfer in the oil groove of a wet clutch. International journal of heat and mass transfer, 34(7), 1791-1798.

Periyadurai, K., Muthtamilselvan, M., & Doh, D. H. (2016). Influence of inclined Lorentz force on micropolar fluids in a square cavity with uniform and nonuniform heated thin plate. Journal of Magnetism and Magnetic Materials, 420, 343-355.

Philip, J. R. (1982). Free convection at small Rayleigh number in porous cavities of rectangular, elliptical, triangular and other cross-sections. International Journal of Heat and Mass Transfer, 25(10), 1503-1509.

Prasad, A. K., & Koseff, J. R. (1996). Combined forced and natural convection heat transfer in a deep lid-driven cavity flow.International Journal of Heat and Fluid Flow, 17(5), 460-467.

Rabbi, K. M., Saha, S., Mojumder, S., Rahman, M. M., Saidur, R., & Ibrahim, T. A. (2016). Numerical investigation of pure mixed convection in a ferrofluid-filled lid-driven cavity for different heater configurations. Alexandria Engineering Journal, 55(1), 127-139.

Rahman, M. M. (2016). Influence of oriented magnetic field on natural convection in an equilateral triangular enclosure filled with water-and kerosene-based ferrofluids using a two-component nonhomogeneous thermal equilibrium model. Cogent Physics, 3(1), 1234662.

Ramakrishna, D., Basak, T., Roy, S., & Pop, I. (2012). Numerical study of mixed convection within porous square cavities using Bejan's heatlines: effects of thermal aspect ratio and thermal boundary conditions. International Journal of Heat and Mass Transfer, 55(21), 5436-5448.26.

Reddy, J. N. (1993). An introduction to the finite element method. New York: McGraw-Hill.

Reddy, J. N., & Gartling, D. K. (2010). The finite element method in heat transfer and fluid dynamics. CRC press.

Ridouane, E. H., Campo, A., & Chang, J. Y. (2005). Natural convection patterns in right-angled triangular cavities with heated vertical sides and cooled hypotenuses. Journal of Heat Transfer, 127(10), 1181-1186.

Sahar, G., Islam, T., Saha, S., & Islama, Q. (2007). Natural convection in a tilted isosceles triangular enclosure with discrete bottom heating. Science & Technology Asia, 12(4), 24-35.

Saleem, M., Asghar, S., & Hossain, M. A. (2011). Natural convection flow of micropolar fluid in a rectangular cavity heated from below with cold sidewalls. Mathematical and Computer Modelling, 54(1-2), 508-518.

Sarris, I. E., Lekakis, I., & Vlachos, N. S. (2002). Natural convection in a 2D enclosure with sinusoidal upper wall temperature. Numerical Heat Transfer: Part A: Applications, 42(5), 513-530.

Sathiyamoorthy, M., & Chamkha, A. (2010). Effect of magnetic field on natural convection flow in a liquid gallium filled square cavity for linearly heated side wall (s). International Journal of Thermal Sciences, 49(9), 1856-1865.

Scherer, C., & Figueiredo Neto, A. M. (2005). Ferrofluids: properties and applications. Brazilian Journal of Physics, 35(3A), 718-727.

Shankar, P. N., & Deshpande, M. D. (2000). Fluid mechanics in the driven cavity. Annual Review of Fluid Mechanics, 32(1), 93-136.

Sheikholeslami, M., & Gorji-Bandpy, M. (2014). Free convection of ferrofluid in a cavity heated from below in the presence of an external magnetic field. Powder Technology, 256, 490-498.

Sheremet, M. A., Pop, I., & Ishak, A. (2017). Time-dependent natural convection of micropolar fluid in a wavy triangular cavity. International Journal of Heat and Mass Transfer, 105, 610-622.

Sheremet, M., Grosan, T., & Pop, I. (2017). Natural convection in a triangular cavity filled with a micropolar fluid. International Journal of Numerical Methods for Heat & Fluid Flow, 27(2), 504-515.

Sigey, J. K., Gatheri, F. K., & Kinyanjui, M. (2004). Numerical study of free convection turbulent heat transfer in an enclosure. Energy Conversion and Management, 45(15), 2571-2582.

Sivakumar, V., Sivasankaran, S., Prakash, P., & Lee, J. (2010). Effect of heating location and size on mixed convection in lid-driven cavities. Computers & Mathematics with Applications, 59(9), 3053-3065.

Song, M., & Viskanta, R. (1994). Natural convection flow and heat transfer within a rectangular enclosure containing a vertical porous layer. International journal of heat and mass transfer, 37(16), 2425-2438.

Tiwari, R. K., & Das, M. K. (2007). Heat transfer augmentation in a two-sided lid-driven differentially heated square cavity utilizing nanofluids. International Journal of Heat and Mass Transfer, 50(9), 2002-2018.

Togrul, I. T. (2003). Determination of convective heat transfer coefficient of various crops under open sun drying conditions. International communications in heat and mass transfer, 30(2), 285-294.

Trevisan, O. V., & Bejan, A. (1986). Mass and heat transfer by natural convection in a vertical slot filled with porous medium. International Journal of Heat and Mass Transfer, 29(3), 403-415.

Vafai, K., & Tien, C. L. (1981). Boundary and inertia effects on flow and heat transfer in porous media. International Journal of Heat and Mass Transfer, 24(2), 195-203.

Varol, Y. (2011). Natural convection in porous triangular enclosure with a centreed conducting body. International Communications in Heat and Mass Transfer, 38(3), 368-376.

Varol, Y., Koca, A., & Oztop, H. F. (2006). Natural convection in a triangle enclosure with flush mounted heater on the wall. International Communications in Heat and Mass Transfer, 33(8), 951-958.

Varol, Y., Oztop, H. F., & Pop, I. (2008). Influence of inclination angle on buoyancy-driven convection in triangular enclosure filled with a fluid-saturated porous medium. Heat and Mass Transfer, 44(5), 617.

Varol, Y., Oztop, H. F., & Pop, I. (2009). Natural convection in right-angle porous trapezoidal enclosure partially cooled from inclined wall. International Communications in Heat and Mass Transfer, 36(1), 6-15.

Varol, Y., Oztop, H. F., & Varol, A. (2007). Effects of thin fin on natural convection in porous triangular enclosures. International Journal of Thermal Sciences, 46(10), 1033-1045.

Varol, Y., Oztop, H. F., & Varol, A. (2008). Free convection heat transfer and flow field in triangular enclosures filled with porous media. Journal of Porous Media, 11(1).

Varol, Y., Oztop, H. F., Mobedi, M., & Pop, I. (2008). Visualization of natural convection heat transport using heatline method in porous non-isothermally heated triangular cavity. International Journal of Heat and Mass Transfer, 51(21-22), 5040-5051.

Wahba, E. M., & Gadalla, M. A. (2009). Heat and fluid flow characteristics inside differentially heated square enclosures with single and multiple sliding walls. Heat Transfer—Asian Research, 38(7), 422-434.

Waheed, M. A. (2009). Mixed convective heat transfer in rectangular enclosures driven by a continuously moving horizontal plate. International Journal of Heat and Mass Transfer, 52(21), 5055-5063.

Wang, S. G., & Hsu, T. H. (1993). Natural convection of micropolar fluids in an inclined rectangular enclosure. Mathematical and computer modelling, 17(10), 73-80.

Wang, S., Faghri, A., & Bergman, T. L. (2010). A comprehensive numerical model for melting with natural convection. International Journal of heat and mass transfer, 53(9-10), 1986-2000.

Yamanaka, Y., Kakimoto, K., Ozoe, H., & Churchill, S. W. (1998). Rayleigh–Benard oscillatory natural convection of liquid gallium heated from below. Chemical Engineering Journal, 71(3), 201-205.

Yapici, K., & Obut, S. (2015). Laminar mixed-convection heat transfer in a lid-driven cavity with modified heated wall. Heat Transfer Engineering, 36(3), 303-314.

Zadravec, M., Hriberšek, M., & Škerget, L. (2009). Natural convection of micropolar fluid in an enclosure with boundary element method. Engineering analysis with boundary elements, 33(4), 485-492